Modelling oxygen transport and tissue damage in the human brain

Yidan Xue

Hertford College

Supervisor: Professor Stephen Payne

Department of Engineering Science

University of Oxford

A thesis submitted for the degree of *Doctor of Philosophy*

Trinity Term 2022

Modelling oxygen transport and tissue damage in the human brain

Yidan Xue

Hertford College, University of Oxford

Healthy brain function depends on continuous blood flow carrying oxygen and metabolites. Ischaemic stroke, caused by an occlusion in the cerebral artery that disrupts blood and oxygen supply and leads to irreversible tissue damage, is one of the leading causes of death and disability in the world.

To complement clinical trials to improve the functional outcomes of stroke patients, computational models have been developed to build a virtual platform (i.e. an *in silico* trial) to test the feasibility of new treatments. However, the role of the human cerebrovascular system in oxygen transport and tissue health remains poorly understood, which limits the utility of current brain models. Therefore, it is necessary to develop new models of oxygen transport and tissue damage for the human brain to improve our understanding of brain physiology and diseases.

This thesis first models oxygen transport in human capillary networks using a Green's function method. The effects of microembolism on oxygen delivery are simulated to derive a quantitative relationship between tissue hypoxia and vessel blockage. In human cortical columns supplied by a single penetrating arteriole, oxygen transport is simulated after the arteriole tree is occluded by a 25 μm microthrombus to mimic a rodent experiment of microembolism. Reasonable agreement has been shown between simulations and experiments measuring the spatial correlation between hypoxic regions and occlusion sites.

A novel 3-state cell death model and a thrombus extravasation model are then proposed to simulate the irreversible tissue damage caused by cerebral microvascular occlusions. The cell death model is further developed to simulate brain tissue damage over time under different ischaemic conditions. A full *in silico* trial of ischaemic stroke can thus be built by coupling the cell death model with existing whole brain models of cerebral blood flow and ischaemic stroke.

Acknowledgements

No man is an island. However, I found it quite difficult to become a piece of the continent during my DPhil, especially in the time of covid pandemic. This thesis would not be possible without the support of many people over the past 3 years, to whom I am truly grateful.

Firstly, I would like to thank my supervisor Stephen Payne for all his inspiration, guidance and support. Stephen introduced me into the exciting field of cerebral blood flow and metabolism, provided the foundation of this work and gave me the freedom to explore the topics that I am truly interested in. In particular, I would like to thank him for his extreme patience in replying to my endless emails and answering to my countless questions; his full support on my decisions; as well as his great mentorship beyond this thesis, especially on multidisciplinary collaborations, career development, proposal writing and presentation skills. I am deeply grateful to Stephen for the best supervision I could ever imagine before I came to Oxford.

I would like to thank all members of the Cerebral Haemodynamics Group. Special thanks go to Tamás Józsa for his critical comments on my work and helpful advice on my research and career; Wahbi El-Bouri for his innovative (now well-known) cerebral microvascular networks, which form the foundation of this thesis; Albert, Jiayu, Wei and Xi for inviting me to their college formals; Ice for her home-made cakes at the group meetings; Selena and Yahya for organising several social events.

I have been fortunate enough to work with Sissy Georgakopoulou and Ed van Bavel from Amsterdam University Medical Centre. Their novel experimental work adds to this theoretical thesis greatly. I would like to thank our other collaborators from the Netherlands: Nerea Arrarte Terreros, Nikki Boodt, Alfons Hoekstra, Charles Majoie, Claire Miller, Raymond Padmos, Noor Samuels and Max van der Kolk, with whom we have built an *in silico* trial of ischaemic stroke.

I would like to thank Eleanor Stride, Rebecca Shipley and Daniel Bulte for their insightful and constructive comments on this thesis. Many thanks to Vicente Grau for being my internal supervisor during the last year of my DPhil. I have been fortunate enough to be the lead tutor for B17 Biomechanics. I would like to thank Amy Zavatsky and Robin Cleveland for organising the course and all my fellow tutors. Beyond my DPhil, I am deeply grateful to Dong-hyuk Shin and Rudolf Hellmuth, who sparked my interest in biomedical engineering during my honours project at Edinburgh and helped me write and publish my first paper. I would also like to thank Sarah Waters for supporting me with my future research at the Mathematical Institute.

I would like to thank all my friends, especially to my great flatmate Ke for our chats, trips and dinners; Ali, Caroline, Guopeng, Matthew and Shree for giving me two happy years in the college accommodation; Allen for visiting me several times; Case for listening to Bach, Mozart and Beethoven together; Haolin and Pengling for their friendship from Edinburgh to Oxford; Imogen for her great support all the way; Jianing for operas in London; Qianbang for recommending me video games that I couldn't play well; Shiyang for face masks when they were all sold out; Wenxin, Xueshi and Youpeng for playing contract bridge and mahjong with me online every weekend.

Finally, I express my deepest gratitude to my parents, grandparents, aunt and uncle for their unconditional support. This thesis is dedicated to them.

Publications

Journal papers:

Xue, Y.*, Georgakopoulou, T.*, van der Wijk, A.-E., Józsa, T. I., van Bavel, E.*, Payne, S. J.* 2022. Quantification of hypoxic regions distant from occlusions in cerebral penetrating arteriole trees. *PLOS Computational Biology.* **18**(8), e1010166. *: co-first/co-senior authors.

Miller, C., Padmos, R. M., van der Kolk, M., Józsa, T. I., Samuels, N., **Xue, Y.**, Payne, S. J., Hoekstra, A. G. 2021. In Silico Trials for Treatment of Acute Ischemic Stroke: Design and Implementation. *Computers in Biology and Medicine.* **137**, 104802.

Xue, Y., El-Bouri, W. K., Józsa, T. I. and Payne, S. J. 2021. Modelling the effects of cerebral microthrombi on tissue oxygenation and cell death. *Journal of Biomechanics.* **127**, 110705.

Conference abstracts as presenter:

Xue, Y., Józsa, T. I. and Payne, S. J. 2022. *Modelling human cerebral tissue damage caused by acute ischaemic stroke.* 9th World Congress of Biomechanics, Taipei. Presentation.

Xue, Y., Payne, S. J. 2020. *Modelling brain metabolism in ischaemic stroke: oxygen consumption and energy budget.* VPH2020 (online), Paris, France. Poster.

Conference abstracts as co-author:

Padmos, R. M., Józsa, T. I., **Xue, Y.**, Payne, S. J. and Hoekstra, A. G. 2022. *Modelling Infarct Growth During Acute Ischeamic Stroke.* The 17th International Symposium on Biomechanics in Vascular Biology and Cardiovascular Disease, Rotterdam, the Netherlands.

Payne, S. J., Józsa, T. I., **Xue, Y.**, Wang, J., Howman, J. C., Newsome, M. Wei, W., Bing, Y., Chen, X., Daher, A., Tong, Z., and El-Bouri, W. K. 2022. *Mathematical models of the cerebral microcirculation in health and pathophysiology.* 7th International Conference on Computational and Mathematical Biomedical Engineering (CMBE2021), Milan, Italy.

Padmos, R. M., Józsa, T. I., **Xue, Y.**, Payne, S. J. and Hoekstra, A. G. 2022. *A multi-scale tissue infarction model for modelling acute ischaemic stroke.* 7th International Conference on Computational and Mathematical Biomedical Engineering (CMBE2021), Milan, Italy.

Contents

Nomenclature

Latin symbols

A - Alive compartment

$\mathbf{b}$ - Body force

B - Blockage fraction

B_0 - Initial blockage fraction

C - Core compartment (only used in a cell death model)

C - Constriction fraction

C_b - Blood oxygen concentration

C_t - Tissue oxygen concentration

$\overline{C_b}$ - Volume-averaged oxygen concentration in the blood vessel

C_{Hb} - Oxygen binding capacity of red blood cells

C_Ω - Concentration of the substrate Ω

$\dot{C}_f$ - Fast core formation

$\dot{C}_s$ - Slow core formation

d - Distance

D - Vessel diameter

D - Dead compartment (in the cell death model)

D_F - Diameter of the feeding vessel

D_t - Diffusion coefficient of oxygen in brain tissue

D_α - Diameter of a child branch

D_β - Diameter of the other child branch

D_Ω - Diffusion coefficient of the substrate Ω

FQ_B - Fraction of blood flow entering a child branch

FQ_E - Fraction of red blood cells entering a child branch

G - Green's function

$\overline{G}$ - Averaged Green's function with respect to angular position

h - Vessel wall thickness

H - Haematocrit

H - Hypoxic fraction (only used in the sigmoidal function)

H - Healthy compartment (only used in a cell death model)

H_D - Discharge haematocrit

H_T - Tube haematocrit

I - Identity matrix

j - Oxygen flux across the vessel wall per unit area

J - Total oxygen flux across the vessel walls

J - Jacobian matrix (only used in analysing the model)

k - Eccentricity of elliptic integral

k_b - Backward rate

k_{cf} - Time constant of fast core formation

k_{cs} - Time constant of slow core formation

k_d - Decay constant of vulnerability

k_e - Time constant of thrombus extravasation

k_f - Forward rate

k_m - Time constant of metabolism

k_p - Time constant of penumbra formation

k_r - Time constant of toxin removal

k_s - Time constant of storage

k_t - Time constant of toxin production

k_{pc} - Time constant of pericyte constriction

$\overline{k_b}$ - Backward rate constant

$\overline{k_f}$ - Forward rate constant

K - Intravascular resistance to oxygen diffusion

K_{O_2} - Oxygen permeability in vessel wall

$\mathbf{K}$ - Permeability tensor

L - Vessel length

L_c - Characteristic length

M_0 - Maximum oxygen consumption rate

N - Hill equation exponent

p - Blood pressure

P - Probability

P - Penumbra compartment (in the cell death model)

P_0 - Michaelis constant for oxygen consumption

P_{50} - PO_2 at half maximal haemoglobin saturation

Pe - Péclet number

P_b - Blood PO_2

P_t - Tissue PO_2

P_v - PO_2 at vessel surface

P^* - Penumbra at the stable node

q - Distribution of source strengths

q_0 - Distribution of source strength per unit length

q_j - Source strength of segment j

q_v - Oxygen diffusive efflux rate per unit length

Q - Flow rate

r - Radial position

Re - Reynolds number

R - Vessel radius

R_t - Krogh cylinder radius

R_v - Vessel radius in the Krogh cylinder model

S - Source term

S - Storage compartment (in the cell death model)

S_h - Healthy storage

S_Ω - Sum of production or loss of the substrate Ω

S^* - Storage at the stable node

t - Time

T - Toxin compartment

T_d - Threshold of toxin to activate the cell death

T_p - Threshold of toxin to propagate the vulnerability

T^* - Toxin at the stable node

$\dot{T}_p$ - Toxin production

$\dot{T}_r$ - Toxin removal

$\mathbf{u}$ - Velocity

U - Average velocity

$\mathbf{v}$ - Convective velocity

V - Average convective velocity

V - Vulnerable compartment/Vulnerability (in the cell death model)

V_b - Blood volume in a vessel

V_{nf} - Fraction of no-flow vessels

V_t - Brain tissue volume

Wo - Womersley number

W - Body weight

$\mathbf{x}$ - A point representing a tissue element

$\mathbf{x}^*$ - A point source on the vessel surface

z - Axial position

Greek symbols

α - Oxygen solubility

α_b - Effective solubility of oxygen in blood

α_t - Effective solubility of oxygen in brain tissue

$\dot{\gamma}$ - Strain rate

Γ - Conductance matrix

δ - Distance from a hypoxic pixel to its closest microsphere

δ_3 - Three-dimensional Dirac delta function

θ - Angular position

λ - Eigenvalue of a matrix

μ - Blood viscosity

μ_{app} - Apparent viscosity

μ_p - Plasma viscosity

μ_{rel} - Relative viscosity

μ_∞ - Casson viscosity

ν - Kinematic viscosity

ρ - Blood density

ρ_t - Brain tissue density

τ - Shear stress

τ_0 - Yield stress

ϕ_j - Source strength of tissue element j

ω - Angular frequency

Abbreviations

AIS - Acute ischaemic stroke

ATP - Adenosine triphosphate

BBB - Blood brain barrier

CBF - Cerebral blood flow

CBF_h - Healthy perfusion

CBV - Cerebral blood volume

CCA - Common carotid artery

$CMRO_2$ - Cerebral metabolic rate of oxygen

CT - Computed tomography

DWI - Diffusion-weighted imaging

ECA - External carotid artery

ICA - Internal carotid artery

INSIST - IN Silico clinical trials for treatment of acute Ischemic STroke

LBM - Lattice Boltzmann method

mRS - Modified Rankin scale

MCA - Middle cerebral artery

MRI - Magnetic resonance imaging

MTT - Mean transit time

ODE - Ordinary differential equation

OEF - Oxygen extraction fraction

PBS - Phosphate buffered saline

PDE - Partial differential equation

PO_2 - Partial pressure of oxygen

$PO_{2,\ in}$ - Inlet blood PO_2

$PO_{2,\ h}$ - Healthy PO_2 in precapillary arterioles

rCBF - Relative cerebral blood flow (of healthy condition)

RBC - Red blood cell

SO_2 - Oxygen saturation of haemoglobin

Chapter 1

Introduction

1.1 Background

The human brain is a highly complex organ that receives information from the environment, makes decisions and controls behaviour. Despite only taking up 2% of the human body weight, the brain consumes 20% of the total energy. The healthy function of brain thus depends on continuous blood supply that brings oxygen and glucose and takes away waste products. In order to deliver the blood to every part of the brain efficiently, the cerebral vasculature has a multi-scale hierarchical structure from large arteries (diameter ~ 1 cm) to capillaries (diameter ~ 10 μm). The arteries mainly supply the pial vessels on the cortex surface in two-dimensions, which feed into penetrating arterioles perpendicular to the cortex surface connecting to isotropic capillary beds [1].

The cerebral microvasculature has a relative robust structure, thanks to the interconnected capillaries; however, the large arteries are much more vulnerable to occlusions. When an artery is blocked by an clot, the blood supply of its downstream regions will be disturbed, leading to energy impairment followed by irreversible tissue damage. This condition is known as ischaemic stroke and accounts for 85% of all stroke

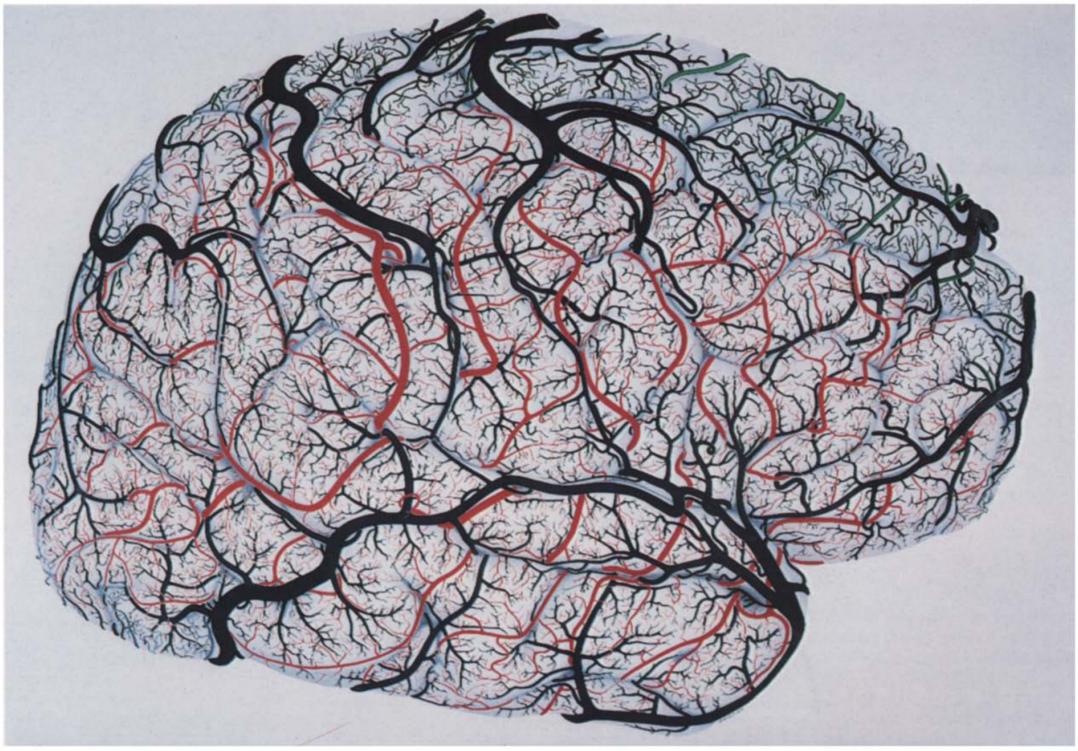

Figure 1.1: Drawing of the cortical pial vessels, where the red vessels bifurcate from the middle cerebral artery, the green vessels bifurcate from the anterior cerebral artery, the blue vessels bifurcate from the posterior cerebral artery and the black vessels are veins. Reproduced with permission from [2].

cases, whilst the other 15% of cases are haemorrhagic stroke.

Ischaemic stroke is one of the leading causes of death and disability in the world. Even within the UK, more than 100,000 people have a stroke each year, which results in more than 30,000 deaths [3]. Although the fatality rate of ischaemic stroke has reduced recently, favourable functional outcomes cannot always be achieved in all patients. Evidence from a recent multi-centre clinical study [4] shows that about half of the stroke patients cannot walk without assistance even after an intra-arterial intervention (e.g., mechanical removal of a clot from the occluded vessels). The disabilities caused by ischaemic stroke have a great impact on individuals, families and the healthcare system. In the UK, the societal cost of stroke is estimated to be £26 billion a year [5].

1.2 Current *in silico* trials and brain models

To improve clinical outcomes for ischaemic stroke patients, novel treatment techniques and strategies are required. Most new treatments and interventions are developed, optimised and carefully evaluated through pre-clinical experiments and clinical trials, before they are permitted to be used and commercialised. However, these clinical trials can be very expensive and time-consuming. Additionally, it is often difficult to determine the reason(s) for new interventions being unsuccessful. These limitations motivate the development of *in silico* trials, which use mathematical models to help to develop and test new treatments and biomedical products [6].

In silico trials depend on patient-specific modelling within a cohort of virtual patients. There has been tremendous progress in patient-specific simulations, especially motivated by the initiatives of the Physiome Project [7] and the Virtual Physiological Human [8]. These models include haemodynamics [9], hearts [10], lungs [11], livers [12], bones [13], pathological conditions like atherosclerosis [14] and cerebral aneurysm [15] and their treatments like thrombectomy [16] and coiling [17].

Despite the extreme complexity of the human brain, there has been a rapid development of its modelling in the past decade [1, 18, 19]. Novel brain models have been developed from the cellular scale [20–22], to the microvascular scale [23–29] and the organ scale [30–38] on diverse topics of physiology, pathology, fluid mechanics, solid mechanics and their biomedical applications. This momentum is highlighted by a recently founded journal *Brain Multiphysics*[1] dedicated to the development of understanding and modelling of the brain.

In the Cerebral Haemodynamics Group at the University of Oxford (now also at National Taiwan University), the research primarily focuses on modelling the cerebral blood flow (CBF) and its application in cerebral autoregulation [39] and ischaemic stroke

[1] `https://www.sciencedirect.com/journal/brain-multiphysics`

[21, 29, 36, 37, 40–43]. These models motivate and form part of the foundation of the INSIST (IN-Silico trials for treatment of acute Ischemic STroke) project[2] [44], which aims to build a computational platform to test novel interventions for ischaemic stroke. Within the project models of virtual patients, thrombosis and thrombolysis [45], thrombectomy [16, 46] and CBF [29, 36, 37, 47, 48] have been developed. In addition, the multidisciplinary team of clinicians and biologists has designed and conducted clinical studies [49–52] and animal experiments [53–56] to aid in the development of numerical models. Recent progress of the INSIST project has been reported in a special issue on thrombus mechanics [57].

1.3 Motivation

These *in silico* models mainly simulate the effects of ischaemic stroke on blood flow both locally and globally. However, little is known about the effects of ischaemia on oxygen transport and irreversible tissue damage in the human brain. Unlike blood flow, oxygen transport has a diffusion component along the gradient of partial pressure of oxygen (PO_2), which is mainly due to the oxygen metabolism of brain tissues. This means that the quantity of oxygen being delivered cannot simply be assumed to be proportional to the blood supply. Moreover, the tissue damage response to ischaemic stroke has been found highly complex [58], which depends on multiple factors including duration, severity and location of ischaemia and tissue type. The lack of models for oxygen transport and tissue damage significantly limits our understanding of the human brain physiology and the application of *in silico* brain models.

The primary aims of this thesis are thus to develop an oxygen transport model for the human microvasculature to aid in understanding the relationship between microvascular geometry and tissue oxygenation under both physiological and pathological conditions; and to develop a tissue damage model to apply these micro-scale simulation results to

[2] `https://www.insist-h2020.eu`

simulate the hypoxic tissue damage in the macro-scale stroke models. In this thesis, the micro-scale is the length scale of cerebral microvasculature (~ 10 μm), where individual capillary can be identified [59]. The macro-scale is the length scale of a clinical imaging voxel (~ 1 mm), where simulation results can be compared with clinical imaging data directly [28].

At the micro-scale, the impact of micro-occlusions, which can be caused by clot fragments after a clot is removed from the blocked vessels mechanically [60], are of particular interest. Firstly, micro-occlusions are one potential cause of the 'no-reflow phenomenon' [61, 62], which significantly affects the clinical outcome after stroke treatment. Secondly, there are recent *in vivo* microembolism experiments yielding quantitative data using a rodent model [53–56] that enable validation for the micro-scale brain models of blood flow and oxygen transport.

At the macro-scale, a mathematical model should be developed to simulate the irreversible tissue damage based on hypoxia caused by microemboli occlusions. The model should predict the brain tissue damage over time under different levels of occlusions, so that the volume of tissue damage can be quantified in organ-scale models in scenarios of microemboli shower. In addition, the cell death model should be further developed to simulate the tissue damage caused by hypoperfusion following an ischaemic stroke [58, 63–65]. The model should also predict the volumes in different tissue states defined by clinicians, namely healthy, core and penumbra [66]. Hence the simulation results can be validated against the clinical data, e.g. from the MR CLEAN dataset [4]. The cell death model can then be coupled in the future with existing stroke models to build a full *in silico* trial of ischaemic stroke.

1.4 Structure of the thesis

Before presenting new models, Chapter 2 provides a more detailed overview of brain physiology and ischaemic stroke. The review starts from the vascular system of the human brain and how to simulate the blood flow passing through this network and the oxygen transport to tissues surrounding it. Then it focuses on ischaemic stroke and existing *in silico* models. Finally, it reviews the cerebral tissue damage caused by ischaemic stroke, highlighting the key role of cell death models in simulating the disease.

Following the literature review, the thesis consists of two parts: Micro-scale: oxygen transport and microembolism (Part I); and Macro-scale: tissue damage (Part II). Part I on micro-scale models is subdivided into two chapters. In Chapter 3, oxygen transport was simulated using a Green's function method in statistically generated capillary cubes based on the human brain data. In addition, micro-occlusions were simulated in a capillary cube to quantify the effects of different levels of microembolism on tissue perfusion and hypoxia. Chapter 4 extends the oxygen transport simulation to a column of cortical tissue supplied by a penetrating arteriole (i.e. a cortical column). This chapter focuses on the spatial correlation between hypoxic regions and a single occlusion site caused by a microsphere of 25 μm in diameter. The same microembolism experiment was also carried out using a rodent model. Distant hypoxic regions away from the occlusion sites were found in both experiments and simulations. To quantify the distribution of these distant hypoxic regions, two novel distance analyses were designed and applied to simulation results and experimental data in exactly the same way, enabling a quantitative comparison between the two. The promising agreement between simulations and experiments indicates the potential role of such numerical models in understanding the hypoxic responses of brain tissues to micro-occlusions.

Part II is also subdivided into two chapters. Chapter 5 develops a 3-state cell death model based on tissue hypoxia and a thrombus extravasation model. Depending upon

the quantitative relationship between tissue hypoxic fraction and vessel blockage fraction (Chapter 3), these models are able to simulate the tissue damage as a function of time under different levels of micro-occlusions. In Chapter 6, the cell death model was further developed to simulate the ischaemic tissue damage following a stroke. Several cell death models were proposed to simulate several scenarios including continued tissue damage or penumbra recovery after the treatment and tissue damage propagation due to the accumulation of toxins. The cell death model was coupled with organ-scale models of blood flow and cerebral perfusion to predict the volumes of brain tissues at different states at different times. Using this workflow of *in silico* models, the effects of treatment time on final infarct volumes and clinical outcomes were simulated in a cohort of virtual stroke patients.

Finally, the research findings of this thesis are summarised in Chapter 7. Possible future work is suggested to improve the models developed in this thesis and broaden their applications.

Chapter 2

Literature review

2.1 Cerebrovascular system

The human brain is a highly complex organ comprising hundreds of billions of brain cells. The interaction and cooperation of these cells lead to perceptions, thoughts, memories and other basic body functions. These activities consume about 20% of the total energy supply, although the brain only takes up 2% of human body weight [1]. The energy supply is maintained by the continuous bloodstream carrying oxygen, glucose and other metabolites inside the cerebral vasculature. Due to the limited storage of oxygen and glucose in brain cells, the cerebral vasculature needs to be tightly coupled with the local energy demand, which results in its multi-scale structure.

2.1.1 Cerebral vasculature

The human cerebral vasculature consists of arteries, arterioles, capillaries, venules and veins, which is consistent with the structure inside other parts of the body. The heart pumps out oxygen-rich blood that feeds the brain through major arteries. The left and right internal carotid arteries supply the brain from two sides of the neck. The left and

right vertebral arteries supply the brain from the back of the neck, and join together to form the basilar artery. With six other major vessels supplying blood to most of the brain regions, these nine vessels form the circle of Willis (see Fig. 2.1) [67]. The circle of Willis guarantees the robustness of blood supply, where there are normally two routes from one point to the other. That is to say that the blood can still be re-routed and supplied to the entire brain, when one of these vessels is occluded. However, variations in the structure of the circle of Willis have been found in more than half of the population [68, 69]. This can be seen as one of the reasons why stroke patients experience varying degrees of hypoperfusion and thus have different post-treatment brain tissue outcomes [70], which will be discussed later.

At a smaller scale, the pial arteries bifurcate from the major arteries and distribute the blood to individual regions of the brain (see Fig.2.2). These arteries mainly supply blood upon the cortex surface. Their inter-connected structure also enables them to provide secondary collateral flow in addition to the circle of Willis during an ischaemic stroke.

From these pial arteries, the root-shape arterioles penetrate through the grey matter and eventually their bifurcating ends become connected to the capillary network. Figure 2.3 presents the cerebral microvasculature in the human brain [24], where the large vessels along the vertical direction are the penetrating vessels. The penetrating arterioles have a diameter from 6 to 40 μm, with an average of about 10 μm [73]. The penetrating arterioles play a key role in delivering the blood and oxygen in the third dimension (perpendicular to the cortex surface) adding to pial arteries. In addition, each penetrating arteriole supplies its own territory of microvasculature and brain tissue, partially due to the high flow resistance of capillary beds. Hence the occlusion of a single penetrating arteriole can lead to a local region of hypoperfusion and then infarction [74–76].

After a few orders of branches of pre-capillary arterioles (note that these have been newly termed the arteriole-capillary transition in a recent review [73]) from the penetrating

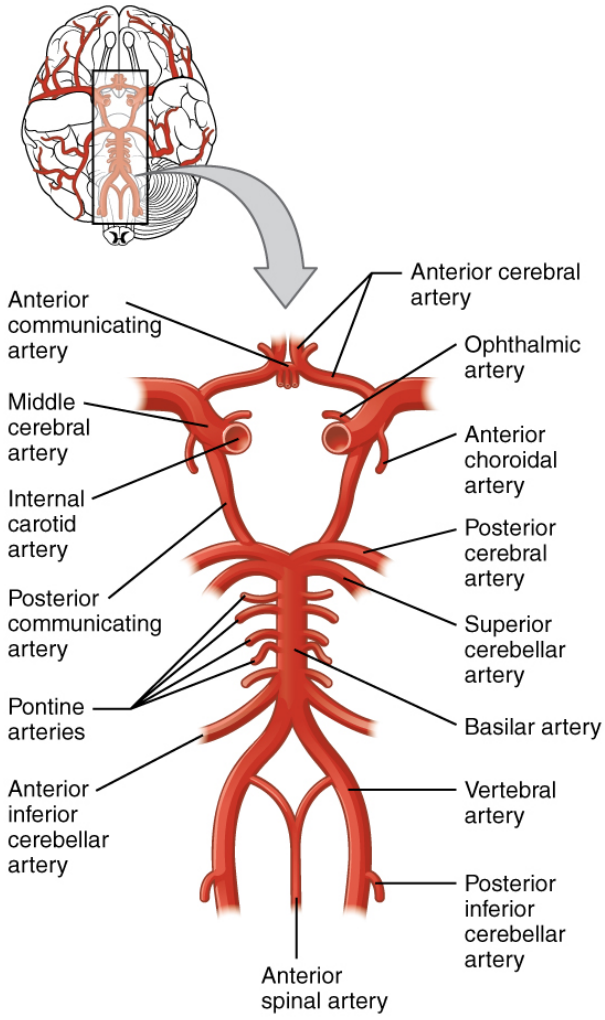

Figure 2.1: Schematic of the circle of Willis. Reproduced without change from [71] under license `https://creativecommons.org/licenses/by/4.0/`.

arteriole trunk, blood and hence oxygen are fed into capillaries where the exchange of metabolites and wastes mainly occur. The capillaries are the smallest vessels in the brain with a diameter from 1.5 to 8 μm [73]. The capillary bed has an isotropic and mesh-like structure, which is highly interconnected and thus more robust to occlusions than penetrating arterioles.

The capillaries join to form penetrating venules after about 6 orders of branches from the penetrating arterioles [77, 78]. The penetrating venules have similar structures to penetrating arterioles, but with larger diameters [2] and smaller vessel density [79]. These

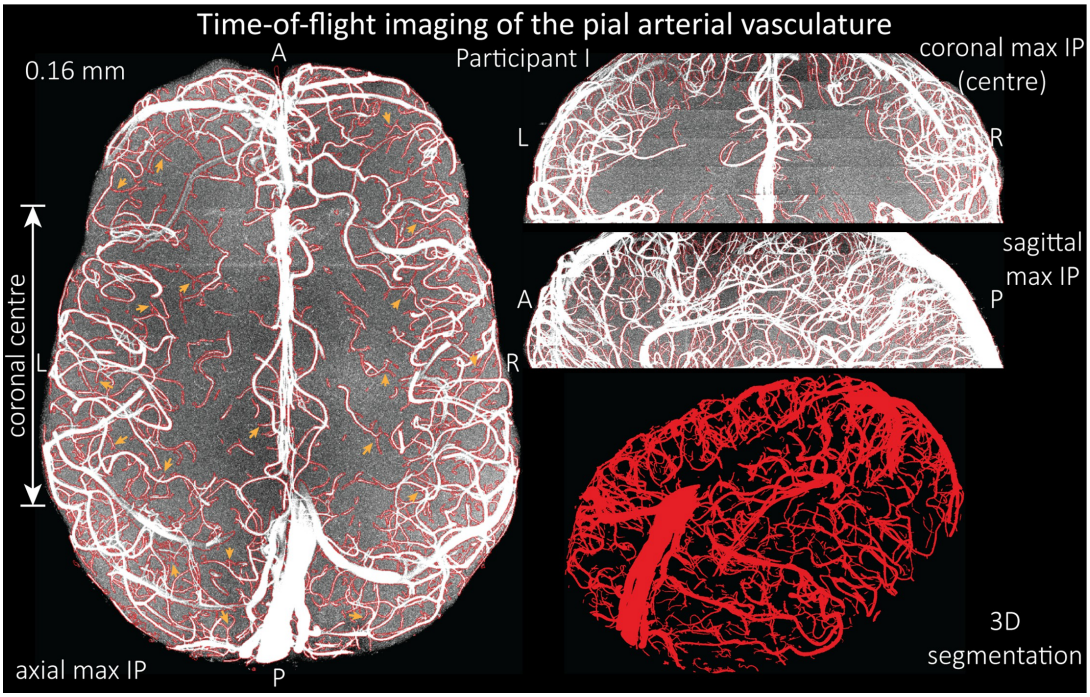

Figure 2.2: Imaging of the pial arterial vasculature of the human brain. Reproduced without change from [72] under license `https://creativecommons.org/licenses/by/4.0/`.

penetrating venules transport the deoxygenated blood back to the pial veins on the cortex surface (see Fig. 1.1). In the end, the blood drains through the sinuses from the front to the back of the head, and finally flows back to the heart through the jugular veins at the neck.

2.1.2 Models of human cerebral vasculature

The models of cerebral vasculature will be reviewed over three length scales from large vessels ($\sim$ 1 mm) to penetrating vessels ($<$ 100 μm) and finally down to capillaries ($\sim$ 10 μm). Although there are many more models of the cerebral vasculature of animals (mainly rodents), the review will focus on the human models since the aim of this thesis is to simulate the oxygen transport and tissue damage in the human brain. Note that the same preference of human over animal models will be made in the rest of this thesis, except

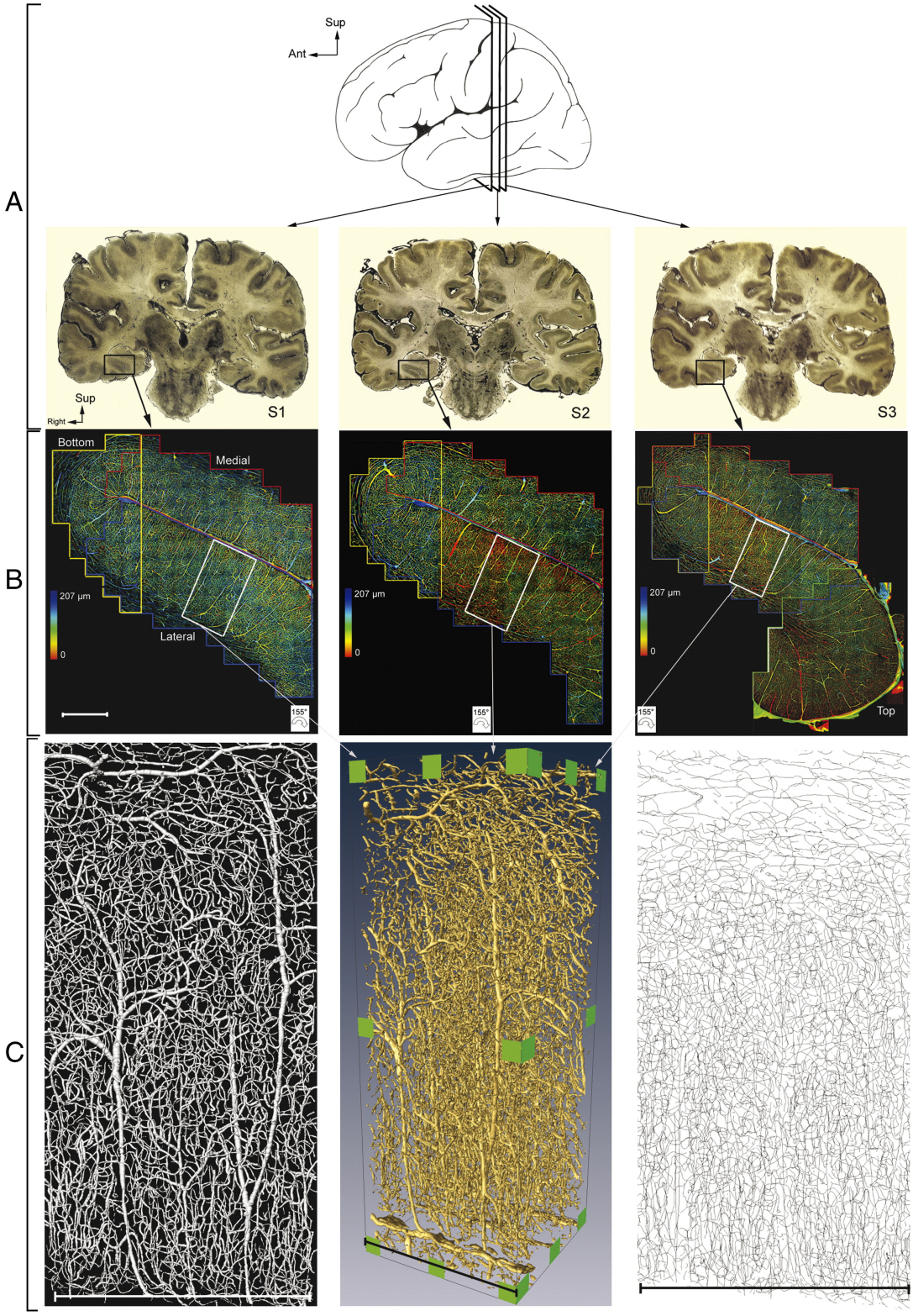

Figure 2.3: Visualisation of cerebral microvasculature in the human brain. Reproduced with permission from [24].

for Chapter 4 where the computational models will be validated against experimental data from rodent models.

The large arteries and veins can be easily imaged in the human brain. As a result, the blood flow in the large arteries has been modelled for more than 50 years [80]. A detailed review on the development of these models can be found in Chapter 2 of [1]. One notable study conducted by Cebral et al. [81] built the model of brain arteries from patient-specific magnetic resonance imaging (MRI). Another model by Padmos et al. [37] built from patient-specific computed tomography (CT) by using a semi-automated artery modelling tool [82]. The Padmos model will later be coupled with a cerebral perfusion model in Section 2.4.4.

By comparison, models of human cerebral microvasculature remain very limited, due to the 'imaging gap' between the resolution of non-invasive imaging techniques and the length scale of cerebral microvasculature. To the best of the author's knowledge, the only detailed human cerebral microvascular data[1] were collected by Duvernoy et al. [2] from 25 patients more than 40 years ago.

Cassot et al. [23] obtained high-resolution ($1.22 \times 1.22 \times 3$ μm^3) 3D images of sulci in the temporal lobe (as shown in Fig. 2.3) from these india ink-injected human brain slices [2] using a confocal laser microscopy. Then a threshold was applied to separate blood vessels (in white) from tissue (in black). The centrelines of blood vessels were determined using a modified distance ordered homotopic (topologically equivalent) thinning method [84]. The radius of each vessel was calculated as the shortest distance from its centreline to the background (brain tissues). Hence the *in vivo* microvascular network was represented by a dataset comprising the centrelines and radii of blood vessels.

Penetrating vessels were extracted from the network using a threshold of vessel resistance,

[1]It should be noted that there have been recent advances in imaging an intact human organ with a resolution down to 2 μm [83], which can potentially play a valuable role in understanding the human cerebral microvasculature.

where the remaining vessels with a resistance above the threshold were identified as capillaries. The vessel resistance was calculated by assuming Poiseuille flow and constant haematocrit of 0.45 in each vessel and using an empirical function of viscosity [85], which will be introduced in Section 2.2. The branching pattern of each penetrating vessel was described by a diameter-defined Strahler system [86]. This workflow enables quantitative studies of the geometry and topology of human cerebral microvasculature [23, 24, 26, 79] following the work of Duvernoy et al. [2], which are invaluable in the field.

These data were used by Linninger et al. [25] to generate human cerebral microvascular networks at the length scale of millimetres, which are comparable to MRI resolution. The same data were also used by El-Bouri and Payne to generate cerebral capillary cubes [27] and penetrating vessels [87] using a statistical algorithm [88]. These 3D human brain networks form the foundation of this thesis.

2.1.3 Statistical cerebral microvascular networks

The pressure-flow relationship is of particular interest in microvascular blood flow and oxygen transport problems. In a microvascular network, it is thus reasonable to treat vessel junctions as nodes and blood vessels as 1D straight pipes connecting these nodes. Hence microvascular networks can be characterised and generated using node coordinates and their connectivity.

A modified spanning tree method [88] was implemented to generate cerebral capillary networks. Firstly, nodes were randomly generated in a cube with additional nodes seeded in the regions of low node density. From the node pair of shortest distance, a tree was generated by repeatedly establishing shortest connections between a node outside of the tree and a node inside the tree. Then the same algorithm was run on the terminal nodes of the tree to build a inter-connected network. Finally, several vessel length filters were applied to the network to fit the vessel length distribution with the experimental data of the human brain [23]. The distribution of vessel diameter was also fitted with

the same experimental study [23]. The algorithm to generate these networks have been introduced in detail in previous studies [88, 89]. A comparison of geometric statistics between generated networks and experimental data can be found in Table 3.1 of [88].

Spatial periodicity was then imposed on these capillary networks to satisfy the periodic assumption used in homogenisation techniques [59]. A typical periodic capillary cube is shown in Fig. 2.4 [27]. Under the assumption of local periodicity, a scale separation can be defined between the micro-scale and the macro-scale (which consists of periodic micro-scale units). Homogenisation techniques can thus be applied to these capillary networks, where cerebral microvasculature can be treated as a continuum porous medium at the tissue scale. The porous medium model of capillary beds can then be coupled with network models of penetrating vessels to construct millimetre-scale models easily [28], which will be further introduced in Section 2.2.6.

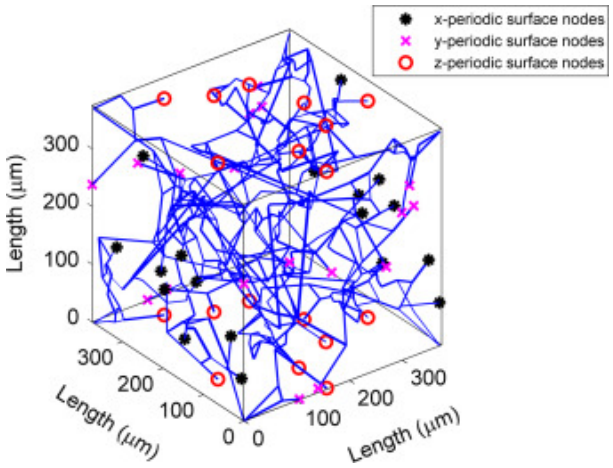

Figure 2.4: A typical periodic capillary network with a voxel size of 375 μm. Reproduced with permission from [27].

The models of penetrating arterioles and venules were constructed using a density-filling algorithm [87]. On the initial trunk of a penetrating vessel, bifurcating nodes were generated following a probability density function given by experimental data [90]. From the bifurcating nodes, child branches were generated, where the order for each child branch was determined using morphological connectivity distributions [79]. The lengths,

radii and branching angles of child branches were found from the length diameter ratio, area ratio and branching angle distribution of penetrating vessels in the human brain [79, 91]. After an initial penetrating vessel tree was generated, the vessels were reassigned orders based on their diameters. Then several vessel density filters were applied to the penetrating vessel until its vessel density is morphologically accurate. A detailed description of this statistical algorithm can be found in [92].

There are also 2D network models built from rat data [93] and human data [94]. These models are useful in studying the dynamic responses of cerebral blood flow and oxygen transport to stimulus. However, these models often assume that each blood vessel supplies a certain part of the brain tissue that can be seen as a compartment, which make them unsuitable for 3D oxygen transport simulations.

2.2 Cerebral blood flow

The primary motivation for constructing models of cerebral vasculature is to simulate blood flow and oxygen transport. This section will first review blood and how it flows in general terms. Then the review will focus on the blood flow at the micro-scale (microcirculation). Lastly, the organ-scale circulation model and the active control of CBF will be reviewed briefly. Before reviewing CBF, it is necessary to distinguish two terms: blood flow and perfusion. In [1], blood flow is used for the flow passing through certain blood vessels, while perfusion is the blood flow passing through a vascular network within a specific volume of tissue. This thesis, however, uses CBF for blood flow in the brain in a more general way and primarily uses perfusion for the blood flow passing through microvascular networks within a certain volume of brain tissue. In a microvascular network introduced in the previous section, perfusion can be quantified as

$$\text{Perfusion} = \frac{\Sigma Q}{V_t} \tag{2.1}$$

where V_t is the volume of brain tissue region supplied by the microvascular network and Q is the flow rate of each vessel feeding into this region.

2.2.1 Blood - a non-Newtonian fluid

Blood consists of plasma and blood cells. Plasma takes up about 55% of the total blood volume and acts as a solute for other molecules. As plasma is mostly composed of water ($> 90\%$), it can be considered as a Newtonian fluid. Blood cells account for another 45% of the blood volume, of which red blood cells (RBC) account for the majority. The RBC is a biconcave disc that is approximately 8 μm in diameter and 2 μm in thickness [95, 96]. The haematocrit (H) is defined as the volume fraction of RBCs in blood.

Although blood is a non-Newtonian fluid, mainly due to the presence of RBCs, it can be assumed Newtonian under high strain rate (normally greater than 200 s^{-1}) and hence in large vessels (generally greater than 0.3 mm in diameter). The Newtonian law of viscosity is thus a suitable approximation in describing the blood behaviour in large arteries or in the cases when the detailed flow field is not of interest [95]:

$$\tau = \mu\dot{\gamma} \tag{2.2}$$

where τ is the shear stress, μ is the viscosity and $\dot{\gamma}$ is the strain rate.

When the strain rate becomes smaller than 200 s^{-1}, the blood viscosity starts to increase. Several models are able to describe this shear thinning behaviour including power-law models and Casson models. The Casson model [97] has the form:

$$\sqrt{\tau} = \sqrt{\mu_\infty \dot{\gamma}} + \sqrt{\tau_0} \tag{2.3}$$

where μ_∞ is the Casson viscosity and τ_0 is the yield stress. These parameters have the typical values of $\mu_\infty = 3.1$ mPa·s and $\tau_0 = 10.86$ mPa under a haematocrit of 45% and a

temperature of 37°C [95].

The non-Newtonian behaviour also starts to dominate blood rheology when the diameter of blood vessel is below a certain threshold. Fåhræus and Lindqvist [98] found that the blood viscosity will drop monotonically when the vessel diameter changes from 0.3 to 0.04 mm as shown in Fig. 2.5. The Fåhræus-Lindqvist effect is of great importance in modelling the blood flow in small arteries and arterioles. However, a limitation of this study is that the blood viscosity in vessels with a diameter smaller than 40 μm was not investigated. The authors stated in their paper [98] that it should be certain that the blood viscosity would finally converge to the plasma viscosity in narrower tubes. This was found to be incorrect when Pries and Secomb analysed more data [99, 100] and carried out new experiments at the length scale of capillaries [85, 101, 102], which will be further discussed in Section 2.2.4.

2.2.2 Haemodynamics in the microcirculation

Blood flow is often taken to be governed by the Navier-Stokes equations for an incompressible Newtonian fluid:

$$\rho(\frac{\partial \mathbf{u}}{\partial t} + \mathbf{u} \cdot \nabla \mathbf{u}) = \mathbf{b} - \nabla p + \mu \nabla^2 \mathbf{u} \tag{2.4}$$

where t is the time, $\mathbf{u}$ is the velocity, ρ is the density, $\mathbf{b}$ is the body force, p is the pressure. As discussed in the previous section, the blood is non-Newtonian especially at the micro-scale. A constant viscosity μ is assumed here for simplicity, but this will be further discussed in Section 2.2.4. The blood flow can be simulated by solving the Navier-Stokes equations numerically [95, 103]. However, the simulation will be very expensive in complex geometries, one example of which would be solving the flow fields in a complex microvascular network.

At the micro-scale, a few assumptions can be made to simplify the Navier-Stokes

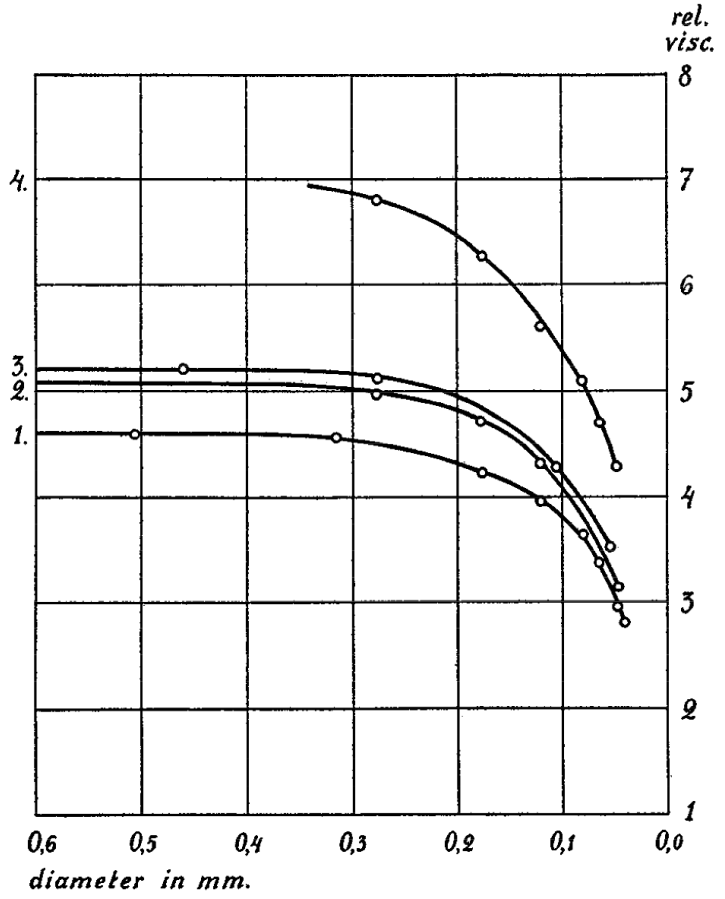

Figure 2.5: Fåhræus-Lindqvist effect. Reproduced with permission from [98].

equations. Firstly, the body force can be neglected. Additionally, the blood flow can be assumed laminar. This can be supported by calculating the Reynolds number (Re):

$$\mathrm{Re} = \frac{\rho D U}{\mu} \tag{2.5}$$

where ρ is the blood density, D is the vessel diameter and U is the average velocity. In the microvasculature, $\mathrm{Re} \ll 1$ due to low flow velocity and small vessel diameter, so that the viscous force dominates the flow and the advection term can be neglected. As well as this, the microcirculation is widely accepted to be assumed steady, due to the compliance of major arteries that is normally termed the Windkessel effect. The pulsatility of flow

can also be defined quantitatively by the Womersley number (Wo):

$$\mathrm{Wo} = R\sqrt{\frac{\omega}{\nu}} \tag{2.6}$$

where R is the vessel radius, ω is the angular frequency and $\nu = \mu/\rho$ is the kinematic viscosity. For a value of $\omega = 2\pi$ that equals to the angular frequency of heart beat (1 Hz), $\mathrm{Wo} \ll 1$ in arterioles and capillaries with a diameter smaller than 100 μm. This indicates that the blood flow in cerebral microvasculature is fully-developed and primarily driven by the pressure gradient.

The assumptions simplify the Navier-Stokes equations to the Stokes flow equation for an incompressible fluid:

$$-\nabla p + \mu\nabla^2\mathbf{u} = 0 \tag{2.7}$$

By assuming 1D, axisymmetric blood flow inside a rigid microvessel, Eq. 2.7 can be written in a cylindrical coordinate as

$$-\frac{\partial p}{\partial z} + \mu\frac{1}{r}\frac{\partial}{\partial r}(r\frac{\partial u_z}{\partial r}) = 0 \tag{2.8}$$

where z is the axial position and r is the radial position. Note that this equation provides a reasonable first order approximation of the axial blood flow [1].

2.2.3 Poiseuille law and network flow model

Solving Eq. 2.8 with no-slip boundary conditions at the vessel walls gives the Hagen-Poiseuille equation:

$$\frac{\Delta p}{Q} = \frac{8\mu L}{\pi R^4} \tag{2.9}$$

where Q is the flow rate and L is the vessel length. The fourth power of radius here indicates that a small change in vessel radius (diameter) can have a substantial impact on blood flow in the vessel, as well as on the vessels in neighbouring regions.

Since there is a linear relationship between flow rate and pressure drop in each vessel (Eq. 2.9), the flow conductance (Γ) can be defined here:

$$\Gamma = \frac{Q}{\Delta p} = \frac{\pi R^4}{8\mu L} \tag{2.10}$$

which is very similar to that in an electric circuit model. The flow conductance enables the direct application of the Poiseuille equation in solving the blood flow in microvascular networks. For example in a network consisting of n nodes, an $n \times n$ conductance matrix can be defined as

$$\Gamma_{ij} = \frac{Q_{ij}}{p_i - p_j} = \frac{\pi R_{ij}^4}{8\mu_{ij} L_{ij}} \tag{2.11}$$

where n is the total node number, i and j are two boundary nodes of each vessel segment and Q_{ij} is the flow rate from i to j. Γ_{ij} is set to 0, if there is no connection between nodes i and j. Conservation of mass at each node yields

$$\sum_{j=1}^{n} (p_i - p_j)\Gamma_{ij} = S_i \tag{2.12}$$

where S_i is the source term at node i, which is non-zero at the network boundary. By coupling Eqs. 2.11 and 2.12 and setting the boundary conditions, pressure at each node and flow in each vessel segment can be easily solved using a standard linear solver. The network flow model has been widely implemented in microvascular simulations [25, 27, 29, 87, 104–111].

At the very beginning of Section 2.2.2, the blood is assumed Newtonian in Eq. 2.4. However, as the blood is in fact strongly non-Newtonian at the micro-scale as discussed in Section 2.2.1, additional models of blood viscosity are thus required to account for these non-Newtonian effects.

2.2.4 Blood viscosity

One way to model the blood viscosity in microvessels is to use the empirical function of apparent viscosity (μ_{app}) [85, 101, 102, 104]. Based on the Poiseuille equation (Eq. 2.9), the apparent viscosity in a vessel can be determined as

$$\mu_{app} = \frac{\pi \Delta p D^4}{128 L Q} \tag{2.13}$$

which can be seen as an effective viscosity in the vessel when the relationship between flow rate and pressure drop is of particular interest. A relative viscosity (μ_{rel}) can also defined here as the ratio between apparent viscosity and plasma viscosity (μ_p) as

$$\mu_{rel} = \frac{\mu_{app}}{\mu_p} \tag{2.14}$$

where plasma viscosity can be assumed as 1.2 mPa·s [87, 112].

The blood viscosity is known to be dependent on both vessel diameter and haematocrit [85]. The effects of vessel diameter on blood viscosity in the range from 0.3 to 0.04 mm on blood viscosity have been studied by Fåhræus and Lindqvist [98] as discussed in Section 2.2.1. Most interestingly, the blood viscosity continues decreasing until the vessel diameter reaches about 7 μm as predicted by Fåhræus and Lindqvist [98]. However, it rises again when the vessel diameter further decreases [99, 100].

An explanation of this non-monotonic behaviour can be found in [96]. The blood viscosity drops when the vessel diameter decreases from 300 to about 7 μm, mainly due to the fact that the RBCs tend to migrate from the blood vessel wall resulting in a cell-free layer near the wall that reduces the resistance. When the vessel diameter further decreases from 7 to approximately 2.7 μm, the cell-free layer becomes narrower until a point where the RBCs can no longer pass through the vessel, leading to a sharp increase in the apparent blood viscosity.

The effects of vessel diameter and haematocrit on blood viscosity can be described by an *in vitro* empirical function [85]:

$$\mu_{rel\ 0.45} = 220{\cdot}e^{-1.3D} + 3.2 - 2.44{\cdot}e^{-0.06D^{0.645}} \tag{2.15}$$

$$C = (0.8 + e^{-0.075D}) \cdot (-1 + \frac{1}{1 + 10^{-11}D^{12}}) + \frac{1}{1 + 10^{-11}D^{12}} \tag{2.16}$$

$$\mu_{rel} = 1 + (\mu_{rel\ 0.45} - 1) \cdot \frac{(1 - H)^C - 1}{(1 - 0.45)^C - 1} \tag{2.17}$$

where $\mu_{rel\ 0.45}$ is the relative viscosity when the haematocrit is 0.45. The *in vitro* viscosity model is mainly based on experiments of human blood in glass tubes. The empirical function can predict the relative viscosity under different vessel diameter and haematocrit as shown in Fig. 2.6.

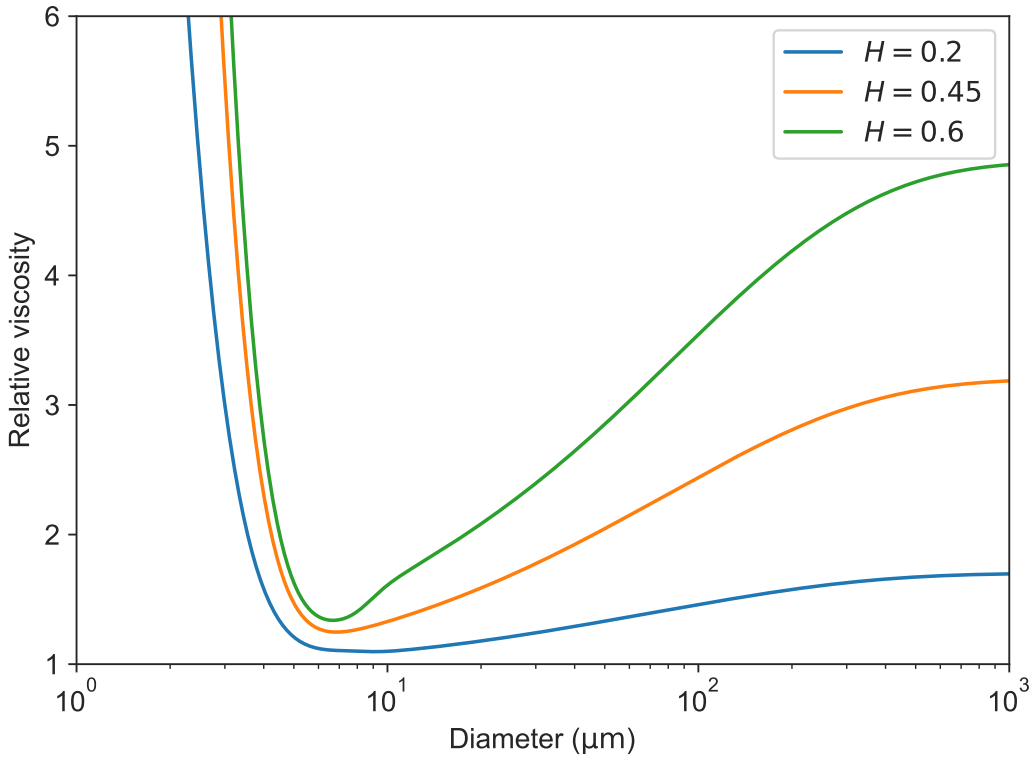

Figure 2.6: Relative viscosity as a function of vessel diameter and haematocrit, based on the *in vitro* viscosity model [85].

Pries et al. [101, 104] also conducted *in vivo* experiments in the rat mesentery models. The authors observed a significant increase in blood viscosity measured *in vivo* compared to that *in vitro*. An explanation for this difference is the presence of endothelial surface layer *in vivo* that restricts the blood flow [113]. These *in vivo* experiments were used to fit new viscosity models [101, 102]. A comparison of three notable viscosity models by Pries et al. (*in vitro*, 1992 [85]; *in vivo*, 1994 [101]; *in vivo*, 2005 [102]) is shown in Fig. 2.7. All these viscosity models have been heavily used in microcirculation studies [96]. In this thesis, the *in vitro* 1992 model [85] has been implemented to prevent the sharp edges in the *in vivo* viscosity curve. However, it should be noted that the simulation results can be substantially affected by changing the viscosity model, as there are considerable differences when the vessel diameter is approximately 10 μm. Since the apparent viscosity is the product of plasma viscosity and relative viscosity (Eq. 2.14), a different value of plasma viscosity can also result in different simulation results.

One way to minimise the effects of different viscosity models on the CBF simulation is to scale the perfusion to the physiological value by adjusting the pressure difference. Another way is to derive a new viscosity model simply based on the mechanical properties of RBCs through high-fidelity numerical simulations [96, 114, 115]. Promising results have been achieved in recent studies [116–119] and more validations are being performed elsewhere to demonstrate the credibility of these models.

2.2.5 Distribution of red blood cells in the microvasculature

Having described the relationship between flow rate and pressure drop in microvessels, the only missing information now is the haematocrit distribution, which the blood viscosity depends on. The distribution of RBCs in the microvasculature is mainly determined by the Fåhræus effect and the phase separation effect.

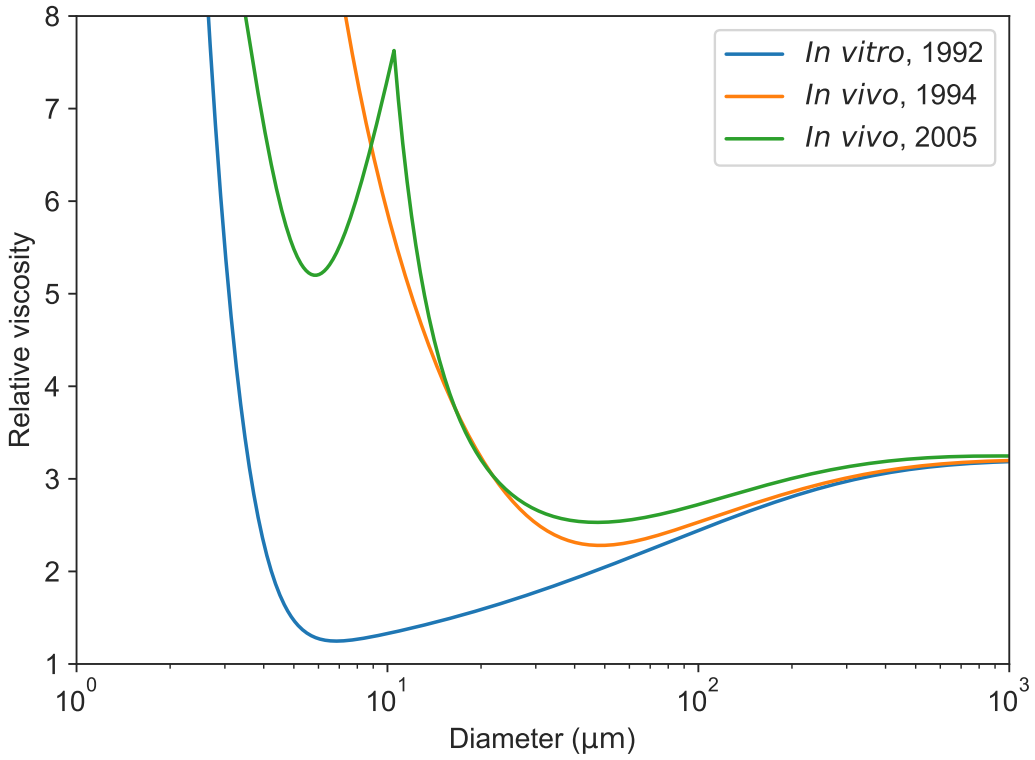

Figure 2.7: Relative viscosity under different vessel diameters and a constant haematocrit of 45% predicted by different viscosity models [85, 101, 102].

2.2.5.1 Fåhræus effect

The cell-free layer also results in the Fåhræus effect [120] that the reduction in haematocrit happens when the blood enters a smaller vessel. The reason for the reduction in haematocrit is mainly due to the same fact that the RBCs tend to flow at the centre of the microvessel. Here two parameters can be defined, namely discharge haematocrit (H_D) and tube haematocrit (H_T). The discharge haematocrit is the haematocrit entering or leaving the vessel, while the tube haematocrit is the haematocrit inside the vessel which is smaller than the discharge haematocrit. This is because the RBCs concentrated at the vessel centre move faster and spend less time passing through the vessel than the plasma along the vessel wall, based on the parabolic velocity profile of Poiseuille flow (Eq. 2.8). An empirical relationship between tube haematocrit and discharge haematocrit was also

proposed by Pries et al. [85]:

$$\frac{H_T}{H_D} = H_D + (1 - H_D)(1 + 1.7e^{-0.35D} - 0.6e^{-0.01D}) \tag{2.18}$$

which is plotted in Fig. 2.8 when the discharge haematocrit changes from 0.1 to 0.6. All curves reach their minimum at approximately 13 μm, where the 45% haematocrit curve has a minimum value of about 72%.

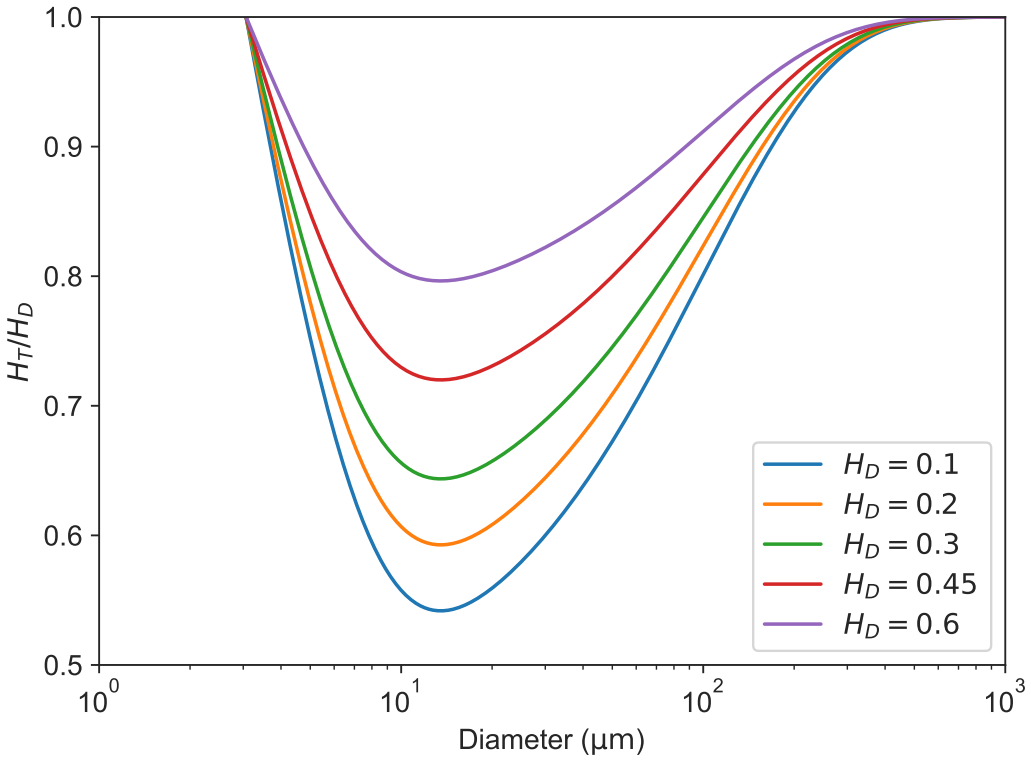

Figure 2.8: The empirical model of Fåhræus effect [85].

2.2.5.2 Phase separation effect

At a microvascular bifurcation, the distribution of RBCs in two child branches is found to be uneven. This is mainly due to the fact that the branch with lower flow rate will get more flow from the layers near the wall with smaller velocity. Because of the cell-free layer near the vessel wall, the lower flow branch thus gets more plasma and less RBCs than the other branch with higher flow rate. This phenomenon is called the phase separation effect,

which can result in highly heterogeneous distributions of RBCs in the microvasculature.

The phase separation effect can also be described by an empirical model [104, 121]:

$$\ln(\frac{FQ_E}{1-FQ_E}) = A + B\ln(\frac{FQ_B - X_0}{1-FQ_B-X_0}) \tag{2.19}$$

$$A = -6.96\ln(\frac{D_\alpha}{D_\beta})/D_F \tag{2.20}$$

$$B = 1 + 6.98(\frac{1-H_D}{D_F}) \tag{2.21}$$

$$X_0 = \frac{0.4}{D_F} \tag{2.22}$$

where FQ_E is the fraction of RBCs entering a child branch, FQ_B is the fraction of blood flow entering this branch, D_α is the diameter of this branch, D_β is the diameter of the other branch and D_F is the diameter of the feeding vessel. A typical case of separation of RBCs when $D_\alpha = 8$ μm, $D_\beta = 6$ μm, $D_F = 9$ μm and $H_D = 0.45$ is shown in Fig. 2.9, where the relationship between RBC fraction and flow fraction has a sigmoidal shape. Note that this empirical function is highly dependent on the vessel diameters that the curve will converge to the linear function $y = x$ very quickly when the vessel diameter increases. This indicates that the phase separation effect is negligible in simulating the blood flow in large arterioles or arteries, when the diameter of the vessels is much larger than that of RBCs. There have been some updated phase separation models by the same authors [102, 122], which are very similar to the original model [104].

Gould and Linninger [123] recently proposed a new phase separation model and fitted it with the same experimental data [121] using only one parameter. The Gould model [123] is plotted in comparison with the Pries model [104] when predicting the RBC partition in the same geometry and flow condition in Fig. 2.9. In the Gould model, the larger child vessel (D_α) always gets more RBCs than the smaller one regardless of the flow rates. The authors claimed that their model [123] has a better fit than the Pries model [104].

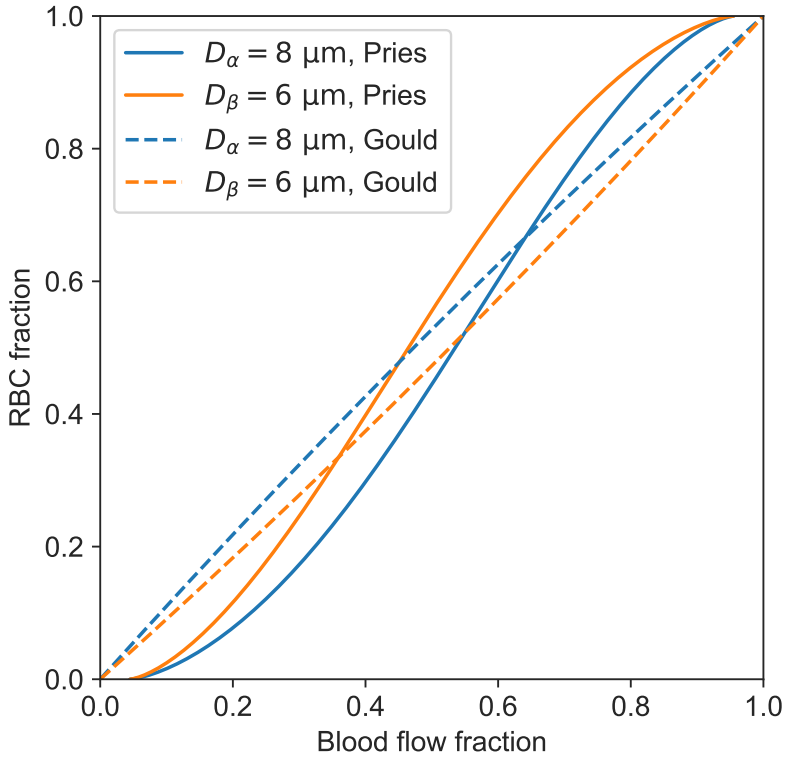

Figure 2.9: RBC fraction in child branches as a function of the flow fraction based on the empirical relationships proposed by [104] and [123], where $D_\alpha = 8$ μm, $D_\beta = 6$ μm, $D_F = 9$ μm and $H_D = 0.45$.

However, this statement has led to a debate on which model is better in predicting the phase separation effect [122].

In this thesis the haematocrit was assigned a constant value of 45%, since the effects of haematocrit distribution models have been found to have secondary effects on blood flow [88, 124]. Another reason is that the possibility that all phase separation models [102, 121–123] over-fit the data cannot be ruled out, since the experimental data cover just a small proportion of the parameter space. The accurate simulation of the phase separation effect requires more *in vivo* experiments and efforts from new high-fidelity simulations [118, 119]. The assumption of constant haematocrit has also been widely implemented in other microcirculation studies [25, 27, 28, 87, 105, 106].

2.2.6 Capillary bed as a porous medium

It is impossible to image the entire microvasculature in the human brain and to simulate the blood flow inside it. This significantly limits the length scale of the simulation of microcirculation. The application of homogenisation theory [59] can aid in overcoming this barrier in converting the microvascular networks as a porous medium at the macro-scale. The microcirculation can thus be simply modelled using Darcy's law:

$$\mathbf{u} = -\mathbf{K}\nabla p \tag{2.23}$$

where $\mathbf{K}$ is the permeability tensor.

El-Bouri and Payne [27] implemented this theory on human cerebral microvasculature by calculating the permeability inside physiologically representative human capillary networks as previously shown in Fig. 2.4. The same authors [28] then coupled the porous medium model of capillary beds with the network model of penetrating vessels [87]. This enabled the simulation of cerebral perfusion drop due to a penetrating arteriole occlusion at the length scale comparable to an MRI voxel for the first time [28]. Reasonable agreement was also found between the pressure drop in simulations and the tissue infarct due to similar occlusions shown in animal experiments [76].

2.2.7 Cerebral circulation models at organ-scale

The application of homogenisation theory to the human cerebral microcirculation also enables the perfusion simulation in the entire brain. By implementing the homogenisation theory on three compartments: penetrating arterioles, capillaries and penetrating venules, the cerebral perfusion can be simulated at the organ-scale as shown in Fig. 2.10 [36]. A similar approach has also been implemented in other CBF models [35, 125, 126].

The presented perfusion model is able to simulate the ischaemic regions after an ischaemic

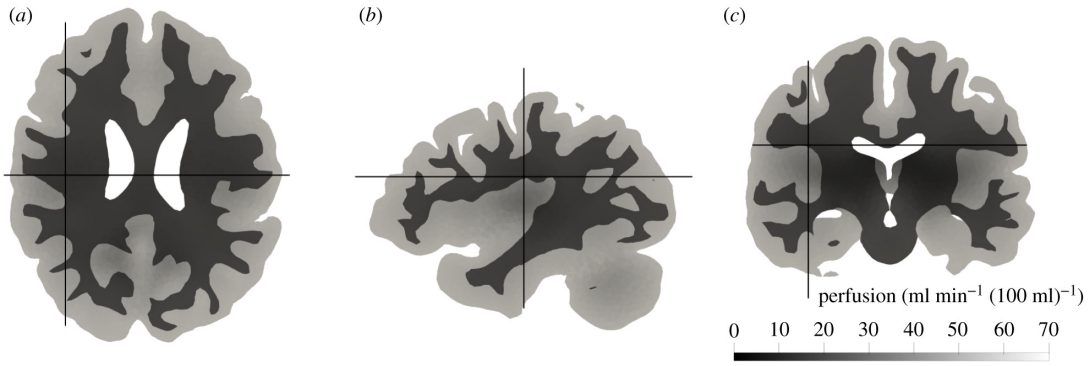

Figure 2.10: Cerebral perfusion simulation at the organ-scale. Reproduced with permission from [36].

stroke for the first time [36]. Satisfactory agreement has been shown between the whole brain simulation and clinical images. The *in silico* simulation of ischaemic stroke will be further reviewed in Section 2.4.4.

2.2.8 Active control of cerebral blood flow

The human brain is a highly dynamic system, where the energy demands vary both spatially and temporally responding to different stimulus [127]. The cerebral blood flow thus needs to be tightly regulated accordingly. The active control of CBF can be classified in two types: global control and local control. A detailed review of both can be found in Chapters 3 and 4 in [1]. Since this thesis is not focused on the active control of CBF, only a very brief summary of these is provided here.

A key mechanism that controls the CBF globally is cerebral autoregulation [39, 128]. Cerebral autoregulation simply describes the fact that the CBF is able to be maintained at a constant level when there is a disturbance of arterial blood pressure, and this was first defined by Lassen [129]. This can be achieved by adjusting the vessel diameter, since vessel resistance is proportional to the fourth power of its diameter in Poiseuille law (Eq. 2.9). However, cerebral autoregulation was found to be much more complex than that, due to the fact that the vessels tend to constrict when the blood pressure is reduced,

which then leads to a higher resistance and a further reduced blood flow. There are plenty of numerical models that explain these mechanisms [130–133]. In this thesis, it is simply assumed that the healthy cerebral autoregulation is able to maintain the perfusion globally when there are occlusions in a relatively small part of the vasculature.

The CBF is also tightly controlled locally. One notable mechanism is known as neurovascular coupling where CBF will rise in the regions of increased neural activity [134]. Despite recognised roles of neurons and astrocytes in regulating the local CBF [134], recent studies find that the pericytes respond rapidly to neural stimulus at the time scale of a few seconds [73, 135]. A recent computational model shows that the dilation of capillaries can happen in just 1 second after the stimulation [136]. These studies suggest that the pericytes can play a key role in adjusting the local CBF at the time scale of seconds.

2.3 Cerebral oxygen transport

The primary role of cerebral blood flow is to deliver oxygen and glucose to brain cells for metabolic uses. Under oxygen-rich conditions, the aerobic metabolism consumes 6 moles of oxygen for each mole of glucose. In another word, the oxygen shortage will usually happen earlier than glucose shortage under ischaemic conditions. The study of oxygen transport in the human brain is thus of great importance in understanding the metabolic response of brain tissue under both physiological and pathological conditions.

Oxygen delivery from blood to brain tissues mainly happens at the micro-scale of penetrating arterioles and capillaries [77, 137], due to their higher vessel density and thinner vessel walls than arteries. In general, cerebral oxygen transport is governed by the mass transport equation:

$$\frac{\partial C_\Omega}{\partial t} + \mathbf{v} \cdot \nabla C_\Omega = \nabla(D_\Omega \cdot \nabla C_\Omega) \pm S_\Omega \tag{2.24}$$

where C_Ω is the concentration of a substrate Ω, $\mathbf{v}$ is the convective velocity, D_Ω is the diffusion coefficient and S_Ω is the sum of production or loss of the substrate. Note that this thesis will focus on the oxygen transport at steady state, which means $\partial C_\Omega/\partial t = 0$. This is mainly because, as found in previous studies [94, 138, 139], the dynamic response of oxygen delivery happens at a time scale of just a few seconds. It is thus much smaller than the time scale of minutes or hours of tissue damage progression following an ischaemic stroke [140] that this thesis will simulate later on (Chapters 5 and 6).

In addition, the Péclet number (Pe) can be defined as the relative magnitude of advection over diffusion:

$$\mathrm{Pe} = \frac{L_c V}{D_t} \tag{2.25}$$

where L_c is the characteristic length, V is the average convective velocity and D_t is the diffusion coefficient of the substrate (oxygen in this case) in brain tissue. It is usually assumed that the diffusion can be neglected in blood vessels ($\mathrm{Pe} \gg 1$) and the advection can be neglected in brain tissue ($\mathrm{Pe} \ll 1$) [1].

This section will first apply the mass transport equation (Eq. 2.24) to oxygen in both blood vessels and brain tissue. Next, it will review the cerebral metabolic rate of oxygen ($\mathrm{CMRO_2}$), which acts as a sink term of oxygen. All of these will finally be coupled in the models of oxygen transport, where a Green's function method will be introduced. All parameter values used in this thesis will be listed there for convenience.

2.3.1 Oxygen transport in blood vessels

Oxygen is mainly carried by the haemoglobin in the RBCs in the blood. Since each RBC is almost fully occupied by haemoglobin, it is normally assumed that the volume fraction of haemoglobin equals to that of RBCs in the blood. The oxygen concentration (C_b) in blood thus consists of two components, which are the oxygen dissolved in plasma and the oxygen carried by haemoglobin respectively. Extra care must be taken here that the

first component has a linear relationship with the blood PO_2 (P_b), while the latter one follows a highly non-linear relationship. Hence the total blood oxygen concentration can be expressed as a function of blood PO_2 as

$$C_b = \alpha_b P_b + C_{Hb} H \mathrm{SO}_2 \tag{2.26}$$

where α_b is the blood oxygen solubility, C_{Hb} is the oxygen binding capacity per unit volume of red blood cells, H is the haematocrit and SO_2 is the oxygen saturation of haemoglobin, which has a non-linear relationship with blood PO_2.

The oxygen saturation in blood is often simulated using a Hill equation:

$$\mathrm{SO}_2 = \frac{P_b^N}{P_{50}^N + P_b^N} \tag{2.27}$$

where N is the Hill equation exponent and P_{50} is the PO_2 at half maximal haemoglobin saturation. A modified Hill equation is also widely used:

$$\mathrm{SO}_2 = 1/(1 + \frac{23400}{P_b^3 + 150 P_b}) \tag{2.28}$$

which is known as the Severinghaus relationship [141]. Both empirical equations are strongly non-linear as shown in Fig. 2.11.

The oxygen transport in a blood vessel can be described in an area-averaged form of the mass transport equation (Eq. 2.24) as

$$V_b \frac{\partial \overline{C_b}}{\partial t} = Q(C_{in} - C_{out}) - 2\pi j R L \tag{2.29}$$

where V_b is the blood volume, $\overline{C_b}$ is the volume-averaged oxygen concentration in the blood vessel, C_{in} and C_{out} are average oxygen concentration at inlet and outlet of a vessel and j is the oxygen flux across the vessel wall per unit area. At steady state, the model

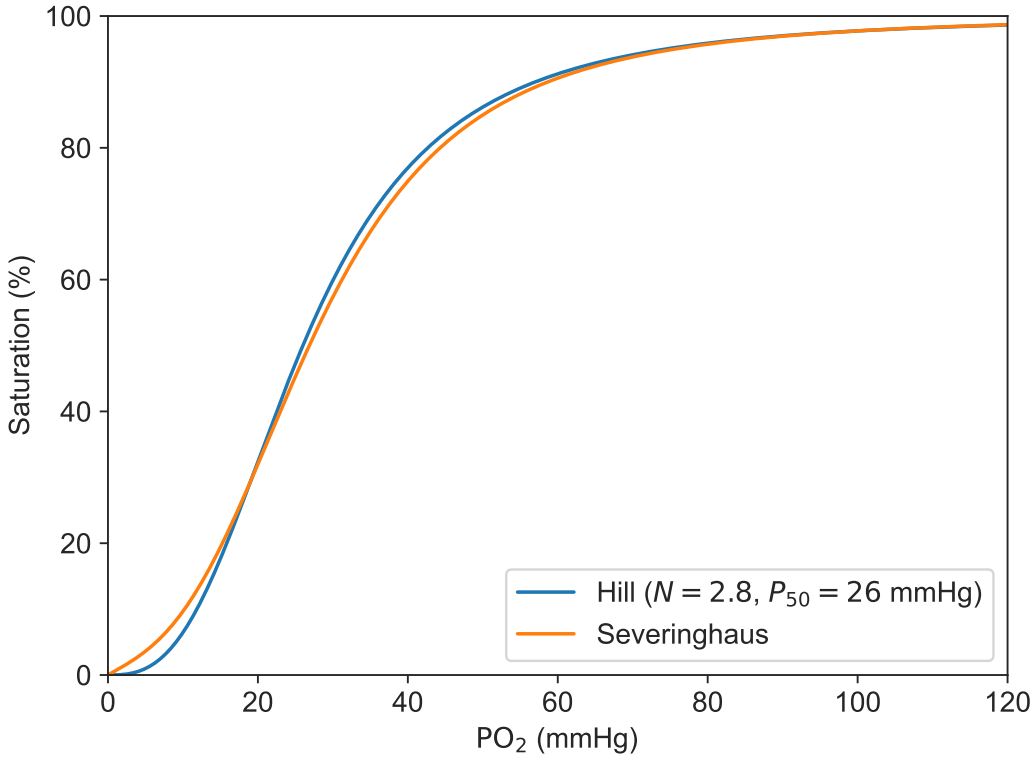

Figure 2.11: Comparison between Hill equation and Severinghaus equation.

can be further simplified as

$$Q\frac{dC_b}{dz} = -q_v(z) \tag{2.30}$$

where q_v is the oxygen diffusive efflux rate per unit length.

In order to maintain an oxygen flux through the vessel wall, a PO_2 gradient at the vessel wall is required. Assuming that the oxygen tension across each vessel cross-section is well-mixed and the vessel wall is part of the tissue, the relationship between vessel surface PO_2 (P_v) and blood PO_2 can be represented by Fick's law:

$$P_v(z) = P_b(z) - Kq_v(z) \tag{2.31}$$

where K is the intravascular resistance to oxygen diffusion based on vessel diameter [142].

2.3.2 Oxygen diffusion in brain tissue

Before introducing the oxygen transport in brain tissue, an assumption needs to be made here that the oxygen diffusion in intracellular and extracellular regions can be homogenised as a single diffusion coefficient of oxygen in brain tissue (D_t). This is mainly due to the fact that oxygen can diffuse freely in both brain cells and interstitial fluids.

At steady state, the oxygen transport in brain tissue can thus be described by a diffusion-reaction equation:

$$M = D_t \nabla^2 C_t = D_t \alpha_t \nabla^2 P_t \tag{2.32}$$

where M is the metabolic rate of oxygen, C_t is the tissue oxygen concentration, ∇^2 is the Laplacian operator, P_t is the tissue PO_2 and α_t is the oxygen solubility in brain tissue which describes the linear relationship between C_t and P_t.

2.3.3 Oxygen consumption in the brain

To solve for the oxygen concentration, the local metabolic rate of oxygen needs to be determined. The oxygen metabolic rate depends on the local tissue PO_2, which can be represented by a Michaelis-Menten relationship:

$$M = \frac{M_0 P_t}{P_t + P_0} \tag{2.33}$$

where M_0 is the maximum metabolic rate of oxygen, P_0 is the Michaelis constant which represents the tissue PO_2 when M reaches half of M_0. The Michaelis-Menten relationship between local oxygen consumption and oxygen tension has been assumed in most previous oxygen transport studies [105, 106, 143, 144]. When $P_t \gg P_0$, M can be seen as a constant very close to M_0. When $P_t \ll P_0$, M follows a linear relationship with P_t. In between these two states, the relationship between M and P_t is non-linear.

There are multiple techniques to measure the healthy $CMRO_2$ ($\sim M_0$) [1], which can lead to a large variability between different studies. Key measurements of human $CMRO_2$ at organ-scale are presented in Table 2.1, which show a variation from 2.8 to 3.8 $cm^3/(100cm^3 \cdot min)$. There is also a power law that has been proposed to scale the $CMRO_2$ measurements in animals to that in human based on the body weight [145]:

$$M_0 \propto W^{-0.1} \tag{2.34}$$

where W is the body weight. Using this relationship the $CMRO_2$ measurements in different animals can be scaled to equivalent $CMRO_2$ values for a human weighting 65 kg, as long as the body weight of the animal (or the average weight of them) is known. If the cerebral tissue density is assumed as 1.05 g/cm^3 [146] and molar volume of gas equals to 22.4 L/mol, the $CMRO_2$ from animal studies can be converted into equivalent human values as listed in Table 2.1. Good agreement has been shown between the human $CMRO_2$ and the scaled animal $CMRO_2$ in recent studies.

2.3.4 Models of oxygen transport in microvasculature

In this section, these models will be coupled to simulate the oxygen transport in the cerebral microvasculature. Three representative models will be introduced here, from 0D, 1D to 3D. A detailed review of models of microvascular oxygen transport can be found in [157].

2.3.4.1 0D compartmental model

If the spatial distribution of oxygen is not of interest, the oxygen transport from blood to tissue can be simply modelled using Fick's law:

$$J = \sum_i^n \frac{K_{O_2,i}}{h_i}(P_b - P_t) \tag{2.35}$$

Literature	$CMRO_2$ $[cm^3/(100cm^3 \cdot min)]$	Equivalent $CMRO_2$ for human $[cm^3/(100cm^3 \cdot min)]$
Kety and Schmidt, 1948 (human) [147]	3.47 ± 0.42	3.47 ± 0.42
Gleichmann, 1962 (dogs, 4.5-10 kg) [148]	7.35 ± 2.42	5.90 ± 1.94
Ganfield et al., 1970 (cats, 2-3 kg) [149]	8.98	6.48
Nilsson and Siesjö, 1976 (male rats, 290-410 g) [150]	7.98 ± 0.21	4.73 ± 0.12
Mintun et al., 1984 (human) [151]	3.08 ± 0.39	3.08 ± 0.39
Madsen et al., 1993 (human) [152]	3.81 ± 0.49	3.81 ± 0.49
Poulsen et al., 1997 (pigs, 40 ± 2 kg) [153]	3.83 ± 0.40	3.65 ± 0.38
Cui et al., 2013 (male mice, 20-40 g) [154]	6.12 ± 0.94	2.84 ± 0.44
Zhu et al., 2013 (male mice, 18-30 g) [155]	6.19 ± 0.38	2.81 ± 0.17
Henriksen et al., 2018 (human) [156]	2.78 ± 0.33	2.78 ± 0.33

Table 2.1: Cerebral metabolic rate of oxygen under healthy conditions scaled to the equivalent values for a human with a body weight of 65 kg.

where J is the total oxygen flux across the vessel walls, K_{O_2} is the oxygen permeability in vessel wall and h is the vessel wall thickness. Note that the brain tissue is essentially homogenised as a single compartment when applying Fick's law. Hence the compartmental model can be easily coupled with the 2D network to study the dynamic response of cerebral blood flow and metabolism [94].

2.3.4.2 1D Krogh cylinder model

The heterogeneous distribution of oxygen concentration in the radial direction of a vessel and its corresponding tissue region can be simulated by using the Krogh cylinder model [158]. The model is based on several assumptions, such as steady-state conditions, constant $CMRO_2$, the PO_2 on the vessel wall is equal to the average PO_2 inside the vessel,

each tissue region is only supplied by a neighbouring vessel and only radial diffusion of oxygen is considered.

The reaction-diffusion equation (Eq. 2.32) can be written in a cylindrical coordinate as

$$D_t \alpha_t \frac{1}{r} \frac{\partial}{\partial r} (r \frac{\partial P_t}{\partial r}) = M \tag{2.36}$$

The boundary conditions can then be set as $P_t(r = R_v) = P_b$ and $\partial P_t / \partial r(r = R_t) = 0$, where R_v is the vessel radius (starting point of diffusion) and R_t is the Krogh cylinder radius (end point of diffusion). This leads to the solution of Eq. 2.36 as

$$P_t(r) = P_b + \frac{M}{4 D_t \alpha_t}(r^2 - R_v^2) - \frac{M R_t^2}{2 D_t \alpha_t} \ln \frac{r}{R_v} \tag{2.37}$$

which gives the radial distribution of tissue PO_2 around a vessel. Additionally, the oxygen flux from the vessel wall can be predicted as

$$j = D_t \alpha_t \left. \frac{\partial P_t}{\partial r} \right|_{R_v} = \frac{M}{2 R_v}(R_t^2 - R_v^2) \tag{2.38}$$

Figure 2.12 shows the tissue PO_2 along the radial direction of a vessel under different values of blood PO_2 as simulated by the Krogh cylinder model (Eq. 2.37). Care should be taken that the Krogh cylinder model can result in negative tissue PO_2 when the blood PO_2 is too low to supply the given cylindrical region. This limitation is mainly due to the assumption of constant $CMRO_2$, that should be reduced in hypoxic regions. A common modified Krogh cylinder model thus couples the original model (Eq. 2.37) with the Michaelis-Menten model of $CMRO_2$ (Eq. 2.33). However, there is no existing analytical solution for the modified Krogh cylinder model. There are other modified versions, such as considering the resistance of vessel wall to oxygen diffusion or the oxygen diffusion along the axial direction [157]. The Krogh cylinder model can aid in developing other theoretical models [1] and analysing the oxygen imaging data at the micro-scale [159].

However, it cannot simulate the oxygen transport in a complex realistic network.

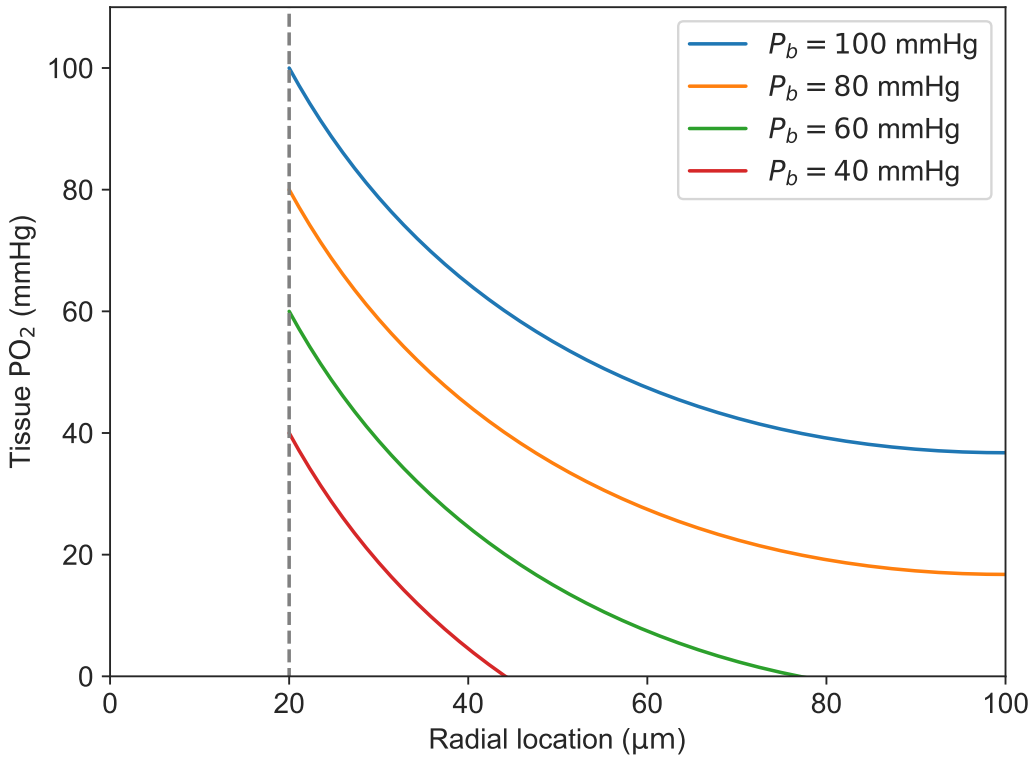

Figure 2.12: Tissue PO_2 along the radial direction of a vessel under different values of blood PO_2 simulated by the Krogh cylinder model, where $R_v = 20$ μm, $R_t = 100$ μm, $M = 6.72 \times 10^{-4}$ cm^3/(cm$^3 \cdot$ s) [94, 160], $D_t\alpha_t = 6 \times 10^{-10}$ cm^3/(cm $\cdot$ s $\cdot$ mmHg) [143, 144].

2.3.4.3 3D finite volume model

The most straightforward way to simulate the oxygen transport in a complex network in 3-dimensions is to solve the diffusion equation using one of a number of available numerical methods [25, 107, 108, 161–165]. In a recent application, Hartung et al. [108] used a finite volume method to simulate the blood flow and oxygen transport in rodent brain networks constructed from *in vivo* two-photon images. Figure 2.13 shows good agreement between the experimental measurements of tissue oxygenation and that simulated by the finite volume simulations in the same cerebral microvasculature. The validation indicates that

the *in silico* simulations are able to reproduce the cerebral tissue oxygenation in a realistic network at the resolution of just 2 μm (third column of Fig. 2.13).

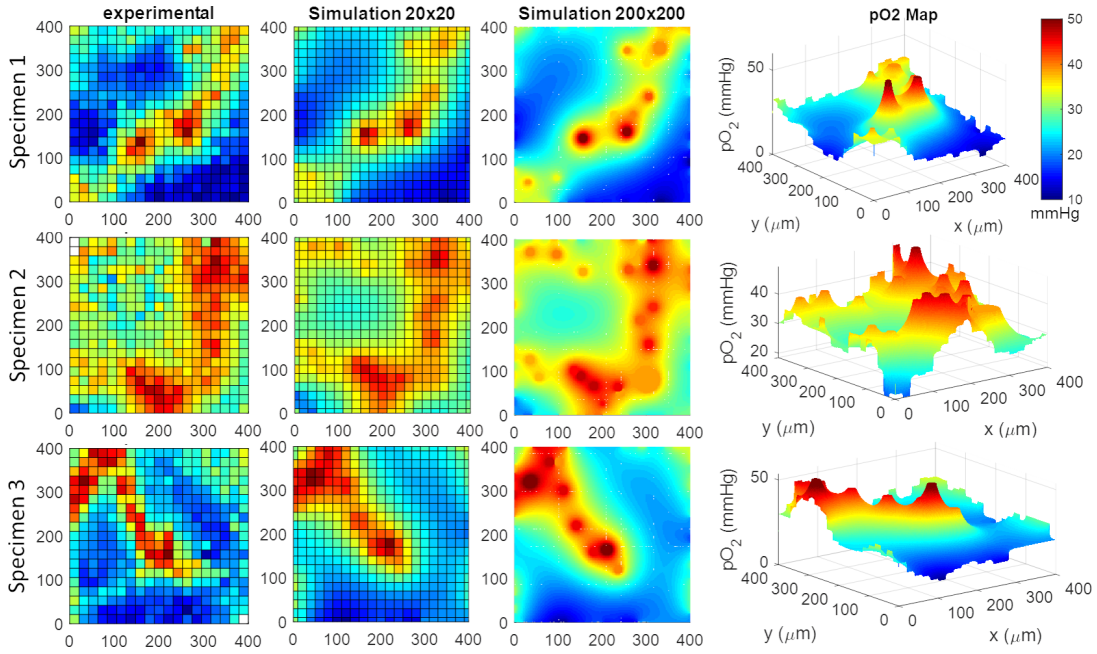

Figure 2.13: Comparison of tissue oxygenation fields between the experimental measurements and the finite volume simulations. Reproduced without change from [108] under license `https://creativecommons.org/licenses/by/4.0/`.

However, these methods usually require intense meshing and solving the 3D diffusion equations, which can be very computationally expensive. This limits the applicability of these models in studying the sensitivity of microvascular geometry on oxygen transport, when extensive simulations need to be performed.

2.3.5 Green's function method

Analytical (or semi-analytical) methods are more computationally efficient to simulate the oxygen transport in microvasculature. Since the oxygen diffusion equation is a linear partial differential equation (PDE), it can thus be solved using a Green's function method [144, 166], which has been implemented in several recent studies [105, 106, 167, 168]. All parameter values used in the Green's function methods are listed in Table 2.2.

Parameter	Description	Value
CBF_h	Healthy perfusion in grey matter	55 mL/100g/min [36, 147, 169]
C_{Hb}	Oxygen binding capacity of red blood cells	0.5 cm^3/cm^3 [144]
$D_t\alpha_t$	Product of oxygen diffusivity and solubility in brain tissue	6×10^{-10} $cm^3/(cm \cdot s \cdot mmHg)$ [143, 144]
H	Haematocrit of inflow blood	0.45 [27]
K	Intravascular resistance to oxygen diffusion	$0.73 - 2.45$ $mmHg \cdot \mu m \cdot s/\mu m^3$ based on the vessel diameter [106, 142]
M_0	Maximum oxygen consumption rate	6.72×10^{-4} $cm^3/(cm^3 \cdot s)$ [94, 160]
N	Hill equation exponent	3 [144, 170]
P_0	Michaelis constant for oxygen consumption	10.5 mmHg [105, 171]
P_{50}	PO_2 at half maximal haemoglobin saturation	38 mmHg [144, 170]
α_b	Effective solubility of oxygen in blood	3.1×10^{-5} $cm^3/(cm^3 \cdot mmHg)$ [144]
ρ_t	Brain tissue density	1.05 g/cm^3 [146]

Table 2.2: Modelling parameters used in the Green's function method.

In the Green's function method, the blood vessels are represented by discrete oxygen sources. The tissue region is divided into small cuboidal elements, each of which is represented by a point at its centre acting as an oxygen sink. Inside each tissue element, the metabolic rate of oxygen is assumed homogeneous and only dependent on the oxygen tension at centre point. According to the potential theory, Green's functions can be defined between these oxygen sources and sinks. Therefore, tissue PO_2 can be simulated

as a superposition of all sources.

According to the potential theory, a Green's function $G(\mathbf{x}, \mathbf{x}^*)$ can be defined between a point source $\mathbf{x}^* = (x_1^*,\, x_2^*,\, x_3^*)$ and a point in the tissue $\mathbf{x} = (x_1,\, x_2,\, x_3)$ as

$$D_t \alpha_t \nabla^2 G = -\delta_3(\mathbf{x} - \mathbf{x}^*) \tag{2.39}$$

where δ_3 is a three-dimensional Dirac delta function. In an infinite domain (as $|\mathbf{x} - \mathbf{x}^*| \rightarrow \infty$, $G(\mathbf{x}, \mathbf{x}^*) \rightarrow 0$), the solution for the Green's function is

$$G(\mathbf{x}, \mathbf{x}^*) = \frac{1}{4\pi D_t \alpha_t |\mathbf{x} - \mathbf{x}^*|} \tag{2.40}$$

By integrating the oxygen potentials from all sources, the potential at $\mathbf{x}$ is

$$P(\mathbf{x}) = \iint_{Sources} G(\mathbf{x}, \mathbf{x}^*) q(\mathbf{x}^*) d\mathbf{x}^* \tag{2.41}$$

where $q(\mathbf{x}^*)$ is the distribution of source strengths.

For each blood vessel, it can be assumed that the source distribution over the vessel surface depends only on the axial position (z) but not on angular position (θ). Hence Eq. 2.41 can be rewritten as

$$q_v(z) = \int_0^L \overline{G}(z, z^*) q_0(z^*) dz^* \tag{2.42}$$

for a single vessel, which can also be extended to a network easily by summing the integration for all vessels. In Eq. 2.42, $q_0(z^*) = 2\pi r \cdot q(z^*, \theta^*)$ is the distribution of source strength per unit length and $\overline{G}(z, z^*)$ is an averaged Green's function calculated

by integrating $G(z,\theta;z^*,\theta^*)$ over the angular positions θ and θ^*:

$$\begin{aligned}\overline{G}(z,z^*) &= \frac{1}{4\pi^2}\int_0^{2\pi}\int_0^{2\pi} G(z,\theta;z^*,\theta^*)d\theta^* d\theta \\ &= \frac{k}{4\pi^2 r}\int_0^{\frac{1}{2}\pi}\frac{1}{\sqrt{1-k^2\sin^2\theta}}d\theta\end{aligned} \tag{2.43}$$

which is an elliptic integral with an eccentricity $k = \sqrt{\frac{4r^2}{(z-z^*)^2+4r^2}}$. Since oxygen flux through vessel wall at each axial position has been solved by Eq. 2.42, PO_2 along each vessel surface can now be solved by using inlet blood PO_2 and Eq. 2.31.

From the PO_2 values on the vessel surfaces, which also act as the boundaries of tissue region, the oxygen diffusion can now be simulated easily using Green's functions (Eq. 2.40). Firstly, for a network that has m vessel segments and n tissue elements, four Green's function matrices need to be defined: an $m\times m$ G_{vv} matrix for PO_2 on the surface of a vessel caused by PO_2 on the surface of another vessel, an $m\times n$ G_{vt} matrix for PO_2 on the surface of a vessel caused by PO_2 of a tissue element, an $n\times m$ G_{tv} matrix for PO_2 of a tissue element caused by PO_2 on the surface of a vessel and an $n\times n$ G_{tt} matrix for PO_2 of a tissue element caused by PO_2 of another tissue element. The centre location of a vessel segment or a tissue element is used when calculating the distance between any two of them that the Green's function depends on. One exception to this is the diagonal term of G_{vv} matrix, which should use the elliptic integration that has been introduced before. These matrices are purely based on network geometry, so they only need to be calculated once for each network.

Next, the vessel surface PO_2 of segment i can be obtained by superposing the Green's functions:

$$P_{v,i} = \sum_{j=1}^{m} G_{vv}^{ij} q_j - \sum_{j=1}^{n} G_{vt}^{ij}\phi_j + G_0 \tag{2.44}$$

where q_j is the source strength of vessel segment j, ϕ_j is the source strength of tissue element j and G_0 is a constant that imposes a total no-flux boundary condition on the

domain boundary, which will be solved in each iteration based on conservation of mass. Similarly, the tissue PO_2 of element i can be calculated as

$$P_{t,i} = \sum_{j=1}^{m} G_{tv}^{ij} q_j - \sum_{j=1}^{n} G_{tt}^{ij} \phi_j + G_0 \tag{2.45}$$

There are currently $m + n + 1$ unknown variables, which are PO_2 of m vessel segments, PO_2 of n tissue elements and the Green's function constant G_0. These variables can be solved from Eqs. 2.44 for m vessel segments, Eqs. 2.45 for n tissue elements and the relationship that total oxygen delivery equals to total oxygen consumption:

$$\sum_{j=1}^{m} q_j = \sum_{j=1}^{n} \phi_j \tag{2.46}$$

Hence the steady state oxygen transport in the microvascular network can now be solved.

The computational cost of Green's function method is significantly cheaper than that of the traditional finite difference methods, especially in a complex network. This is mainly because that the 3D diffusion equations are transformed into 1D Green's functions, which only need to be calculated once at the beginning of the simulation.

The Green's function can be implemented on microvascular networks using an open-source C++ package[2] developed by Secomb et al. [144]. Figure 2.14 shows a recent application of the Green's function method in a microvascular network in the mouse brain [106]. The same method will be applied to the human networks later on in this thesis. All Green's function simulation scripts needed to simulate oxygen transport in the human brain (which will be presented in Chapters 3 and 4) can be found in an online repository[3].

[2] `https://physiology.arizona.edu/people/secomb/greens`
[3] `https://github.com/YidanXue/cerebral_oxygen_transport`

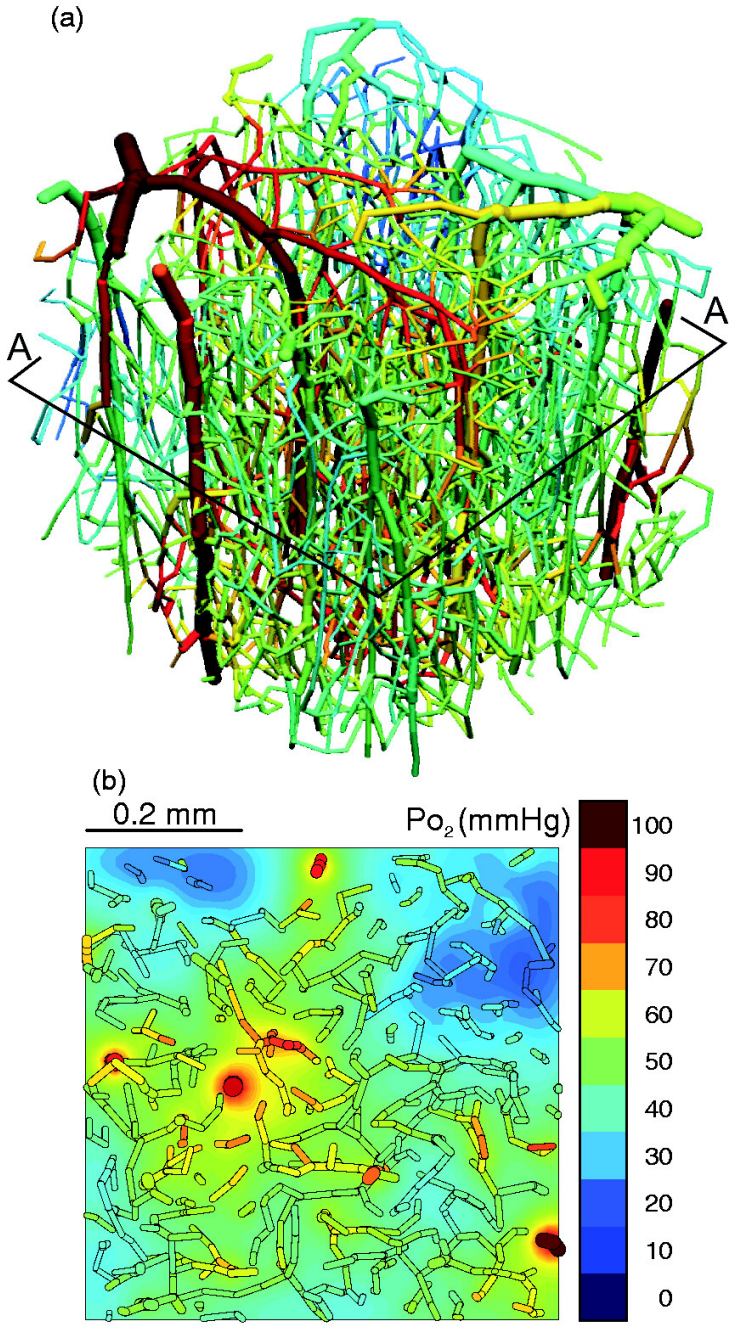

Figure 2.14: Oxygen transport and tissue oxygenation simulated by the Green's function method in a mouse cerebral microvasculature. Reproduced with permission from [106].

2.4 Stroke and its modelling

Having introduced the models of cerebral blood flow and oxygen transport at the micro-scale, this section will discuss how these models can be linked to macro-scale

simulations and their wider clinical applications. This section will first review ischaemic stroke and its treatment. Then it will introduce the medical imaging of stroke and the current clinical challenges of ischaemic stroke. Finally, this section will discuss how *in silico* models of ischaemic stroke can aid in optimising the stroke treatment.

Stroke is one of the leading causes of death and disability in the world. Just in the UK, about 100,000 strokes occur each year [1]. There are mainly two types of stroke, namely ischaemic stroke and haemorrhagic stroke, which account for 85% and 15% of cases, respectively. The ischaemic stroke is usually caused by the occlusion of a major artery that leads to hypoperfusion in brain tissue. The haemorrhagic stroke is caused by the rupture of blood vessels and the resulting bleeding, which results in an increase in intracranial pressure and then a reduction in CBF. Since this thesis mainly develops models in the context of ischaemic stroke, the review will thus focus on it and its models. For modelling of haemorrhagic stroke, the reader is referred to other recent works [172, 173].

2.4.1 Ischaemic stroke and clinical interventions

The rate of survival following an ischaemic stroke is relatively high, but stroke patients are very likely to have certain levels of disability after the treatment, which will significantly reduce their quality of life [1]. Scoring systems have been developed to quantify the patient's disability after the stroke treatment to test its effectiveness. The most commonly used scale is known as the modified Rankin scale (mRS), which is a 7-point scoring system ranging from 0 (no symptoms) to 6 (death) [174]. The mRS has been used in recent clinical trials incluing MR CLEAN [4] and HERMES [175]. Figure 2.15 shows the mRS in patients with intra-arterial treatment plus usual care (intravenous administration of alteplase) or usual care alone at 90 days after the stroke onset in the MR CLEAN project [4]. The patients with intra-arterial treatment are more likely to have better functional outcomes (lower mRS), although the mortality rate is not significantly affected (mRS = 6).

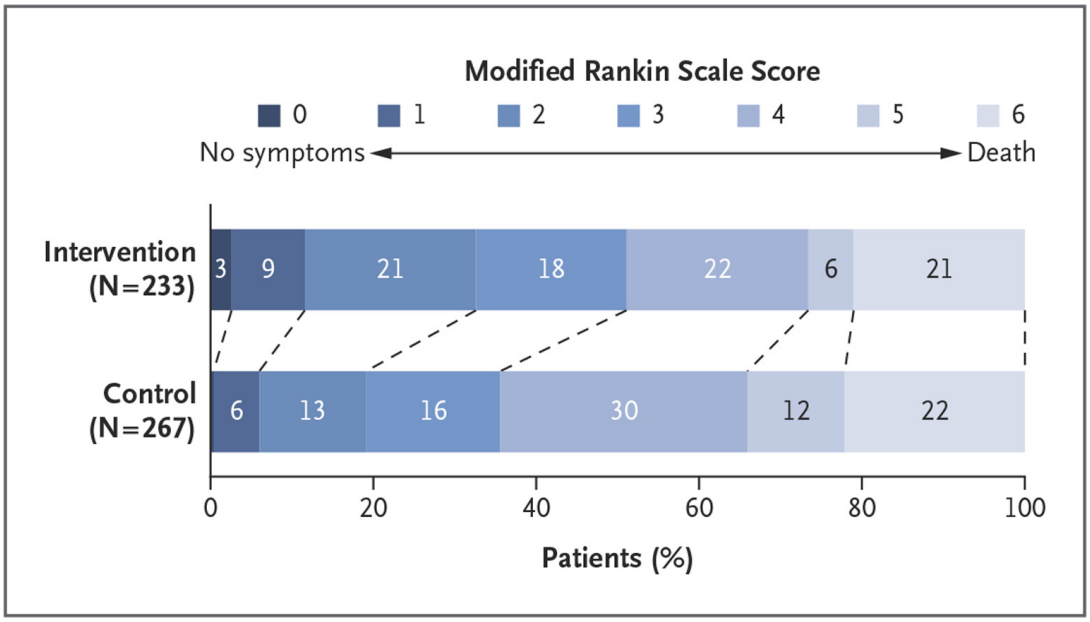

Figure 2.15: The modified Rankin scale in patients with intra-arterial treatment plus usual care (intervention group) or usual care alone (control group) at 90 days after the stroke onset in the MR CLEAN project. Reproduced with permission from [4], Copyright Massachusetts Medical Society.

There are currently two types of intra-arterial treatment, which are thrombectomy and thrombolysis. Thrombectomy removes the clot from the occluded blood vessels using mechanical devices. The other one is thrombolysis, which injects thrombolytic drugs to dissolve the blood clot. These intra-arterial treatments have recently been shown to be effective within the first few hours of the stroke onset [4, 175–177]. However, it remains controversial whether the combined therapy of thrombectomy and thrombolysis leads to better or worse clinical outcome than using thrombectomy alone [178].

2.4.2 Medical imaging of stroke

Medical imaging plays a key role in decision making and outcome assessment for the treatment of ischaemic stroke, since it can be used either to measure properties of the vasculature or to identify the regions of ischaemic tissue. A detailed overview of imaging techniques for brain perfusion measurements can be found in [179]. When imaging

ischaemic stroke, CT and MRI are preferred over other imaging techniques, since they are faster and less invasive [1, 180].

2.4.2.1 Computed tomography

Computed tomography uses rotating X-rays to build 2D images of the brain, which can be stacked to reconstruct a 3D image. Contrast agents are always used with CT to enhance the imaging of the blood. Xenon (Xenon-enhanced CT) and iodine (perfusion CT) are the most commonly used contrast agents, which can be administered by inhalation and injection respectively. Xenon-enhanced CT can measure the CBF with a spatial resolution of up to approximately 4 mm, while perfusion CT can measure CBF, cerebral blood volume (CBV) and mean transit time (MTT) with a spatial resolution of up to approximately 1-2 mm [179]. The short half-life of inhaled Xenon enables Xenon-enhanced CT to be used for repeatable tests to investigate the brain physiology. On the other hand, perfusion CT is an ideal choice for emergency departments, due to its shorter scan time, better resolution and ability to measure CBV and MTT [179]. The ischaemic region often shows an increase in MTT and a decrease in CBF and CBV [1]. Measurements of CBF and CBV are extremely useful in identifying core and penumbra, which will be introduced in Section 2.5.2.1.

2.4.2.2 Magnetic resonance imaging

Magnetic resonance imaging can measure the CBF by applying a perpendicular magnetic fields and measuring the rotation of the magnetic moment of protons in water. Time constants of the magnetic moment relaxation, which strongly depend on tissue composition, can be measured in the brain to distinguish different tissue types. In general, MRI provides maps of intensity based on the number of protons in each pixel [1]. Following an ischaemic stroke, the ischaemic core usually shows a reduction of apparent diffusion coefficient of water, caused by depolarisation of brain cells due to energy failure. This phenomenon leads to the use of diffusion-weighted imaging (DWI), which can provide

an early evaluation for stroke patients. In addition, DWI (regions of dead tissue) can be compared against perfusion-weighted imaging (regions of hypoperfusion), where the mismatch between the two is regarded as the salvageable tissue that is hypo-perfused but not dead yet [1].

Magnetic resonance imaging can measure CBF, CBV and MTT with a spatial resolution of up to approximately 2 mm [179]. It is able to identify the region of risk by using a threshold of signal intensity, but there is no common protocol on how to divide the regions of irreversible and reversible tissue damage based on the signal [179]. In addition, the lesions identified on DWI are sometimes found to be reversible [181]. Compared with CT, MRI has the other disadvantages of longer scan time and not being applicable to patients with a pacemaker or other implanted metallic devices in imaging ischaemic stroke [1, 179].

2.4.3 No-reperfusion phenomenon and microembolism

Favourable functional outcomes cannot always be achieved after thrombectomy [4, 175–177]. As shown in Fig. 2.15, even after the intra-arterial intervention, about half of the patients are not able to walk without assistance (mRS $>$ 3). One reason for this is the fact that patients tend to have different collateral flow status following an ischaemic stroke [70], primarily due to the variations in the circle of Willis in the population [68, 69]. Another reason is that the clinical outcome is highly dependent on the treatment time [175], since infarct can form in one hour in the ischaemic core [140]. Moreover, many patients cannot fully restore their brain tissue perfusion even after the clot is removed from the occluded vessel, which is known as the no-reperfusion phenomenon [61, 62, 182].

The reasons for no-reperfusion remain unclear, although there are many hypotheses including microembolisms caused by clot fragmentation [29, 60, 183], capillary constriction controlled by pericyte contraction and death [135, 184], flow stalls in capillaries [185, 186] and tissue oedema resulting from blood-brain barrier disruption

[42, 187]. One challenge in understanding the no-reperfusion phenomenon is that all these hypotheses involve abnormal changes in the microvasculature, which are far below the resolution of clinical images. Both animal models and numerical models have thus been developed to bridge this 'imaging gap'.

At the micro-scale, subtle geometrical or topological changes in the microvasculature will lead to local ischaemia and infarct, due to the close coupling between brain cells and microvasculature. Through the use of rodent models, recent experiments [55, 76] have showed that microembolisms could induce ischaemia, hypoxia and infarct formation at the micro-scale. In the same rat model of microembolism, Georgakopoulou et al. [56] further investigated the spatial relationship between the hypoxic regions and the occlusion sites. It is slightly surprising that considerable hypoxic regions formed distally from the occlusion locations as shown in Fig. 2.16, since the mini-stroke experiment [76] observed localised tissue infarction after the occlusion of a penetrating arteriole. A potential explanation is that the 15 μm and 25 μm microspheres occluded the branches of penetrating arterioles [56] instead of the entire arteriole tree [76], which would lead to a different mechanism of hypoxic tissue damage. The differences between these two experiments and the spatial analysis of the hypoxic regions will be further discussed in Chapter 4.

In addition, the tissue response to microembolism is not purely passive. Recovery of hypoxic and ischaemic regions was observed in the rat brain in 7 days following the microembolism [55]. One possible explanation to the recovery mechanism is that the microemboli can be extravasated, so that the occluded blood vessels can be recanalised as shown in Fig. 2.17 [53, 54, 188–190]. One piece of evidence supporting this hypothesis is that more than half of the microemboli can be extravasated within a week [53, 54, 190], which agrees with the time scale of tissue recovery [55].

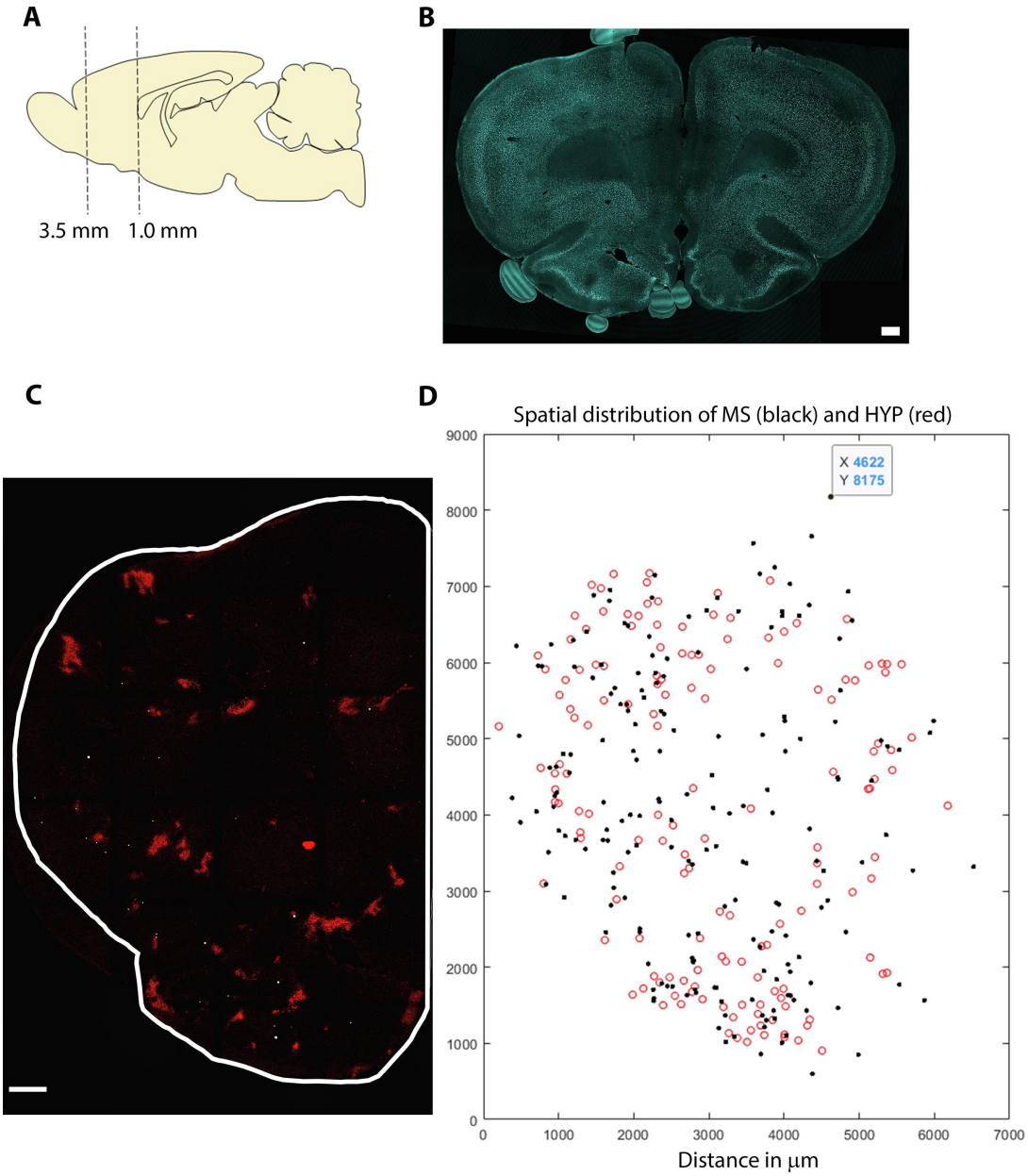

Figure 2.16: The distant effects between the hypoxic regions and the occlusion sites, where 3D occlusion locations (black) and 3D hypoxic regions (red) are plotted on a 2D plane. Reproduced without change from [56] under license `https://creativecommons.org/licenses/by/4.0/`.

2.4.4 In silico models of ischaemic stroke

Novel treatments are continuously being explored and developed to improve the clinical outcome of stroke patients. Testing the safety and efficacy of these new treatment

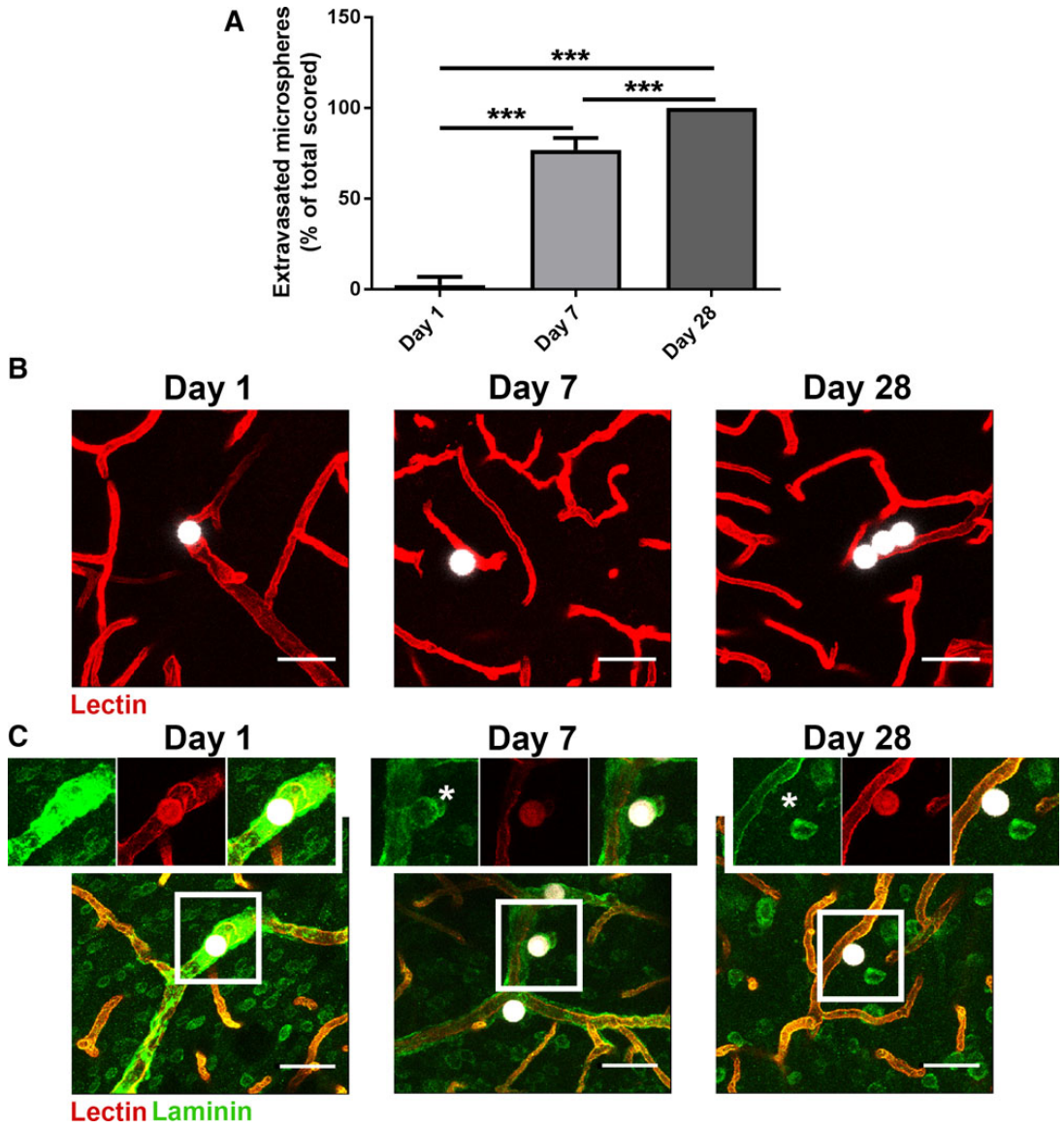

Figure 2.17: Extravasation of microemboli from the blood vessels in the rat brain. Reproduced with permission from [53].

techniques usually requires pre-clinical animal experiments and clinical trials, which can be very expensive and time-consuming, due to the fact that the rate of successful translation from animal models to humans is really low [191, 192]. Additionally, the brain pathophysiology following an ischaemic stroke has been shown to be highly complex and remains poorly understood. To aid in optimising stroke treatments and better understanding the stroke mechanisms, *in silico* models of ischaemic stroke have been developed.

The INSIST project aims to build computational models of ischaemic stroke through multi-centre multidisciplinary collaborations [44]. The project has developed models of virtual stroke patients[4], thrombosis and thrombolysis [45], thrombectomy [16, 46] and CBF and tissue damage [29, 36, 37, 47, 48]. The CBF models will be the focus here, since they will be coupled with the tissue health models developed in this thesis.

At the micro-scale, as mentioned in previous sections, the perfusion drop caused by a single penetrating arteriole occlusion has been simulated in a voxel at the length scale comparable to the MRI resolution [28]. Using the same vascular models [27, 87], the effects of cerebral microemboli on microvascular permeability can be quantified in cortical columns [29], enabling its coupling with the organ-scale models [36]. The study also suggests that the impact of microthrombi on cerebral reperfusion is highly dependent on the thrombectomy techniques and the microvascular geometry. Note that there are also other models on the effects of micro-occlusions on perfusion [111, 193].

However, none of these models simulates the effects of micro-occlusions on oxygen transport and tissue damage, which limit their application and potential validation against animal microembolism experiments on hypoxic tissue damage [55, 56]. Despite strong correlations between hypoxia and ischaemia, it cannot simply be assumed that the hypoxic region can be represented by the ischaemic region at the micro-scale. This is partly due to the fact that the blood pressure difference, which drives the blood flow, only contributes to the advection term of oxygen transport but not to the diffusion term (Eq. 2.24). For instance, in the absence of the blood pressure gradient, oxygen can still diffuse up to 100 μm in the radial direction of a vessel as previously shown in the Krogh cylinder model (Fig. 2.12). Hence in addition to existing blood flow models, new oxygen transport models are necessary to simulate the cerebral tissue hypoxic response to microemboli. These oxygen transport models will be developed in Chapters 3 and 4.

At the macro-scale, the CBF can be simulated by coupling the 1D blood flow model

[4] `https://mdmtest.shinyapps.io/INSIST-VP/`

for large arteries [37] with the 3D perfusion model representing the microvasculature [36]. As shown in Fig. 2.18, the cerebral perfusion model is able to simulate the tissue hypoperfusion following a right middle cerebral artery (MCA) occlusion, where the simulated ischaemic region matches the CT scan of a MCA stroke patient one week after the treatment [36]. Its ability to capture perfusion changes following an ischaemic stroke and its treatment at the organ-scale enables the development of other *in silico* clinical trials.

Despite this, these passive models are not able to simulate the time-dependent tissue damage progression, which includes effects of treatment time on infarct formation due to ischaemia, tissue recovery after treatment, and secondary tissue damage caused by no-reperfusion. It limits their application in optimising the stroke treatment techniques. As a result novel cell death models are required to couple with these stroke models to simulate the time-dependent tissue damage. Before introducing the development of cell death models in Chapters 5 and 6, the mechanisms and models of cerebral tissue damage will be introduced.

2.5 Cerebral tissue health

This section will review the cerebral tissue damage following an ischaemic stroke. It will first introduce the cerebral metabolism. Then it will discuss the cerebral tissue damage under ischaemic conditions at different scales. Lastly, existing cell death models of ischaemic stroke will be reviewed.

2.5.1 Cerebral metabolism

Inside the brain, there is a special layer of tight junctions of endothelial cells between blood vessels and tissues, which is called the blood brain barrier (BBB) [194]. Small molecules like water, oxygen and carbon dioxide can diffuse freely into the tissue through the BBB. However, the transport of larger molecules, like glucose, is regulated by the

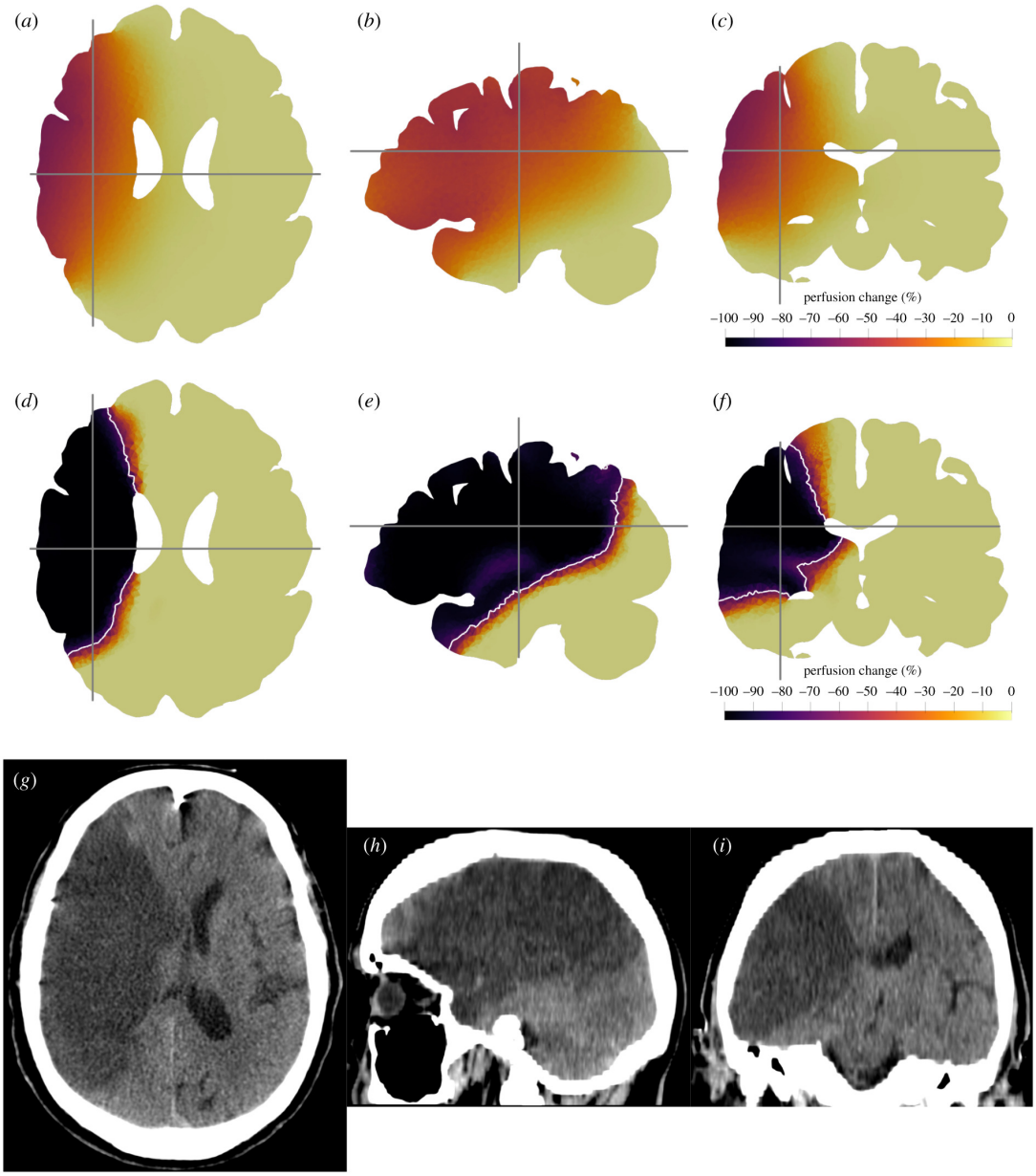

Figure 2.18: Cerebral perfusion after a right middle cerebral artery occlusion in simulations using isotropic (a-c) or anisotropic (d-f) permeability fields and clinical images (g-i). Reproduced with permission from [36].

BBB, and thus usually depends on the presence of certain transporting proteins [195].

After passing through the BBB, oxygen and glucose are taken by brain cells to produce adenosine triphosphate (ATP), which acts as an energy 'currency'. Based on the energy budget model [196, 197], about 75% of these ATP molecules are consumed by information

processing activities. When there is sufficient oxygen, the aerobic metabolism of 1 mole glucose and 6 moles oxygen can produce about 36 moles of ATP. In the absence of oxygen, however, 1 mole of glucose can only produce 2 moles of ATP through anaerobic metabolism. Thus ATP production will be largely reduced in hypoxic conditions, which can lead to energy impairment of brain cells.

In general, the brain cells can be categorised into neurons and glial cells. Neurons are basic elements for brain signalling, supported by glial cells both physically and chemically [198]. The close metabolic coupling between neurons and glial cells has been simulated in previous studies [20, 22, 199]. Recent studies also suggest that astrocytes (one type of glial cells) are highly involved in neural activities, especially in regulating the structure of the neural network and processing of calcium ions [200, 201]. One major difference between neurons and glial cells is that the neurons have very limited energy storage, due to the fact that they cannot synthesise glycogen. This indicates that the neurons are extremely vulnerable, when the energy supply is interrupted.

2.5.2 Cerebral tissue damage due to ischaemia

Ischaemic stroke will usually disturb the energy supply in the territory downstream of the occluded artery. The energy impairment can then lead to tissue damage happening at different length scales and time scales. In addition, clinicians usually have different definitions for the status of cerebral tissue damage, which adds extra complexity in understanding the ischaemic tissue damage in the human brain.

2.5.2.1 Concepts of brain tissue damage used by clinicians

The brain tissue with ischaemic damage can usually be identified as core or penumbra. The corresponding volumes of these tissue damage are important factors used in clinical studies. As shown in Fig. 2.19, the core is usually at the centre of the ischaemic region and surrounded by the penumbra [58]. Due to the large reduction in CBF, the brain

cells in the core will depolarise, which can lead to irreversible cell damage in a very short time [58]. The penumbra region, however, experiences a relatively mild reduction in CBF that will lead to increased OEF and dysfunction of brain cells, but with the potential for recovery [58, 66]. Although the concepts of core and penumbra are still controversial [202], this thesis is based on the working hypothesis that core and penumbra represent the tissue with irreversible and reversible tissue damage. The volume of irreversible tissue damage is usually measured by noncontrast CT at 3-9 days after the stroke onset, which is regarded as a key criteria of clinical outcome and known as the final infarct volume [4].

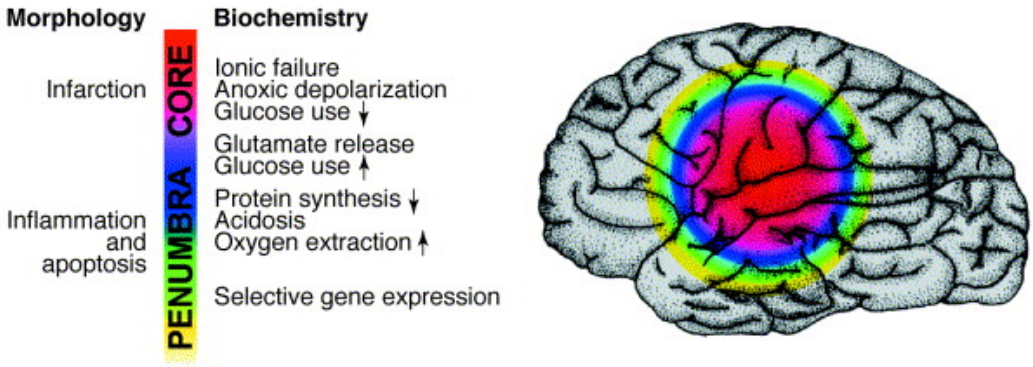

Figure 2.19: Morphology and biochemistry of core and penumbra. Reproduced with permission from [58].

In clinical practice, the identifications of core and penumbra also depend on imaging techniques and selection criteria [66, 203–205]. Since the simulation results in this thesis will be validated against the clinical data from the MR CLEAN project [4], the selection criteria for CT perfusion imaging used by MR CLEAN are listed here. In MR CLEAN, the core is the tissue with CBV below 1.2 mL/100g [206] and the penumbra is the tissue with CBF below 27 mL/100g/min [207]. Note that the same criteria are used here for both grey matter and white matter, despite differences in their baseline perfusion [208]. Another point to note is that CBF and CBV are both perfusion-related quantities, the medical imaging of which represents the distribution of blood supply deficiency instead of that of tissue damage. These two maps can be converted into each other by assuming constant perfusion between stroke onset and treatment, as well as the prior knowledge of final

tissue outcomes under different perfusion values [209]. However, the simple conversion from perfusion to tissue damage neglects the temporal mechanisms of cell death, which will become a significant limitation when investigating the effects of treatment time on tissue recovery and final clinical outcome.

2.5.2.2 Progression of cerebral ischaemic injury at different scales

Cerebral ischaemic injury has a highly non-linear relationship with both time and perfusion. To illustrate these non-linear dynamics, animal experiments are reviewed here ranging from the cellular scale to the organ scale.

As shown in Fig. 2.20, Garcia et al. [65] investigated the percentage of neurons in intact, ischaemic and necrotic states in the ischaemic hemisphere at different time points following a right MCA occlusion in the rat brain. A highly non-linear cellular response to ischaemia is shown in that the neurons become ischaemic very quickly in the first 4 hours (in a relatively linear way), while the necrosis happens in only 10% of the cells in the same period. However, the percentage of necrotic cells rises sharply after that, from 15% at 6 hours to 65% at 12 hours. This study provides temporal and quantitative results on the cellular response to ischaemia from intact to ischaemic and finally to necrotic tissue. Moreover, its observations support the assumptions of 3 cellular states of healthy, vulnerable and dead as used in previous cell death models [210]. By using more than 150 rats, this study also investigated the percentage of necrotic neurons and ischaemic regions over a period of up to 7 days following the right MCA occlusion, which can be useful in studying the longer term effects of ischaemic stroke on tissue damage. However, the data in this study are unsuitable to fit the parameters of a perfusion-based cell death model, due to the lack of perfusion measurements.

In another study using monkey models, Jones et al. [64] studied the infarct formation threshold of perfusion at different times after a MCA occlusion as shown in Fig. 2.21. The threshold was found to have a sigmoidal shape in that no infarct forms even in the

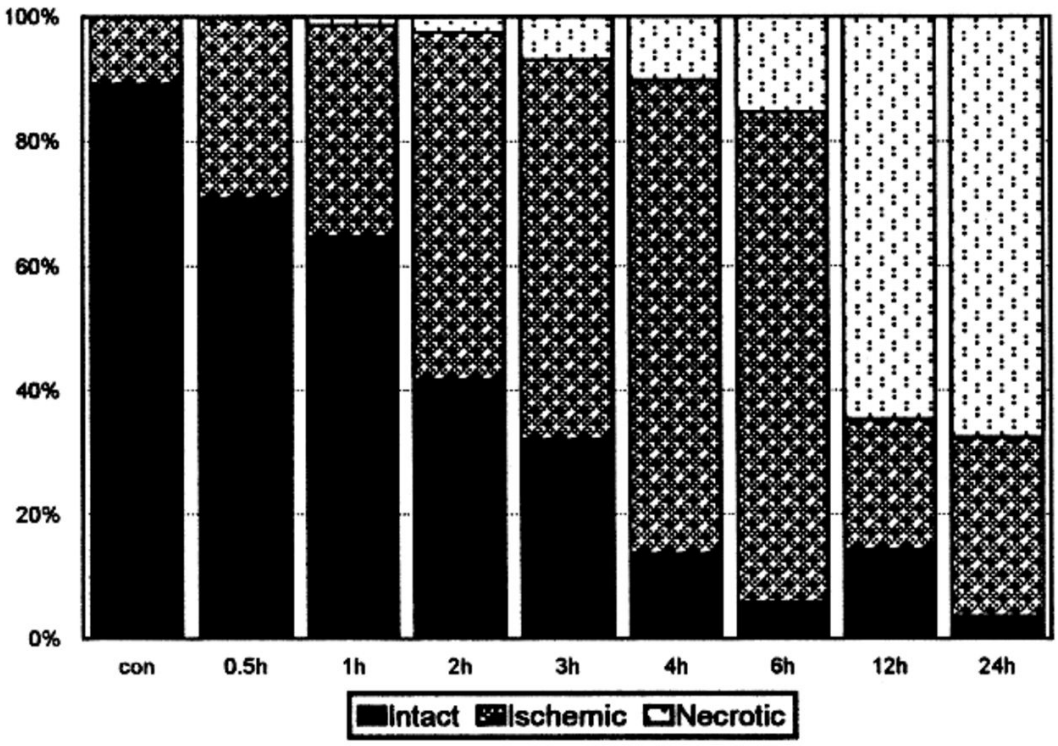

Figure 2.20: Percentage of neurons in intact, ischaemic and necrotic states in the ischaemic hemisphere at different time points following a right MCA occlusion in rats. Reproduced with permission from [65].

regions where the perfusion drops to about 2 mL/100g/min, followed by a linear increase towards a perfusion threshold of 18 mL/100g/min, above which no infarct forms even under a permanent occlusion. The experimental data (dashed curve) shown in Fig. 2.21 will be used to fit cell death models in Chapter 6, since they include information for both perfusion and time. However, it should be noted that the sigmoidal curve is only a prediction from limited temporal data points.

Lastly, it is worth examining how these local non-linear tissue responses lead to infarct progression at the organ-scale. Dijkhuizen et al. [211] used a rat model and DWI to measure the volume fraction of ischaemic tissue (tissue with a reduced apparent diffusion coefficient of water) in the ischaemic hemisphere from 0.5 to 6 hours after a MCA occlusion. The experiments found a sharp increase of ischaemic tissue fraction from

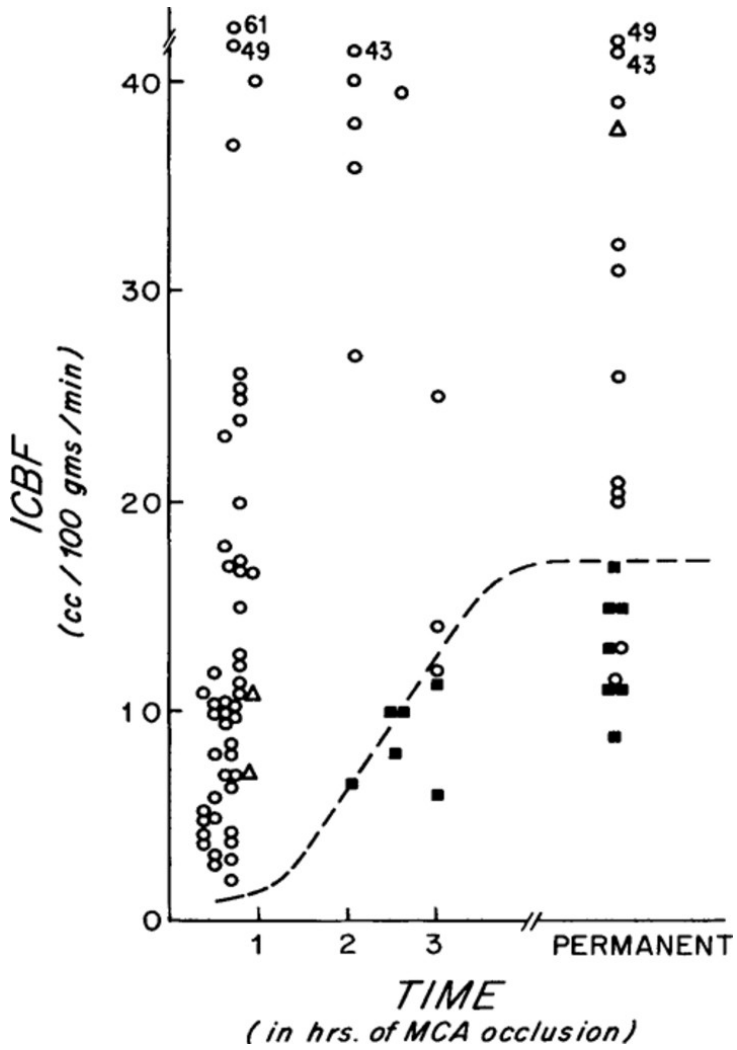

Figure 2.21: The infarction threshold of perfusion at different times following a MCA occlusion in monkeys. Reproduced with permission from [64].

0 to 18.4% in the first 45 minutes, which is then followed by a linear increase to 33.7% at 5 hours after the occlusion. This study suggests that there is likely to be a two-phase ischaemic damage mechanism at the organ-scale, and that the ischaemic core forms very quickly in the regions of severe hypoperfusion, followed by a slow expansion of damage in the neighbouring tissue.

2.5.3 Cell death models of ischaemic stroke

Due to the complexity of tissue injury responses to ischaemia, only a few computational models have been developed to simulate the tissue damage following an ischaemic stroke [21, 40, 41, 212–218]. The inputs of these models include blood flow, oxygen and glucose supply and neural activity. The model output is usually tissue viability. These models have struck different balances between complexity and computational efficiency, while some models are built from detailed cellular metabolism [21, 40, 41] and others focus on the damage mechanisms [212, 213, 215]. However, only one model is coupled with a 3D brain geometry model [40] and none of these models has been validated against or completely fitted to the experimental data, which limits their applications significantly.

The main reason for such limited validation is that most of these models have tens of parameters, some of which are essentially impossible to be measured *in vivo*. Another reason is that the temporal data of cerebral ischaemic tissue damage to fit these time-dependent models are in fact very limited. Most of these experiments with good temporal data have been reviewed in Section 2.5.2.2. Hence simplified cell death models are necessary to build a validated pipeline of *in silico* simulation of ischaemic stroke, with insights from validated cell death models on other biomedical problems [210]. These new models will be introduced in Chapters 5 and 6.

2.6 Summary

In this chapter, an overview of the cerebrovascular system is first presented, focusing on its multi-scale structure from major arteries down to capillaries. At the micro-scale, models of cerebral blood flow and oxygen transport have been reviewed and discussed. Next, this chapter introduces the ischaemic stroke, a scenario that these micro-scale models can be applied to, and its current clinical challenges. To aid in addressing these challenges, *in silico* models have been developed, which are now able to simulate the perfusion

change at the organ-scale following an ischaemic stroke. Finally, the cerebral tissue damage responding to ischaemia is reviewed, highlighting the significance of developing novel cell death models and coupling these models with the current macro-scale blood flow models, to enable their wider applications in time-dependent simulations of cerebral tissue damage.

Based on these previous studies, this thesis will develop new models to study the effects of cerebral microembolism on oxygen transport in Chapters 3 and 4 in Part I. It will then move to the macro-scale to simulate the impact of cerebral ischaemia and hypoxia on tissue damage in Chapters 5 and 6 in Part II.

Part I

Micro-scale: Oxygen transport and microembolism

Chapter 3

Modelling the effects of cerebral microemboli on oxygen transport and tissue oxygenation

---

The work presented in this chapter has been published in [219]: Xue, Y., El-Bouri, W. K., Józsa, T. I. & Payne, S. J. Modelling the effects of cerebral microthrombi on tissue oxygenation and cell death. *Journal of Biomechanics* **127**, 110705 (2021).

Abstract

Thrombectomy, the mechanical removal of a clot, is the most common way to treat ischaemic stroke with large vessel occlusions. However, perfusion cannot always be restored after such an intervention. It has been hypothesised that the absence of reperfusion is at least partially due to the clot fragments that block the downstream

vessels. This chapter presents a novel model to quantify the effects of cerebral microthrombi on oxygen transport to tissue in terms of hypoxia and ischaemia. The oxygen transport was simulated with the Green's function method on physiologically representative microvascular cubes, which was found independent of both microvascular geometry and length scale. After microthrombi occlusions, the tissue hypoxic fraction can be described as a sigmoidal function of vessel blockage fraction. The quantitative relationship between microthrombi and tissue hypoxia is now possible to be implemented in the whole brain model or coupled with a cell death model to model the tissue damage as a function of time. This will play a significant role in *in silico* models of ischaemic stroke and thrombectomy.

3.1 Introduction

Stroke is one of the leading causes of death and disability in the world, while ischaemic stroke accounts for about 85% of cases [220]. During ischaemic stroke, large vessel occlusions lead to a significant reduction in cerebral blood flow (CBF) to regions of the brain and hence to brain tissue death [58]. Thrombectomy, the mechanical removal of a clot, is the most common surgical treatment to recanalize the vessel [176]. It remains unclear why complete reperfusion cannot always be achieved after mechanical recanalization. It has been hypothesised that the absence of reperfusion may be caused by downstream micro-occlusions, blood–brain barrier disruption or brain oedema [182]. In this chapter, the impact of microthrombi, which fragment off large clots during thrombectomy [60, 182, 183], on tissue oxygenation and health is investigated.

Due to the limited resolution of current imaging techniques, it may not be possible to monitor microthrombi occlusions inside the human cerebral microvasculature, and hence to study the related clinical outcomes [183, 221, 222]. Rodent models have thus been widely used to investigate cerebral microembolisms and micro-infarcts but these studies rely on assumed similarity between the human and rodent cerebral vasculature [53, 74–76].

In silico modelling can be used as an alternative to study the effects of microthrombi on human brain tissues. Previous *in silico* microvasculature models include the capillary beds [25, 27, 89] and penetrating vessels [25, 87] generated from morphological data of the human cortex [23, 26, 79]. Recently, the effects of a penetrating vessel occlusion were simulated for the first time at a length scale comparable to that of MRI voxels, which can be directly validated against clinical images [28].

The multidisciplinary INSIST project aims to build a computational platform to evaluate medical interventions and devices for ischaemic stroke treatments [44]. As part of the project, virtual patients with organ-scale brain models are developed to simulate blood flow, oxygen transport and infarct progression during an ischaemic stroke [36, 37]. A model that simulates clot fragmentation and the resulting effects on perfusion and oxygen transport can be directly coupled with the current whole brain model to investigate the reasons for reperfusion failure after thrombectomy.

In silico models have been proposed to determine the impact of microthrombi occlusions on perfusion in the microvasculature [29, 111, 193]. Previously, the effects of clot fragmentation on perfusion after thrombectomy have been studied [29]. The clot fragmentation and micro-emboli shower simulations were based on in vitro experimental data [60]. Blood flow was modelled inside statistically representative microvasculature models, including penetrating arterioles and capillaries [27, 28, 87]. The perfusion drops in microvascular voxels and cortical columns and their relationships with different blockage percentage were investigated. However, none of the aforementioned models simulate the impact of microthrombi on tissue oxygenation and cell death which is necessary to validate our in silico whole brain model against clinical imaging data from post-thrombectomy patients.

In this chapter, the Green's function method [144, 166] is applied on physiologically representative capillary cubes [27] to investigate the effects of microvascular geometry

and length scale on cerebral oxygen transport. In addition, the work presented in this chapter aims to answer how cerebral perfusion and tissue oxygenation respond to different degrees of micro-occlusions quantitatively. The simulation results of tissue hypoxia at the micro-scale can be used as inputs for cell death modelling in the organ scale models, which will be introduced in Chapter 5.

3.2 Methods

The methods used in this chapter will be presented here. The section will start by introducing the vascular networks and blood flow simulation. Then, the Green's function method for oxygen transport simulation will be introduced. Finally, the micro-occlusion simulations will be presented. Most of the models used in this chapter can be found in Chapter 2. All key parameters used in this chapter have been summarised and referenced in Table 2.2.

3.2.1 Capillary networks and blood flow simulation

Statistically representative human capillary networks are used here for blood and oxygen transport simulations [27]. Blood flow was simulated through these networks using Poiseuille's law assuming a constant haematocrit of 45%. The perfusion in each capillary cube was scaled to 55 mL/100g/min under healthy conditions [36, 147, 169]. Details of capillary networks and blood flow simulation can be found in Sections 2.1.2 and 2.2.3.

3.2.2 Oxygen transport simulation

Oxygen delivery from microvasculature to tissue was simulated using the well-established Green's function method [144, 166]. In Green's function simulations, oxygen transport and metabolism depend on PO_2 both in the blood vessels and the tissue. Oxygen transport was simulated by an integration of oxygen strength fields acting on each cubic tissue region. The cerebral metabolic rate of oxygen was assumed to follow a

Michaelis-Menten relationship dependent upon tissue PO_2 (Eq. 2.33). The relationship between the blood oxygen saturation and the blood PO_2 was assumed to be described by a Hill equation (Eq. 2.27). The governing equations of these models are summarised in Section 2.3.

The inlet PO_2 ($PO_{2,\ in}$) was then varied from 13 mmHg to 50 mmHg in steps of 1 mmHg in each capillary cube, in order to explore a wide range of values. After running the simulation, PO_2 and oxygen consumption were analysed to obtain the average tissue PO2, hypoxic fraction (taken here to be the fraction of tissue at a value of PO_2 below 10 mmHg) [55], $CMRO_2$ and oxygen extraction fraction (OEF, fraction of blood oxygen taken by tissue). An example capillary cube and its Green's function solutions under both normal and hypoxic conditions are shown in Fig. 3.1.

3.2.3 Microthrombi simulation inside the microvasculature

To mimic the presence of microthrombi inside the microvasculature, random occlusions were introduced in selected vessels of a 375 μm capillary network. A specified number of vessels was occluded to give a blockage fraction ranging from 1% to 20% in steps of 1% (rounded to the closest integer). At each blockage fraction, 5 different simulations were carried out with $PO_{2,\ in}$ set to be 40 mmHg [77]). Hence a total of 100 micro-blockage simulations have been run in this study.

In order to maintain network periodicity, the vessels connected to boundary nodes were excluded from occlusions. In addition, any occlusion simulation that divided the network into multiple isolated parts was disregarded to keep the connectivity, so that the conductance matrix (Eq. 2.11) remained invertible and the flow could be solved with the existing algorithm [27]. For the same purpose, the maximum blockage fraction was set as 20%.

After randomly blocking the vessels, the perfusion was simulated with the same pressure

drop along the capillary cube as applied under healthy conditions, based on the assumption of normal cerebral autoregulation [39]. The same Green's function simulation and data post-processing were performed as described earlier.

3.2.4 Numerical procedure

The linear equations governing the blood flow were solved in MATLAB R2019b (MathWorks, USA)[1]. The oxygen diffusion–reaction equations were simulated by Green's function methods using the publicly available implementation[2], written in C++ and recently applied to oxygen delivery [105, 106]. Curve fitting (non-linear least square optimization in SciPy), ordinary differential equations solving (integrate library in SciPy) and post-processing were carried out in Python [223].

3.3 Results

3.3.1 Green's function simulation in capillary cubes

A typical 375 μm capillary cube is shown in Fig. 3.1a, where the blood vessel diameter is represented by the line thickness. Figures 3.1b and 3.1c display the 3D tissue PO_2 distributions in the same capillary network simulated by the Green's function method under healthy condition ($PO_{2,\ in}$ = 40 mmHg) and hypoxic condition ($PO_{2,\ in}$ = 20 mmHg) respectively. Figures 3.1e and 3.1f show the tissue oxygenation on a horizontal plane placed at the centre of the cube (Fig. 3.1d), where black crosses are the intersecting points between the blood vessels and the plane. The tissue oxygenation is distributed heterogeneously in the capillary cube and closely correlated with the microvascular geometry.

[1]This code has been written for [27]: El-Bouri, W. K., Payne, S. J. Multi-scale homogenization of blood flow in 3-dimensional human cerebral microvascular networks. *Journal of Theoretical Biology* **380**, pp.40-47 (2015), which is not part of this thesis.

[2]The code can be found at: `https://physiology.arizona.edu/people/secomb/greens`, which is not part of this thesis.

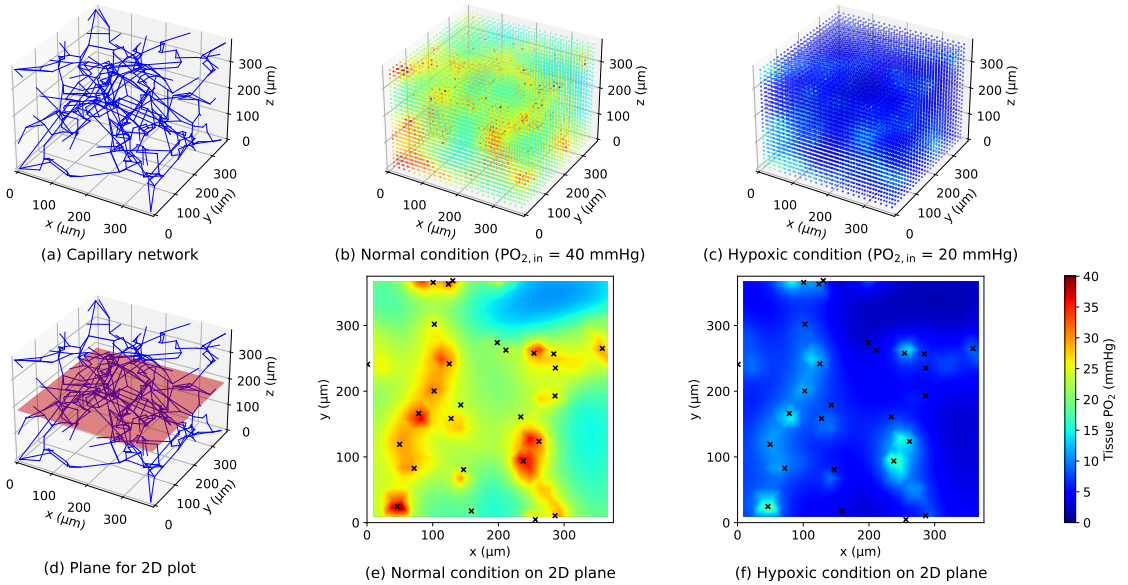

Figure 3.1: 3D visualisation of a typical 375 μm capillary cube (a) and its tissue oxygenation solved by the Green's function method under normal condition (b) and hypoxic condition (c). A horizontal plane (d) is placed in the centre of the cube and the tissue oxygenation on the plane is plotted under both normal (e) and hypoxic (f) conditions. The black crosses indicate the intersecting points between the centre lines of blood vessels and the plane.

3.3.2 Independence of oxygen transport on microvascular geometry and length scale

The simulation results of oxygen transport in microvascular cubes of two sizes (375 μm and 625 μm) are presented in Figs. 3.2a and 3.2b respectively. In each figure, the solid lines represent the average results among 10 different cubes and the error bars show the standard deviation among these 10 cubes. Average tissue PO_2 drops linearly from 28 to 2 mmHg when inlet blood PO_2 changes from 50 to 13 mmHg (Fig. 3.2). However, the hypoxic fraction has a strong non-linear growth from 0 to 100% in the same range of $PO_{2,\ in}$.

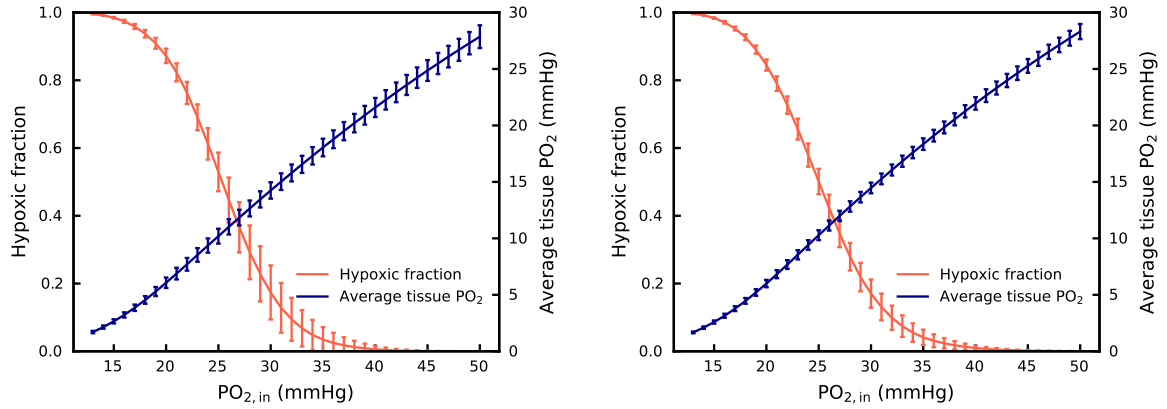

(a) 375 μm (b) 625 μm

Figure 3.2: Hypoxic fraction and average tissue PO_2 in the capillary networks with cube sizes of (a) 375 μm and (b) 625 μm when $PO_{2,\,in}$ is from 50 to 13 mmHg. The error bar shows the standard deviation of the results among 10 different cubes.

The simulation results of oxygen consumption are shown in Fig. 3.3. Cerebral metabolic rate of oxygen decreases non-linearly from 2.9 to 0.5 $cm^3/100cm^3/min$ alongside an oxygen extraction fraction increase to compensate the oxygen shortage, when $PO_{2,\,in}$ drops from 50 to 13 mmHg.

The small standard deviation of results between different capillary cubes indicates that the oxygen transport at microvasculature scale is largely independent of the specific geometry of individual capillary networks, as long as they are generated based on the same morphometric data (see error bars in Figs. 3.2 and 3.3). Moreover, the standard deviation in 625 μm cubes is smaller than that in 375 μm suggesting that the effects of microvascular topology and geometry on oxygen transport becomes increasingly negligible in a larger domain of interests.

The small difference between the results in cubes of two sizes (375 μm and 625 μm) implies that the oxygen transport is independent of length scales above a few hundred micrometres. This finding is consistent with previous works of blood flow simulation [27].

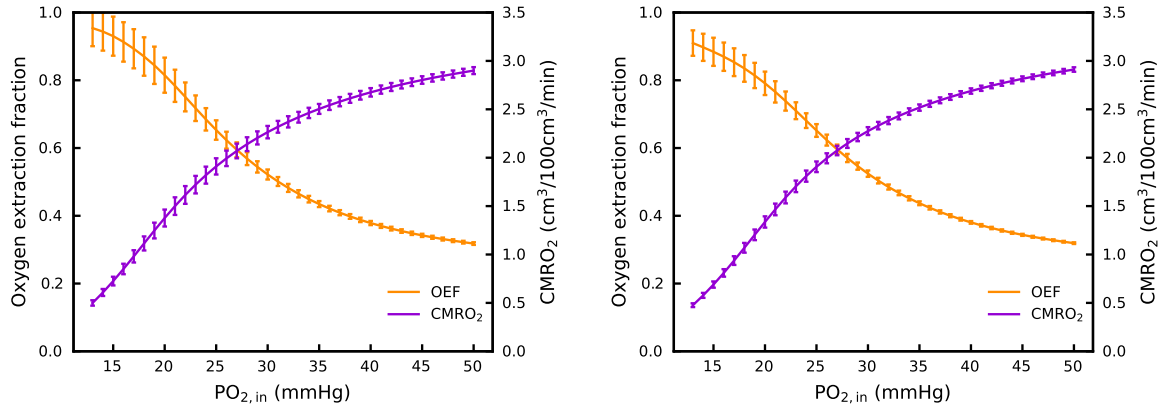

(a) 375 μm

(b) 625 μm

Figure 3.3: Oxygen extraction fraction and oxygen consumption rate in the capillary networks based on cube sizes of (a) 375 μm and (b) 625 μm when $PO_{2,\ in}$ is from 50 to 13 mmHg. The error bar shows the standard deviation of the results among 10 different cubes.

3.3.3 Effects of hypoxic threshold on hypoxic fraction

In this thesis, the threshold of hypoxia was set as 10 mmHg, which was used by our experimental collaborators [55, 56]. In order to broaden the applicability of this work, the effects of different hypoxic threshold on hypoxic fraction were studied. In Fig. 3.4, the average hypoxic fraction of 10 different 375 μm capillary cubes were plotted under hypoxic thresholds from 6 to 14 mmHg. These curves have similar sigmoidal shape, however, they move horizontally when the threshold varies. These results mean that the hypoxic threshold used in simulations should match that in experiments carefully for a high-quality validation study. A validation of the spatial relationship between hypoxic regions and occlusion sites will be presented in next chapter.

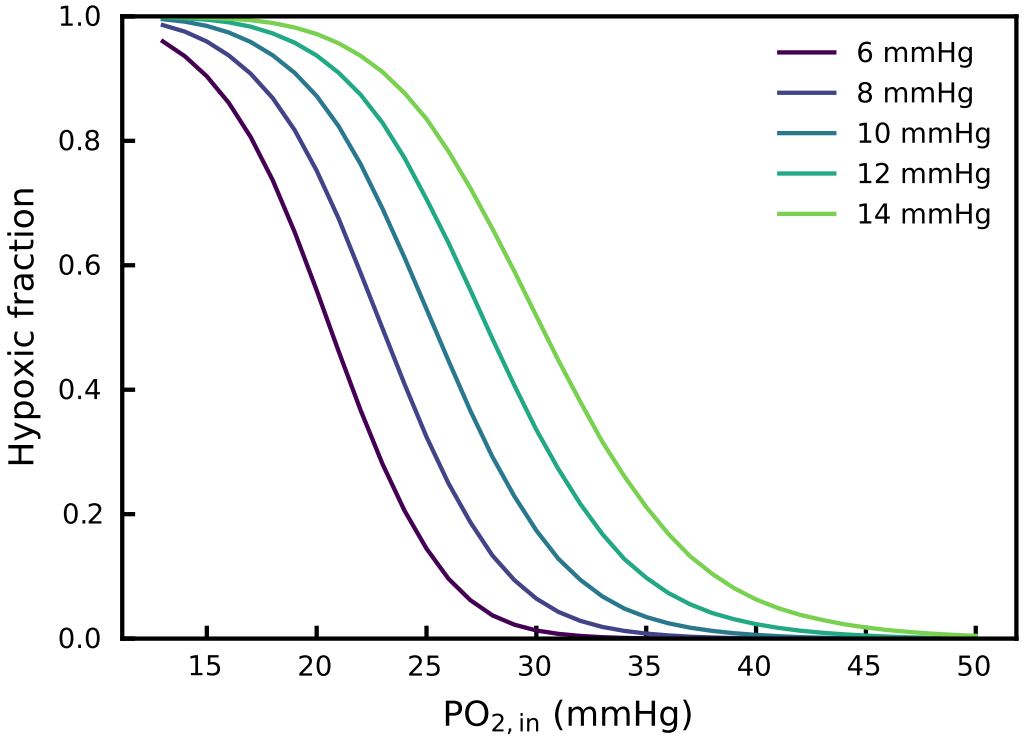

Figure 3.4: The average hypoxic fraction in 10 capillary cubes (375 μm) against $PO_{2,\,in}$ under hypoxic thresholds from 6 to 14 mmHg.

3.3.4 Microthrombi have significant impact on tissue hypoxia beyond 10% vessel occlusions

Figure 3.5 shows a typical 375 μm capillary cube (a) and its microvascular geometry after a 10% blockage (b) and a 20% blockage (c). The relative blood flow rate in each vessel is also plotted in each figure. There is a mild perfusion drop from the healthy network to the same network with 10% blockage, where most vessels still have blood flow (coloured in dark blue). However, the blood flow in some vessels drop sharply (coloured in light blue or white) when another 10% of the vessels are occluded. The perfusion drop inside the microvasculature is highly heterogeneous based on the occlusion locations.

The tissue oxygenation in the healthy network (d) drops accordingly in the 10% blockage

cube (e) and in the 20% blockage cube (f) as shown in Fig. 3.5. Despite the reduced mean PO_2, most tissue can remain healthy (PO_2 greater than 10 mmHg) under 10% blockage. However, there is a huge drop in tissue PO_2 when the blockage fraction increases from 10% to 20%, where large hypoxic regions also appear. The tissue hypoxia thus follows a strong non-linear relationship with the vessel blockage fraction. The hypoxic tissue also distributes heterogeneously in the capillary cube, while a match between regions of perfusion drop (light blue vessels in Fig. 3.5c) and hypoxic tissue regions (purple regions in Fig. 3.5f) can be observed, which indicates that the cerebral tissue hypoxia is mostly due to the ischaemic microvasculature. These simulation results show the tissue hypoxic response to ischaemia in a qualitative way.

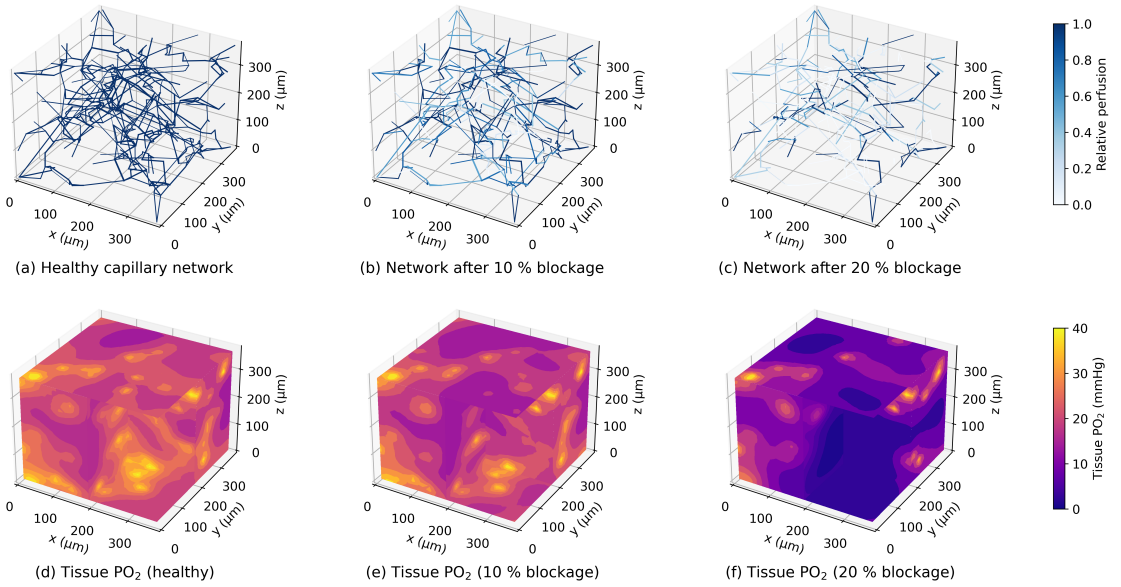

Figure 3.5: 3D visualisation of a typical 375 μm capillary cube (a) and the same network after 10% blockage (b) and 20% blockage (c). The tissue oxygenation was simulated with a inlet PO_2 of 40 mmHg under conditions of healthy (d), 10% blockage (e) and 20% blockage (f).

Figure 3.6 presents the quantitative change in perfusion and hypoxic fraction after different fraction of vessels in the capillary cube are occluded. The perfusion drops

linearly with the increase of blockage fraction (Fig. 3.6a), which can be described by a linear equation:

$$\text{rCBF} = -3.059B + 1 \tag{3.1}$$

where rCBF is the relative perfusion of healthy condition (55 mL/100g/min). It should be noted that this relationship is only valid until $B = 0.327$ where the perfusion will drop to zero. Since the same pressure drop was applied on two opposite surfaces of the cube as done in the healthy condition, the perfusion drop is purely due to the increased network resistance caused by micro-occlusions. The linear decrease of perfusion against the increase of blockage fraction agrees with previous simulations [29, 193]. The slop of decrease here is -3.06%/%, which is also comparable to -2.5%/% [193] and -3.2%/% [29] reported in previous studies.

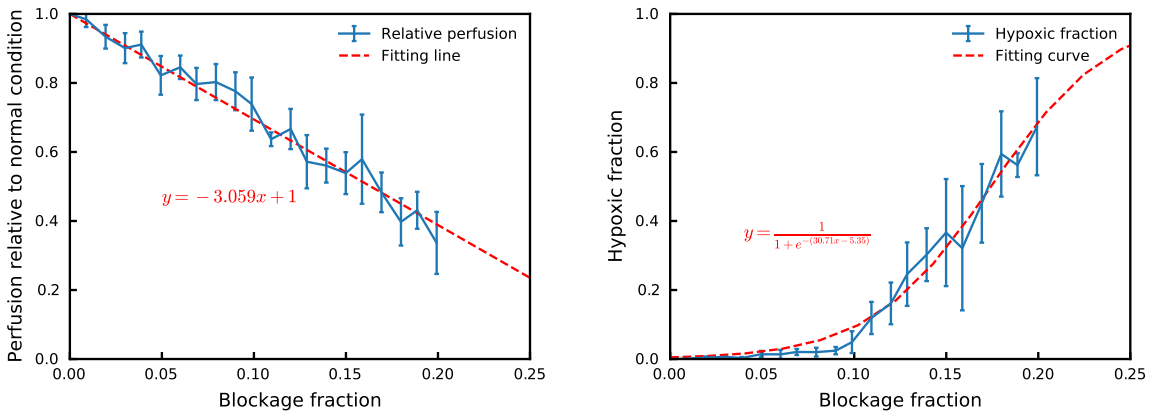

(a) Perfusion

(b) Hypoxic fraction

Figure 3.6: The perfusion (a) and hypoxic fraction (b) as functions of microthrombi blockage fraction.

The hypoxic fraction has a highly non-linear relationship with the blockage fraction (Fig. 3.6b). It remains almost unchanged until the blockage fraction reaches 10%. Beyond this threshold, the hypoxic fraction increases steeply to about 70% when the blockage fraction is 20%. Although simulation with a blockage fraction greater than 20% was not performed due to the disruption of network connectivity (the network would be divided

into isolated parts), it is reasonable to assume that the hypoxic fraction will approach 100% quickly (the entire tissue becomes hypoxic due to no blood supply) and become stable after that. This behaviour can be fitted with a sigmoidal function as

$$H = \frac{1}{1 + e^{-(30.71B - 5.35)}} \tag{3.2}$$

This sigmoidal function quantify the tissue oxygenation response (hypoxia) to the structural change in microvasculature (micro-occlusion). It will be coupled with a cell death model in Chapter 5 to simulate the hypoxic tissue damage in a scenario of microthrombi blockage after thrombectomy.

3.3.5 Microthrombi volume at micro-scale agrees with thrombus volume at macro-scale

Thrombus volume is a significant factor to quantify the potential severity of microembolisms after an unsuccessful thrombectomy. It is possible to estimate the total thrombus volume in microvasculature for a certain blockage fraction based on the microvascular geometry, which can be compared against the pre-treatment volume to verify if all microthrombi end in the capillary bed.

For example under a blockage fraction of 10%, there are 56 microthrombi inside a 375 μm capillary cube. By assuming that each vessel is blocked by a single spherical thrombus with a diameter equal to the diameter of the corresponding vessel, the total volume of microthrombi in this cube is 8.43×10^{-9} mL, which results in 1.60×10^{-4} mL microthrombi volume per mL of brain tissue. If there are 10% microembolisms in a territory of 100 mL fed by a MCA, the total microthrombi volume will be 1.60×10^{-2} mL.

Assuming that the volume of a thrombus is 0.17 mL [224] and 25% of its fragments are transported into the microvasculature, the total microthrombi volume will be 4.25×10^{-2} mL. It is about 2.66 times of the volume predicted from 10% capillary occlusions.

Hence the thrombus volume predicted from our model at micro-scale agrees with the macro-scale measurement in the same order of magnitude. If all 25% of clot fragments reach the capillary bed, it is likely to cause occlusions in 26.6% of capillaries, which will lead to a tissue hypoxic fraction of 94.4% based on Eq. 3.2.

3.4 Discussion

In this chapter, the Green's function method was applied on physiologically representative capillary cubes to simulate oxygen transport in the human cerebral microvasculature for the first time. The oxygen transport is closely coupled with the microvascular geometry, and thus leads to a heterogeneous distribution of oxygen levels in the tissue. In addition, it is also largely affected by the boundary condition of inlet blood oxygenation. However, the averaged oxygen transport and metabolism at the length scale of the capillary cubes based on the same morphometric data, are found to be independent of specific microvascular geometries.

Next, this chapter investigates the effects of microthrombi occlusions on cerebral oxygen transport. Cerebral perfusion drops linearly with the increase of the number of vessels occluded in the microvascular network, which leads to a linear equation between perfusion and blockage fraction. However, the tissue hypoxic fraction has a strong non-linear relationship with the blockage fraction. The relationship can be described by a sigmoidal function, which will be used to model the hypoxic tissue damage in Chapter 5. Finally, the microthrombi volume was estimated for a 10% blockage inside a capillary cube. The total microthrombi volume was found to have a nice agreement with the *in vivo* thrombus volume measured at macro-scale.

The physiologically representative capillary cubes used here remove the needs to reconstruct the network geometry from very limited human brain network data and to set the boundary conditions. The Green's function method significantly reduces the

computational costs of solving the oxygen transport in a complex network by transforming 3D diffusion equations into 1D Green's functions. The application of the Green's function method on statistical capillary cubes provides an novel workflow to investigate oxygen transport in the human microvasculature with limited experimental data and much reduced computing power. The pipeline can also be adapted to new oxygen delivery scenarios easily as long as the morphometric data and parameter values are provided.

Since the oxygen transport is found to be independent of both microvascular geometry and length scale, the local behaviour inside a capillary cube is possible to be scaled up to the cortical column scale [28] and the organ scale [36, 37]. It also helps to prevent running Green's function simulations in a very complex network, which can be computationally expensive.

One limitation of this study is the assumption of no oxygen supply from larger vessels. However, multiple studies have shown that cerebral oxygen transport happens over several vessel generations primarily from pre-capillary arterioles to capillaries [77, 93, 94, 137]. The oxygen transport from penetrating arteriole trees cannot be simulated with these capillary cubes, which limits the length scale where the model developed here can be used. However, the model of penetrating arterioles [87] will be coupled with these capillary cubes in the next chapter. Therefore, this limitation only exists in this chapter and its application in Chapter 5.

Another limitation is the partial use of animal data and parameters, while this study aims to study the effects of microthrombi on oxygen transport in the human brain. For example, rat data have been used to derive the parameters in the Hill equation (Eq. 2.27), which describes the non-linear relationship between oxygen tension and oxygen saturation in the blood. Here it is simply assumed that the physiology of blood flow and oxygen transport is very similar in human and rats. Once more human data are available, these models can be adapted to these new parameter values easily.

In addition, constant haematocrit in microvasculature was assumed in this study. However, the red blood cells are not evenly distributed at microvascular bifurcations or trifurcations *in vivo* due to phase separation effects [96, 121], which can lead to variances of blood flow and oxygen transport at local scale, since viscosity and oxygen carrying capacity of blood are both dependent on haematocrit. Previous studies have suggested that the effects of uneven haematocrit distribution on blood flow are likely to be second order at the length scale of capillary cubes [27, 88]. This has also been discussed in Section 2.2.5.2.

Lastly, the models proposed in this study are purely passive, although local perfusion and oxygen transport is actively and tightly controlled [1]. In addition, this chapter focuses on the averaged properties inside the capillary cubes, while neglecting the heterogeneous distribution of hypoxic regions [56]. The spatial relationship between hypoxic regions and occlusion sites will be investigated in the next chapter.

Summary

This chapter has applied the Green's function method on physiologically representative cerebral capillary cubes to study the effects of micro-occlusions on oxygen transport. The oxygen transport inside human cerebral microvasculature is found to be independent of both geometries and length scales of the cubes. Cerebral perfusion drops linearly with the increase of vessel blockage fraction. However, the relationship between tissue hypoxic fraction and vessel blockage fraction is highly non-linear, which can be fitted with a sigmoidal function. It is now possible to quantify the hypoxic damage of microthrombi occlusions due to unsuccessful thrombectomy, which can then be coupled with other established brain models. In Chapter 4, the oxygen transport will be simulated in cortical columns and the simulation results will be validated against animal data from our collaborators. In Chapter 5, the sigmoidal function of hypoxia against blockage will be coupled with a cell death model and a microthrombi extravasation model to simulate the cerebral tissue damage as a function of time.

Chapter 4

Quantification of hypoxic regions distant from occlusions in cerebral penetrating arteriole trees

---

The work presented in this chapter has been published in [225]: Xue, Y.*, Georgakopoulou, T.*, van der Wijk, A.-E., Józsa, T. I., van Bavel, E.* and Payne, S. J.* Quantification of hypoxic regions distant from occlusions in cerebral penetrating arteriole trees. *PLOS Computational Biology* **18**(8), e1010166 (2022). *: co-first/co-senior authors. In this chapter, the animal experiments were conducted by Theodosia Georgakopoulou under the supervision of Professor Ed van Bavel at Amsterdam University Medical Centre, and these are not part of this thesis. The analysis of brain slice images is, however, part of this thesis. The works conducted by Theodosia Georgakopoulou will be clearly stated in the footnote.

Abstract

The microvasculature plays a key role in oxygen transport in the mammalian brain. Despite the close coupling between cerebral vascular geometry and local oxygen demand, recent experiments have reported that microvascular occlusions can lead to unexpected distant tissue hypoxia and infarction. To better understand the spatial correlation between the hypoxic regions and the occlusion sites, both *in vivo* experiments and *in silico* simulations were used to investigate the effects of occlusions in cerebral penetrating arteriole trees on tissue hypoxia. In a rat model of microembolisation, 25 µm microspheres were injected through the carotid artery to occlude penetrating arterioles. In representative models of human cortical columns, the penetrating arterioles were occluded by simulating the transport of microspheres of the same size and the oxygen transport was simulated using a Green's function method. The locations of microspheres and hypoxic regions were segmented, and two novel distance analyses were implemented to study their spatial correlation. The distant hypoxic regions were found to be present in both experiments and simulations, and mainly due to the hypoperfusion in the region downstream of the occlusion site. Furthermore, a reasonable agreement for the spatial correlation between hypoxic regions and occlusion sites is shown between experiments and simulations, which indicates the good applicability of *in silico* models in understanding the response of cerebral blood flow and oxygen transport to microemboli.

4.1 Introduction

Due to the high metabolic demands and its limited capacity for storage, the mammalian brain depends on near constant CBF to sustain sufficient nutrient and oxygen delivery [226]. Adequate CBF is maintained by the process of cerebral autoregulation (the response of cerebral vessels to blood pressure changes) [128]. Based on local neuronal activation [227], tissue oxygenation is ensured by a compact and complex microvascular

network of arterioles and capillaries [2].

The acute effects that follow a sudden CBF reduction, such as loss of consciousness in case of a syncope [228] and irreversible neurological damage in case of a cardiac arrest or acute ischaemic stroke (AIS) [229, 230], underline the brain's vulnerability to anoxia. Next to global CBF disruption and large vessel occlusion, cerebral microinfarcts can also lead to detectable brain damage [222]. Such microinfarcts can result from microemboli [231], which can be released into the cerebral circulation under a number of conditions, including atrial fibrillation, unstable plaques [232], or endovascular treatment (the mechanical removal of a thrombus in AIS patients) [233]. However, due to the low resolution of brain imaging techniques, cerebral microinfarcts in humans are mainly discovered only after post-mortem examination.

Evidence of the effects of micro-occlusions on brain tissue thus primarily comes from rodent studies. Such studies have shown that micro-occlusions, formed in response to the intra-arterial injection of microemboli, can lead to multiple regions of ischaemia, hypoxia and infarction [55, 234–238], cognitive dysfunction [239, 240], blood brain barrier permeability, astrogliosis and inflammation [54, 241]. Using a sophisticated photothrombotic technique which selectively occludes individual penetrating arterioles, Shih et al. not only monitored the formation and progress of a single microinfarct but also assessed the resulting cognitive deficits [76, 242]. Such experiments have also confirmed that arterioles have a poor network of anastomoses [74].

Despite these studies, little quantitative information exists on the relationship between micro-occlusion sites, ischaemic territory, and hypoxic area. Given the known vulnerability of penetrating arterioles to obstruction and the distant effects of a single microinfarct on the surrounding tissue [242], it is important to quantify both the extent to which blood vessel architecture affects tissue oxygenation, and how blood vessel architecture and clot location determine the fate of brain tissue viability after blood

flow obstruction. A better understanding of brain oxygenation is not only relevant for an improved understanding of the response of the circulation to stimuli but can serve as a starting point for treatment of cerebrovascular diseases [128, 243]. For instance, quantitative data on brain tissue damage caused by microemboli could lead to the improvement of medical devices used for post-AIS endovascular treatment.

To this end, numerical models have recently been developed to aid in understanding the structure of cerebral microvasculature [25, 27, 28, 87, 94, 105–107, 144, 244], and the effects of micro-occlusions on blood flow [28, 29, 111, 193] and oxygen transport [108]. In Chapter 3, the oxygen transport was simulated in cerebral capillary cubes using the Green's function method [144] and quantified the tissue hypoxia responding to different level of micro-occlusions. However, the penetrating arterioles were not included in the previous model, which limited the length scale that it was able to represent and thus made it difficult to compare predictions to the microembolisation experiments [55, 56] that aim at the penetrating arterioles [73].

This chapter thus investigated further the effects of micro-occlusions in penetrating arteriole trees (the vessels between the capillaries and the pial circulation) on tissue hypoxia using both experimental and numerical methods. In the animal experiments, 25 μm (in diameter) polystyrene microspheres were injected through the common carotid artery (CCA) of rat models, which led to tissue ischaemia and hypoxia. Then part of the intervention hemisphere in each animal was reconstructed and segmented the locations of microspheres and hypoxic regions in a 3D coordinate system. In the simulations, a number of human cortical column networks were first constructed. These networks were then occluded by microspheres of the same size, and the Green's function method was applied to simulate oxygen transport. Two novel distance analyses were conducted to investigate the spatial relationship between hypoxic regions and occlusion sites in both experiments and simulations in an identical manner. This enabled direct comparisons to be made between experimental and numerical results and thus to quantify the relationship

between the locations of micro-occlusions and hypoxic regions. These results will be valuable in further understanding the response of cerebral tissue to micro-occlusions.

4.2 Methods

4.2.1 Animal experiments[1]

4.2.1.1 Animal surgeries

All animal experiments were approved by the ethics committee of the University of Amsterdam, University Medical Center (permit number: DMF321AA). For the required procedures the ARRIVE guidelines and European Union guidelines for the care laboratory animals (Directive 2010/63/EU) were followed. Six Wistar rats (n=6, 50% female, 16-20 weeks old, Charles River) were used. The animals received ad libitum food and water and were pair-housed in standard plastic cages with a 12h:12h light-dark cycle.

Surgeries were performed exactly as described earlier by Georgakopoulou et al. [56]. Briefly, animals were anesthetized with a mixture of 100% oxygen and isoflurane (Isoflutek 1000 mg/g; Laboratorios Karizoo SA, Barcelona, Spain). After exposure of the left CCA at the bifurcation level, the external carotid artery and occipital artery were temporarily ligated with a surgical suture (size 6.0). To mimic microembolisation, 200 µl of fluorescent microspheres (DiagPoly™ Custom made Plain Fluorescent Microparticles, Excitation wavelength 656 nm, Emission wavelength 674 nm, Creative Diagnostics®, Shirley, NY; 5500 microspheres were injected of 25 μm in diameter) resuspended in a sterile 2% bovine serum albumin solution of phosphate buffered saline (PBS), was injected via the left CCA using an insulin syringe (29 G) as shown in Fig. 4.1(a). Microspheres were lodged in the left hemisphere, leaving the right hemisphere as a control, as depicted in Fig. 4.1(c).

[1]The animal experiments were conducted by Theodosia Georgakopoulou at Amsterdam University Medical Centre. Only the Python codes used in Section 4.2.1.4 are part of this thesis.

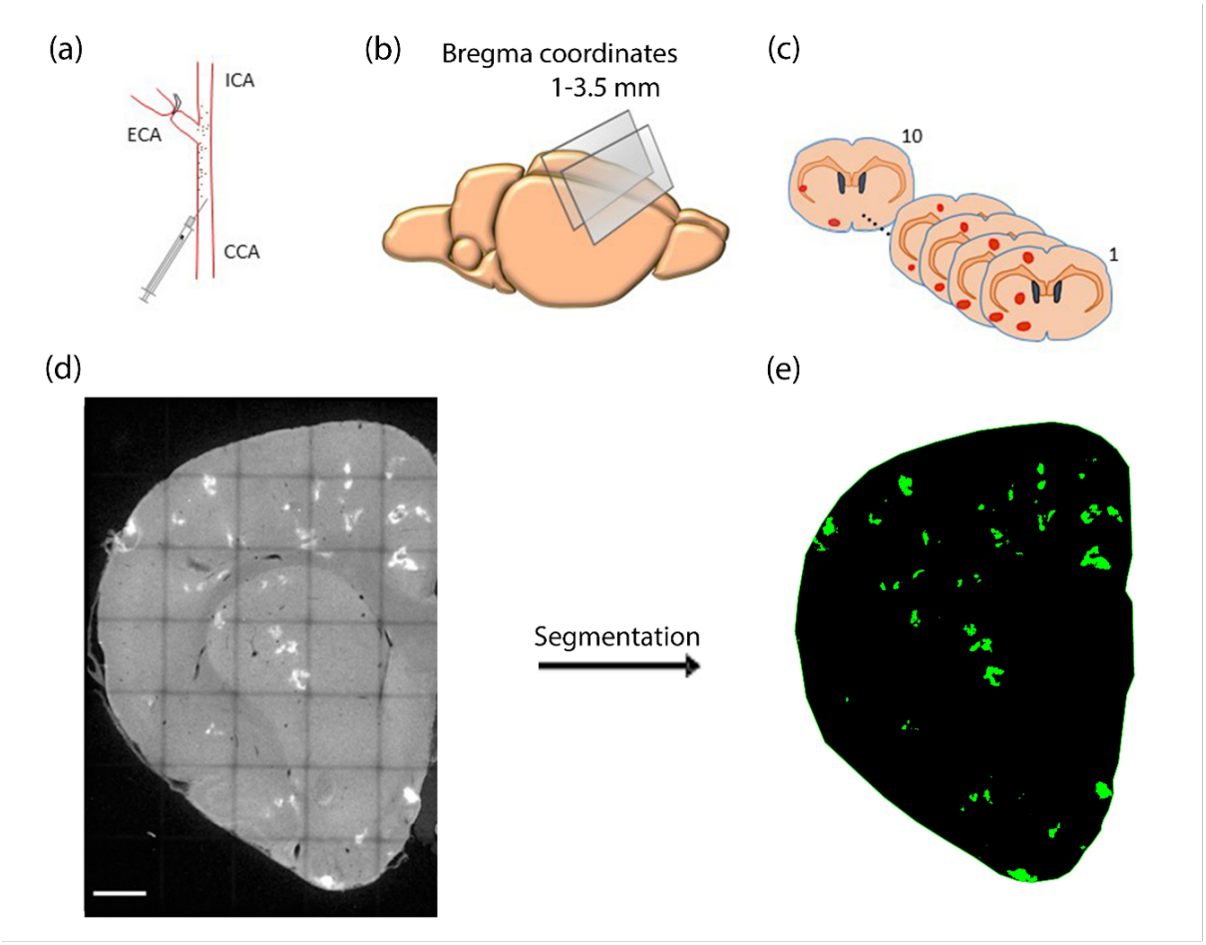

Figure 4.1: (a) Microembolisation model: Injection of microspheres via left CCA; (b) Brain sections (50 μm thick) were made between 1-3.5 mm bregma coordinates; (c) Ten consecutive coronal brain sections were selected for the brain damage reconstruction. Brain tissue damage (in red) was mainly confined on the intervention hemisphere; (d) Maximum intensity projection (MIP) of a 50 μm thick coronal brain section of the intervention hemisphere with hypoxic regions (white). Tilescan image was made using confocal imaging, Scale bar 1000 μm; (e) The same brain section as in (d) after the segmentation of hypoxic regions (green) in the IMARIS software. CCA - common carotid artery; ICA - internal carotid artery; ECA - external carotid artery.

4.2.1.2 Tissue preparation and immunohistochemistry

Animals were killed 24 hours post-surgery. Pimonidazole hydrochloride (60 mg/kg; Hypoxyprobe™ Pacific Blue Kit, HP15-x, Burlington, MA) was used as a marker of

hypoxia and lectin (1 mg/kg; DyLight 594 labeled lycopersicon Esculentum tomato, Vector Laboratories, DL-1177, Burlingame, CA) as a marker of ischaemia [55]. Pimonidazole hydrochloride is a probe which binds to cells that have a PO_2 smaller than 10 mmHg and lectin is a dye which stains perfused blood vessels intravenously. Brain removal, brain pre-processing, and immunohistochemistry of brain sections (50 μm thick) were performed as described previously [55]. Mouse anti-pimonidazole (Hypoxyprobe™ Pacific Blue Kit, HP15-x, 1:500) antibody was used to detect Hypoxyprobe and hence to visualize hypoxia.

4.2.1.3 3D reconstruction of intervention hemisphere

For the spatial analysis between microspheres and brain damage, a 500 μm thick volume of the intervention hemisphere was reconstructed. Ten consecutive coronal brain sections (50 μm thick) devoid of tearing were selected from the forebrain between 1 and 3.5 mm of the bregma as shown in Fig. 4.1(b)-(c). Tilescan z-stack images (resolution: x,y: 3.033 μm and z: 5 μm) of the intervention hemisphere were acquired using a confocal laser scanning microscope SP8 (Leica Microsystems, Wetzlar, Germany) with a 10x objective. To facilitate alignment, the z-stack images were converted to maximum intensity projection (MIP) images as depicted in Fig. 4.1(d). To this end, the ImageJ software (Rasband, W.S., ImageJ, U. S. National Institutes of Health, Bethesda, Maryland, USA) was utilised, whereas MIP images were aligned using the AMIRA software (Visage Imaging, Inc., San Diego, CA, USA). The resultant z-resolution was thus 50 μm.

4.2.1.4 Segmentation of microspheres, ischaemic and hypoxic regions

Reconstructed brain volumes of the intervention hemisphere were inserted in IMARIS 9.3, a 3D analysis software (Bitplane Inc., St. Paul, MN, USA) and the spot creation wizard and surface creation wizard were used to automatically segment microspheres and hypoxic regions respectively (Fig. 4.1(e)). Ischaemic regions were segmented manually by an experienced researcher. The segmented volumes were exported from IMARIS as numbers

in excel files and as .tiff binary images, separate for each segmented element (microspheres, ischaemic and hypoxic regions). To quantify how deep in the cortex microspheres were lodged, their distance from the cortical surface were calculated manually, using Leica LAS X software (Leica Microsystems, Germany).

Custom Python codes were used to locate the microspheres and hypoxic regions in the .tiff images to enable distance computations. The 2D binary MIP images were then converted to 3D based on the given z-coordinate of the centre of the coronal brain sections. Images of hypoxic regions were downsampled into $15.165 \times 15.165 \times 50$ μm^3 voxels to enable direct comparison with the $15 \times 15 \times 15$ μm^3 resolution employed in the simulations, as described in the following subsection.

4.2.2 Computational models

4.2.2.1 Physiologically representative cortical columns

To simulate the oxygen transport in a cortical column supplied by a single penetrating arteriole, existing models of penetrating arterioles [87] and capillaries [27] were coupled together. Note that these networks were generated from human cerebral microvasculature data [23, 26, 79]. To represent a tissue volume of $375 \times 375 \times 1500$ μm^3, four periodic 375 μm capillary cubes were stacked along the depth of the cortical column. A penetrating arteriole model was then placed at the centre of the column with its inlet aligned with the cortical surface. The branches of the arteriole tree outside the column were trimmed and the boundary nodes were each connected to the closest node of the capillary network. Figure 4.2 displays typical examples of: (a) a capillary network; (b) a penetrating arteriole tree; and (c) a typical cortical column assembled from these two networks. The geometric information of the 10 example cortical columns generated here is summarised in Table 4.1.

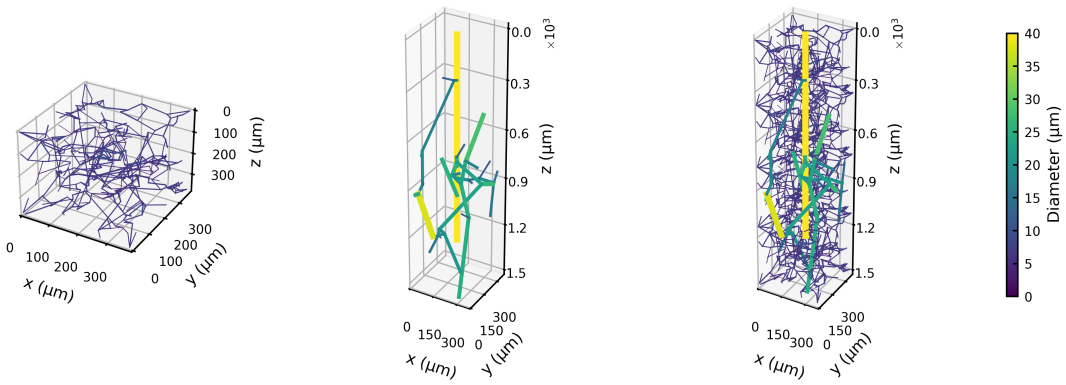

(a) Capillary network (b) Penetrating arteriole (c) Cortical column

Figure 4.2: Geometry of (a) a capillary network, (b) a penetrating arteriole and (c) a cortical column built from the penetrating arteriole and the capillary cubes.

	Simulation	Literature
Surface density of arterioles	$7.11/\text{mm}^2$	$5.63 - 10/\text{mm}^2$ [79, 245]
Vessel density	$10846 \pm 163/\text{mm}^3$	$10129/\text{mm}^3$ [24]
Vascular volume fraction	$2.82 \pm 0.22\%$	2.70% [24]

Table 4.1: Geometric information of cortical columns.

4.2.2.2 Blood flow simulation

The blood flow in the microvasculature is assumed to be in quasi steady state. The flow is also assumed to be purely laminar because of the low Reynolds number of about 0.5 in arterioles and about 0.003 in capillaries [95]. In addition, it was assumed that the flow was fully developed and axisymmetric with zero velocity components in the radial and circumferential directions. Hence the Hagen-Poiseuille equation (Eq. 2.9) can be used for blood flow in each vessel. The blood viscosity was calculated by using the empirical function of vessel diameter and haematocrit (Eq. 2.14-2.17) [85]. The haematocrit was taken to be a constant value of 0.45 [27] and the plasma viscosity was taken to be 1.2

mPa·s [87, 112].

Details of blood flow simulation can be found in Section 2.2.3. In this study, all boundary nodes were assumed to have the same pressure, except for the arteriole inlet node at the top of the column. The blood pressure difference between arteriole inlet and boundary nodes was adjusted to maintain a normal perfusion of 55 mL/100mL/min in each column [36, 147, 169]. All blood flow simulations were carried out using custom Python scripts.

4.2.2.3 Oxygen transport simulation

Oxygen transport simulations were performed using the Green's function method [144, 166]. The same Green's function method used in Chapter 3 was implemented here. The cerebral metabolic rate of oxygen was assumed to have a Michaelis-Menten relationship with tissue PO_2 (Eq. 2.33). The relationship between blood oxygen saturation and blood PO_2 was simulated by a Hill equation (Eq. 2.27). A detailed description of these models can be found in Section 2.3. The parameter values used in the Green's function method can be found in Table 2.2, except for the blood PO_2 at arteriole inlet, which was set as 90 mmHg. Custom Python scripts were written to read the network geometry and to post-process the simulation results.

4.2.2.4 Blockage simulation

To simulate occlusion in the arteriole tree, a bead with a size of 25 μm was introduced at the arteriole inlet of each of the 10 cortical columns. The bead was assumed to be carried by the blood flow and to be trapped at the inlet of the first vessel that it reached with a diameter smaller than the bead size of 25 μm. This led to 6-15 occlusion scenarios in each cortical column, due to different column geometries, which resulted in a total of 91 scenarios in 10 columns. Here it was simply assumed that the probability of each blockage in a column is the same since there is currently no suitable bead transport model in the cerebral microvasculature. In addition, only one bead is assumed to be present in

each arteriole due to the low bead density found in animal experiments (0.43/column, Section 4.3.1). Hence, it was assumed that there are only two situations of the cortical column supplied by one penetrating arteriole: one bead or no bead. After the blockage simulation, the hypoxic regions were identified in each column as the tissue voxels with a PO_2 smaller than 10 mmHg, i.e., matching the experimental setting.

4.2.3 Distance calculations for both experimental and simulated data

Two types of distance analysis were performed to establish spatial relationships between vessel blockages and hypoxic regions, namely the pixel-based Gx function and the hypoxic intensity. These two analyses were conducted in identical ways in *in vivo* experiments and *in silico* simulations, which enables high-fidelity comparisons to be made between the two. Note that the regions outside of the brain tissue in experiments and outside of the cortical columns in simulations were excluded from these distance analyses.

The pixel-based Gx function is defined here as the cumulative fraction of distances from the hypoxic regions to their closest microspheres:

$$\text{Pixel} - \text{based Gx}(d) = P(\delta < d) \tag{4.1}$$

where d is the distance, P is the probability and δ is the distance from a hypoxic pixel to its closest microsphere. Note that this analysis is different from the Gx function conducted in the previous study, which used the centre of each hypoxic region instead [56]. In the simulations, the small number of voxels with PO_2 below 10 mmHg under healthy condition were excluded from the pixel-based Gx function analysis.

The hypoxic intensity is defined as the volume fraction of hypoxic tissue in a sphere of a certain radius around a microsphere, which is thus a function of distance. Around each microsphere the hypoxic intensity was calculated up to a radius of 500 μm with

a step size of 50 μm. In each cortical column, the hypoxic intensity was averaged for all possible blockage sites since it has been assumed that the same probability of each blockage scenario in each column.

To investigate the spatial correlations between hypoxic regions and microspheres in the experiments, Monte-Carlo simulations of microspheres were conducted; these simulations provided the control situation against which the randomness of the distributions obtained here were compared. The control points were randomly generated in the intervention hemisphere in each animal, where the density of points was equal to the *in vivo* bead density in the same brain region. Then the same hypoxic intensity analyses were conducted around these control points, which were compared against the hypoxic intensity calculated in experiments.

4.3 Results

4.3.1 Ischaemic and hypoxic distribution patterns after blocking the cerebral arterioles in a rat model of microembolisation[2]

Table 4.2 shows the number and density of microspheres and the resulting ischaemia and hypoxia per animal. The density of 25 μm microsphere of 2.03/mm^3 (average of 6 animals) results in a volume fraction of 1.66×10^{-5} mL beads per mL cerebral tissue. If it is assumed that the beads are entirely present in a territory of 100 mL supplied by a middle cerebral artery in a human, the total thrombus volume will be 1.66×10^{-3} mL. This value is significantly smaller than a typical thrombus volume of 0.17 mL [224], which indicates that the micro-occlusions considered in this study correspond to a case where only about 1% of a larger thrombus is embolised during thrombectomy and thrombolysis.

[2]The animal experiments were conducted by Theodosia Georgakopoulou at Amsterdam University Medical Centre.

Animal	Number of microspheres	Microspheres density ($1/mm^3$)	Total volume of 10 brain sections ($1/mm^3$)	Fraction of ischaemia in hemisphere	Fraction of hypoxia in hemisphere
1	25	1.23	20.32	0.51%	0.81%
2	41	1.97	20.86	1.90%	1.40%
3	47	1.89	24.84	2.69%	2.38%
4	26	1.29	20.18	0.64%	0.30%
5	88	4.07	21.61	2.19%	1.68%
6	35	1.73	20.28	0.98%	1.15%

Table 4.2: Number and density of microspheres, total brain volume and % of ischaemia and hypoxia per animal. These numbers were measured in the reconstructed brain volumes with a thickness of 500 μm.

A typical example of a blocked arteriole is shown in Fig. 4.3 where a single 25 μm microsphere blocks an arteriole of similar size and leads to ischaemia (absence of lectin staining-red) and hypoxia (green). Since the animals are killed 24 hours post-surgery, neuronal cell death has already taken place which explains in some cases the absence of hypoxic cells from the lesion core. The implications of this will be discussed later.

Figure 4.4 shows the distribution of microspheres (white) and the resulting ischaemic (red) and hypoxic (green) regions in each animal. Due to the stochastic nature of the microsphere distribution the resulting ischaemia and hypoxia are not confined to one brain region but are dispersed throughout the brain structures (Cortex, Striatum, Corpus callosum). It was found that 73% of the microspheres were lodged in the cortex with the remaining found in deeper brain structures. From the microspheres lodged in the cortex only 0.07% were found on the cortical surface and the majority were lodged at a mean distance of 940.69 ± 122.54 μm from the cortical surface. Although ischaemia and hypoxia are distributed heterogeneously, there is a reasonable match (36.1 ± 5.3% of hypoxic regions are also ischaemic) between the two in the affected brain hemisphere

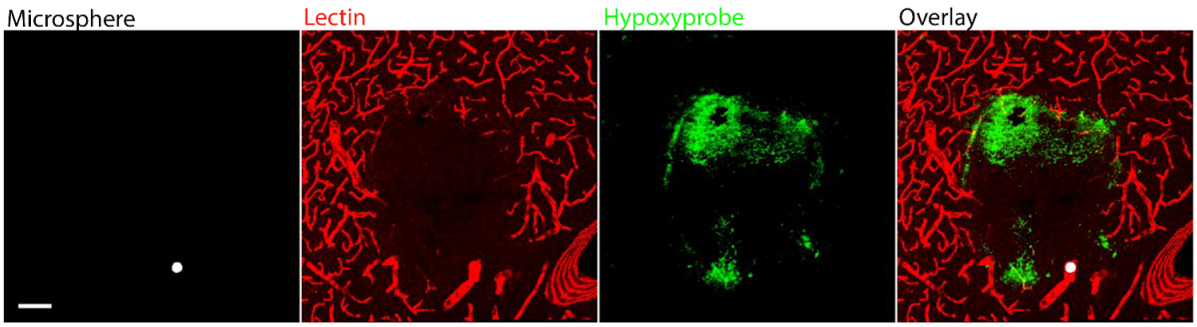

Figure 4.3: Maximum intensity projection (MIP) of a 50 μm thick brain section of the intervention hemisphere showing a typical example of a 25 μm (diameter) microsphere causing ischaemia (absence of lectin-red) and hypoxia (green) in the rat brain. Scale bar 100 μm.

within each animal (yellow colour in overlay channel Fig. 4.4).

4.3.2 3D distance analysis reveals two patterns of hypoxic intensity and a strong correlation between microspheres and hypoxic damage[3]

In a previous study where a mixture of microspheres was injected via the CCA, a spatial correlation over hundreds of micrometres between microspheres and centroids of hypoxic regions was found by applying a point pattern 3D distance analysis [56]. However, this experimental setup was not suitable to isolate the effects of a single microsphere or a single size of microspheres on brain tissue oxygenation. Thus, here only one size of microspheres were injected and a different approach for the 3D distance analysis was used. In particular, the hypoxic intensity, as a function of the distance from each microsphere, was measured, where each hypoxic intensity curve thus represents the distribution of hypoxic regions around a single 25 μm microsphere.

[3]The animal experiments were conducted by Theodosia Georgakopoulou at Amsterdam University Medical Centre. The analysis of these experimental data is part of this thesis.

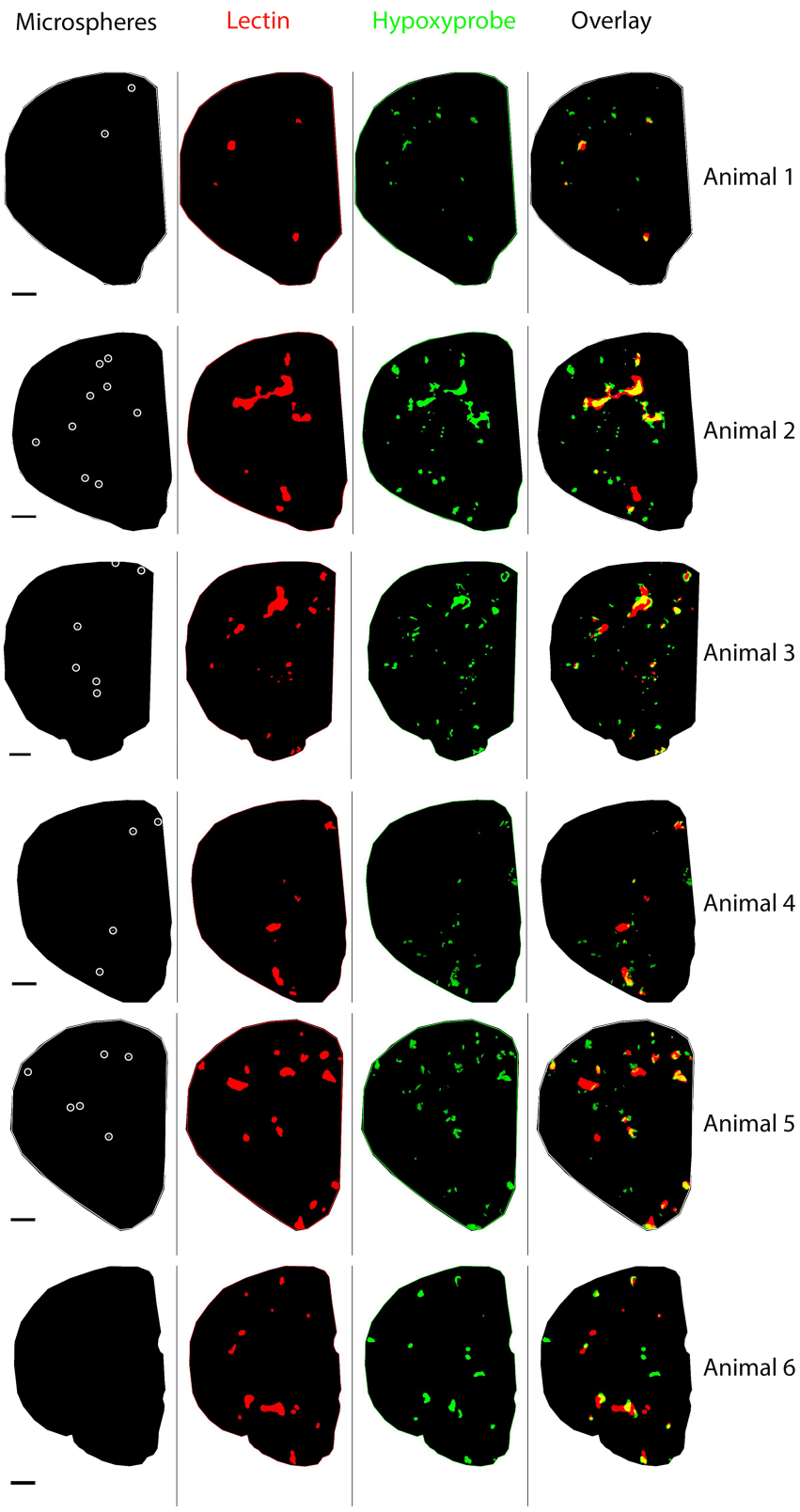

Figure 4.4: Per animal a representative segmented brain section of the intervention hemisphere. From left to right: microspheres (centre of white circles), ischaemia (red), hypoxia (green) and overlay of the three channels. In yellow is shown the overlap between ischaemia and hypoxia. Scale bar 1000 μm.

As shown in Fig. 4.5, there are cases in all 6 animals where hypoxic intensity decreases to less than half within the first 200 μm and cases where hypoxic intensity starts from zero and reaches 10-20% within the first 200 μm. To elucidate this phenomenon, the hypoxic intensity patterns were categorised into two types (Fig. 4.6(a)), based on the criterion of whether the slope is negative when the radius increases from 50 to 100 μm (Type A: accounting for 30.9% of the cases when considering all 6 animals), or positive (Type B: 69.1% of the cases). Note that the cases of full hypoxia and no hypoxia inside a radius of 100 μm were categorised as type A and type B respectively. Representative examples for both types are shown in a 2D schematic in Fig. 4.6(b).

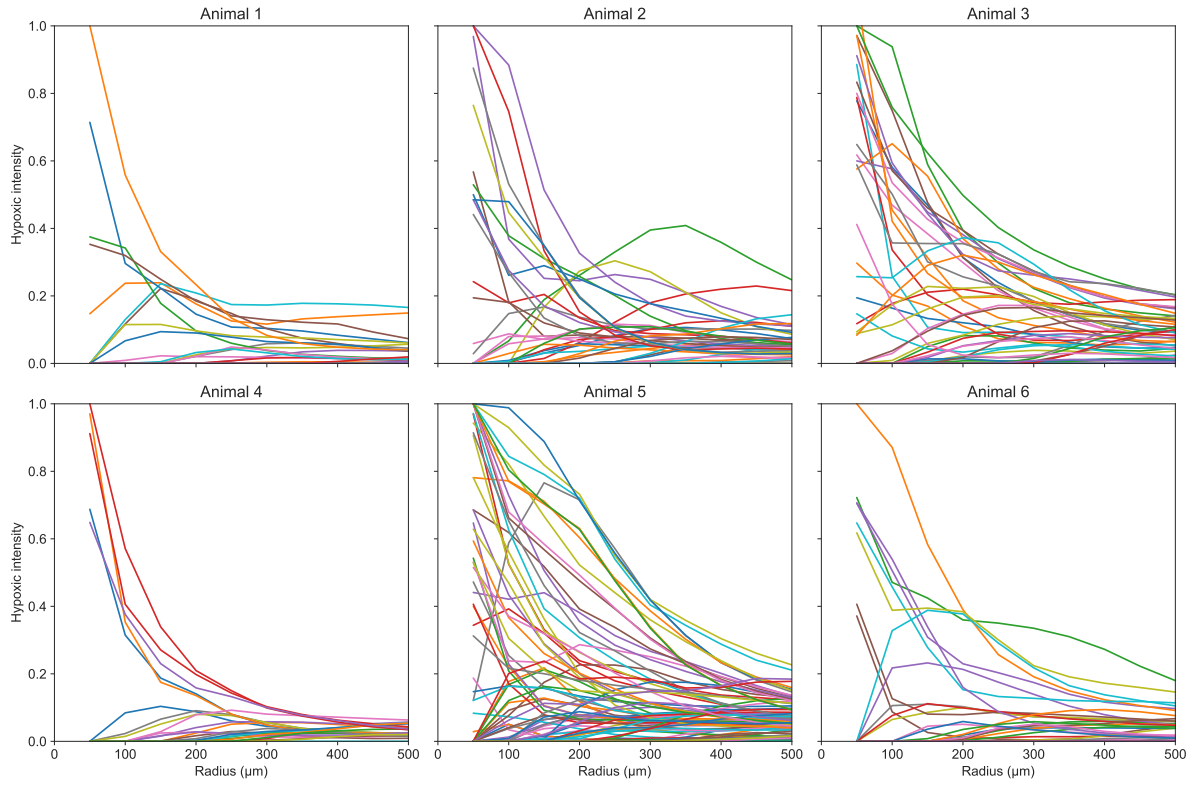

Figure 4.5: Per animal the mean hypoxic intensity as a function of the distance from a microsphere.

To further investigate whether the hypoxic regions form locally or distally around the microspheres, the two types of hypoxic intensity were categorised into four subtypes

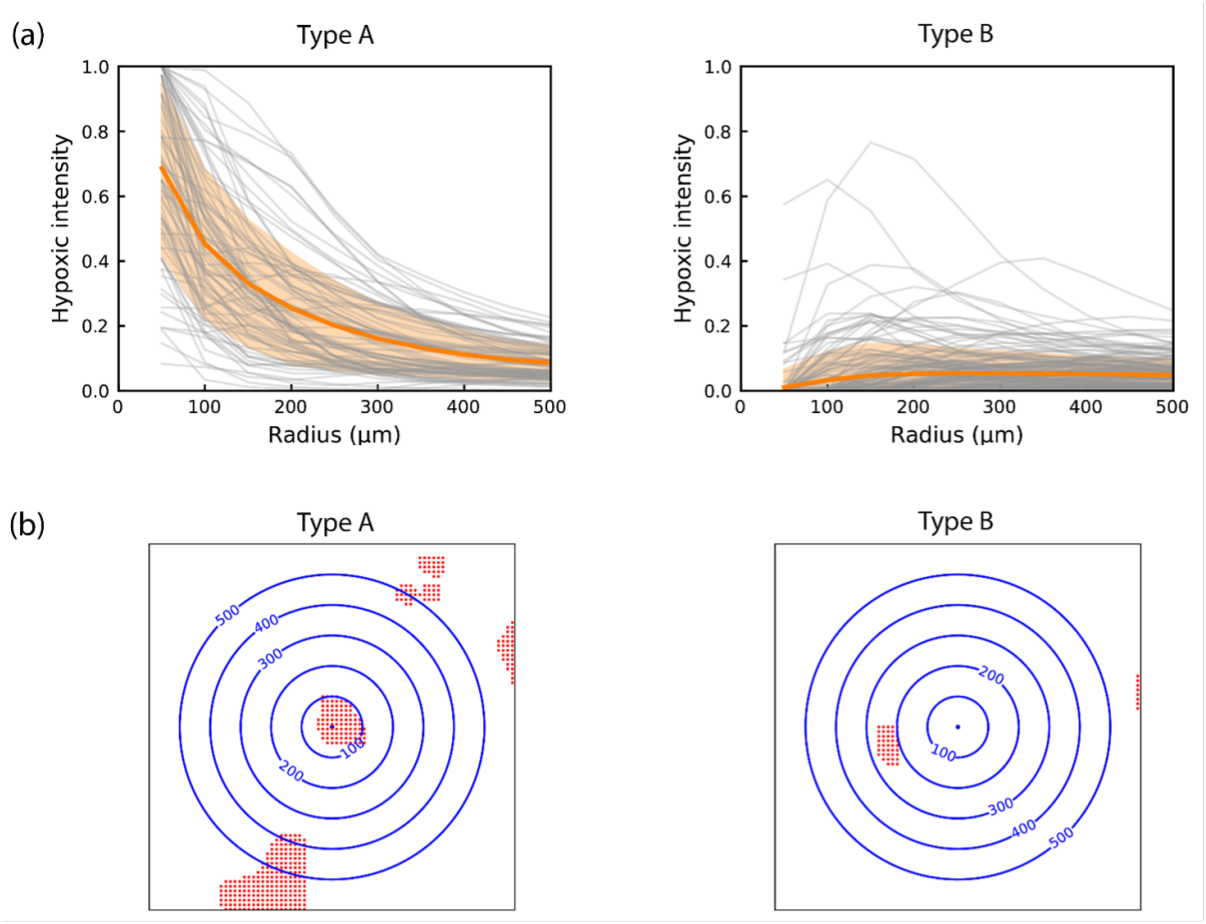

Figure 4.6: (a) Two types of hypoxic intensity. Type A is characterised by negative slope and Type B by positive slope. Mean ± standard deviation (filled areas) (all microspheres of n=6 animals); (b) Representative examples of the two types of hypoxic intensity. A 2D schematic of the 3D hypoxic intensity analysis. Using a microsphere as a starting point, the number of hypoxic pixels (red) were calculated in spheres of increasing radius (blue concentric circles).

based on the presence or absence of hypoxic regions within 100 μm of the microsphere. The percentage of each subtype in all 6 animals is listed in Table 4.3. Hypoxic regions are absent within 100 μm of the microsphere in the majority of the type B cases, which also account for 49.2% of all cases. Thus, approximately half of the 25 μm microspheres did not lead to local hypoxia in our experiments.

	Type A	Type B
Hypoxic regions present within 100 μm of the microsphere (local hypoxia)	30.9%	19.8%
Hypoxic regions absent within 100 μm of the microsphere (no local hypoxia)	/	49.2%

Table 4.3: Percentage of cases of type A and type B hypoxic intensity with or without hypoxic regions within 100 μm of the microsphere.

Next, it was tested whether there was a correlation between microspheres and hypoxic pixels. To do this, Monte-Carlo simulations were performed using random control points. The Monte-Carlo simulations shown in Fig. 4.7 for all animals are found to give results that are below the curves of the experimental data: this thus indicates a degree of correlation between individual microspheres and resulting hypoxic regions. Note that only the hypoxic intensity calculations for experimental results were introduced here; the pixel-based Gx function results will be presented in Section 4.3.5.

It should be noted that these distance calculations do not consider the vessel architecture. Due to tissue deformation and other technical issues such as brain section alignment, blood vessel reconstructions based on confocal imaging of brain sections are not sufficiently accurate. Even in a brain tissue made transparent by means of clearing techniques, blood vessel segmentation remains challenging. This knowledge gap is thus addressed using the numerical simulations presented below.

4.3.3 Heterogeneous distribution of tissue oxygenation in the cortical column

Figure 4.8 shows the tissue oxygenation in a typical cortical column as solved by the Green's function method. The simulations suggest that oxygen is distributed highly heterogeneously in the tissue within a cortical column. However, it is highly coupled

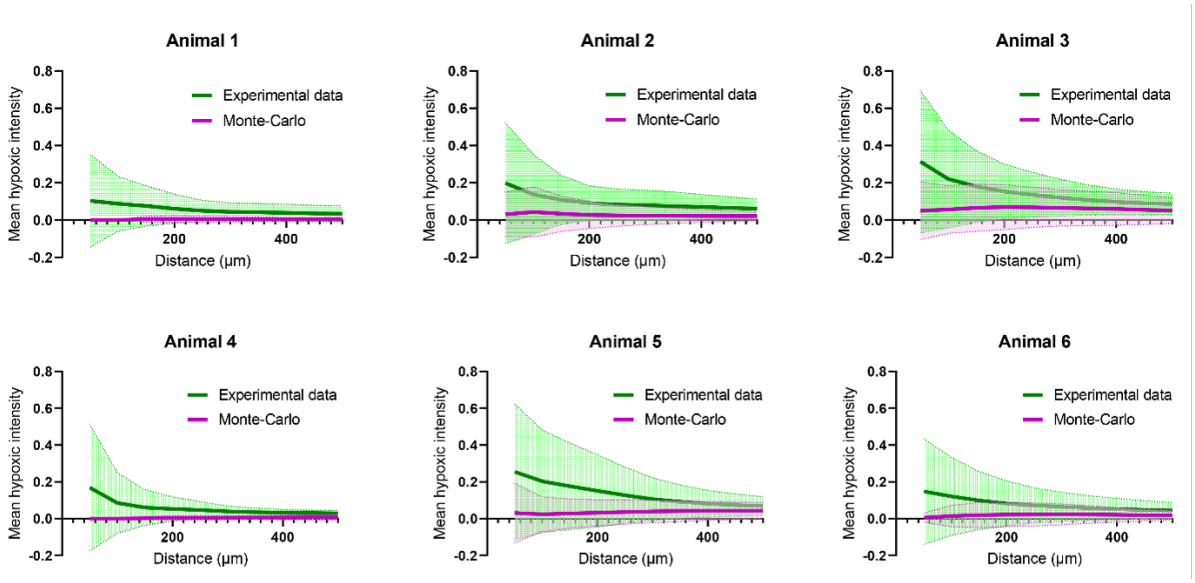

Figure 4.7: Per animal experimental data versus Monte-Carlo simulations. Monte-Carlo simulations: hypoxic intensity as a function of the distance from random control points. Mean ± standard deviation (filled areas) (all microspheres or control points of n=6 animals).

with the microvascular geometry, especially the geometry of the arteriole tree.

To investigate the effects of arteriole and capillary geometries on oxygen transport, two simulations were performed: one in a cortical column with the same arteriole structure as shown in Fig. 4.8(a) but using a different capillary network (Fig. 4.9), and the other in a cortical column using the same capillary geometry but connected to a different arteriole tree (Fig. 4.10). The change in capillary geometry or arteriole geometry leads to a root-mean-square difference of 9.7 or 15.9 mmHg for PO_2 in each tissue voxel in the column, respectively. However, these local variations were found to only have negligible effects on the overall PO_2 distribution in the column (Fig. 4.2).

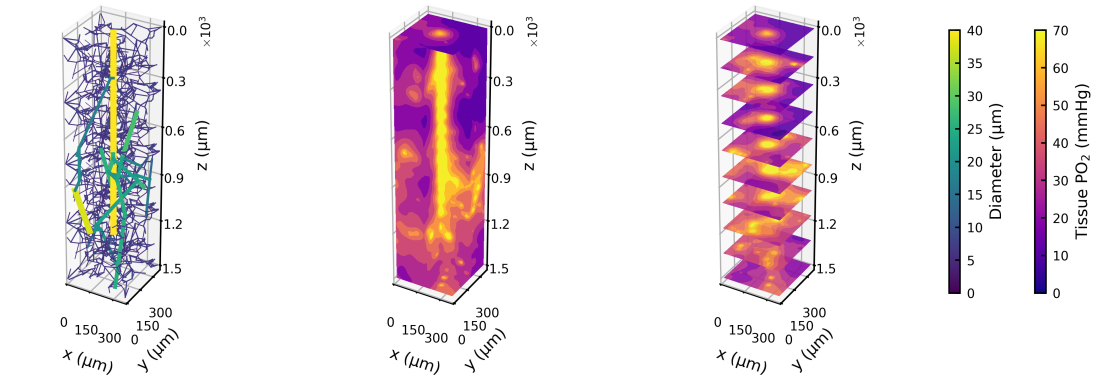

(a) Network geometry (b) PO_2 map in 3D (c) PO_2 on 2D slices

Figure 4.8: The geometry of a typical cortical column (a) and its tissue oxygenation (b, c) solved by the Green's function method.

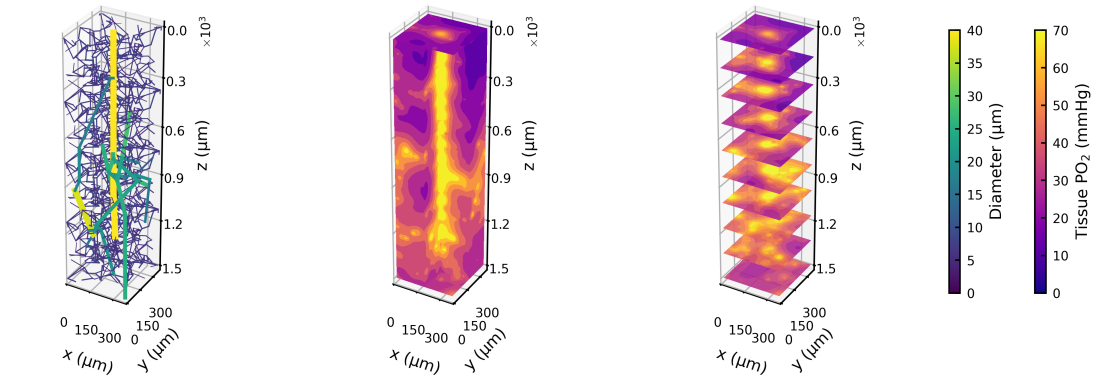

(a) Network geometry (b) PO_2 map in 3D (c) PO_2 on 2D slices

Figure 4.9: The geometry of a column with the same arteriole geometry as shown in Fig. 4.8(a) but different capillary geometry (a) and its tissue oxygenation (b, c).

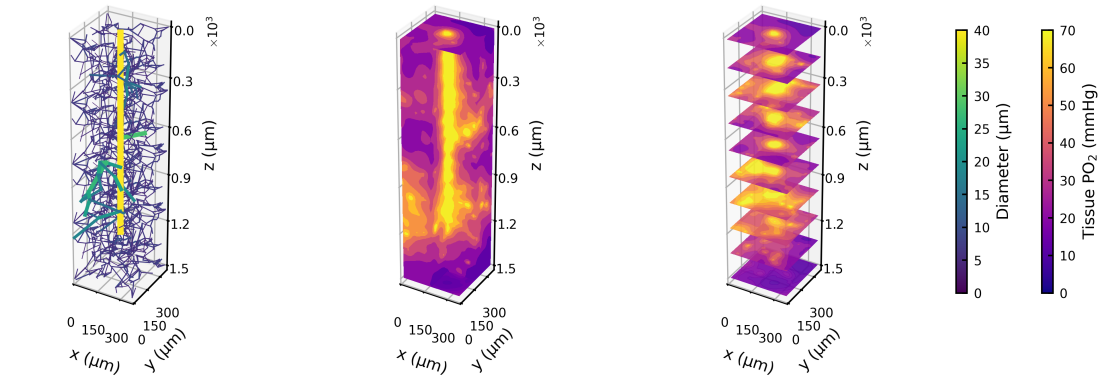

(a) Network geometry (b) PO_2 map in 3D (c) PO_2 on 2D slices

Figure 4.10: The geometry of a column with the same capillary geometry as shown in Fig. 4.8(a) but different arteriole geometry (a) and its tissue oxygenation (b, c).

4.3.4 Response of tissue oxygenation to blockage on the arteriole tree

Figure 4.12 displays three different 25 μm blockage scenarios in the same cortical column, where the blockage locations are indicated by blue spheres. The micro-blockage leads to perfusion drops in the downstream vessels and corresponding regions. The reduction in blood flow (in dark grey) because of the occlusion site is strongly heterogeneous in the column. In addition, the relative perfusion drop in the whole column is 18.5% (a), 50.7% (b) and 8.2% (c) respectively in these three blockage scenarios; this value is thus highly dependent on the blockage location and the specific downstream microvasculature.

The tissue PO_2 drop is also distributed unevenly in the column. However, the regions of tissue PO_2 drop (in red), which are primarily located around the blood vessels with largest flow rate drops (in dark grey), match those of reduced perfusion closely. The PO_2 drop then leads to hypoxic regions (PO_2 smaller than 10 mmHg), which are shown as

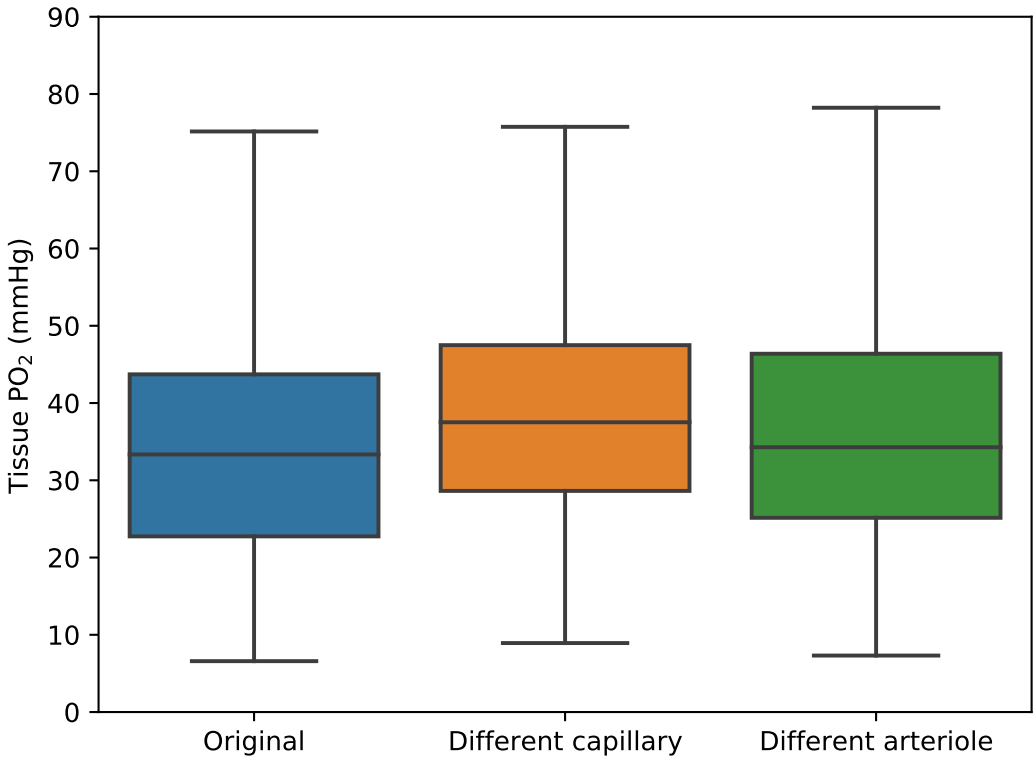

Figure 4.11: Tissue PO_2 distribution in cortical columns shown in Figs. 4.8, 4.9 (using a different capillary cube) and 4.10 (using a different penetrating arteriole tree).

red dots in the bottom row of Fig. 4.12. The tissues near the column centre are found to be unlikely to become hypoxic, due to the oxygen supply from the penetrating arteriole trunk. These simulations thus indicate that the tissue hypoxia caused by occlusion in the arteriole tree is mainly due to the perfusion shortage that occurs in the region downstream of the occlusion site.

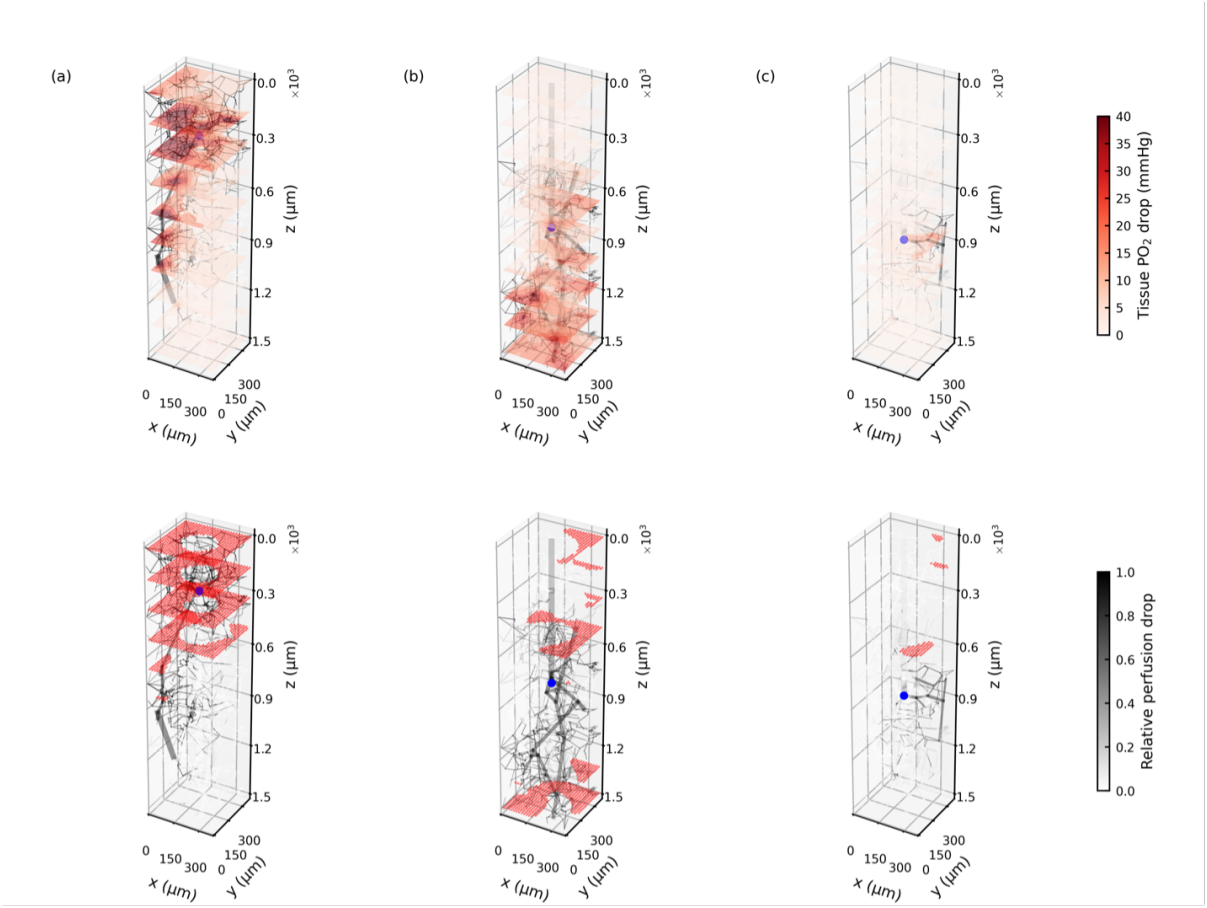

Figure 4.12: The top row shows the drops in relative perfusion and tissue oxygenation in response to 3 different 25 μm blockage (blue sphere) in the same arteriole tree. The bottom row shows the hypoxic regions (PO_2 smaller than 10 mmHg, coloured in red) in response to the same blockages.

4.3.5 Comparisons between simulations and experiments show agreements on pixel-based Gx function and discrepancies on hypoxic intensity

Figure 4.13 presents the results of two distance analyses in both experiments and simulations. The pixel-based Gx function has a consistent sigmoidal shape in each animal in experiments (Fig. 4.13(a)) and in each cortical column in simulations (Fig. 4.13(b)).

This results in small standard deviations between each animal and between each cortical column as shown in Fig. 4.13(c). In addition, there is a close match for the pixel-based Gx function between experiments and simulations in that they both reach 50% at around 300 μm and reach about 90% at 800 μm. However, the experimental curve is found to start to increase at shorter distances than in the simulations, which indicates that there are more hypoxic regions in the vicinity of occlusion sites in experiments than was found in the simulations.

These discrepancies are more clearly shown in the hypoxic intensity results. The experimental hypoxic intensity curves decrease as the radius increases (Fig. 4.13(d)), however, most of the simulated hypoxic intensity curves increase at the start (Fig. 4.13(e)). The reason for this difference is that the experiments have more type A hypoxic intensity (30.9%), while there is only one case out of 91 simulations that is type A (Fig. 4.14). This leads to some significant differences between experiments and simulations (Fig. 4.13(f)). The standard deviation of the hypoxic intensity is also larger than that of the pixel-based Gx function in both experiments and simulations. These results will be further discussed in the next section.

4.4 Discussion

In this chapter, the effects of micro-occlusions in the cerebral penetrating arteriole trees on tissue hypoxia were examined using both *in vivo* animal experiments and *in silico* simulations. Two novel distance analyses, namely hypoxic intensity and pixel-based Gx function, were carried out identically in both experiments and simulations. The first method focuses on the distribution of hypoxic regions around each microsphere. By comparison, the latter one zooms out to examine the cumulative fraction of distance between the microsphere and the resultant hypoxic regions in the reconstructed or simulated brain tissue volumes. To the best of our knowledge, this is the first study on the spatial relationships between occlusion sites and hypoxic regions that combines

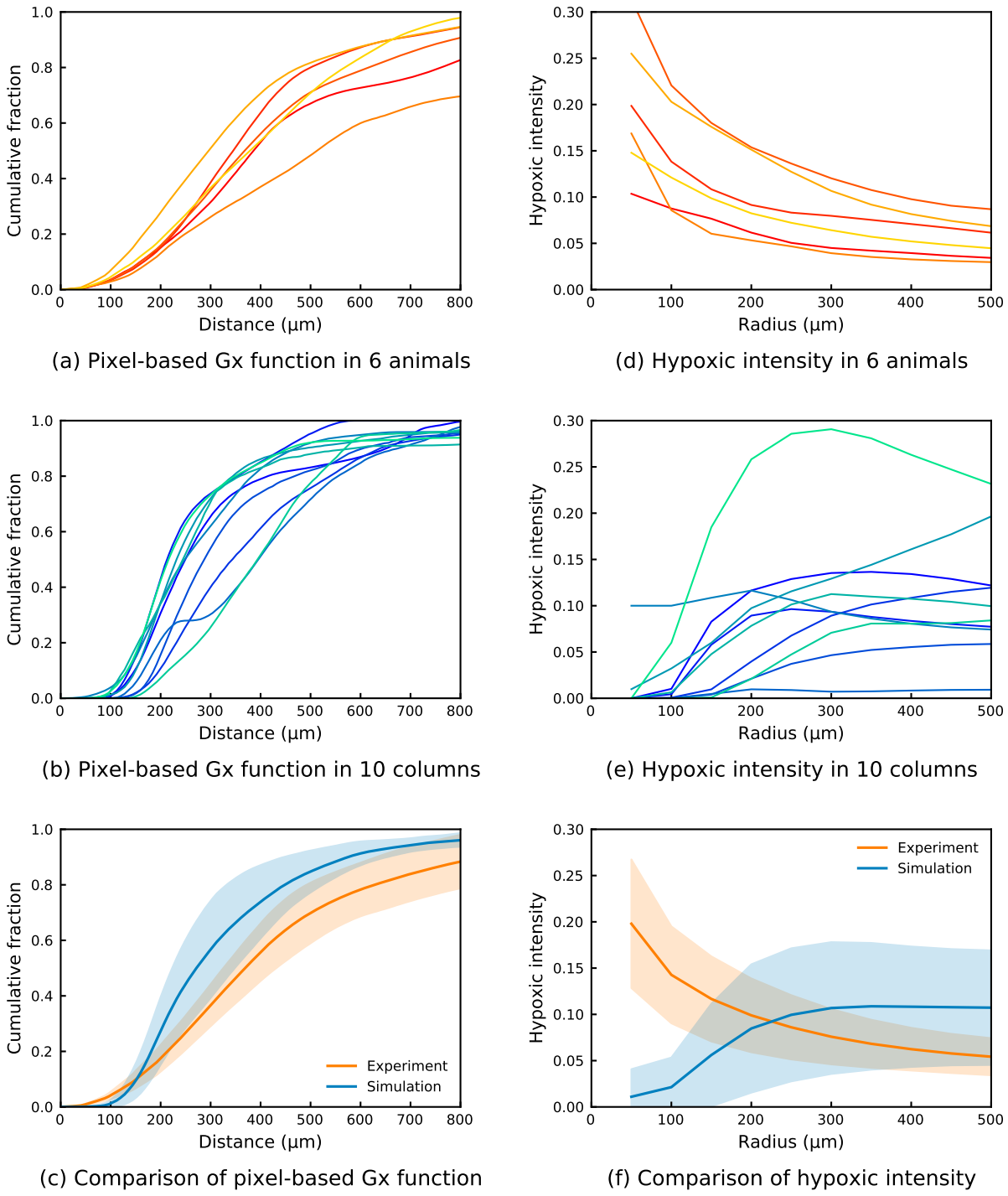

Figure 4.13: Comparisons of pixel-based Gx function and hypoxic intensity between experiments and simulations. The error bar of experiments shows the standard deviation between 6 animals. The error bar of simulation shows the standard deviation between 10 cortical columns.

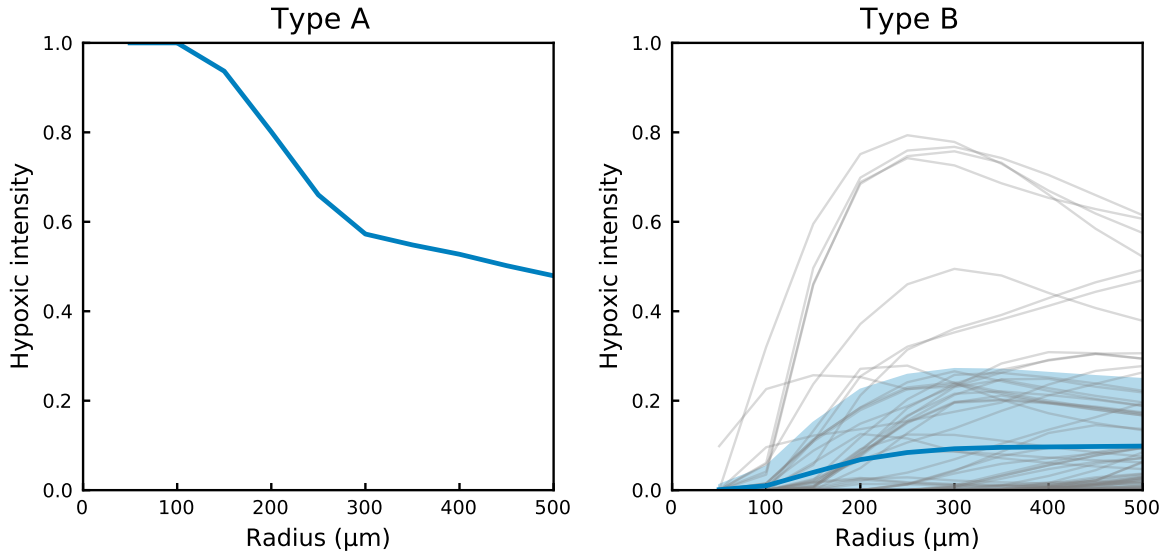

Figure 4.14: Two types of hypoxic intensity in simulations.

both experimental and numerical methods, and the first that considers occlusions over different generations of the penetrating arteriole trees.

Reasonable agreement in pixel-based Gx function results have been shown between experiments and simulations. These results suggest that hypoxic regions can form distally from the occlusion sites, in agreement with previous experimental findings using mixed microspheres of several sizes [56]. However, other discrepancies in hypoxic intensity have been shown between experiments and simulations. The hypoxic intensity patterns were thus further categorised into two types, where type A decreases and type B increases as the radius increases from 50 to 100 μm. Type A hypoxic intensity represents the scenario where significant hypoxic regions present near the occlusion site, whereas type B represents the case when most hypoxic regions form far away from the occlusion site. Type B hypoxic intensity was found to be the dominant case in both experiments (69.1%) and simulations (98.9%). This also agrees with the pixel-based Gx function that more than 90% of the hypoxic regions are more than 150 μm from the microsphere instead of around the occlusion site.

4.4.1 Reasonable agreement between ischaemic and hypoxic regions

Using a rat model of microembolisation, the percentage of overlap between ischaemia and hypoxia was assessed in a limited brain volume of the affected hemisphere, 24 hours post-surgery. A $36.1 \pm 5.3\%$ overlap was found between ischaemia and hypoxia. In the previous work where a mixture of microsphere sizes were injected and the animals were killed after 1, 3 and 7 days, infarction volume at day 7 was found to be similar to that at day 1, suggesting that infarction develops within 24 hours after microembolisation [55]. As a consequence, the cells which had already undergone cell death were missed in the presented experimental data. This can explain the ischaemic regions which were not hypoxic. In cases where hypoxic regions did not overlap with ischaemia, larger ischaemic regions, which are formed due to multiple occlusions of the same or different arterial trees, are likely responsible for these results. Hypoxic regions could span beyond the analysed tissue (500 μm thick). As a result, only the hypoxia in our analysed brain tissue is detected, while the ischaemic source is further away in the z-direction. Considering the pathological process of infarct growth and the distal effects of large ischaemic regions, the overlap between ischaemia and hypoxia in our experiments is reasonable.

4.4.2 Distal hypoxic regions

In the experimental data, both local (< 100 μm, 50.8% of all cases) and distal (> 100 μm, 49.2% of all cases) effects due to micro-occlusions were shown. Contrary to previous *in vivo* rodent studies where the occlusion site was highly correlated to brain tissue damage [74, 76, 242], distal effects were found after occlusion of penetrating arteriole branches using a rat model of microembolisation [56]. Our simulations suggest that a 25 μm microsphere will occlude a branch of the penetrating arteriole, which will lead to hypoperfusion downstream of the occlusion site in the corresponding cortical column (Fig. 4.12). The hypoperfusion will then result in distal tissue hypoxia from the occlusion

site. This is partially supported by the overlap between ischaemic and hypoxic regions in the experiments.

According to blood vessel diameter measurements, rat penetrating arterioles range in size from 10-30 μm [76]. The injected microspheres of 25 μm in diameter should target the first few branches of penetrating arterioles. However, most of the microspheres were detected to be lodged at a distance > 500 μm below the cortical surface. This discrepancy could be explained by the arterial wall elasticity in combination with the blood flow which may push the microspheres distally from the cortical surface [246]. Since the vessel architecture was not imaged directly, microspheres could block either a penetrating arteriole at a lower level or branches of a penetrating arteriole. Even in the cases where the perfusion volumes may be smaller, the effects of blocked arterioles span a greater distance than was found in *in vivo* occlusions of penetrating arterioles using photothrombosis [74, 76].

To understand the discrepancy found between microembolisation and the photothrombotic model, differences between the two techniques are discussed here. Firstly, in the current experimental study, microspheres are lodged not only in the cortex but also in deep brain structures. Whereas cortical columns are thoroughly examined under controlled circumstances, deeper brain structures and their vessel architecture, perfusion and oxygenation are poorly investigated due to limited depth resolution of live imaging techniques [247]. In addition, despite the high resolution gained by tissue clearing or other modern techniques [248–250], effective image segmentation remains challenging [251]. Secondly, in our microembolisation model the tissue hypoxia can be a result of multiple occluded arteriole(s). In the distance calculations both cases were included, and no distinction was made between the two, since blood vessel architecture was not considered and it was not possible to trace back the effects of every microsphere. Thirdly, hypoxia was examined 24 hours after microembolisation, missing the tissue where neuronal cell death has already taken place. Lastly, some microspheres may not necessarily lead to ischaemia or hypoxia, because of a certain degree of collateralization.

As a result, microspheres without any detectable brain damage may wrongly be matched to tissue hypoxia created by other occlusion(s). However, this scenario can be excluded based on the simulations, where most single penetrating arteriole occlusions (98.9%) led to distal hypoxic regions thus confirming the experimental findings. Taken together, the inclusion of deep brain structures in our distance analysis and the synergistic effect of multiple occluded arterioles [56] could explain the discrepancies found between the microembolisation versus photothrombotic model, although further detailed work will be required to establish this more accurately.

4.4.3 Comparisons between simulations and experiments

In this study, numerical simulations were matched with experiments as closely as possible to enable high fidelity comparisons and validations between the two. The validation of *in silico* models against *in vivo* experimental data remains a challenging step for most biomedical simulations, especially for non-linear scenarios like drug delivery and oxygen transport which can result in highly heterogeneous distribution of these substances in tissues. In a recent study, Hartung et al. [108] simulated blood flow and oxygen transport using the reconstructed microvasculature from *in vivo* images, which led to a very good agreement between the simulated oxygen fields and the two-photon oxygen images. This validation [108] focused on tissue oxygenation under healthy scenarios, thus our work provides a further investigation into the pathological effects of micro-occlusions on tissue hypoxia by comparing the spatial relationships. The validation indicates that the modelling approach is an appropriate one for this scenario and thus supports its wider use in understanding the response of brain tissue to microemboli.

As part of the INSIST project [44], computational models of AIS have been developed at multiple scales to aid in optimising AIS treatments and developing medical devices. The micro-scale models presented here and in previous works ([29] and Chapter 3) can in future be coupled with organ-scale models of AIS [36, 37, 47] and play a key role in

predicting the secondary tissue damage caused by microthrombi after an unsuccessful thrombectomy [16, 46].

Next, several differences between the experimental and numerical setups are highlighted. The cerebral microvascular networks used in the simulations [27, 87] were generated from the statistical data of the human brain [23, 26, 79]. However, the experiments were conducted in rat brains. Despite topological similarities between human and rodent networks, the human capillaries have been found to have longer vessels and larger spacings between vessels than rodent capillaries [252]. In addition, the venules were not included in the simulations, because the occlusions are primarily on the arteriole side. These geometrical differences can potentially lead to discrepancies between simulations and experiments, which should be quantified in future work.

In addition, the blood flow and oxygen transport models in this study are purely steady and passive. However, the hypoxic regions were measured and segmented 24 hours after the microembolisation in experiments. In this time interval, the brain can have active responses to vessel blockage and tissue ischaemia and hypoxia including autoregulation [1, 39], pericyte constriction [73, 135], microsphere clearance [53, 190] and pathological response like infarct formation [55]. These time-dependent events were not considered in the simulations but should be included in future studies.

Discrepancies of hypoxic intensity have been shown between simulations and experiments, which are mainly since there are more type B hypoxic intensity trends found in the simulations than in the experiments. This discrepancy can be partially explained by the differences between the two, which have been discussed previously. In the simulations, it is assumed that the bead occludes a branch of the penetrating arteriole with a diameter smaller than 25 μm at the vessel inlet, which tends to be near the column centre. As shown in Fig. 4.12, the hypoxic regions are mainly caused by the hypoperfusion in the regions downstream of the occlusion site and at the column boundary, which will lead

to a type B hypoxic intensity. However, in the experiments, microspheres were found to be lodged further away from the cortex surface (940.69 ± 122.54 μm), probably due to the vessel wall elasticity in combination with the blood flow. The occlusions will thus more readily happen at the arteriole-capillary transition or the capillary scale. In such a case, more hypoxic regions may form locally (type A) instead of in the regions downstream of the occlusion (type B) in the experiments. It thus leads to fewer type B cases in the experiments than the simulations. In addition, these effects are found to be relatively minor on the pixel-based Gx function, because the hypoxic regions caused by a capillary occlusion tend to be much smaller than these caused by a penetrating arteriole occlusion, which thus only contribute insignificantly to the pixel-based Gx function using the cumulative fraction. However, these hypotheses need further investigations when a fuller description of the vascular geometry is available.

4.4.4 Limitations

One of the major experimental limitations is the z-resolution of the individual coronal brain sections. Although initially a z-step of 5 μm was used when taking the confocal overview images, the z-resolution changed to 50 μm when converting the images to MIP for the 3D reconstruction of the brain tissue. Due to the low z-resolution and technical issues such as the deformation of brain sections, no blood vessel geometry was considered in the experimental data. In addition to the limited z-resolution of individual brain sections, the total z-dimension of the reconstructed brain volume (500 μm), was low compared to the x and y dimensions (7000-8000 μm). As a result, the contribution of microspheres outside the reconstructed brain region to tissue hypoxia was hard to predict. This is something that could add uncertainty to the experimental findings. We tackled these limitations by incorporating *in silico* models of cortical columns and comparing the experimental data as closely as possible to the simulations.

One of the steps in our distance analysis workflow involved the segmentation of brain

sections to include the brain anatomy in the calculations. Despite gentle handling of the brain tissue during the staining procedure we could not avoid one section of animal 3 becoming broken. For this particular case, the previous section was used instead, since the total area and anatomy of consecutive sections were found to be very similar.

One limitation of the simulations is the assumption of one bead or no bead per column, due to the low bead density in the experiments. However, more beads can occlude the same column and the combined effects of multiple blockages on hypoxic regions could affect both the hypoxic intensity and the pixel-based Gx function. Moreover, the occlusions were found to be very mild in the study when we compared the thrombus volume in our models with the thrombus volume measured by clinics. This indicates that there will tend to be more severe micro-occlusions caused by thrombus fragments after an unsuccessful thrombectomy. Hence, we need to be cautious in applying the results presented in this paper directly to clinical studies.

Another limitation is the assumption of the same probability of possible bead locations in the same column since there is currently no available bead transport model in the cerebral microvasculature. This has also been a limitation in recent studies on the effects of cerebral microthrombi on blood flow and oxygen transport ([29] and Chapter 3). The microemboli transport model will thus need to be developed and coupled with current oxygen transport models in future work.

Summary

To aid in understanding the formation of hypoxic tissues caused by micro-occlusions in the penetrating arteriole trees, this chapter use rodent experiments and simulations of human vascular networks to study the spatial correlations between the hypoxic regions and the occlusion locations. The results suggest that hypoxic regions can form distally from the occlusion site, which agrees with the previous observations in the rat brain.

These distant hypoxic regions are primarily due to the lack of blood flow in the brain tissues downstream of the occlusion. Moreover, a reasonable agreement of the spatial relationship is found between the experiments and the simulations, which indicates the applicability of *in silico* models to study the effects of microemboli on the brain tissue.

Part II

Macro-scale: Tissue damage

Chapter 5

Modelling the effects of cerebral microemboli on hypoxic tissue damage

---

The work presented in this chapter has been published in [219]: Xue, Y., El-Bouri, W. K., Józsa, T. I. & Payne, S. J. Modelling the effects of cerebral microthrombi on tissue oxygenation and cell death. *Journal of Biomechanics* **127**, 110705 (2021).

Abstract

The healthy brain function depends on the continuous oxygen supply. Recent experiments have shown that microembolism can lead to hypoxia and then infarct formation. The effects of microthrombi on oxygen transport and tissue oxygenation have been studies in previous chapters. However there is currently no mathematical model on hypoxic tissue

damage, which limits the application of these micro-scale models and their validation against the experimental and clinical data.

In this chapter, a novel 3-state cell death model was developed to simulate the hypoxic tissue damage. In addition, a thrombus extravasation model was proposed to simulate the recovery and fitted to the data from a rodent experiment. These models were coupled with the sigmoidal function between tissue hypoxic fraction and vessel blockage fraction (Eq. 3.2) to simulate the cell viability over time under different microvascular occlusions. The cell viability was found to be strongly dependent on the initial severity of microembolism, primarily due to the non-linear relationship between blockage fraction and hypoxic fraction. The cell death model presented here will broaden the application of oxygen transport models developed in Chapter 3, enabling their implementation in the organ-scale models.

5.1 Introduction

The human brain only comprises 2% of the body weight, but it accounts for 20% of the total energy consumption. In addition, the brain has a very low capacity of energy storage. Its healthy function thus highly relies on the continuous supply of oxygen and glucose. Due to the high metabolic rate and relatively slow diffusion of oxygen in the brain tissue, the distribution of oxygen primarily depends on the microvasculature, where each cell is located in close proximity to a blood vessel.

The close coupling between brain cells and capillaries also implies that the local energy supply can be easily disturbed by subtle geometrical or topological changes. Recent experimental studies using rodent models found that microembolism could lead to tissue ischaemia and hypoxia and infarct formation [55, 76]. Similar scenarios were also investigated using computational models in Chapters 3 and 4. One key finding from previous chapters is that most of the brain tissue will maintain healthy oxygenation

when less than 10% of capillaries are occluded. However, it will become hypoxic ($PO_2 < 10$ mmHg as defined before) very quickly when more capillaries are occluded. This non-linearity will lead to the non-linear tissue pathological response to different level of micro-occlusions.

In addition, recent experiments reported that microthrombi could be extravasated and the vessels could thus be recanalised in the rodent brain [53, 54, 188–190]. The thrombus extravasation can potentially lead to recovery of ischaemia and hypoxia on the time scale of days, where most ischaemic regions recover at Day 3 and most hypoxic regions recover at Day 7 [55]. These recovery mechanisms can have an significant impact on quantifying the effects of microemboli on brain tissue damage.

However, the effects of microthrombi on tissue health in the human brain are poorly understood. This is mainly due to the limited resolution of non-invasive imaging techniques, resulting in an 'imaging gap' relating to human cerebral microvasculature. To fill this gap, *in silico* models have been developed to study the effects of microemboli on blood flow [28, 29] and oxygen transport (Chapters 3 and 4). Although these models are able to quantify tissue hypoxia in the human brain, there is still a 'modelling gap' between tissue ischaemia/hypoxia and tissue damage, especially when predicting the tissue damage as a function of time. This gap limits the application of these micro-scale models and the validation against the clinical data.

To this end, cell death models are required to simulate the infarct formation and propagation due to the tissue hypoxia caused by micro-occlusions. Although many cell death models have been developed in previous studies [40, 210, 212–217], these models have neither been focused on the brain nor been validated, which limits their applications. One notable model was developed by O'Neill et al. [210], which simulated hyperthermic cell death using only 5 parameters and was validated against the experimental data. By comparison, Orlowski et al. [40] implemented a detailed cerebral metabolism model on

a 3D human brain mesh, which appears to be too complex to be validated. The ideal model for hypoxic tissue damage will thus be a model that combines the advantages of these previous models.

The aim of this chapter is to develop a cell death model that can simulate both hypoxic tissue damage and microemboli extravasation, while not losing simplicity. The model should also be built upon micro-scale simulation results (primarily Chapter 3), so the cerebral tissue damage over time under different micro-occlusions can be modelled easily. The cell death model will play a key role in the simulation of ischaemic stroke and broaden the application of micro-scale models presented in this thesis.

5.2 Thrombus extravasation model

Due to the thrombus extravasation, it was assumed that a certain fraction of occluded vessels could be recanalised over a certain period of time. Hence the vessel blockage fraction decays exponentially with time as

$$B = B_0 e^{-k_e t} \tag{5.1}$$

where B_0 is the initial blockage fraction and k_e is the extravasation time constant. The time constant k_e was found to be 2.03×10^{-6} 1/day by using the data points from a recent extravasation study in a rat model [53] as shown in Fig. 5.1.

5.3 Three-state cell death model

A novel hypoxia-based 3-state cell death model was proposed here based on a similar concept from previous work studying hyperthermic cell death [210]. The cell has three states in the model, namely alive (A), vulnerable (V) and dead (D). The sum of the fraction of cells in these three states in the brain tissue is always 1, which can be expressed

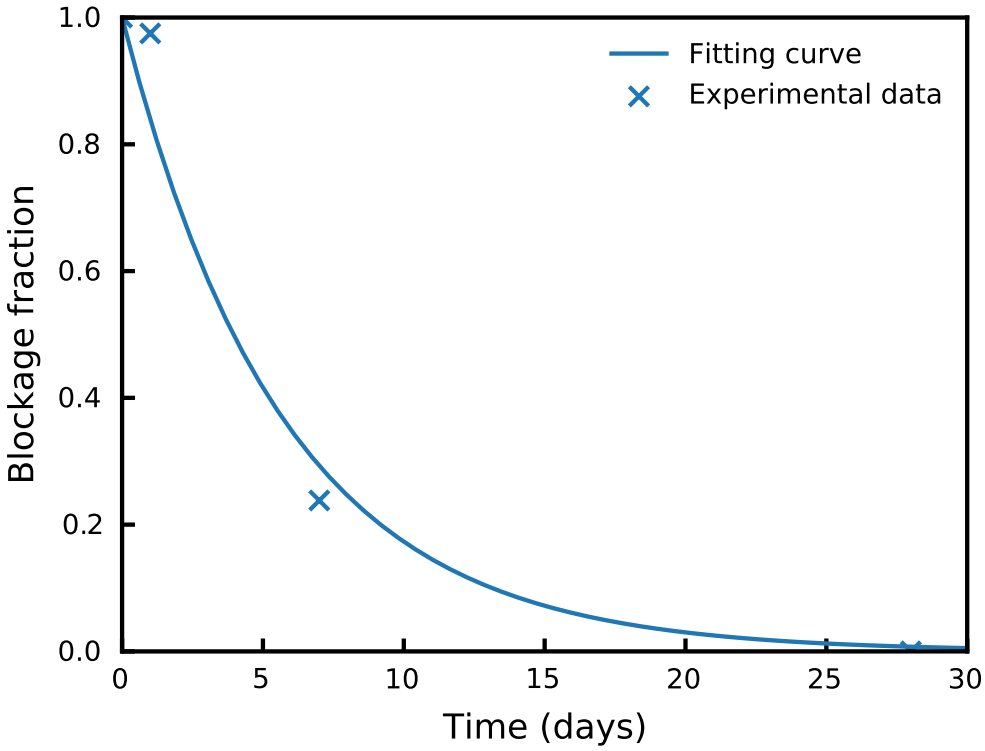

Figure 5.1: The fraction of microthrombi extravasated from occluded vessels over time. The data points at 0, 1, 7 and 28 days after the initial blockage are taken from an experimental study using a rat model [53].

as

$$A + V + D = 1 \tag{5.2}$$

The vulnerable compartment represents the cells that may have experienced energy impairment but still have potential for recovery. Hence there are reversible pathways with a forward rate (k_f) and a backward rate (k_b) between alive and vulnerable compartments. These two rate constants are purely based on the tissue hypoxic fraction, which is a sigmoidal function of vessel blockage fraction (Eq. 3.2). The balance between alive and vulnerable compartments is thus determined by the vessel blockage fraction. When the vulnerable cells experience further hypoxic damage, they will become dead in an irreversible pathway with the same forward rate k_f. The cell death model can be

summarised as

$$A \underset{k_b}{\overset{k_f}{\longleftrightarrow}} V \xrightarrow{k_f} D \tag{5.3}$$

$$\frac{dA}{dt} = -k_f A + k_b V \tag{5.4}$$

$$\frac{dD}{dt} = k_f V \tag{5.5}$$

The forward rate k_f and the backward rate k_b depend solely on the tissue hypoxic fraction (H) and the healthy fraction ($1 - H$) respectively as

$$k_f = \overline{k_f} H \tag{5.6}$$

$$k_b = \overline{k_b}(1 - H) \tag{5.7}$$

where the forward rate constant $\overline{k_f} = 6 \times 10^{-5}$ 1/s represents the forward rate under full hypoxia and the backward rate constant $\overline{k_b} = 4 \times 10^{-5}$ 1/s is the backward rate under no hypoxia.

5.4 Cell viability with increasing microembolism

By coupling the sigmoidal function between hypoxic fraction and blockage fraction (Eq. 3.2) with the thrombus extravasation model (Eq. 5.1) and the cell death model (Eq. 5.3), it is now possible to simulate cell viability (i.e. the fraction of cells that are not dead in a certain volume of brain tissue) under different microthrombi occlusions. The simulation results of tissue hypoxia and viability over 7 days under initial blockage fraction from 0 to 25% are presented in Fig. 5.2.

In the scenario of no blockage (Fig. 5.2a), the tissue remains healthy. There is a small gap between the alive compartment at 7 days and 100%, since the hypoxic fraction predicted by the sigmoidal function (Eq. 3.2) is not exactly 0 when the blockage fraction is 0. However, this difference is negligible in the time scale of interests in the usual clinical

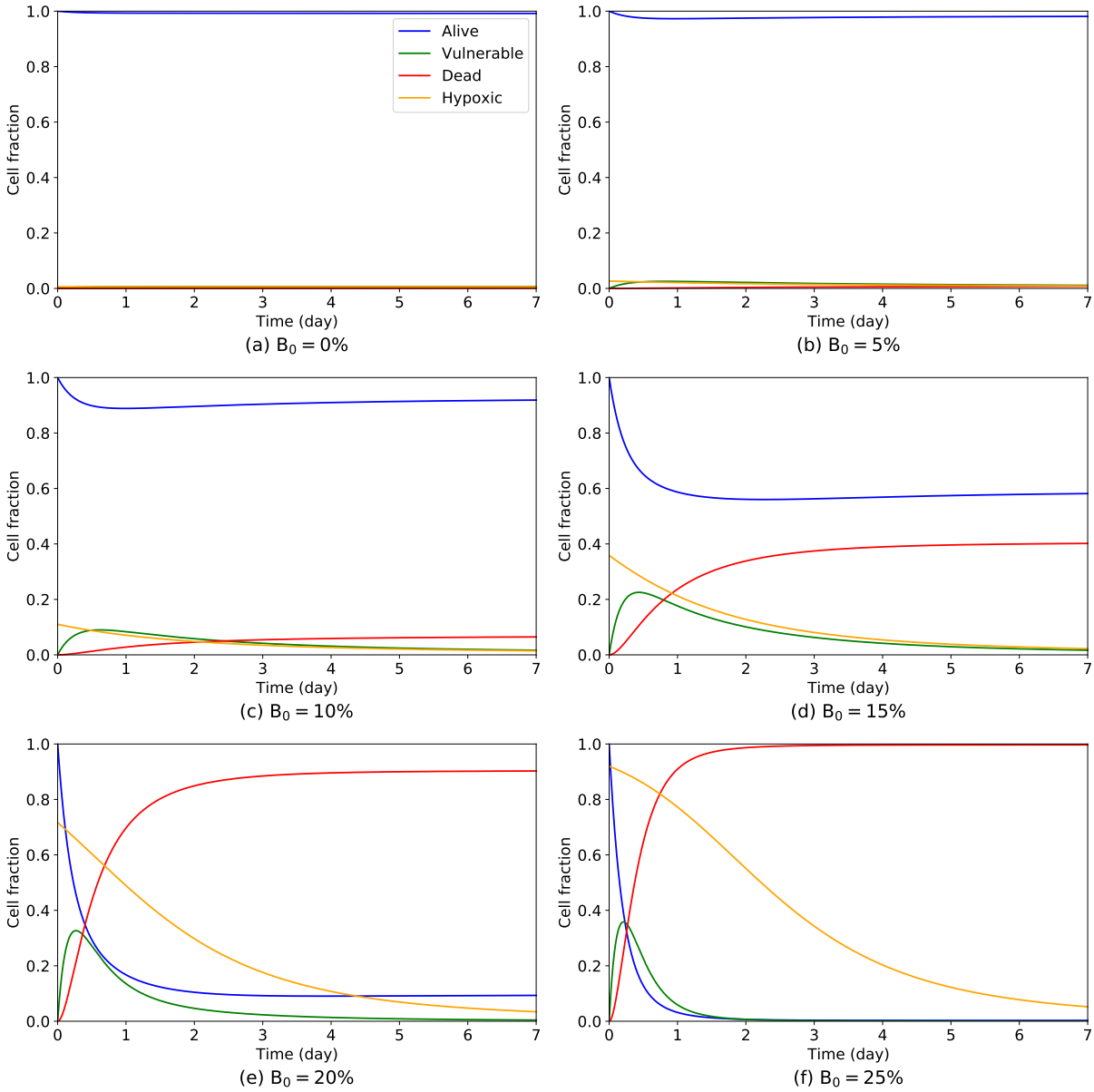

Figure 5.2: The tissue hypoxia and viability over 7 days under different initial blockage fractions.

practice. After mild occlusions with blockage fraction smaller than 10% (Figs. 5.2b and 5.2c), most cells can remain alive, due to the interconnected nature of the topology of capillary network and the thrombus extravasation.

Based on the highly non-linear relationship between blockage fraction and hypoxic fraction (Eq. 3.2), the further increase of blockage fraction beyond 10% will result in

a sharp increase in the cell death rate and the final fraction of dead cells. These can be observed in Figs. 5.2d and 5.2e. Under the initial blockage fraction of 25% (Fig. 5.2f), almost all cells will become dead after day 2, since the forward cell death rate is much larger than the thrombus extravasation rate.

5.5 Sensitivity analysis

Since there is currently no study on the quantitative relationship between local hypoxia and local infarction to fit the 3-state cell death model, a sensitivity analysis was conducted to demonstrate the non-linear behaviour of the model. In Fig. 5.3, the fractions of dead cells after 7 days of occlusions in different fraction of vessels were simulated under different forward rate constants ($\overline{k_f}$) and backward rate constants ($\overline{k_b}$) from 1×10^{-5} to 1×10^{-3} 1/s. The constant values used in Fig. 5.2 are indicated as the red cross in each subfigure.

There are clear thresholds between alive (dark blue) and dead (bright yellow) in each figure separating the final cell states of alive and dead. This threshold is caused by the non-linear behaviour of the model where the final cell state is the winner of two competing mechanisms, which are hypoxic damage caused by microembolism, and thrombus extravasation that relieves the microembolism. In addition, the thresholds between alive and dead can also be explained by the competing effects of the forward rate constant and the backward rate constant on the vulnerable cells. When the backward rate constant is much larger than the forward rate constant, there is no tissue damage due to many more cells being saved from the vulnerable compartment than dying.

5.6 Discussion

In this chapter, a thrombus extravasation model was proposed and fitted with a recent rat experiment [53]. In addition, a 3-state cell death model was developed to model the hypoxic cell death [210]. These models were then coupled with the sigmoidal

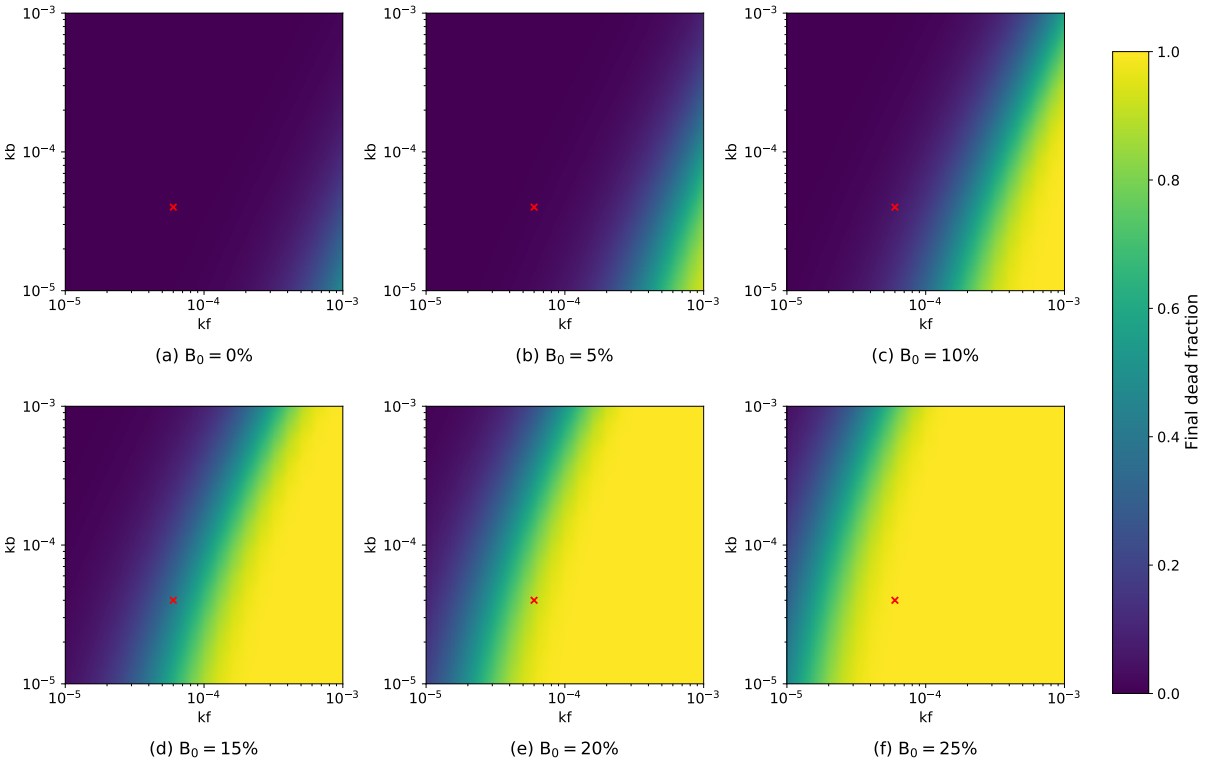

Figure 5.3: Final fraction of dead cells after 7 days under different initial blockage fractions and rate constants in the 3-state cell death model. The forward and backward rate constants used in Fig. 5.2 are indicated as the red cross.

function of tissue hypoxic fraction under different vessel blockage fraction. By using this pipeline the brain tissue damage after different degrees of microembolisms can now be modelled as a function of time. The cell viability predicted from these models will aid in understanding the potential secondary tissue damage caused by thrombus fragments following an unsuccessful thrombectomy.

Modelling irreversible tissue damage in the human brain is a key module to simulate the ischaemic stroke, however, it was usually neglected in previous cerebral metabolism models [20, 21, 40]. Here a 3-state cell death model was developed from a previous model on hyperthermic cell death [210], which is able to simulate the highly non-linear process of cell death based on tissue hypoxia. It can thus be coupled with the oxygen transport

simulation results presented in Chapter 3 and broaden the application of these micro-scale models in clinical contexts. In addition, it enables a straightforward way of implementing micro-scale simulation results in the whole brain models [36, 37], which forms the basis of the next chapter.

It should be noted that the cell death model proposed here is a significant simplification of the *in vivo* physiological process of hypoxic tissue damage. The proposed cell death model is just one of the simplest models which can simulate a strongly non-linear scenario with only two parameters. Therefore, it can prevent over-fitting when the temporal quantitative data of hypoxic tissue damage are currently very limited [55]. The cell death model proposed in this chapter will be further developed in the next chapter.

The simulation includes a thrombus extravasation model to mimic the re-perfusion and hypoxia relaxation at the capillary scale. However, despite this, the presented model is mostly passive, neglecting the fact that blood flow and oxygen transport are actively and tightly controlled at multiple scales [1, 39].

Summary

This chapter has developed a cell death model to simulate the hypoxic tissue damage caused by microembolism. Additionally, it is able to model the thrombus extravasation which leads to recovery after mild occlusions. Coupled with the relationship between hypoxic fraction and blockage fraction as presented in Chapter 3, the model can predict the cerebral tissue damage over time under different level of microembolism. In the next chapter, the cell death model will be further developed and implemented at the organ-scale to build a full ischaemic stroke model.

Chapter 6

Modelling cerebral tissue damage caused by acute ischaemic stroke

---

Part of the work presented in this chapter (Section 6.2) has been implemented in [253]: Miller, C., Padmos, R. M., van der Kolk, M., Józsa, T. I., Samuels, N., Xue, Y., Payne, S. J., Hoekstra, A. G. In Silico Trials for Treatment of Acute Ischemic Stroke: Design and Implementation. *Computers in Biology and Medicine* **137**, 104802 (2021). Part of the work (Section 6.3) has been presented at the 9th World Congress of Biomechanics [254] as Xue, Y., Józsa, T. I. & Payne, S. J. Modelling human cerebral tissue damage caused by acute ischaemic stroke. (2022).

6.1 Introduction

Brain tissue is extremely vulnerable to disruptions in energy supply, due to the fact that the neurons have very limited energy storage. This means that pathological events will

occur in the ischaemic regions shortly after a stroke. There is evidence from animal models [65, 211] that these damage mechanisms can happen at the time scale of minutes after the stroke. However, the pathological mechanisms of the human brain are poorly understood at this time scale, since the time from stroke onset to randomisation is about 3 hours and the time from onset to intraarterial treatment is about 4 hours [4]. The status of each patient are usually only known at two time points (no infarct at the onset time and a certain infarct volume at the treatment time) with a few hours in between. Hence to investigate the effects of treatment time on the clinical outcomes of stroke patients, in the recent HERMES project [175], the patients were divided into groups of different treatment time, while distributions of other patient characteristics were matched between different groups. The clinical outcomes of stroke patients were then compared among groups of different treatment time. In this way, however, it is impossible to know the effects of different treatment time or option on the outcome of each individual patient. In addition, it is even more difficult to understand the pathophysiology of the human brain in responses to ischaemia at the time scales (e.g. minutes after the stroke onset), where no human data are available.

In previous chapters, the responses of human brain tissue to ischaemia and hypoxia have been investigated at the length scales where available human data are very limited. Using numerical models, even the impact of the occlusion of a single capillary on brain tissues at the length scale of micrometres can be quantified and validated against the animal data. Similarly, it should be possible to use mathematical models and animal data to examine the responses of human brain tissue to ischaemia at the time scales where the human data are limited. These models can then be coupled with existing CBF models [29, 36, 37] to build a full model of ischaemic stroke at multiple length and time scales.

Over the past few decades, several cell death models have been developed for ischaemic stroke. These models can be divided into two types: mechanistic models [42, 212–218] and cellular metabolism models [21, 40, 41]. The mechanistic models focus on the modelling

of pathological scenarios (e.g., cortical spreading depression or oedema) whilst tending to neglect the physiological meaning of model variables and parameters. The metabolism models build upon cellular physiology, however, they usually have tens of or even more than a hundred model parameters that are essentially impossible to be measured or quantified *in vivo*. Another limitation of all these models is the lack of parameter fitting or validation. Additionally, most of these models have not been applied to a brain model with a realistic 3D geometry (for one exception see [40]).

This chapter thus aims to develop a cell death model, which should be validated against available animal or clinical data and applied to the organ-scale brain models. In particular, the model should be able to simulate the tissue state as a function of time under different values of perfusion, so the penumbra and core (infarct) volumes can be predicted in an *in silico* trial of ischaemic stroke [44]. Considering the limited temporal resolution of tissue damage data in both animal stroke models [64, 65, 211] and clinical studies [4, 175, 255, 256], a mechanistic approach will be employed here to prevent overfitting the model parameters. In this case, the 3-state cell death model developed in the last chapter is taken to be a reasonable starting point.

6.2 A toxin-based cell death model

The 3-state cell death model presented earlier can simulate the tissue damage due to microembolisms, however, it is not fully suitable to simulate the tissue damage caused by ischaemic stroke. One limitation of the model is that it is not able to simulate any continued tissue damage after perfusion is restored [255, 256], since its forward rate is purely based on hypoxia that is zero under healthy perfusion. This indicates that the 3-state model cannot simulate the expansion of infarct regions after the stroke treatment. A toxin-based cell death model, which was developed from the 3-state model, is thus presented here to address this challenge.

6.2.1 Model

The toxin-based cell death model is presented in Fig. 6.1. Compared with the 3-state cell death model, the vulnerable compartment has been removed and a toxin compartment has been added. The toxin compartment represents the level of toxin in the brain tissue. In the proposed model, it is assumed that toxic molecules (e.g., potassium ions and glutamate) are produced and released from brain cells under hypoxic stresses [58] at a constant rate. The toxin production rate is thus proportional to the tissue hypoxic fraction:

$$\dot{T}_p = k_t H A \tag{6.1}$$

where k_t is the toxin production time constant and H is the hypoxic fraction, which will be simulated as a function of perfusion in the following section. The toxin removal is assumed to be based on both the healthy tissue fraction and the non-hypoxic tissue fraction:

$$\dot{T}_r = k_r(1-H)AT \tag{6.2}$$

where k_r is the toxin removal time constant. These two equations give the toxin dynamics as

$$\frac{dT}{dt} = \dot{T}_p - \dot{T}_r = k_t H A - k_r(1-H)AT \tag{6.3}$$

The forward death rate is assumed to be proportional to the toxin level as

$$\frac{dD}{dt} = k_f T A \tag{6.4}$$

which leads to a continued tissue damage after treatment (when perfusion is restored and hypoxia is relieved) because the toxin requires additional time to be removed.

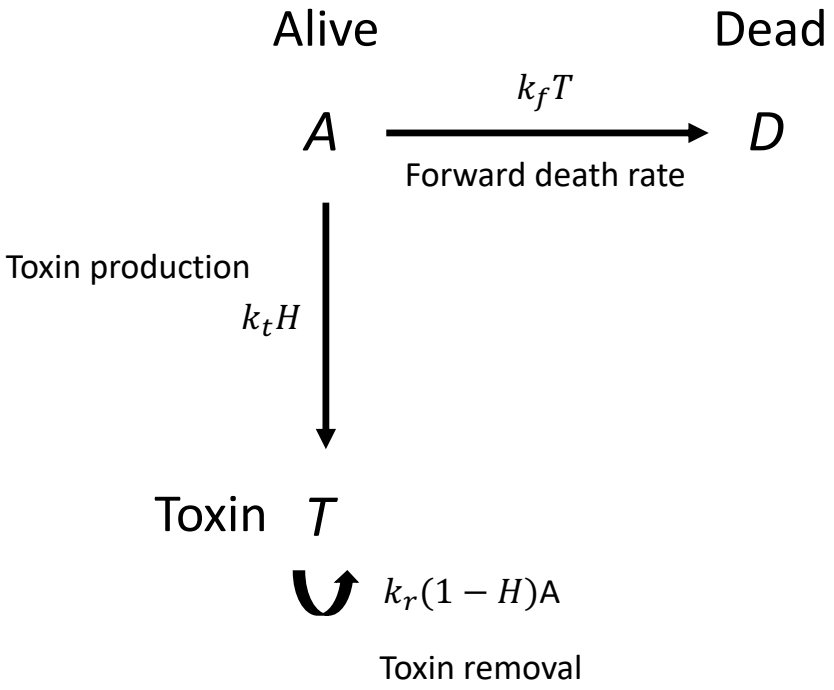

Figure 6.1: Schematic view of the toxin-based cell death model.

6.2.2 Hypoxia as a sigmoidal function of ischaemia

To investigate the relationship between hypoxia and perfusion, the physiologically representative capillary cubes [27] and Green's function method [144] used in Chapter 3 were used. The tissue hypoxic fraction was simulated under different perfusion values from 0 to 60 mL/100mL/min. The unit can be converted to mL/100g/min by dividing by a tissue density (normally around 1 g/mL [146]). The perfusion value was assumed to be the same as the output from the whole brain perfusion model [36], which enabled an easy coupling between the two models.

Figure 6.2 presents the hypoxic fraction and average tissue PO_2 under different values of perfusion in 10 capillary cubes (375 μm) that were used in Chapter 3. The inlet blood PO_2 was set to be 43.2 mmHg by assuming the same OEF from A4 to V4 as predicted by

the 2D network model [94] and using the Green's function method to simulate the effects of inlet PO_2 on OEF (Fig. 3.3). The hypoxic fraction was found to follow a sigmoidal relationship with perfusion, which is similar to its relationship with inlet blood PO_2 (Fig. 3.2). However, unlike the linear relationship between average tissue PO_2 and inlet blood PO_2, the average tissue PO_2 follows a Michaelis-Menten curve with perfusion.

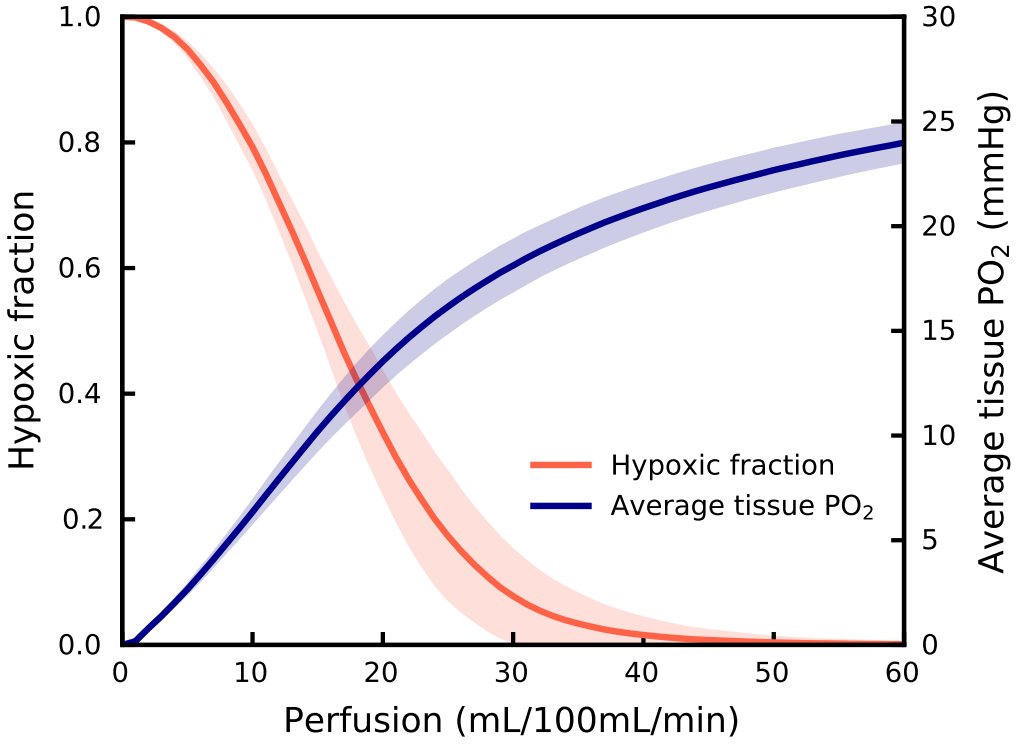

Figure 6.2: Hypoxic fraction and average tissue PO_2 in 10 capillary cubes (375 μm) under perfusion from 0 to 60 mL/100mL/min. The shaded area shows the standard deviation.

The relationship between tissue hypoxic fraction and perfusion was fitted with a sigmoidal function:

$$H = 1 - \frac{1}{1 + e^{-(0.2017 * \mathrm{CBF} - 3.3734)}} \tag{6.5}$$

where the CBF is in the unit of mL/100mL/min. All parameter fitting was conducted using SciPy (non-linear least square optimization) [223] in this chapter, if not specified otherwise. The fitting is shown in Fig. 6.3, where the simulation curve is taken to be the

average of the simulation results for 10 cubes.

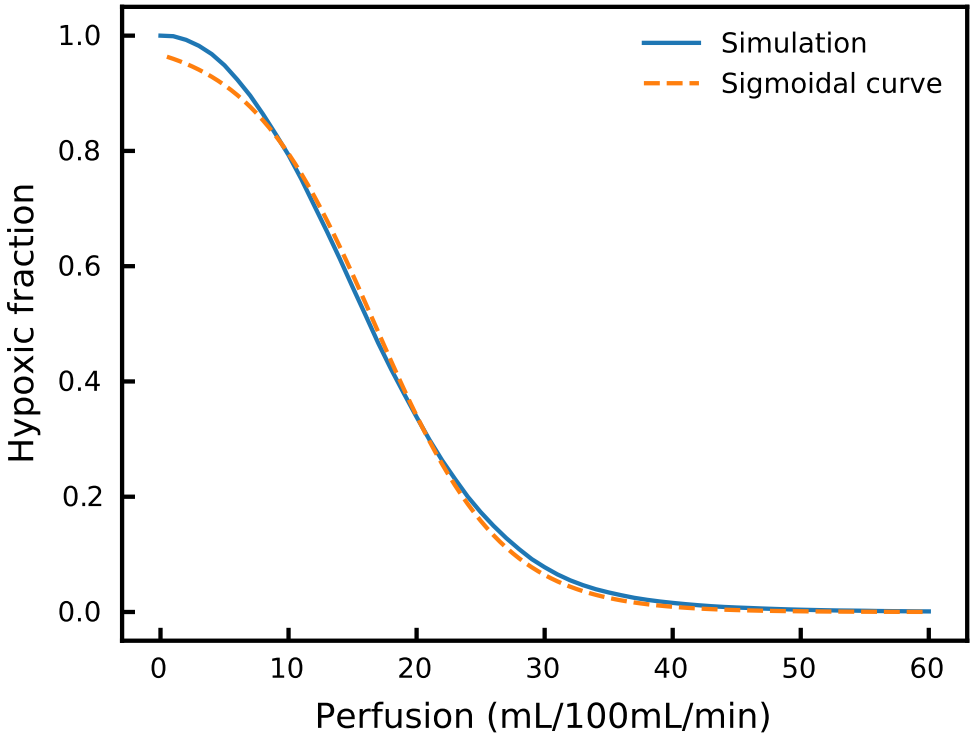

Figure 6.3: Hypoxic fraction fitted as a sigmoidal function of perfusion.

In addition, the hypoxic fraction was simulated under different values of perfusion and oxygen inlet in a 375 μm capillary cube as shown in Fig. 6.4. The hypoxic fraction was found to be a function of these two variables as

$$H = 1 - \frac{1}{1 + e^{-(0.0009 * \mathrm{CBF} * {\mathrm{PO}_2}^{3/2} - 4.0420)}} \tag{6.6}$$

where the CBF and PO_2 are in the units of mL/100mL/min and mmHg, respectively. The inlet PO_2 has a power of 1.5, which indicates that it has a larger impact on tissue hypoxia than perfusion. It should be noted that this simulation was carried out in a single capillary cube to reduce the total simulation number (currently 240), which is different from previous simulations that were run in 10 cubes.

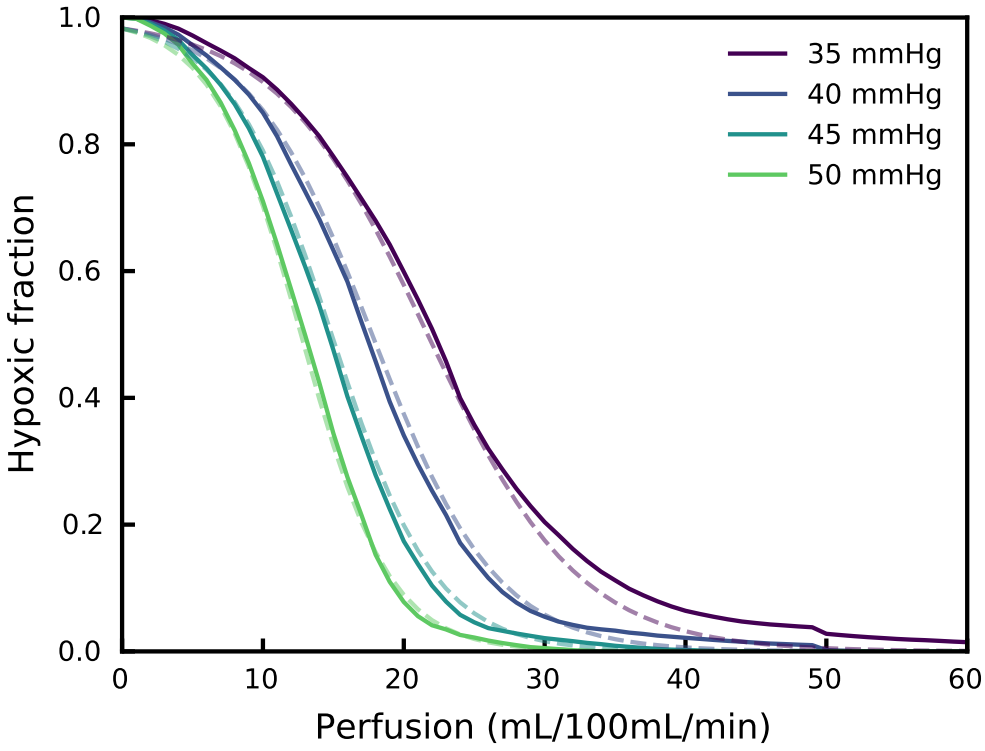

Figure 6.4: Hypoxic fraction as a function of perfusion and inlet PO_2.

6.2.3 Parameter fitting

The monkey data of infarct formation time under different perfusion [64] (see Section 2.5.2.2) were used to fit the model parameters (k_t, k_r and k_f), where it was assumed that the infarct formed when $D \geq 80\%$. The parameters were found to be: $k_t = 2.6717 \times 10^{-4}$ 1/s, $k_r = 1.93015 \times 10^{-3}$ 1/s and $k_f = 3.8172 \times 10^{-4}$ 1/s.

In Fig. 6.5, the tissue dead fraction is shown in a 2D map of perfusion and time against monkey data. Reasonable agreement is shown between the simulation and the experimental data in the time scale of 6 hours. However, at a longer time scale of 2 days, the simulated tissue damage starts to appear in regions with a perfusion greater than the threshold of 18 mL/100mL/min (if brain tissue density is 1 g/mL) in the monkey data. This is mainly because the forward tissue damage pathway (Eq. 6.4) is proportional to

the toxin level, which is not exactly zero as long as the hypoxic fraction is non-zero. This indicates that the proposed model will over-estimate the tissue damage over a long time, which limits the time scale of its application.

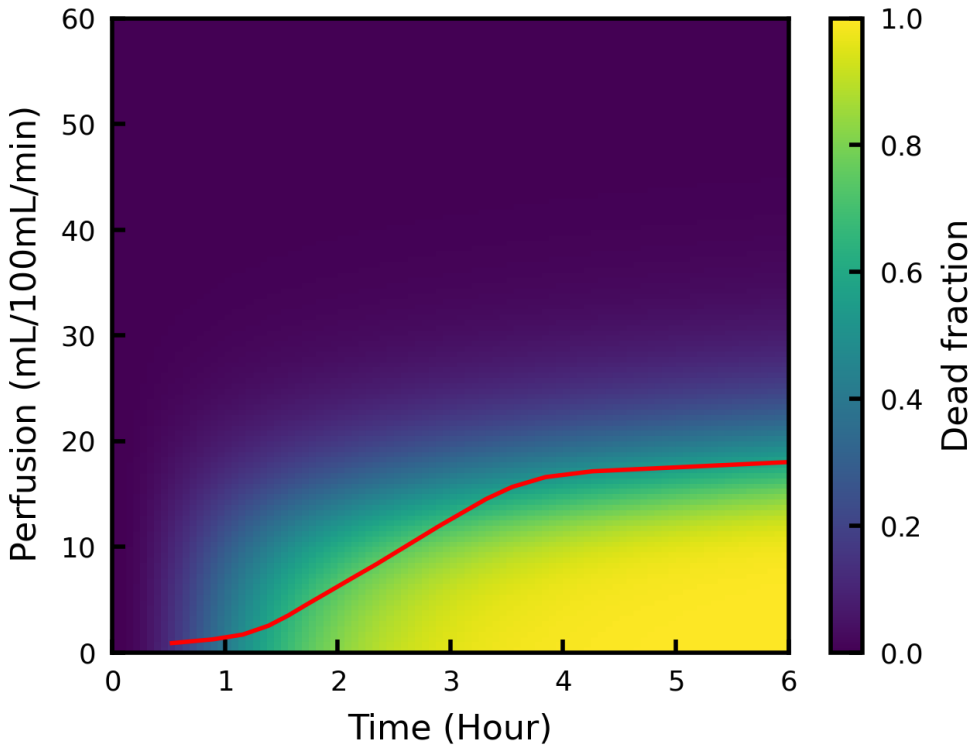

Figure 6.5: The dead fraction predicted by the cell death model under different values of perfusion and time. The red line shows the experimental data of a monkey model [64].

6.2.4 Implementation[1]

The toxin-based cell death model has been implemented in an *in silico* trial of ischaemic stroke [44, 253] as shown in Fig. 6.7, where models of blood flow [37], tissue perfusion [36] and tissue damage are coupled together. The coupling of these models has been introduced in other studies [253, 257]. In brief, cell death was simulated by solving local

[1]The cell death model has been implemented in [253]: Miller, C., Padmos, R. M., van der Kolk, M., Józsa, T. I., Samuels, N., Xue, Y., Payne, S. J., Hoekstra, A. G. In Silico Trials for Treatment of Acute Ischemic Stroke: Design and Implementation. *Computers in Biology and Medicine* **137**, 104802 (2021). The implementation of this toxin-based cell death model in virtual patients was performed by our collaborators at the University of Amsterdam, and is not part of this thesis.

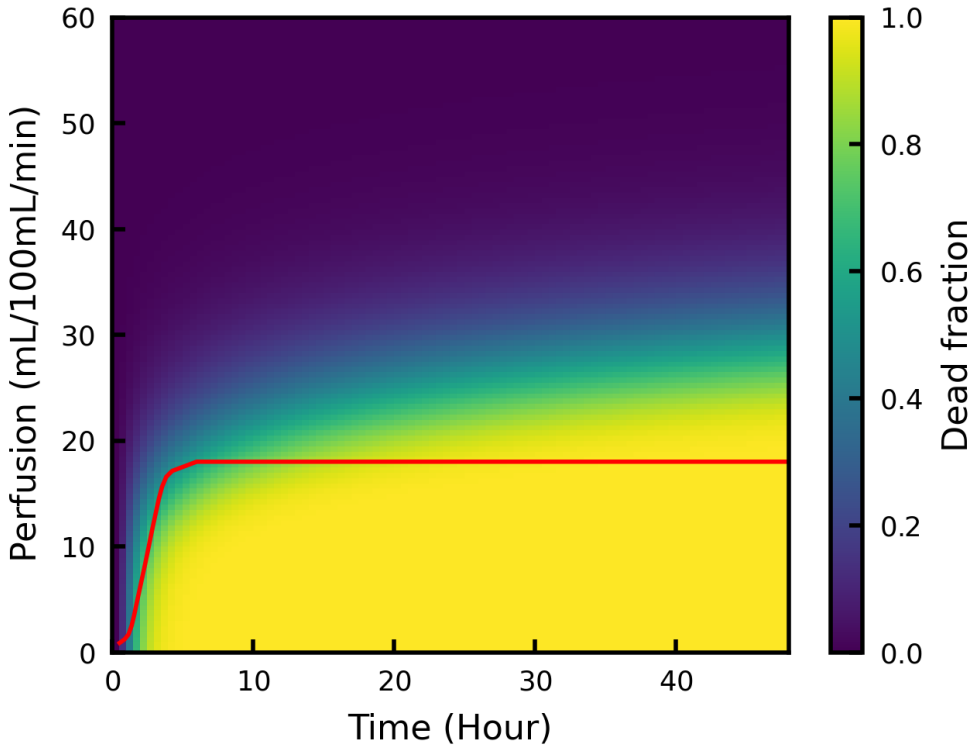

Figure 6.6: The dead fraction predicted by the cell death model under different values of perfusion and time up to 2 days. The red line shows the experimental data of a monkey model [64].

ODEs (based on the perfusion value) in each mesh element of the organ-scale perfusion model. The ODEs were solved by SciPy [223] in this chapter. The cell death model parameters were fitted to the data from monkey grey matter [64]. However, significant differences in baseline perfusion and its threshold for infarct have been observed between grey and white matters [208, 258, 259]. Based on the average of simulated baseline perfusion in grey and white matters, a scaling ratio of 2.7 was used to scale up the perfusion values in the white matter, so that the cell death model could be applied in the white matter region directly.

Stroke onset and treatment were assumed as instant events for simplicity. These events were simulated by adjusting the boundary conditions of the blood flow model, which led

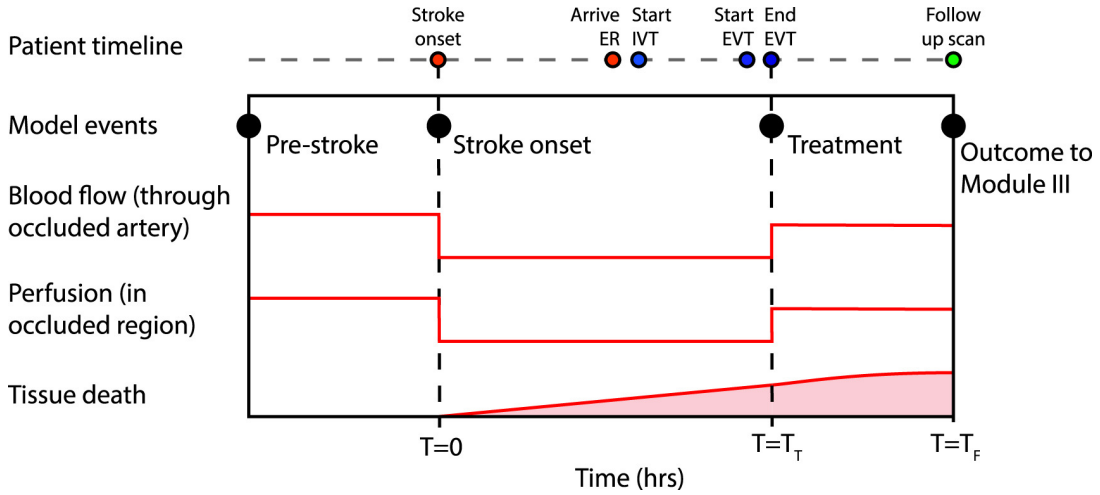

Figure 6.7: Schematic of an *in silico* trial of ischaemic stroke. Module III uses the infarct volume and patient characteristics to predict the clinical outcome of each patient. Reproduced without change from [253].

to perfusion change in the occluded region (Fig. 6.8) and the resulting tissue hypoxia due to ischaemia initiated the cell death model. The tissue damage progresses quickly after the stroke onset and before the treatment. The progression continues even after the treatment, because the toxin removal takes additional time and the remaining toxin is still able to drive the cell death. A simulation of relative perfusion change and final infarct volume is shown in Fig. 6.9.

Using the pipeline, two *in silico* trials were conducted in 500 virtual patients with best case (successful thrombectomy and perfusion restores) and worst case (unsuccessful thrombectomy and perfusion does not restore) treatments. Based on a statistical model of clinical outcome (mRS) on final infarct volume and patient characteristics, the clinical outcomes of best case and worst case patients could be modelled as shown in Fig. 6.10. The simulation results are qualitatively reasonable in that better stroke treatment leads to better clinical outcome, but this simulation has not been validated yet. It should be noted that there remains ongoing development of the virtual patient model, the cell death model and the statistical clinical outcome model respectively. A validation of

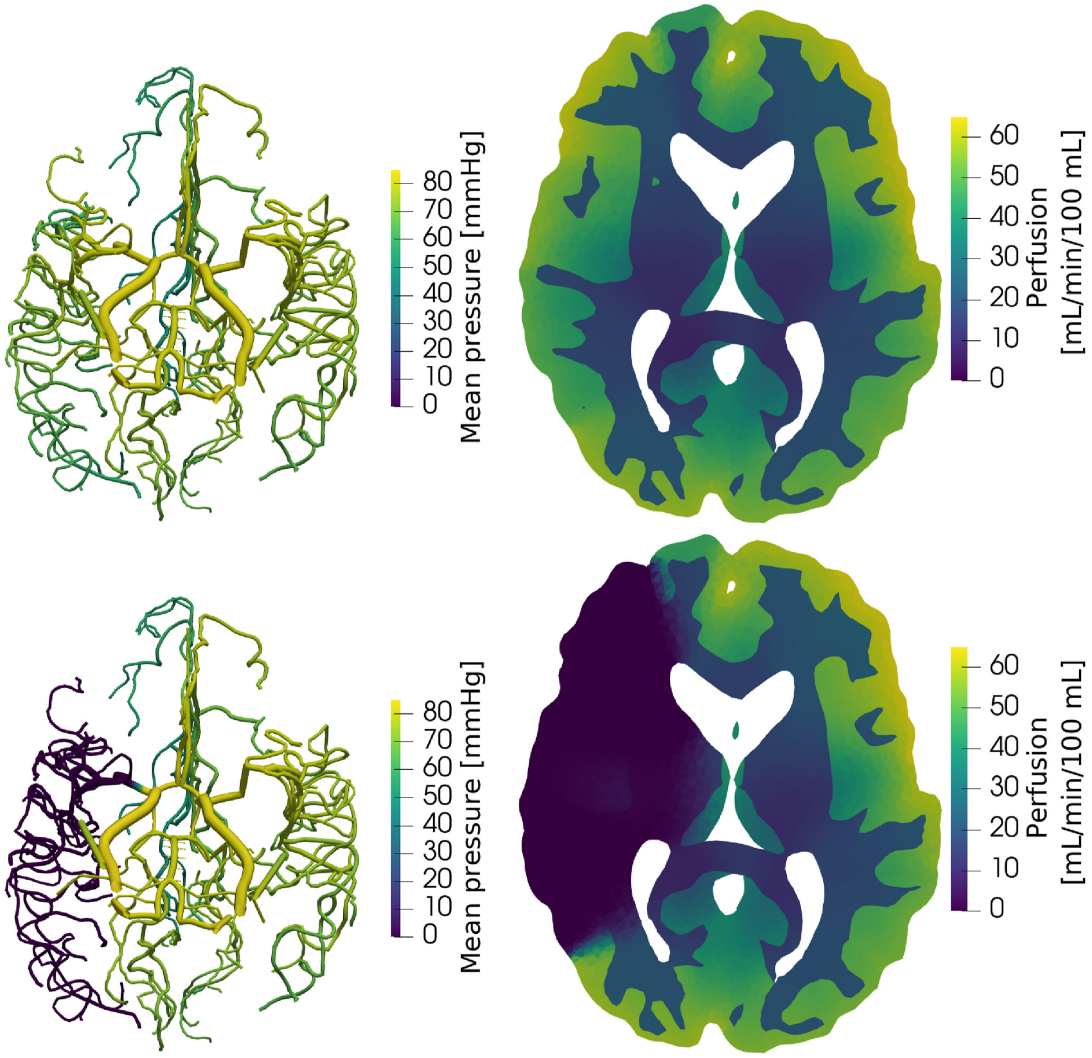

Figure 6.8: Simulation of blood pressure (left) and perfusion (right) before (top) and after an ischaemic stroke (bottom). Reproduced without change from [253].

the complete *in silico* trial will only be performed when each of its modules has been developed and validated.

6.2.5 Discussion

This section presents a toxin-based cell death model that can simulate the continued cerebral tissue damage after the stroke treatment. The Green's function method simulates the tissue hypoxia in representative capillary cubes under different perfusion. This leads to a sigmoidal relationship between the two. The tissue hypoxia triggers the production

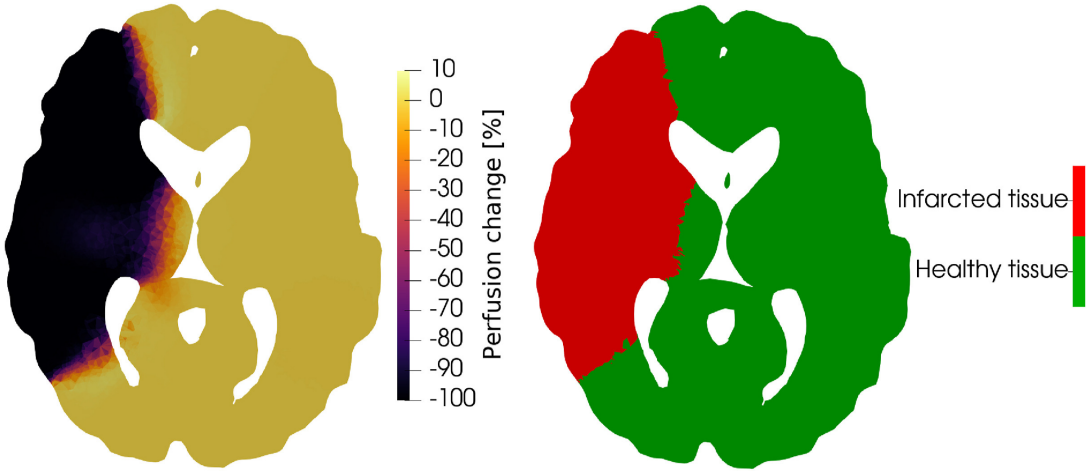

Figure 6.9: Simulation of relative perfusion change and final infarct volume after an ischaemic stroke. The final infarct volume is 332 mL. Reproduced without change from [253].

of toxic molecules, the level of which drives the tissue damage. The proposed model only has 3 parameters that have been fitted to the monkey data. The model has been coupled with cerebral blood flow and perfusion models, enabling the *in silico* trial of ischaemic stroke of the INSIST project. The workflow is able to predict qualitatively reasonable outcomes of stroke patients under different conditions.

It should be noted that the proposed model is a simplification of a series of brain pathophysiological events following an ischaemic stroke. This is a limitation of all models presented in this chapter, so it will not be discussed again in the following sections. The model is also based on a key assumption that cerebral tissue damage is only driven by the toxic molecules that are produced and released from hypoxic brain cells. Additionally, toxin diffusion is neglected in this proposed model, because it is extremely computationally expensive to solve the 3D diffusion equation in a complex mesh at each time step. The toxin diffusion will therefore be considered in Section 6.4.

Furthermore, the model overestimates the infarct at the time scale of days (Fig. 6.6), since there is no stopping criterion for the forward tissue damage pathway. In addition,

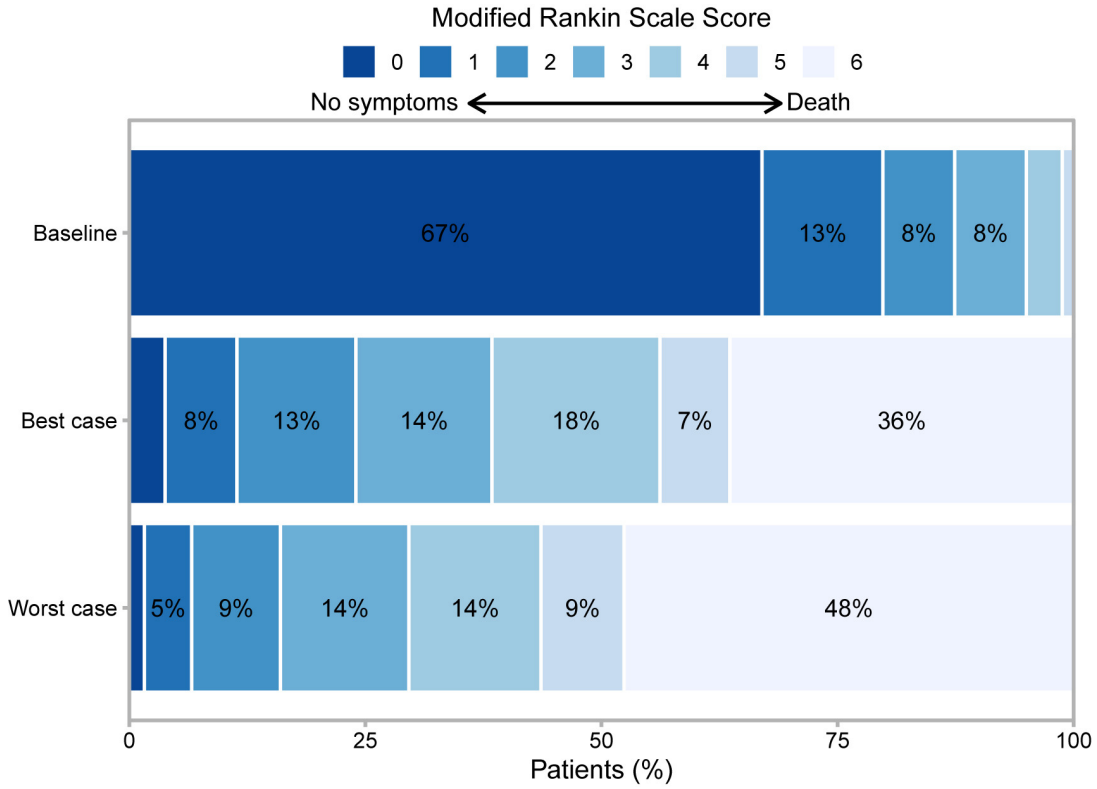

Figure 6.10: The modified Rankin Scale based on final infarct volume and patient characteristics at baseline (mRS at treatment), best case and worst case scenarios. Reproduced without change from [253].

the lack of recovery mechanism (e.g. the backward pathway in the 3-state model) means that the model cannot simulate penumbra recovery after treatment. These limitations indicate that further development of the cell death model is required for better simulation of cerebral tissue damage.

6.3 A cell death model based on storage-toxin dynamics

To simulate the penumbra recovery, a penumbra compartment (P) was added between alive and dead. The penumbra is very similar to the vulnerable compartment in the 3-state model, representing the cells that may have experienced energy impairment but

have potential to recover. The alive and dead compartments were replaced by healthy (H) and core (C) based on the clinical representations respectively. In addition, a new storage compartment (S) was defined to represent the energy state of the tissue and thus the potential for recovery, whilst the toxin compartment represented the potential for damage as before. Similar variables of storage have been defined in previous models [212, 213]. Details of the proposed model are presented below.

6.3.1 Model

The compartments of healthy, penumbra and core represent the fraction of tissue in each state, hence their sum is 1:

$$H + P + C = 1 \tag{6.7}$$

The relationship between them is assumed to have the same manner as that proposed for the 3-state model:

$$H \leftrightarrow P \rightarrow C \tag{6.8}$$

where the pathway between healthy and penumbra is reversible and the core formation is irreversible, which matches the clinical definitions of these tissue states.

For simplicity, variables of relative perfusion of healthy status (F), metabolism (M), storage and toxin are between 0 and 1. The relative energy supply is assumed to be equal to the relative perfusion. The energy metabolism is based on the fraction of alive cells (not core):

$$M = H + 0.25P \tag{6.9}$$

where it is assumed that the healthy cells can maintain full energy metabolism, while the cells in the penumbra state can only maintain the metabolism for housekeeping, which is 25% of the total energy consumption based on the energy budget model [197].

The dynamics between storage and toxin are based on a non-linear competitive

mechanism. A simple cell death model investigating the competitive dynamics can be found in [216]. The storage dynamics are based on the energy supply, metabolism and the current states of storage and toxin:

$$\frac{dS}{dt} = k_s F e^{-T}(1 - S) - k_m M e^{T} S \tag{6.10}$$

where k_s is the storage time constant and k_m is the metabolic time constant. The build-up of energy storage is proportional to the energy supply and is strongly modulated by the toxin level. The energy consumption is based on the current tissue state (Eq. 6.9) and also modulated by the toxin level. Under healthy conditions ($F = 1$, $M = 1$, $T = 0$), the steady-state storage ($dS/dt = 0$) is

$$S_h = \frac{k_s}{k_s + k_m} \tag{6.11}$$

The toxin dynamics are based on the above variables, as well as the current fraction of dead cells (C):

$$\frac{dT}{dt} = k_t(1 - S)(1 - F)e^{-S}e^{C}(1 - T) - k_r F e^{S} T \tag{6.12}$$

where k_t is the time constant for toxin production and k_r is the time constant for toxin removal. The toxin production is assumed to be proportional to the energy deficiency $(1 - F)$, the storage level and the current tissue damage. The toxin removal is assumed to be proportional to the energy supply and positively correlated with the storage level. Under healthy conditions ($F = 1$, $M = 1$), the steady-state toxin ($dT/dt = 0$) is 0.

The penumbra formation and recovery is simulated by

$$\frac{dP}{dt} = k_p(e^{T} - 1)H - k_b(e^{S} - 1)P - \frac{dC}{dt} \tag{6.13}$$

where k_p is the time constant of penumbra formation and k_b is the time constant of penumbra recovery (backward rate). The steady-state penumbra fraction is assumed to

be based on storage and toxin levels.

The last term of Eq. 6.13 (dC/dt) is the core formation, which consists of two pathways, namely fast ($\dot{C}_f$) and slow ($\dot{C}_s$). The fast core formation is assumed to be based on the relative magnitudes of storage and toxin:

$$\dot{C}_f = \begin{cases} k_{cf}(T-S)P & \text{for } T > S \\ 0 & \text{for } T \leq S \end{cases} \tag{6.14}$$

which is only non-zero when the level of toxin is greater than that of storage. However, the slow core formation is assumed to be purely based on the current fraction of core:

$$\dot{C}_s = k_{cs}(e^C - 1)(1 - C) \tag{6.15}$$

which ensures that the core compartment will eventually reach 100% if the core has formed in the tissue region. The core formation is then the sum of these two pathways:

$$\frac{dC}{dt} = \dot{C}_f + \dot{C}_s = \begin{cases} k_{cf}(T-S)P + k_{cs}(e^C - 1)(1 - C) & \text{for } T > S \\ k_{cs}(e^C - 1)(1 - C) & \text{for } T \leq S \end{cases} \tag{6.16}$$

Typical values of the 8 model parameters are listed in Table 6.1. Note that there are no available experimental or clinical data to fit all these parameters. Hence a dynamical system analysis will be presented instead later on.

6.3.2 Model behaviour under different perfusion values

The tissue state and viability can be simulated under different perfusion values as shown in Fig. 6.11. Under healthy perfusion (Fig. 6.11a), there is no core or penumbra formation and the tissue storage state maintains at the healthy state. Under mild ischaemic conditions (Figs. 6.11b and 6.11c), the energy storage decreases and the toxin

Parameter	Time constant of	Value
k_s	Storage	2×10^{-4}
k_m	Metabolism	1×10^{-4}
k_t	Toxin production	2×10^{-4}
k_r	Toxin removal	1×10^{-4}
k_p	Penumbra formation	4×10^{-4}
k_b	Penumbra recovery	6×10^{-4}
k_{cf}	Fast core formation	5×10^{-4}
k_{cs}	Slow core formation	1×10^{-5}

Table 6.1: Model parameters used in the storage-toxin cell death model. All parameters have the unit of 1/s.

increases slightly, which leads to mild penumbra formation. There is no core formation, since the storage is always greater than or equal to the toxin. The tissue damage under these states is thus reversible (see Fig. 6.12).

However, the tissue damage becomes irreversible and the core forms when the ischaemia is more severe (Figs. 6.11d-f). The reason for this transition in model behaviour is that the toxin level exceeds the storage level, which initiates the tissue damage mechanisms. The core formation is faster when the relative perfusion is smaller. Note that there is a recovery of storage compartment at the second phase of core formation (Figs. 6.11d and 6.11e). This is primarily due to reduced metabolic demands caused by irreversible cell death (Eq. 6.9). This storage recovery does not indicate the recovery of the tissue, since the core formation has been initiated and the slow core formation (Eq. 6.15) will lead to a steady state of $C = 0$.

Figure 6.12 presents the same simulations but with a successful treatment at 3 hours. The perfusion is assumed to fully recover ($F = 1$) in these simulations. In the cases without core formation (Fig. 6.12a-d), the tissue damage is fully reversible. However, the tissue damage is irreversible, if the toxin has already been greater than the storage before the treatment time, even if the core fraction is small (Fig. 6.12e).

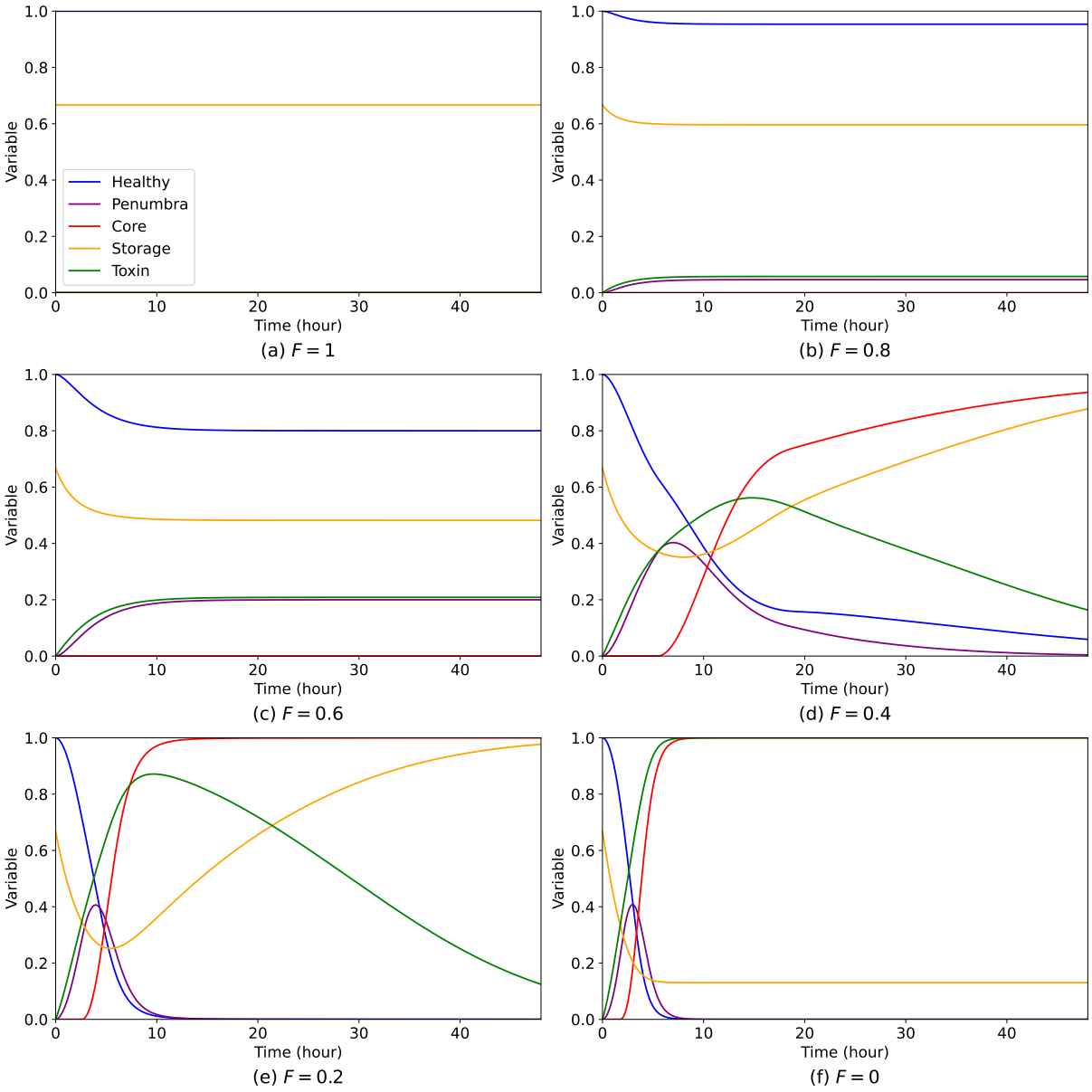

Figure 6.11: The tissue state and viability under different perfusion values in 2 days.

One notable case is shown in Fig. 6.12d when the relative perfusion is 40%. Without treatment the tissue region with less than 40% relative perfusion will lead to core formation (with the model parameters provided in Table 6.1). A treatment at 3 hours saves the tissue, since the core formation has not started until then ($T < S$). This means that the treatment at 3 hours can be seen as timely for tissue at 40% relative perfusion. However, a much later treatment at, e.g. 10 hours, will be ineffective in saving the tissue.

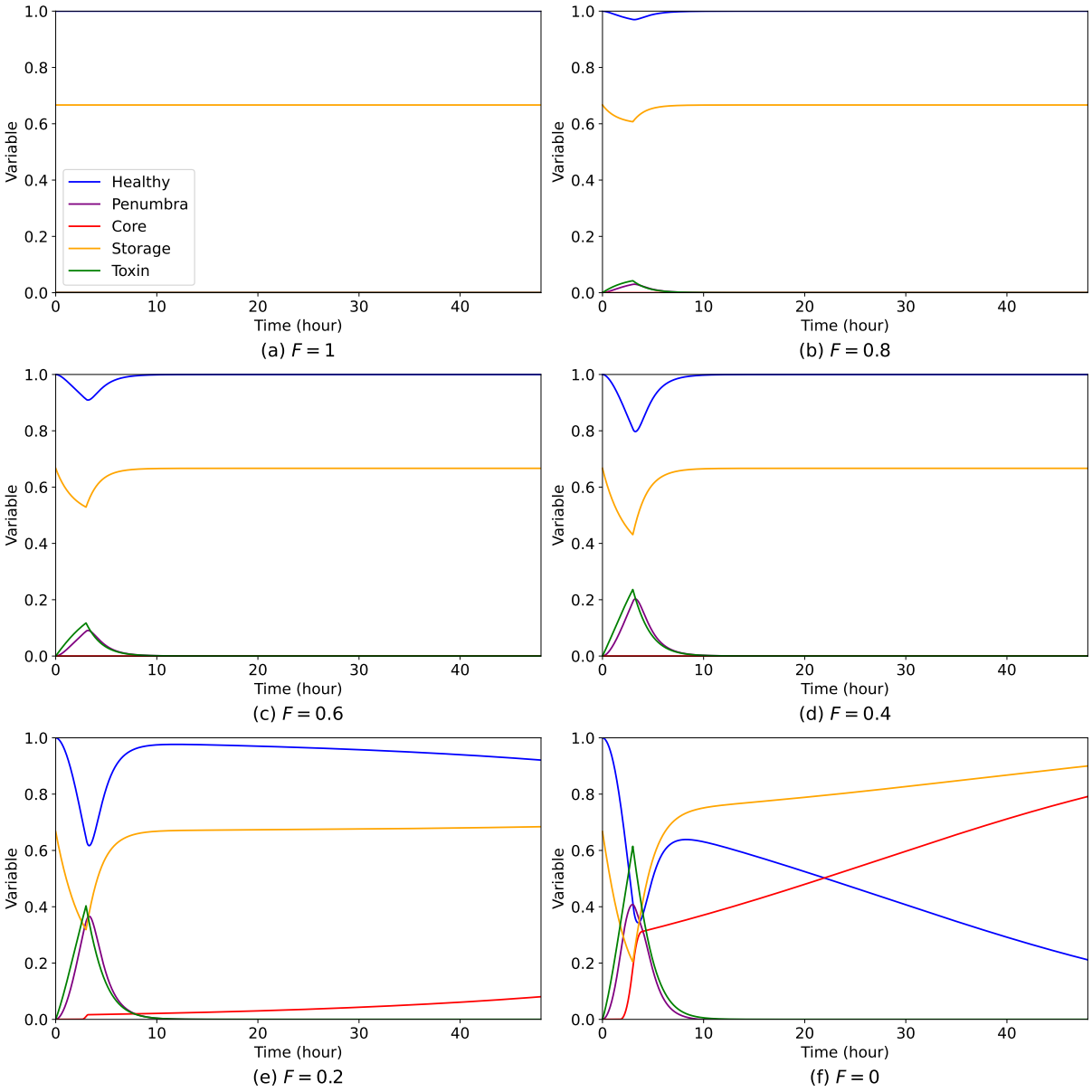

Figure 6.12: The tissue state and viability under different perfusion values in 2 days with the treatment at 3 hours.

These simulations indicate that the proposed model is able to simulate the effects of treatment time on the final outcomes of brain tissues and thus patients, which will be better demonstrated using the phase plane analysis presented in the next section.

6.3.3 Dynamical system analysis

6.3.3.1 A single stable node of the model

Before conducting the phase plane analysis, it is necessary to determine the number of fixed points and their properties in the proposed dynamical system. If the core formation has started, it is clear that there is only one stable node at $(C, P, H) = (1, 0, 0)$, due to the slow core formation (Eq. 6.15). This will lead to $(S, T) = (1, 0)$ unless $F = 0$, based on Eqs. 6.10 and 6.12.

When there is no core formation, the system can be simplified into a three-dimensional system of storage, toxin and penumbra. By solving $dS/dt = 0$, $dT/dt = 0$ and $dP/dt = 0$ analytically, it can be proven that there is one and only one fixed point in the parameter space $S, T, P \in [0, 1]$, as long as all parameters are positive. At the fixed point (S^*, T^*, P^*), a Jacobian matrix can be defined as

$$J = \begin{pmatrix} \frac{\partial \dot{S}}{\partial S} & \frac{\partial \dot{S}}{\partial T} & \frac{\partial \dot{S}}{\partial P} \\ \frac{\partial \dot{T}}{\partial S} & \frac{\partial \dot{T}}{\partial T} & \frac{\partial \dot{T}}{\partial P} \\ \frac{\partial \dot{P}}{\partial S} & \frac{\partial \dot{P}}{\partial T} & \frac{\partial \dot{P}}{\partial P} \end{pmatrix}_{(S^*, T^*, P^*)} \tag{6.17}$$

By solving

$$\det(J - \lambda I) = 0 \tag{6.18}$$

where det is the matrix determinant and I is the identity matrix, all λ (eigenvalues of the Jacobian matrix) have been found to be negative real numbers under the current parameter values (see Table 6.1) and $F \in [0, 1]$. Therefore, the fixed point is a stable node (also known as an attractor) under all possible relative perfusion values [260]. The movement of stable nodes under different relative perfusion values is plotted in Fig. 6.13. It should be noted that this figure only represents the stable nodes in the three-dimensional space (S, T and P) before the core formation. Using the full cell death

model, the stable nodes do not exist in the region of $T > S$.

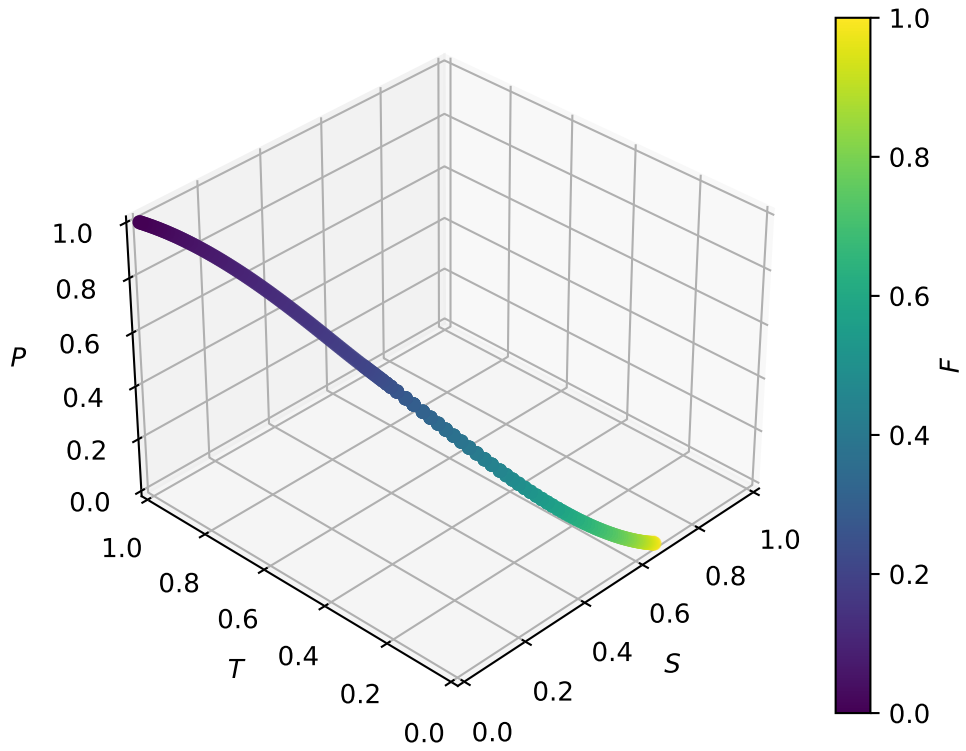

Figure 6.13: Stable nodes in the state space of S, T and P under relative perfusion values from 0 to 1 using the parameter values listed in Table 6.1.

Having examined the stable node in the proposed model and implemented parameter values, it is worth examining whether the node is always stable with any arbitrary positive parameter values. Since it is very challenging to solve the non-linear system analytically, a numerical analysis was conducted. In the numerical simulation, it was assumed that all parameters have the same value and an order of magnitude from 1 to 1×10^{-9} with $F \in [0, 1]$. Under all these conditions, the Jacobian matrix (Eq. 6.17) was found always to have three negative eigenvalues. Hence the dynamical system has a stable node in the 3D space of S, T and P when the order of magnitudes of the parameters is from 1 to 1×10^{-9}.

6.3.3.2 Phase plane of storage and toxin

Next, 2D phase planes of storage and toxin will be presented in several scenarios to demonstrate the model behaviour. Figure 6.14 shows the phase planes of storage and toxin $[(dS/dt, dT/dt)$ on $(S, T)]$ under two conditions, where a red dot represents the attractor, a red line indicates the threshold of $T = S$ and the relative magnitude of derivative is scaled using a colourmap. As shown in the top figure, the attractor is at the bottom of the plane where $T = 0$ under the healthy condition. In the bottom figure, the attractor is above the threshold of $T = S$ and almost reaches a state of full toxin before the tissue develops into core completely.

Figure 6.15 presents two scenarios with the same tissue state ($H = 0.5$ and $P = 0.5$) but different relative perfusion values. In the top figure, the attractor is below the core formation threshold when perfusion is maintained at 50% of its healthy level in the tissue region. However, the attractor moves above the threshold when the relative perfusion further drops to 40%, which will initiate the core formation. This figure highlights the key role of relative perfusion in determining the final tissue state (core or not).

6.3.3.3 Trajectories under different perfusion

In each simulation, the phase plane of storage and toxin in fact changes continuously over time based on the tissue state. Figure 6.16 presents the trajectory of model variables in each 2D plane when the relative perfusion changes from 0 to 1. In Fig. 6.16a, two types of model behaviours are shown. When $F > 0.45$, the trajectory is just a short curve from the initial state $(S_h, 0)$ to the steady state as shown in Fig. 6.13. When $F \leq 0.45$, the trajectory tries to reach the steady state at the beginning, but rotates clockwise and finally converges to $(1, 0)$ due to the core formation starting from $T > S$. The penumbra formation and its further progression into core are shown in Figs. 6.16b and 6.16c. The core formation is shown in Figs. 6.16d-6.16f.

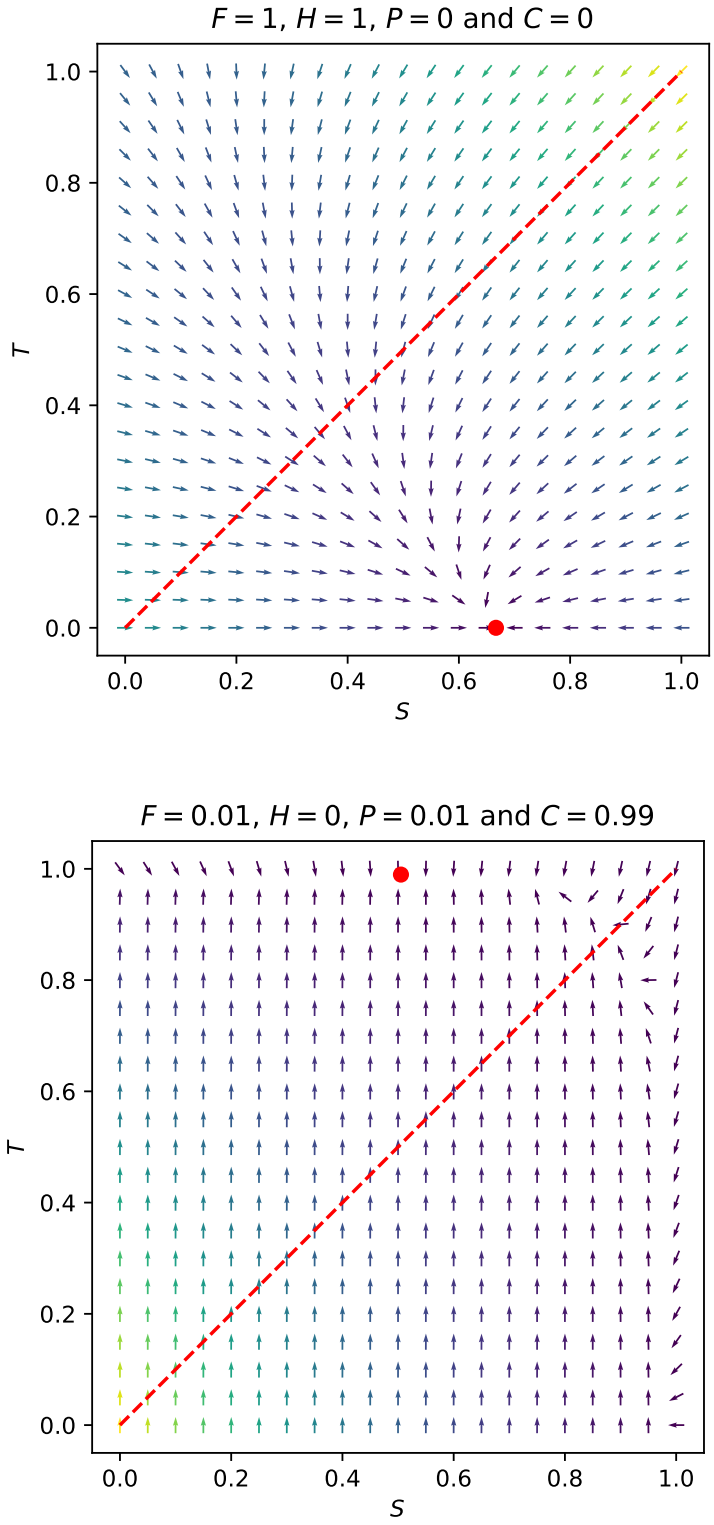

Figure 6.14: Phase planes of storage and toxin under healthy and core conditions. The red dot represents the attractor and the red line indicates the threshold of $T = S$. The derivatives on the phase plane are shown by a vector field, where the relative magnitude of derivative is scaled using a colourmap.

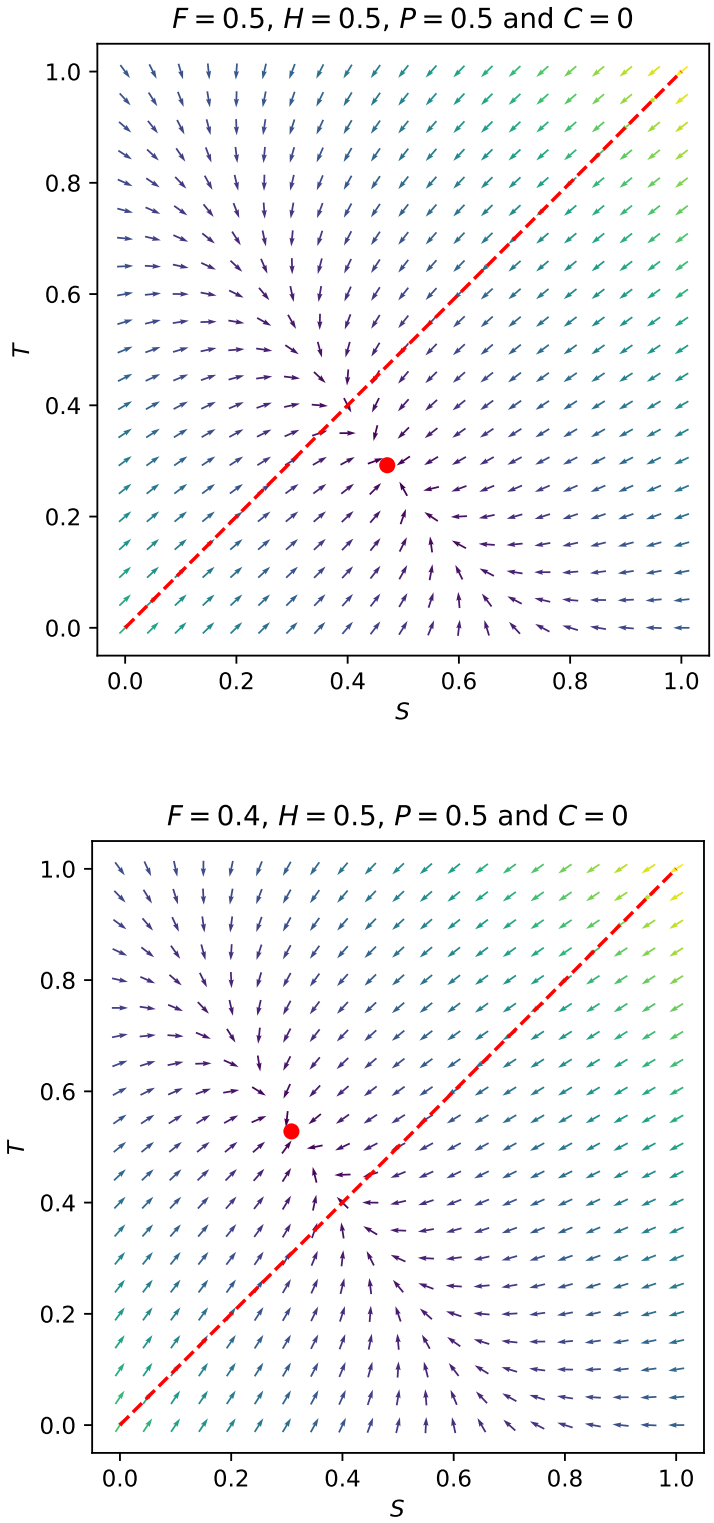

Figure 6.15: Phase planes of storage and toxin under different perfusion that will or will not lead to the core formation. The red dot represents the attractor and the red line indicates the threshold of $T = S$. The derivatives on the phase plane are shown by a vector field, where the relative magnitude of derivative is scaled using a colourmap.

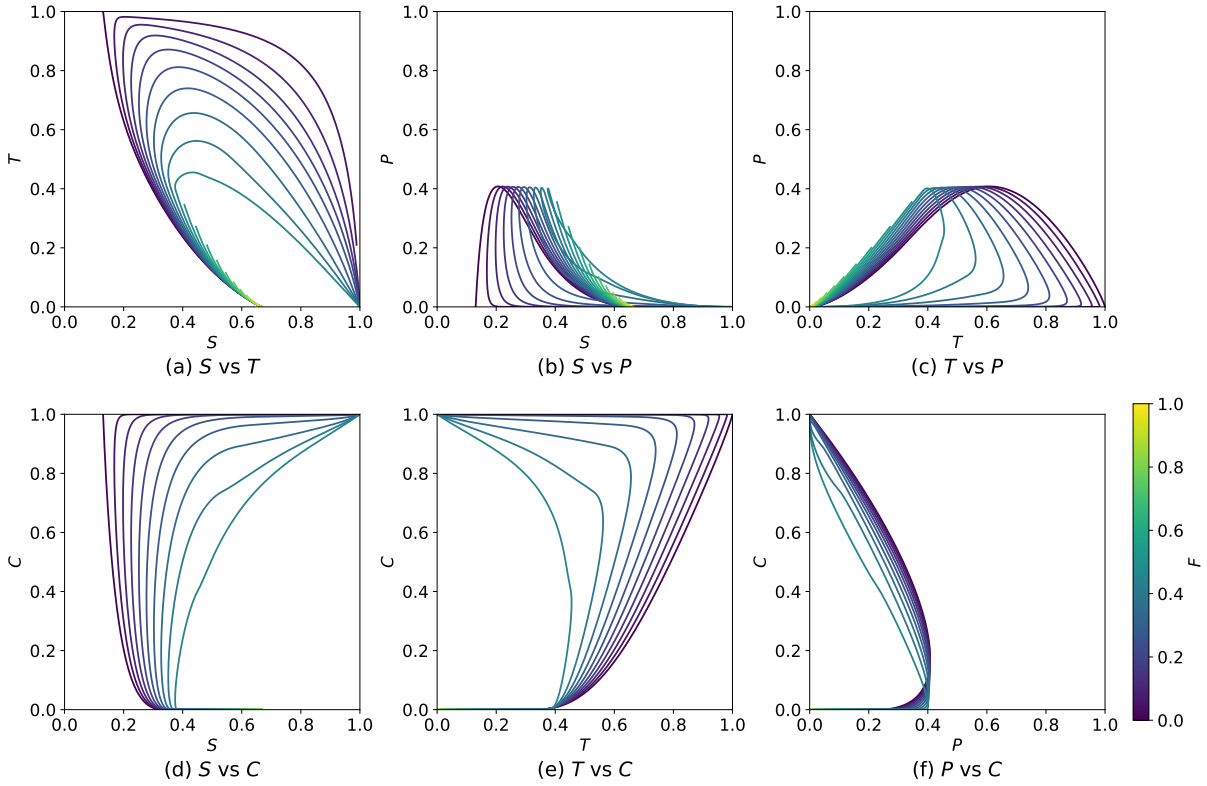

Figure 6.16: Trajectories of model variables (S, T, P and C) under relative perfusion values from 0 to 1.

6.3.3.4 Effects of treatment time on the model behaviour

These trajectories are extremely useful in investigating the effects of stroke treatment time on cerebral tissue viability. In brief, only a treatment that happens before the core formation can be seen as effective. This is because, based on the definition of core the tissue will finally become 100% core as long as the core formation has started.

Figure 6.17 shows the model behaviour under different values of perfusion with a treatment at 3h or 6h after the stroke onset. In these simulations, it is assumed that the treatment will lead to a full perfusion recovery. When the reperfusion is at 3h after the stroke, the tissue with ischaemia of $F \leq 0.25$ will become core. Compared with the simulation results presented in the previous section, tissues with $0.25 < F \leq 0.45$

will be saved by the treatment. However, the tissue under an ischaemia of $F \leq 0.4$ will become core when the reperfusion is at 6h after the stroke onset. This indicates that the treatment at 6h is only effective to the tissue with $0.4 < F \leq 0.45$, and a treatment that is 3 hours earlier can further save the tissue with $0.25 < F \leq 0.4$. It should be noted again that these simulations are based on the parameter values listed in Table 6.1, which have not been fitted to any experimental or clinical data. Hence these simulations only suggest that the model can simulate the fact that earlier treatments usually lead to better clinical outcomes, without any clinical or quantitative significance at this stage. The model can be fitted at a later stage, when more data are available. Suggestions for future experiments to fit the model will be presented in Section 7.2.6.

6.3.4 Implementation at the organ-scale

The model can be implemented at the organ-scale [36] using the same method that was introduced in Section 6.2.4. Note that the ODEs of the proposed model are more complex than these of the toxin-based model, so it takes longer to solve these equations in the same brain mesh. To enable the comparisons between the simulations and clinical images, the DWI scale was assumed to be a linear weighting of 3 tissue compartments as

$$DWI = 0.1H + 0.5P + C \tag{6.19}$$

Hence $DWI \in [0.1, 1]$, where 0.1 and 1 represent healthy and core, respectively. The DWI value for the healthy tissue was set to be 0.1 based on the fact that the intensity of DWI in the healthy brain regions is non-zero [261].

Figure 6.18 presents a DWI simulation in the whole brain model following an ischaemic stroke with a treatment at 3 hours after onset. After the stroke onset, the damage progression in each tissue mesh element is based on the local perfusion. After the treatment, brain tissues that are still in the penumbra state (centre and bottom of the bright regions) will have a gradual recovery. However, the tissues that have already

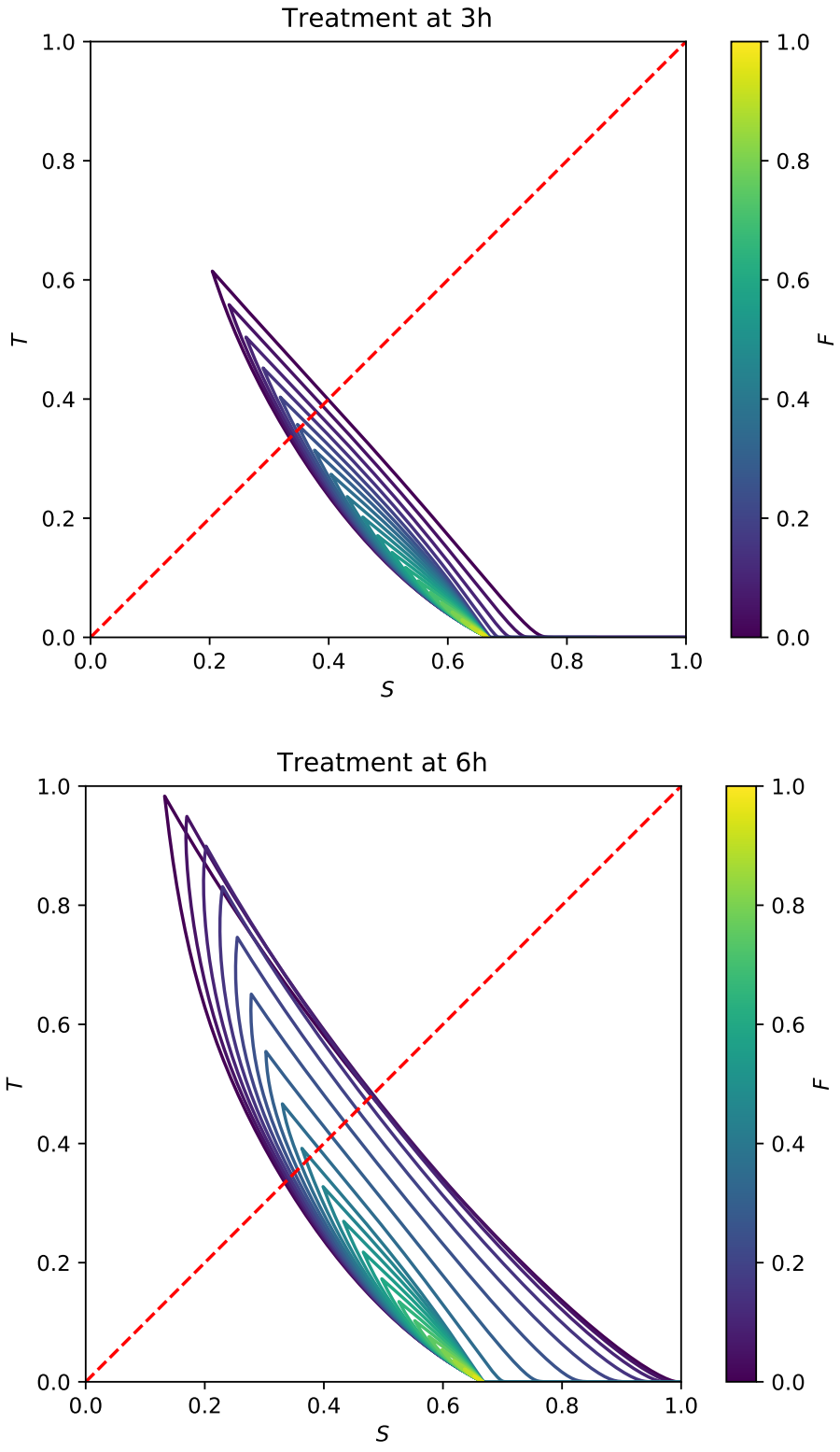

Figure 6.17: Effects of treatment time (3h or 6h) on cerebral tissue viability under relative perfusion values (before treatment) from 0 to 1. The red line indicates the threshold of $T = S$.

experienced core formation (other bright regions) will not recover after the treatment. These different tissue responses to treatment depend on whether the level of toxin is greater than that of storage at the treatment.

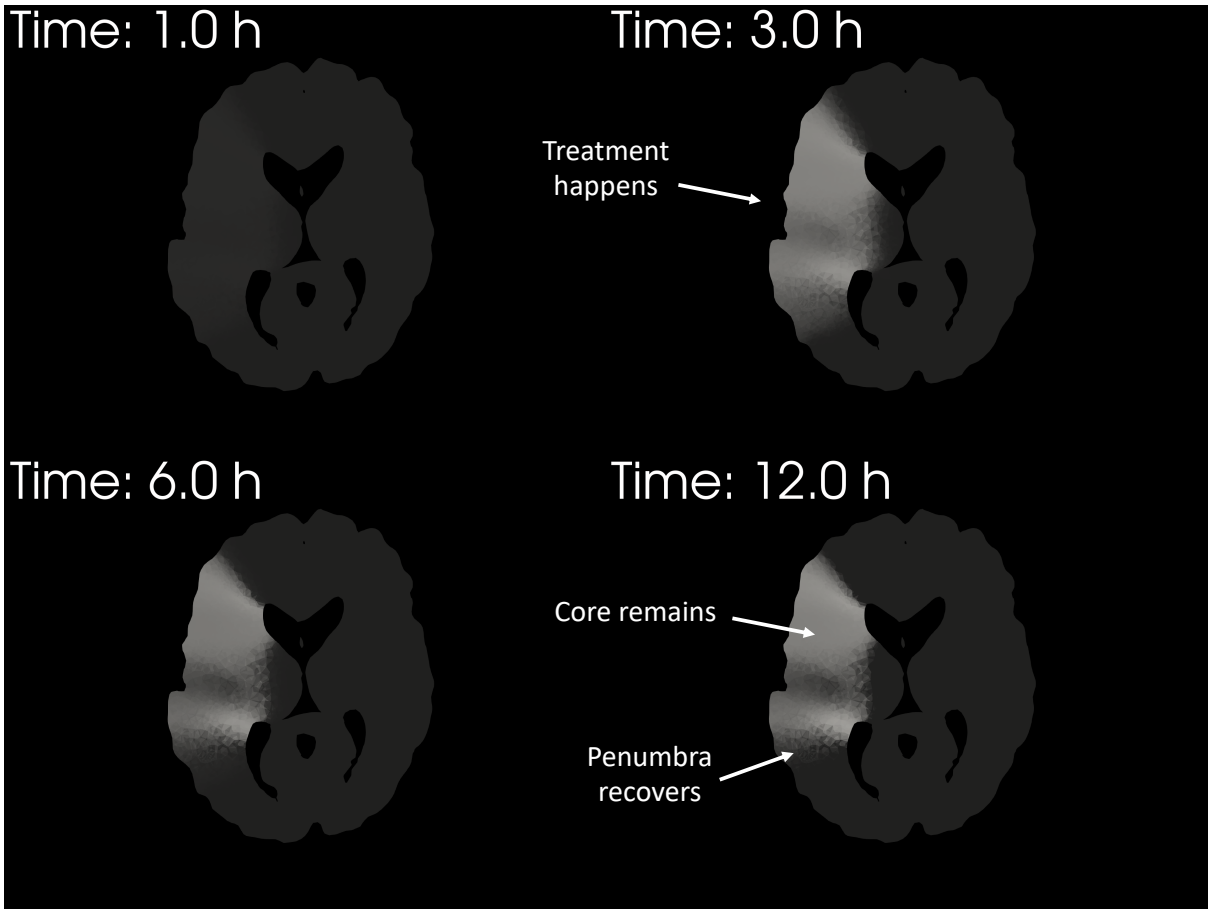

Figure 6.18: The prediction of DWI following an ischaemic stroke with a treatment at 3 hours after onset. Simulation results are shown on a 2D brain slice in a 3D brain model at 4 representative time points.

6.3.5 Discussion

This section develops a cell death model with a competitive mechanism between storage and toxin, which represent the potentials of recovery and damage, respectively. The brain tissue has 3 states, namely healthy, penumbra and core, that match the clinical definitions. Similar to the 3-state model presented in Chapter 5, the pathway between

healthy and penumbra is reversible, while it is irreversible between penumbra and core. There are 4 variables and thus 4 ODEs in the proposed model with 8 parameters.

The model is able to simulate the penumbra recovery in the tissue regions with mild ischaemia after a timely treatment. In addition, it can also model the continued core formation in the regions with severe ischaemia or in response to late treatment. The choice of recovery or damage mechanism after treatment depends on the relative magnitude of storage and toxin at the time point of treatment. With a simple linear equation, the model can simulate the DWI scale (or other clinical images, e.g. CT perfusion) in the whole brain model with different scenarios. The model thus broadens the application of *in silico* trials of ischaemic stroke and enables future comparisons to be made between these simulations and clinical images.

It should be noted that the model parameters of the proposed model have not been fitted to experimental or clinical data, since there are currently no data with satisfactory temporal resolution to fit all 8 parameters. In addition, the diffusion of toxin is not considered in the model, which means it cannot simulate the expansion of infarct regions in the scenario of no treatment (i.e. the infarct region will not exceed the ischaemic region). These limitations thus led to the development of a new cell death model presented in the next section.

6.4 A cell death model with damage propagation

In principle, there are three ways to simulate the damage propagation (primarily toxin diffusion) in the human brain following an ischaemic stroke. Firstly, the toxin diffusion can be simulated by solving the 3D diffusion equation of toxic molecules using a numerical method (e.g. a finite element method). This method gives the most accurate simulation results, but it requires solving the 3D diffusion PDEs at every time step (or solving them once per every few time steps), which can be very computationally expensive for fine

brain meshes.

The second way to simulate toxin diffusion is to use a cellular automata model [262]. The cellular automata simulation is much cheaper than solving the diffusion equations numerically. However, it requires transforming the brain meshes into a lattice grid. Since the cellular automata is a discrete model, it can only predict the presence or absence of toxin at each lattice at each time point, while losing the spatial distribution of toxin levels. This makes the cellular automata model unable to simulate different cell death rate based on different toxin levels. Moreover, it is very challenging to define a toxin removal mechanism after treatment based on this set of discrete toxin states.

A third way is to use a time-dependent Green's function method [263]. The time-dependent Green's function adds an additional dimension of time to the Green's function defined in a three-dimensional space (which has been introduced and used several times in this thesis). This method gives an analytical solution of the toxin diffusion that is much cheaper than using a discretisation method. Although it is straightforward to impose a total no-flux condition on the boundary of the brain tissue, it is almost analytically impossible, however, to impose a pointwise no-flux boundary condition, due to the complex brain geometry. It is obvious that the flux of toxin through the boundary of brain tissue (i.e. skull) violates physical laws.

Hence a new model is required here to simulate the propagation of tissue damage with a reasonable balance between accuracy, model intricacy and computational cost. The model should simulate the expansion of infarct from severe ischaemic regions in the absence of treatment. Additionally, the expansion should be stopped within a certain range from the ischaemic regions (or the whole brain will become infarct when the simulation time continues for long enough).

6.4.1 Model

6.4.1.1 Local tissue damage

The local tissue damage model is very similar to the toxin-based cell death model (Section 6.2). The major difference between these two models is that the model presented in this section is based on cerebral perfusion instead of hypoxia to enable an easier coupling with the organ-scale perfusion model.

Firstly, the vulnerability ($V \in [0, 1]$) of each brain tissue element is defined as the reduction of relative perfusion:

$$V = 1 - \text{rCBF} \tag{6.20}$$

The toxin dynamics are simulated as

$$\frac{dT}{dt} = k_t V(1 - T) - k_r(1 - V)AT \tag{6.21}$$

where the first term is the local toxin production and the second term is the local toxin removal. When the toxin level is greater than a threshold (T_d), the forward death pathway is activated:

$$\frac{dD}{dt} = \begin{cases} k_f AT & \text{for } T > T_d \\ 0 & \text{for } T \leq T_d \end{cases} \tag{6.22}$$

This threshold prevents the overestimation of tissue damage over a long time (Fig. 6.6).

6.4.1.2 Damage propagation

Before simulating the damage propagation, the brain meshes and perfusion results for each virtual patient were converted to 3D imaging voxels[2] with a size of $2 \times 2 \times 2$ mm^3. This enables the validation of perfusion results against medical images at a similar resolution.

[2]This work was conducted by Dr Tamás Józsa and will be published in the future, and is not part of this thesis. It should also be noted that the brain meshes used in this section are different from these in other sections. These new brain meshes can be found in [264].

The tissue damage simulation will also be conducted in these 3D voxels.

To simulate the infarct expansion, the 3D field of vulnerability is updated every half an hour in the tissue damage simulation time. During the update step, the vulnerability will propagate to neighbouring voxels with an exponential decay, when the local toxin is greater than a threshold of T_p:

$$V(i',j',k') = max(V(i',j',k'), V(i,j,k) \times k_d) \quad \text{for } T > T_p \tag{6.23}$$

where $i' = i+1$ or $i' = i-1$ or $j' = j+1$ or $j' = j-1$ or $k' = k+1$ or $k' = k-1$. Hence the infarct expansion is driven by the propagation of vulnerability, which is purely based on perfusion. In another word, this simulation is only based on the perfusion values and brain geometries.

6.4.2 Parameter fitting

There are six model parameters, where four of them (k_f, k_t, k_r and T_d) govern the local tissue damage and the other two (k_d and T_p) control the global mechanisms. The local parameters were fitted to the monkey data [64], where it was assumed again that the infarct formed when $D \geq 80\%$. The healthy perfusion in the grey matter was assumed to be 60 cm^3/100g/min. A cost function was defined as the sum of squares of the difference between the simulated dead fraction and $D = 80\%$ at each data point in the monkey data. In addition, a penalty of 100 was added to the cost function, if the dead fraction at 7 days under 18 cm^3/100cm^3/min (which is the infarct threshold of the monkey data) was greater than 80%. By minimising the cost function, the parameters were found to be: $k_f = 6.0644 \times 10^{-4}$ 1/s, $k_t = 4.2981 \times 10^{-3}$ 1/s, $k_r = 9.9923 \times 10^{-2}$ 1/s and $T_d = 0.091639$. The parameter fitting is plotted against the monkey data in Figs. 6.19 and 6.20 at different time scales.

Next, the global parameter k_d was fitted with the maximum final infarct volume of 400

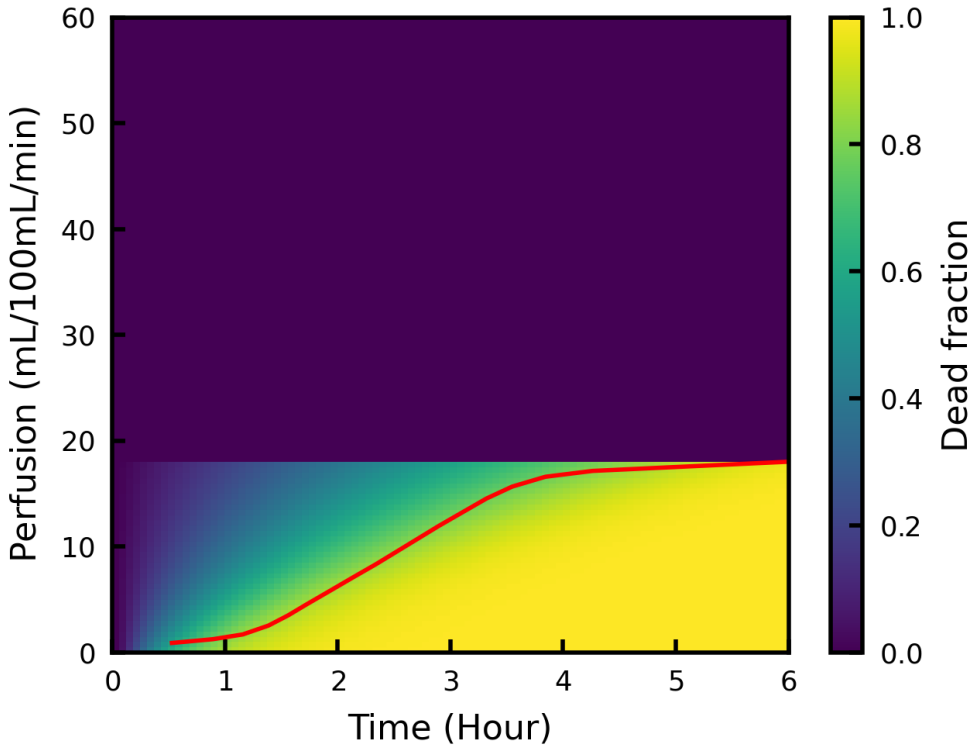

Figure 6.19: The dead fraction predicted by the cell death model under different perfusion and time. The red line shows the experimental data of a monkey model [64].

mL [70] using a virtual patient with the largest infarct volume based on the perfusion map (volume of the regions with a relative perfusion below 30%) and no collateral flow. The resulting value of k_d was found to be 0.95118, which would result in a final infarct volume of 400.072 mL in that patient (the absolute error was set to be below 0.1 mL). The parameter T_p was assumed to be 0.5 in these simulations and it can be fitted easily again in the future when more clinical data become available.

6.4.3 Implementation of the model in virtual patients

The model was next implemented in 75 virtual patients with patient-specific brain geometries based on age and sex [264]. For each patient, the cerebral perfusion was simulated under the healthy condition and the right MCA occlusion condition, respectively. The relative perfusion was thus calculated by dividing the perfusion map

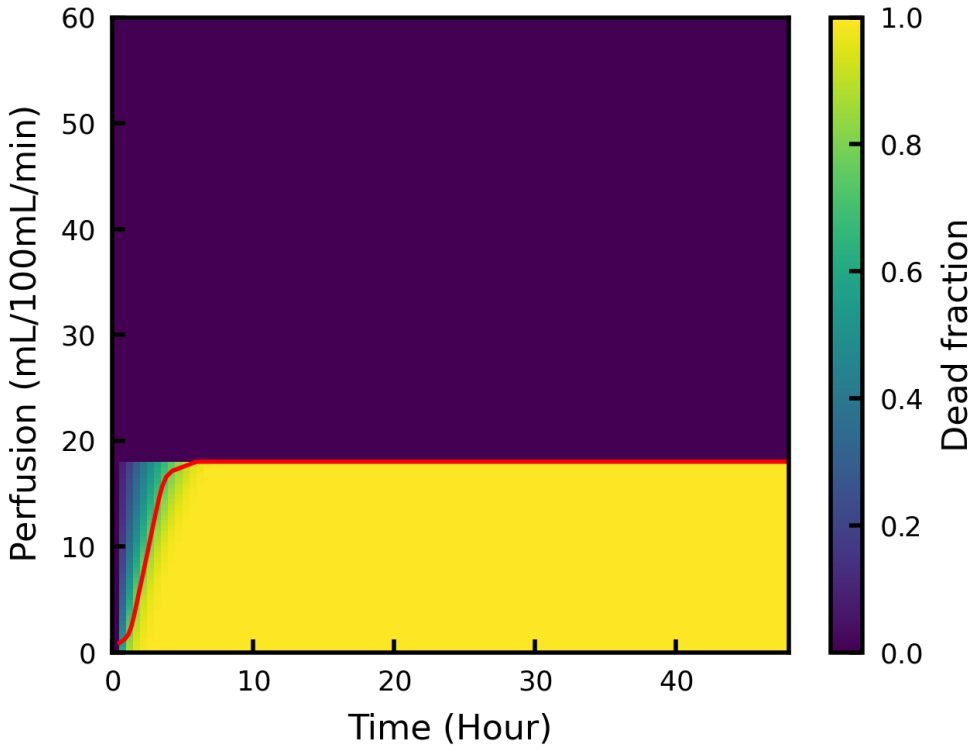

Figure 6.20: The dead fraction predicted by the cell death model under different perfusion and time up to 2 days. The red line shows the experimental data of a monkey model [64].

after ischaemic stroke by that in the healthy condition. Coupled with the cell death model, the infarct can be simulated in the whole brain based on the results of relative perfusion. The simulation time for each patient for 2 days following the stroke onset is about 10-20 minutes on one core of a standard laptop.

Figure 6.21 shows the simulation of infarct growth in a virtual patient (who has the maximum infarct volume of 400 mL) without treatment and collateral flow. A fast local infarct growth happens in the ischaemic region during the first few hours after the stroke onset. After that, a slow infarct expansion starts and lasts for about one day. The infarct expansion is caused by the propagation of the vulnerability fields (originally defined as the reduction of relative perfusion) from the ischaemic voxels to the neighbouring regions, due to the accumulation of toxins.

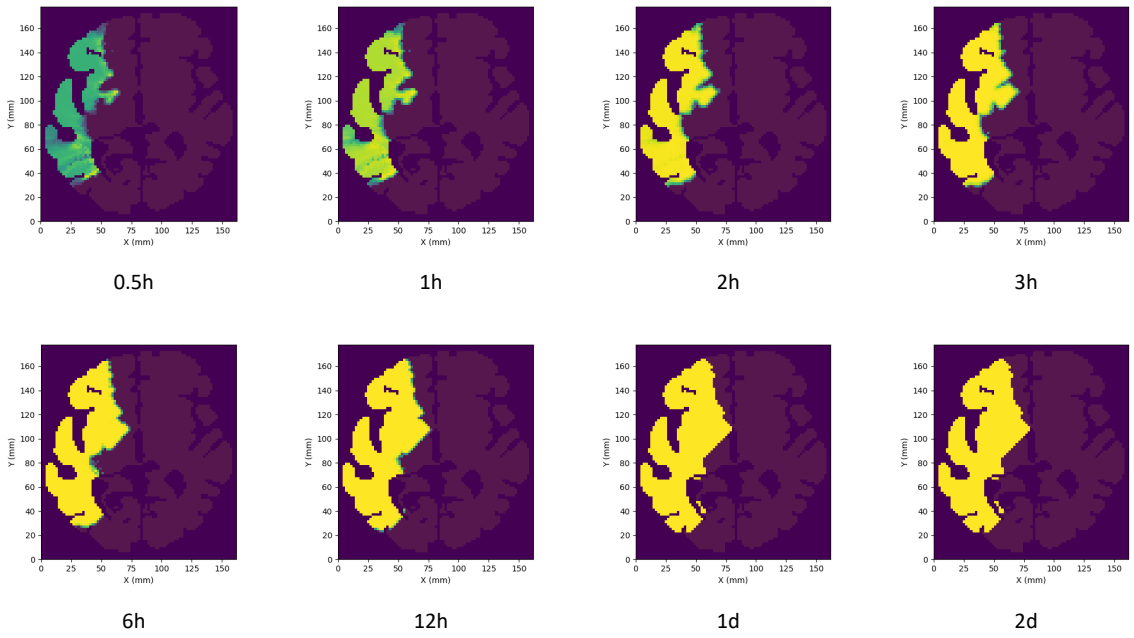

Figure 6.21: Simulation of infarct growth without treatment and collateral flow. Simulation results are shown on a 2D brain slice in a 3D brain model at 8 time points. The dead fraction is shown using a colourmap, where yellow represents 1 and dark blue represents 0.

Figure 6.22 shows the vulnerability propagation in the same brain slice as used for plotting in Fig. 6.21. The vulnerability will propagate to the neighbouring voxels with an exponential decay (Eq. 6.23), when the local toxin level is greater than the propagation threshold T_p. As a consequence of the exponential decay, the vulnerability will become smaller when it is further from the original ischaemic region. Hence there is a certain location, where the toxin level will no longer exceed the propagation threshold T_p and the infarct expansion will thus end (e.g. at the green regions in Fig. 6.22). Note that the time step of propagation was set as half an hour, so the propagation speed was thus purely based on the threshold T_p. Since the value of T_p was not fitted due to the lack of time-dependent data of infarct volume, the time-dependent results here only show the qualitative behaviour of the proposed model.

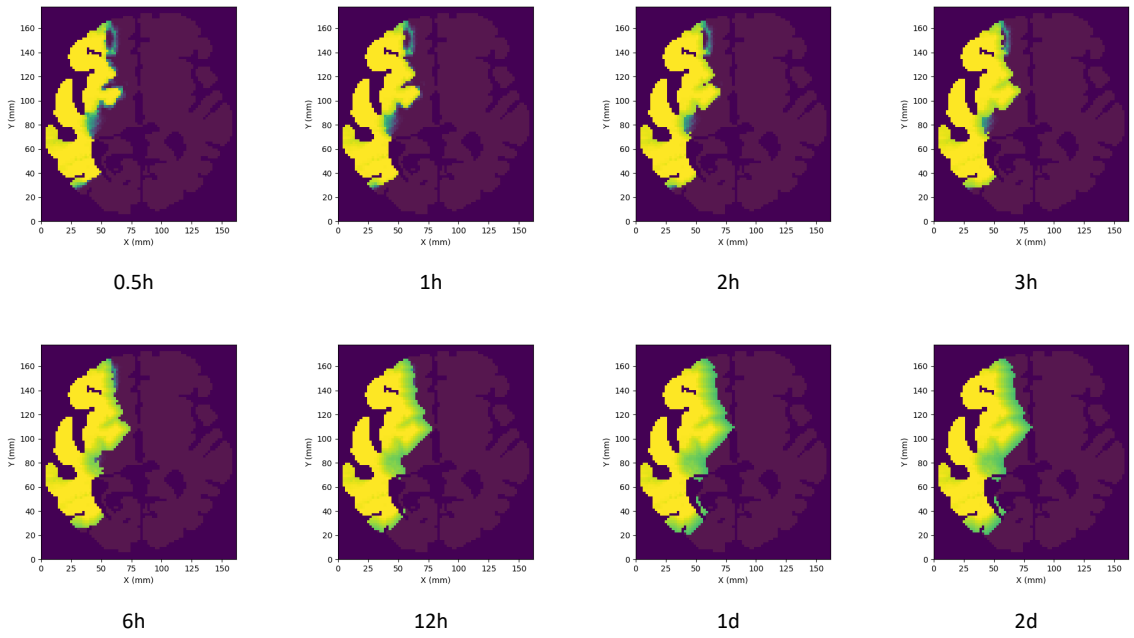

Figure 6.22: Simulation of vulnerability propagation without treatment and collateral flow. Simulation results are shown on a 2D brain slice in a 3D brain model at 8 time points. The vulnerability is shown using a colourmap, where yellow represents 1 and dark blue represents 0.

The same simulation pipeline has been applied to all 75 virtual patients. Under the conditions of no treatment and no collateral flow, the infarct (core) volumes of these patients are plotted in Fig. 6.23. The infarct volume increases rapidly to 150-200 mL in the first hour, and then expands to a region of 250-400 mL in one day. The final infarct volume simulated by the cell death model is greater than that predicted by a threshold of 30% relative perfusion, as shown in Fig. 6.24. The difference between the two is mainly due to the expansion of vulnerability in the cell death model.

6.4.4 Discussion

This section presents a cell death model with damage propagation, so that it can simulate the infarct expansion following an ischaemic stroke when the treatment is absent. This

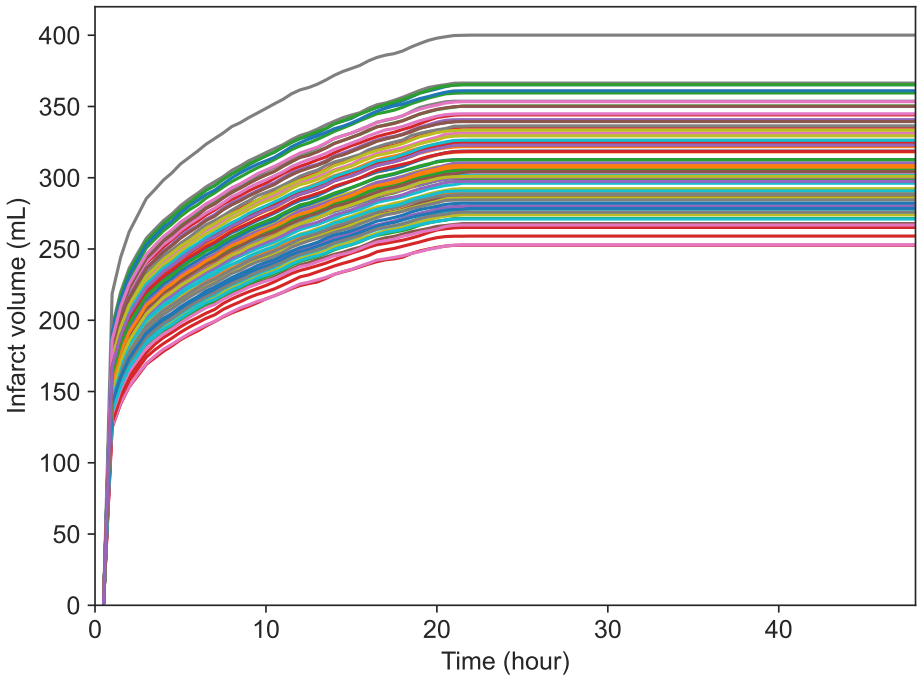

Figure 6.23: The infarct volume of 75 virtual patients in 2 days after an ischaemic stroke.

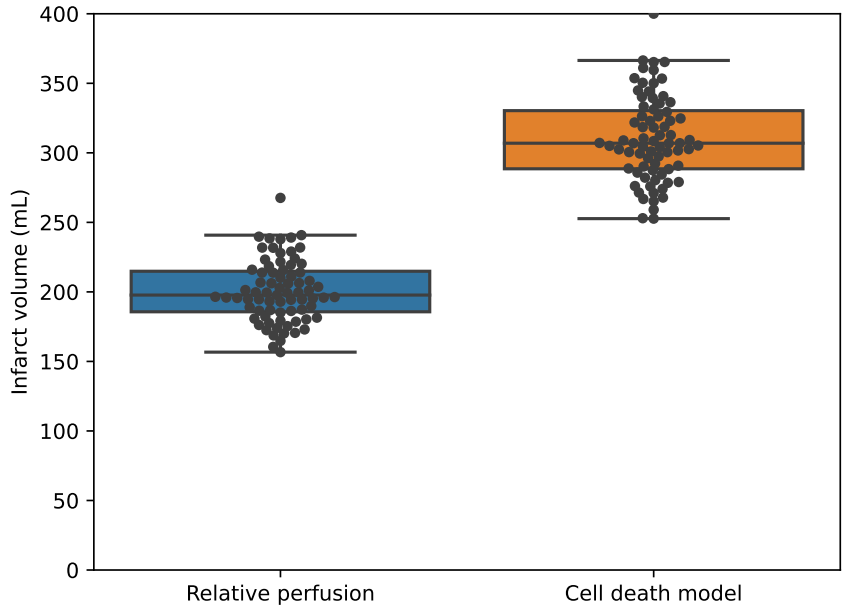

Figure 6.24: The final infarct volumes of 75 virtual patients simulated using the relative perfusion or the cell death model.

model is based on the idea of cellular automata models, but it uses the local toxin level to simulate the non-linear tissue damage mechanisms. The dynamics of local tissue damage have been fitted to the monkey data and the final infarct volume of the worst-case patient has been fitted to the maximum infarct volume in the MR CLEAN dataset.

This model was then implemented in 75 virtual patients, so the infarct volume of each patient could be simulated as a function of time. In addition, the infarct growth without the treatment has been clearly shown in Fig. 6.24 by comparing the final infarct volume simulated by the cell death model against that simulated by the threshold based on relative perfusion.

One limitation of the model is that the parameter controlling the infarct expansion speed has not been fitted to clinical or experimental data. Another limitation is that the distribution of final infarct volume has not been validated against the value from the MR CLEAN dataset, because the new patient-specific brain meshes [264] and tissue-level collateral flow simulations have not yet been completed. The further parameter fitting and validation of the proposed model will be carried out once the perfusion model has been completed.

6.5 Modelling the constriction of capillary pericytes in micro-occlusions

Having developed the cell death models driven by toxin mechanisms, this section focuses on another pathological scenario: capillary constriction by pericytes evoked by ischaemia [135]. The model presented in this section thus provides an alternative way to simulate irreversible tissue damage using the micro-scale simulation results (Chapter 3) and the thrombus extravasation model (Chapter 5), but at a smaller length scale than the models presented in Sections 6.2-6.4.

6.5.1 Background

Pericytes are isolated contractile cells embedded within the microvascular vessel walls that have been found to control the blood flow under healthy conditions and to constrict blood vessels under ischaemic conditions [265]. In a recent review by Hartmann et al. [73], it is proposed that there are two types of pericytes: ensheathing pericytes in the arteriole-capillary transition zones and capillary pericytes on capillaries. Since the models presented in this chapter are developed from the capillary scale, this section will focus on the latter type of pericytes.

In the experimental study conducted by Hall et al. [135], ischaemia evoked capillary pericytes constriction and eventually death. The constriction was found to happen over the time scale of minutes, which can lead to a vessel diameter decrease of more than 60 %. The capillaries usually have diameters from 1.5 to 8 μm [73]. Therefore, the capillaries constricted by pericytes tend to have much larger flow resistance than healthy capillaries, due to the resistance being inversely proportional to the fourth power of radius. In addition, the irreversible pericyte damage also happens at the time scale of minutes, since pericytes were found dead only 20 minutes after the onset of ischaemia [135]. In addition to the response of pericytes to ischaemia in minutes, they can have effects on the cerebral microvasculature at other time scales from hours to days [266]. However, this section only focuses on the pericyte impairments caused by ischaemia and hypoxia at the time scale from minutes to hours.

Despite their role in controlling the blood flow, the number of numerical models on pericytes is very limited. A recent study simulated the role of pericytes in cerebral autoregulation [136]. However, the pathological constriction of pericytes has not been modelled yet to the best of the author's knowledge. Hence a model on capillary pericyte constrictions generated by microthrombi occlusions is presented here purely based on previous simulations and models presented elsewhere in this thesis.

6.5.2 Models

The model begins by assuming that the effects of pericyte constriction on capillaries are equivalent to microthrombi occlusions, due to the highly non-linear increase of flow resistance in response to the decrease of vessel diameter as discussed in the previous section. However, the vessels occluded by pericyte constriction cannot be recanalised by extravasation mechanisms. In addition, it was assumed that the microthrombi occlusion and the pericyte constriction are two independent events in the cerebral microvasculature. The fraction of no-flow vessels can thus be estimated as

$$V_{nf} = B + C - B \times C \tag{6.24}$$

where B is the blockage fraction as defined in Chapter 3 and C is the constriction fraction (the fraction of vessels constricted by pericytes). Hence the tissue hypoxic fraction can be predicted using the sigmoidal function (originally Eq. 3.2 for microthrombi occlusions) as

$$H = \frac{1}{1 + e^{-(30.71 V_{nf} - 5.35)}} \tag{6.25}$$

Then the pericytes were assumed to be evenly distributed in the cerebral tissue. In a tissue region, the fraction of hypoxic pericytes is thus equal to the volume fraction of hypoxic tissue. A similar idea in simulating thrombus extravasation can be used here that a certain fraction of pericytes under energy impairments due to hypoxia will constrict in a certain period of time. It can be written as an ordinary differential equation (ODE) of C:

$$\frac{dC}{dt} = k_{pc}(H - C) \tag{6.26}$$

where k_{pc} is the time constant of pericyte constriction and $(H - C)$ is the fraction of pericytes that have energy impairments due to hypoxia but are not constricted or dead yet. Note that Eq. 6.26 is a reversible model in that more pericytes will constrict when

the tissue hypoxic fraction is greater than the pericyte constriction fraction, while the pericyte constriction will recover when the tissue hypoxic fraction is smaller than the pericyte constriction fraction due to thrombus extravasation.

The vessels blocked by microthrombi will be recanalised over time thanks to thrombus extravasation:

$$\frac{dB}{dt} = -k_e B \tag{6.27}$$

which is equivalent to the thrombus extravasation model (Eq. 5.1) when the initial blockage fraction is B_0.

Since there are currently no quantitative data on the pericyte death rate under ischaemia or hypoxia, the two model parameters were assumed here as $k_{pc} = 1 \times 10^{-4}$ 1/s and $k_e = 1 \times 10^{-4}$ 1/s only to study the model dynamical behaviour. The choice of these parameter values was also based on the assumption that pericyte constriction and thrombus extravasation happen at approximately the same time scale. Once more experimental data become available, the parameters governing the behaviour of pericyte constriction can be fitted easily with those data.

6.5.3 Results

With this model the fraction of vessels constricted by pericytes can be simulated under different initial blockage fractions as shown in Fig. 6.25. It is clear that there are two types of behaviours dependent on the initial condition of vessel blockage: recovery and dead (or irreversible damage). When the initial blockage fraction is below a certain threshold (around 10%), thrombus extravasation is the dominant mechanism over pericyte constriction which thus results in recovery. Conversely, the pericyte constriction dominates the process when the initial blockage fraction is greater than the threshold.

To further study these two types of dynamical behaviours and how different parameter values affect them, a critical blockage fraction ($B_{0,c}$) was defined as the threshold of initial

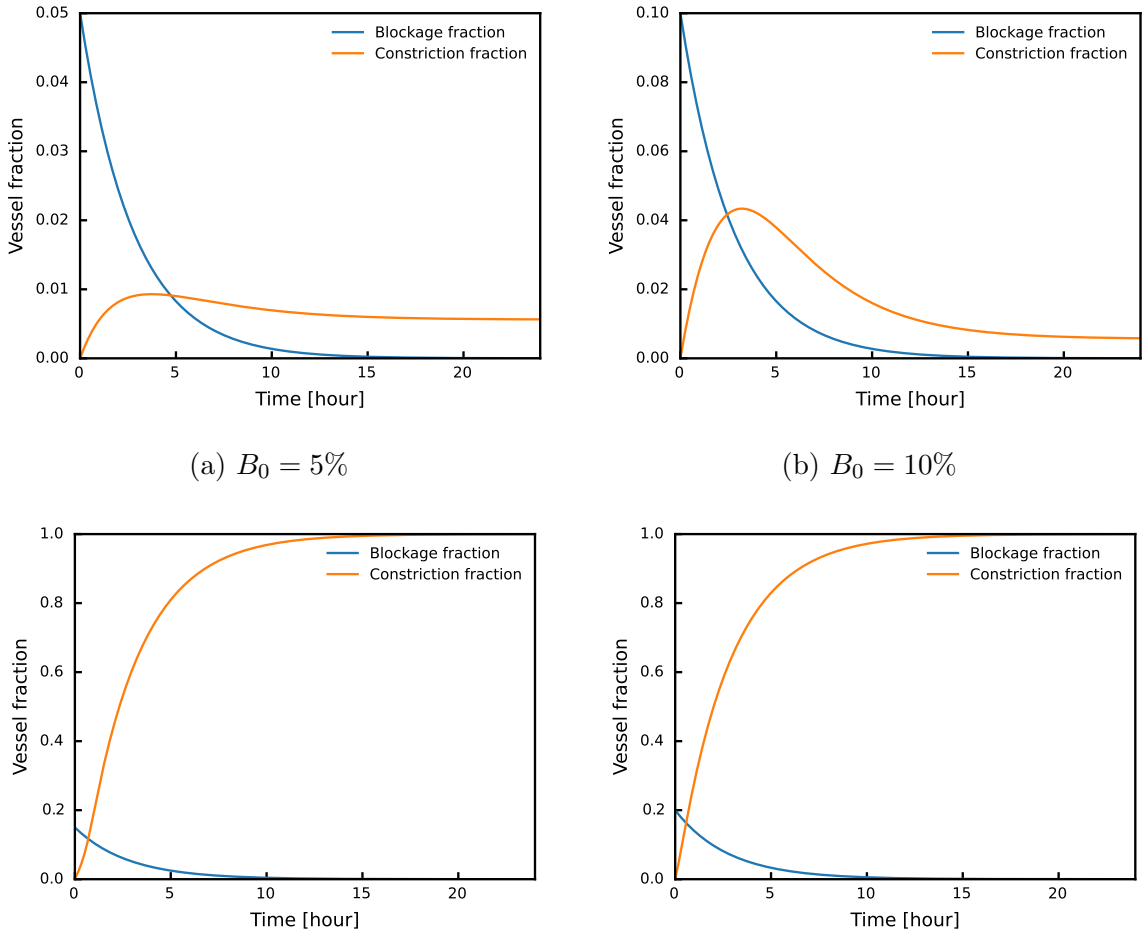

(a) $B_0 = 5\%$ (b) $B_0 = 10\%$

(c) $B_0 = 15\%$ (d) $B_0 = 20\%$

Figure 6.25: Pericyte constriction and vessel blockage fraction under different initial vessel blockage fraction.

blockage fraction that separates the final state of recovery or dead. Then the critical blockage fraction was simulated when the ratio of pericyte constriction time constant and thrombus extravasation time constant varied from 0.01 to 100 as shown in Fig. 6.26.

When k_{pc} is much larger than k_e, a small initial blockage fraction will lead to death. When k_e is much larger than k_{pc}, there will be no irreversible damage even though all vessels are occluded at the beginning, because the thrombus extravasation occurs much faster than the pericyte constriction. When k_{pc} and k_e are within one order of magnitude, $B_{0,c}$ has a non-linear relationship with k_{pc}/k_e. Note that $B_{0,c}$ is mostly in the range from

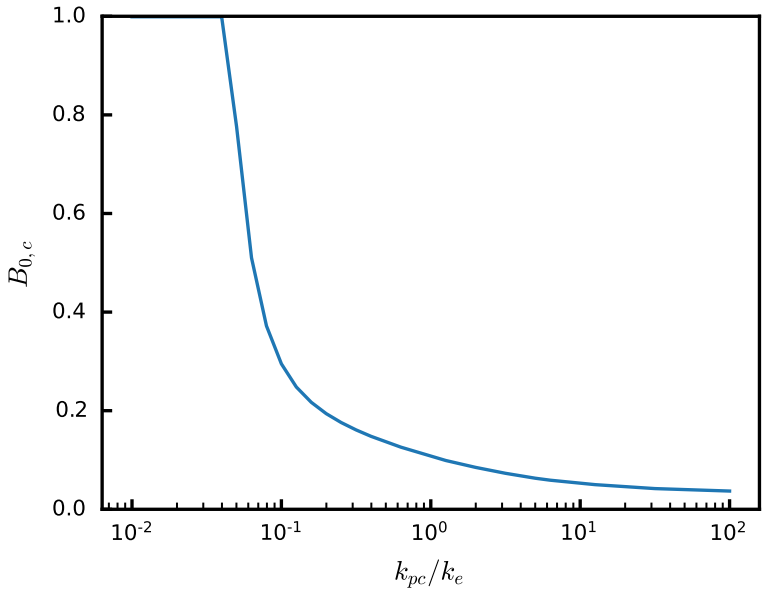

Figure 6.26: The critical blockage fraction when the ratio of pericyte constriction time constant and thrombus extravasation time constant is from 0.01 to 100.

0.1 to 0.2, when the pericyte constriction and the thrombus extravasation happen at the same time scale. The reason for this is that the hypoxic fraction, which drives the pericyte constriction, responses most sharply to the change in blockage fraction when it is between 10% and 20% (Fig. 3.6b). Hence a small change of initial blockage fraction in that range can result in a considerable change in tissue hypoxic fraction and thus a completely different model state in the end.

6.5.4 Discussion

The proposed model aims to simulate the brain tissue damage caused by pericyte constrictions, which will lead to capillary occlusions [135]. There are two types of dynamical behaviours of recovery and death, which are decided by the initial blockage fraction and the relative time scale between pericyte constriction and thrombus extravasation. Due to the lack of experimental data on pericyte death in ischaemia and hypoxia, the parameter fitting was replaced by a parametric study on how the different

time scales of pericyte constriction and thrombus extravasation can affect the model behaviour. This pericyte constriction model is thus left here as the basis for future development.

6.6 Comparison of the cell death models

Finally, this chapter will be concluded by a comparison of the 4 cell death models presented above as shown in Table 6.2. The inputs of these models are primarily perfusion and/or hypoxia that have been simulated using our existing models introduced in Chapters 2 and 3. Since these models only aim to simulate the primary pathological scenarios during an ischaemic stroke, the models are very concise and each of them has only a few variables and parameters. Most parameters have been fitted to experimental or clinical data, except for the storage-toxin model.

The toxin-based model and the pericyte model were built upon micro-scale simulations. As a result, these two models have a more physiological basis, but they are also heavily dependent upon the credibility of the simulation results in these micro-scale models (Chapter 4 can act as a quantitative validation of these models). Meanwhile, the other two models that build upon the relative perfusion results can be coupled with the organ-scale models more easily.

As shown in Table 6.2, all models are able to simulate the continued tissue damage after the perfusion is restored or the hypoxia is relieved. This improvement (from the model presented in the previous chapter) is due to the introduction of an additional parameter (toxin) that accumulates during the hypoxic or ischaemic stress and drives the tissue damage. This makes sure that the tissue damage will continue when the stress of energy shortage is eased by treatment. In addition to this, the models with more functions usually have more unknown parameters and they are also more complicated to be implemented in the existing workflow and validated. The storage-toxin model is most

	Toxin model	Storage-toxin model	Damage propagation model	Pericyte model
Input	Perfusion (hypoxia)	Relative perfusion	Relative perfusion	Blockage (hypoxia)
Variables	2	4	3	2
Model parameters	3	8	6	2
Fitted parameters	3	0	5	2
Additional parameters (derived from other simulations)	3	0	0	2
Continued tissue damage after treatment	Yes	Yes	Yes	Yes
Penumbra recovery	No	Yes	No	No
Core finally reaches 100%	No	Yes	No	Yes
Infarct expansion without treatment	No	No	Yes	No
Thresholds in the model	No	Yes	Yes	No
Identifying core and penumbra	No	Yes	No	No
Scaling perfusion between grey and white matters	Yes	No	No	N/A
Implemented in the INSIST project	Yes	No	Yes	No
Validation	Not yet	No	Not yet	No

Table 6.2: Comparison of the cell death models presented in Chapter 6.

suitable to investigate the penumbra formation and recovery. The damage propagation model is most appropriate to simulate the final infarct volume. The toxin model, however, is the simplest one to be implemented in an *in silico* trial of ischaemic stroke.

6.7 Conclusions

The primary aim of this chapter has been to develop a cell death model in order to simulate the cerebral tissue damage caused by an ischaemic stroke. Four cell death models were developed, bringing together the models and concepts presented in previous chapters. To the best of the author's knowledge, the toxin-based cell death model (Section 6.2) and the damage propagation model (Section 6.4) are the first cerebral cell death models that have been fitted to experimental data and implemented in realistic 3D brain geometries. These models promote the concept of this thesis of applying the current knowledge from animal stroke models to human research using mathematical models.

The cell death models presented in this chapter have different levels of functionality and thus complexity. They are able to predict the volumes and distributions of tissues in different states by coupling with the existing organ-scale brain models. The simulation results indicate that the treatment time has a significant impact on the final infarct volume, due to the accumulation of toxins in the ischaemic regions after the stroke onset. Using the current workflow of *in silico* trial of ischaemic stroke, these models will be able to simulate other scenarios with various patient characteristics and treatment types and their effects on the infarct volume and thus final clinical outcome.

Chapter 7

Conclusions and future work

7.1 Summary of the thesis

This thesis focused first on simulating oxygen transport from cerebral microvasculature to brain tissues under both healthy and micro-embolism conditions, before developing cell death models to understand the tissue damage responses to hypoxia. The cell death model was then further developed to simulate the tissue damage caused by ischaemic stroke.

7.1.1 Part I: Oxygen transport and microembolism at the micro-scale

In Chapter 3, the initial model was developed from the length scale of a capillary cube of hundreds of micrometres. Oxygen transport was simulated in these cubes representing the human cerebral microvasculature using a Green's function method. The oxygen transport results in these capillary cubes were found to be independent of the length scale above hundreds of micrometres and the specific microvascular geometry. Next, microvascular occlusions, for example as might be caused by clot fragments from an

unsuccessful thrombectomy, were simulated in a capillary cube. With the same boundary conditions, the reduction of perfusion was found to be proportional to the fraction of vessels blocked in the capillary network. However, the fraction of tissues that become hypoxic has a strongly non-linear relationship to the vessel blockage fraction, which could be fitted to a sigmoidal function. This relationship is of great importance, since it provides a quantitative description of hypoxic tissue responses to different levels of microthrombi occlusions, which can be estimated using the total microthrombi volume. An agreement between the microthrombi volume at the micro-scale and the thrombus volume at the macro-scale has been demonstrated by calculations based on the microvascular geometry.

Chapter 4 scaled up the oxygen transport simulations from the length scale of capillaries to a cortical column supplied by a penetrating arteriole. The cortical column model enabled the investigation of spatial correlation between the hypoxic regions and the occlusions in penetrating arteriole trees cause by microthrombi with a size of 25 μm. The spatial correlation was quantified by defining two distance metrics. Hence the simulation results and the animal data from our collaborators could be analysed by the same metrics and compared against each other. Distant hypoxic regions were observed in both simulations and experiments. These distal hypoxic regions were found to be caused by the hypoperfusion in the region downstream of the occlusion location in the penetrating arteriole. These findings complement previous research on the local tissue hypoxia caused by the occlusion of an entire penetrating arteriole and open up new directions for future work on quantifying the distant hypoxic regions.

Another notable result is a reasonable agreement of the spatial correlation between hypoxic regions and occlusion sites between simulations and experiments. This is the first study that provides a validation of the oxygen transport in cerebral microvasculature under pathological conditions. The validation suggests that the oxygen models in this thesis are suitable for investigating the response of brain tissue to micro-occlusions.

7.1.2 Part II: Tissue damage at the macro-scale

From Chapter 5 the focus of the work moved from the micro-scale to the macro-scale to simulate the hypoxic tissue damage caused by microthrombi occlusions. A novel 3-state cell death model was developed for this purpose. A thrombus extravasation model was also proposed to simulate the recanalisation of occluded vessels and thus the recovery of hypoxic tissues. The thrombus extravasation model was fitted to experimental data from a rodent model. Based on the sigmoidal relationship between hypoxic fraction and blockage fraction derived in Chapter 3, the cell viability for different levels of microvascular occlusions can be simulated over time. The final cell viability was found to be highly dependent on the initial microvascular blockage fraction, especially when the blockage fraction was between 10% and 20%.

In Chapter 6, the 3-state model was further developed to simulate the cerebral tissue damage caused by ischaemic stroke. Different types of cell death models were developed, some of which were built upon the micro-scale models developed in previous chapters and others were purely mechanistic. These models were fitted to experimental data from a monkey stroke model. The functionality of these models includes the simulation of continued tissue damage after treatment, penumbra recovery and tissue damage propagation. Coupled with organ-scale cerebral perfusion model, the cell death model is able to simulate the final infarct volume after an ischaemic stroke. The coupled computational models form the basis of an *in silico* trial of ischaemic stroke, which enables the study of effects of different treatment times and options on the final clinical outcomes of stroke patients.

7.2 Future work

7.2.1 Modelling microthrombi transport in the human brain

In Chapters 3 and 4, oxygen transport and micro-occlusions were simulated in cerebral microvascular networks. In these studies, it was assumed that each potential location had the same probability of being occluded by microthrombi, since there were no available microthrombi transport models in the (cerebral) microvasculature. This is a broad assumption that ignores the heterogeneous distribution of microthrombi and its impact on oxygen transport and tissue oxygenation. In another recent model of microemboli occlusions [29], microemboli transport was assumed to be purely based on the flow rate, i.e. the partition of microemboli at each vessel bifurcation was the same as flow rate partition. However, this partition law of microthrombi also lacks validation, especially given the fact that both flow condition and bifurcation geometry can have a significant impact on the partition of RBCs [121]. Considering the rapid development and remarkable progress of models of cerebral microcirculation and micro-occlusions [29, 108, 111, 193, 244], a model of microthrombi transport will be invaluable to these existing models and aid in their further applications. Through a one-year EPSRC Postdoctoral Research Associate position at the Mathematical Institute, this will be an immediate future research direction following the submission of this thesis.

The model will be built upon existing cerebral circulation models [27, 36, 37, 87] and thus have a similar multi-scale structure. The micro-scale simulations will be conducted using a lattice Boltzmann method (LBM) [103, 267], where the fluids will be simulated by LBM, the deformable microthrombi and RBCS by a finite element method and the fluid-structure interaction by an immersed boundary method [114]. This workflow has already been applied to recent RBC simulations [118, 119, 268, 269]. The new module required here is thus a mechanical model of microthrombi, which will be dependent on the volume fraction of RBCs in their compositions and built upon recent in vitro thrombus

experiments [50, 270, 271].

The micro-scale simulations of microthrombi transport will start from a single vessel bifurcation towards cerebral microvascular networks [27, 87]. To facilitate implementation of micro-scale simulations of microthrombi at the macro-scale, the micro-scale behaviours will be homogenised so that they can be represented by a continuum model of microthrombi permeability at the macro-scale. At the macro-scale (primarily arteries), the microthrombi transport will be assumed purely based on the blood flow, since the vessel diameter is much larger than the microthrombi size. The micro-scale model can be coupled with the macro-scale model in a similar way as the CBF coupling [257] to build a multi-scale microthrombi transport model for the full brain.

The validation of micro-scale models will be carried out against rodent experiments of microembolisation, which have already been used to validate the oxygen transport models in Chapter 4. In the new experiments, it will be possible to image the *in vivo* 3D microvasculature with the microthrombi locations within the rat brain. The simulations of microthrombi transport will be conducted in these networks, enabling a comparison between the simulated microthrombi and their *in vivo* locations.

The microthrombi simulations will be conducted in patient-specific brain models generated from the MR CLEAN dataset [4]. After microemboli shower due to an unsuccessful thrombectomy [272], the blood permeability of cerebral microvasculature will be affected in the territory where the microthrombi are present [29]. Therefore, the impact of microthrombi on cerebral perfusion, in terms of spatial distribution and heterogeneity, will be quantified and validated against the medical images from the MR CLEAN project [4].

Note that the developed microthrombi model can also be applied to other scenarios including the transport of contrast agents [273], drugs, platelets [274] and micro-bubbles in the human brain, broadening the applications of current brain models.

7.2.2 Homogenisation of the oxygen diffusion passing through cellular structures

As discussed in Chapter 2, most oxygen transport models treat brain tissue as a homogeneous medium. This is mainly due to the fact that oxygen can diffuse freely through cell membranes and intracellular structures, although a recent study has pointed out that there are multiple intracellular and extracellular pathways of oxygen diffusion [275]. On the other hand, however, the oxygen sinks in the brain tissue are primarily isolated mitochondria (with a size at the length scale of 1 μm [276] and a volume fraction of a few percents [277]), the distribution of which is highly heterogeneous.

The homogenisation theory for blood flow and oxygen transport through microvascular networks has been developed in previous studies [59]. This theory has been applied in the human brain microvasculature to homogenise the blood flow [27] and oxygen transport [92, 278] to scale up the models from the length scale of inter-capillary distance ~ 50 μm to the length scale of an imaging pixel $\sim$ 1 mm. Since these models are built above the length scale of tens of micrometres, these models also treat the brain tissue as a homogeneous medium for oxygen diffusion.

An interesting future activity would be to incorporate the cellular scale ~ 1 μm into the existing models and examine whether the effects of isolated sinks can be homogenised at the middle length scale of 50 μm or the largest length scale of 1 mm, especially when the oxygen transport is governed by diffusion and metabolism (low Pe). This analysis will be invaluable to future studies of oxygen transport.

There are recent studies on the homogenisation of transport past isolated sinks with various strengths [279]; randomly distributed isolated sinks in 1D [280] and 2D/3D [281]. These works use a Green's function to describe the sinks and provide a theoretical starting point. From an engineering point of view, this problem can also be investigated by

solving the 3D diffusion equations in a Krogh cylinder model or a capillary cube [27] with continuum sinks and isolated sinks mimicking the sizes and distributions of mitochondria, and then comparing the simulation results between the two.

7.2.3 Effects of ageing on oxygen transport

Ageing has a significant impact on cerebral vasculature and blood flow [282–284]. The effects of ageing on cerebral microvasculature have been quantified in a recent study by Graff et al. [285], where the ageing networks were found to have reduced permeability and thus more vulnerable to micro-occlusions. A next step combining the Graff model [285] and the model from Chapter 3 of this thesis could be to examine oxygen transport in these ageing networks using the Green's function method [144]. Another future direction would be simulating oxygen transport and micro-occlusions in ageing cortical columns using the same workflow and distance analyses as presented in Chapter 4, and validating the spatial relationship between tissue hypoxia and occlusion sites against the microembolisation models of ageing rats.

7.2.4 Time-dependent Green's function methods

In Section 6.4, the possibilities of using a time-dependent Green's function method on toxin diffusion problems were discussed. However, a more straightforward application of such method would be in oxygen transport and drug delivery simulations. The theory for these problems has been developed in [263] and the simulation codes have been published online. The periodic capillary cubes [27] will minimise the effects of boundary conditions on simulation results, which will thus be preferential candidates to carry out these simulations. The dynamic responses of tissue oxygenation to changes in flow and metabolism in these 3D cerebral networks will add to the existing knowledge of these obtained by 2D network models [94].

7.2.5 Sensitivity analysis of model parameters

The oxygen transport simulation results presented in Chapters 3 and 4 depend on the parameter values in mathematical models and numerical schemes. The validity of simulation results and related conclusions highly depends on the robustness of the choice and estimation of these parameters. A sensitivity analysis study of these parameter values will thus enhance the credibility of simulation results and provide a foundation for uncertainty quantification and validation. In addition, such analysis will improve our understanding of the applicability of the proposed models. For example, the sensitivity of oxygen transport simulations to changes in CBF and $CMRO_2$ will affect the applicability of the models to different states (e.g. stimulation/no stimulation) and brain regions of the subject, respectively [286]. A sensitivity analysis of cerebral perfusion model [47] has recently been conducted, where the effects of changes in physiological and numerical parameters on simulated brain perfusion and infarct volume (estimated purely based on a threshold of perfusion value) were investigated. Sensitivity studies of cerebral oxygen transport and tissue damage models can be carried out in a similar way.

7.2.6 Experiments for model parameter fitting and validation

Parameter fitting is usually the most challenging step when developing a mathematical model. Several models in this thesis have not been fitted to experimental or clinical data, which limits the application of these models. The difficulty is mainly due to the imbalance between the large number of parameters and the poor temporal and spatial resolution of experimental data. Suggestions for future experiments are thus listed below to aid in fitting and validating the models presented in this thesis.

An experiment that quantifies the brain cell viability at different times under different perfusion values will be extremely useful in fitting the parameters of the cell death models and further developing these models. As reviewed in Chapter 2, Garcia et al. [65] counted

the percentage of neurons in intact, ischaemic and necrotic states under ischaemia at different times in the rat brain, however, this study lacks information about perfusion that is a major model input. Conversely, Jones et al. [64] measured the perfusion value under ischaemia in the monkey brain, but the authors only categorised the tissue viability as alive or dead with poor temporal resolutions. An experiment combining the merits of these two experiments will provide ideal data for the cell death models. In addition, more data points in the first few hours after ischaemia, when the core formation happens, will be extremely helpful to fit the parameters of rate constants.

The thrombus extravasation model was fitted to only 4 data points (including one representing fully healthy state at day 0) from an experimental study using a rodent model of microembolism [53] as shown in Fig. 5.1. A future experimental study of thrombus extravasation with more temporal data points will refine current parameter fitting of the thrombus extravasation model. In addition, another recent study showed that occlusions at the capillary scale could be recanalised on the time scale of hours, if the vessels were occluded by smaller microspheres [190]. It will be interesting to investigate the effects of microthrombi size on the time scale of their extravasation, if such data will be available in future experiments. The proposed model (Eq. 5.1) can be adjusted accordingly by expressing k_e as a function of thrombus size.

The roles of pericytes in both regulating blood flow in health and disturbing re-perfusion in cerebrovascular diseases have been increasingly appreciated [73, 135]. In Section 6.5, a tissue damage model based on pericyte constriction and dying has been presented. An experimental study of fraction of pericyte viability at different times under different perfusion values will enable the parameter fitting and validation of the proposed model. Future experimental work on measuring changes in capillary diameter constricted by pericytes over time under different perfusion values will allow development of more detailed models of pericyte constriction and its effects on tissue damage. The possibility to carry out such experiments and modelling work has been highlighted by a recent study

on monitoring and modelling the capillary dilation induced by pericytes after the stimulus of calcium ions [136].

7.3 Concluding remarks

The human brain has a highly complicated circulatory system. Therefore, it is not surprising that its structure and function remain poorly understood. In this thesis, new mathematical models have been created and applied to aid in understanding the key roles of cerebral circulation in maintaining oxygen transport and tissue health in a quantitative manner. These models improve current understanding of brain physiology, broaden the application of brain models in *in silico* trials and open up new collaborations between engineers, biologists, clinicians and mathematicians in brain research. However, it is clear that current brain models are still far from what would be required to build a fully virtual representation of cerebral blood flow and metabolism, where various physiological and pathological mechanisms should be considered at the same time across multiple length and time scales. In another word, modelling the human brain will be an active and exciting field until this goal is finally achieved.

Bibliography

[1] Payne SJ. Cerebral blood flow and metabolism: A quantitative approach. New Jersey: WORLD SCIENTIFIC; 2017.

[2] Duvernoy HM, Delon S, Vannson JL. Cortical blood vessels of the human brain. Brain Research Bulletin. 1981;7(5):519–579. doi:10.1016/0361-9230(81)90007-1.

[3] Office for National Statistics. Leading causes of death, UK: 2001 to 2018; 2020. https://www.ons.gov.uk/peoplepopulationandcommunity/healthandsocialcare/causesofdeath/articles/leadingcausesofdeathuk/latest#toc.

[4] Berkhemer OA, Fransen PSS, Beumer D, Van Den Berg LA, Lingsma HF, Yoo AJ, et al. A randomized trial of intraarterial treatment for acute ischemic stroke. New England Journal of Medicine. 2015;372(1):11–20. doi:10.1056/NEJMoa1411587.

[5] Patel A, Berdunov V, Quayyum Z, King D, Knapp M, Wittenberg R. Estimated societal costs of stroke in the UK based on a discrete event simulation. Age and Ageing. 2020;49:270–276. doi:10.1093/ageing/afz162.

[6] Viceconti M, Henney A, Morley-Fletcher E. In silico clinical trials: how computer simulation will transform the biomedical industry. International Journal of Clinical Trials. 2016;3:37. doi:10.18203/2349-3259.ijct20161408.

[7] Hunter PJ, Borg TK. Integration from proteins to organs: the Physiome Project. Nature Reviews Molecular Cell Biology. 2003;4:237–243. doi:10.1038/nrm1054.

[8] Viceconti M, Hunter P. The Virtual Physiological Human: Ten Years

After. Annual Review of Biomedical Engineering. 2016;18:103–123. doi:10.1146/annurev-bioeng-110915-114742.

[9] Steinman DA. Image-Based Computational Fluid Dynamics Modeling in Realistic Arterial Geometries. Annals of Biomedical Engineering. 2002;30:483–497. doi:10.1114/1.1467679.

[10] Peirlinck M, Costabal FS, Yao J, Guccione JM, Tripathy S, Wang Y, et al. Precision medicine in human heart modeling. Biomechanics and Modeling in Mechanobiology. 2021;20:803–831. doi:10.1007/s10237-021-01421-z.

[11] De Backer JW, Vos WG, Gorlé CD, Germonpré P, Partoens B, Wuyts FL, et al. Flow analyses in the lower airways: Patient-specific model and boundary conditions. Medical Engineering & Physics. 2008;30:872–879. doi:10.1016/j.medengphy.2007.11.002.

[12] Lauzeral N, Borzacchiello D, Kugler M, George D, Rémond Y, Hostettler A, et al. A model order reduction approach to create patient-specific mechanical models of human liver in computational medicine applications. Computer Methods and Programs in Biomedicine. 2019;170:95–106. doi:10.1016/j.cmpb.2019.01.003.

[13] Poelert S, Valstar E, Weinans H, Zadpoor AA. Patient-specific finite element modeling of bones. Proceedings of the Institution of Mechanical Engineers, Part H: Journal of Engineering in Medicine. 2013;227:464–478. doi:10.1177/0954411912467884.

[14] Filipovic N, Rosic M, Tanaskovic I, Milosevic Z, Nikolic D, Zdravkovic N, et al. ARTreat Project: Three-Dimensional Numerical Simulation of Plaque Formation and Development in the Arteries. IEEE Transactions on Information Technology in Biomedicine. 2012;16:272–278. doi:10.1109/TITB.2011.2168418.

[15] Cebral JR, Castro MA, Appanaboyina S, Putman CM, Millan D, Frangi AF. Efficient pipeline for image-based patient-specific analysis of cerebral aneurysm hemodynamics: technique and sensitivity. IEEE Transactions on Medical Imaging. 2005;24:457–467. doi:10.1109/TMI.2005.844159.

[16] Luraghi G, Bridio S, Matas JFR, Dubini G, Boodt N, Gijsen FJH, et al. The first virtual patient-specific thrombectomy procedure. Journal of Biomechanics. 2021;126:110622. doi:10.1016/j.jbiomech.2021.110622.

[17] Morales HG, Larrabide I, Geers AJ, Aguilar ML, Frangi AF. Newtonian and non-Newtonian blood flow in coiled cerebral aneurysms. Journal of Biomechanics. 2013;46:2158–2164. doi:10.1016/j.jbiomech.2013.06.034.

[18] Goriely A, Geers MGD, Holzapfel GA, Jayamohan J, Jérusalem A, Sivaloganathan S, et al. Mechanics of the brain: perspectives, challenges, and opportunities. Biomechanics and Modeling in Mechanobiology. 2015;14:931–965. doi:10.1007/s10237-015-0662-4.

[19] Mardal KA, Rognes ME, Thompson TB, Valnes LM. Mathematical Modeling of the Human Brain: From Magnetic Resonance Images to Finite Element Simulation. vol. 10. Springer International Publishing; 2022.

[20] Cloutier M, Bolger FB, Lowry JP, Wellstead P. An integrative dynamic model of brain energy metabolism using in vivo neurochemical measurements. Journal of Computational Neuroscience. 2009;27:391–414. doi:10.1007/s10827-009-0152-8.

[21] Orlowski P, Chappell M, Park CS, Grau V, Payne S. Modelling of pH dynamics in brain cells after stroke. Interface Focus. 2011;1:408–416. doi:10.1098/rsfs.2010.0025.

[22] Jolivet R, Coggan JS, Allaman I, Magistretti PJ. Multi-timescale Modeling of Activity-Dependent Metabolic Coupling in the Neuron-Glia-Vasculature Ensemble. PLOS Computational Biology. 2015;11:1–23. doi:10.1371/journal.pcbi.1004036.

[23] Cassot F, Lauwers F, Fouard C, Prohaska S, Lauwers-Cances V. A novel three-dimensional computer-assisted method for a quantitative study of microvascular networks of the human cerebral cortex. Microcirculation. 2006;13(1):1–18. doi:10.1080/10739680500383407.

[24] Lauwers F, Cassot F, Lauwers-Cances V, Puwanarajah P, Duvernoy H. Morphometry of the human cerebral cortex microcirculation: General

characteristics and space-related profiles. NeuroImage. 2008;39(3):936–948. doi:10.1016/j.neuroimage.2007.09.024.

[25] Linninger AA, Gould IG, Marinnan T, Hsu CY, Chojecki M, Alaraj A. Cerebral microcirculation and oxygen tension in the human secondary cortex. Annals of Biomedical Engineering. 2013;41(11):2264–2284. doi:10.1007/s10439-013-0828-0.

[26] Lorthois S, Lauwers F, Cassot F. Tortuosity and other vessel attributes for arterioles and venules of the human cerebral cortex. Microvascular Research. 2014;91:99–109. doi:10.1016/j.mvr.2013.11.003.

[27] El-Bouri WK, Payne SJ. Multi-scale homogenization of blood flow in 3-dimensional human cerebral microvascular networks. Journal of Theoretical Biology. 2015;380:40–47. doi:10.1016/j.jtbi.2015.05.011.

[28] El-Bouri WK, Payne SJ. Investigating the effects of a penetrating vessel occlusion with a multi-scale microvasculature model of the human cerebral cortex. NeuroImage. 2018;172(January):94–106. doi:10.1016/j.neuroimage.2018.01.049.

[29] El-Bouri WK, MacGowan A, Józsa TI, Gounis MJ, Payne SJ. Modelling the impact of clot fragmentation on the microcirculation after thrombectomy. PLOS Computational Biology. 2021;17(3):1–25. doi:10.1371/journal.pcbi.1008515.

[30] Vardakis JC, Chou D, Tully BJ, Hung CC, Lee TH, Tsui PH, et al. Investigating cerebral oedema using poroelasticity. Medical Engineering & Physics. 2016;38:48–57. doi:10.1016/j.medengphy.2015.09.006.

[31] Garcia-Gonzalez D, Jayamohan J, Sotiropoulos SN, Yoon SH, Cook J, Siviour CR, et al. On the mechanical behaviour of PEEK and HA cranial implants under impact loading. Journal of the Mechanical Behavior of Biomedical Materials. 2017;69:342–354. doi:10.1016/j.jmbbm.2017.01.012.

[32] Weickenmeier J, Jucker M, Goriely A, Kuhl E. A physics-based model explains the prion-like features of neurodegeneration in Alzheimer's disease, Parkinson's disease, and amyotrophic lateral sclerosis. Journal of the Mechanics and Physics of Solids. 2019;124:264–281. doi:10.1016/j.jmps.2018.10.013.

[33] Bing Y, Garcia-Gonzalez D, Voets N, Jérusalem A. Medical imaging based in silico head model for ischaemic stroke simulation. Journal of the Mechanical Behavior of Biomedical Materials. 2020;101:103442. doi:10.1016/j.jmbbm.2019.103442.

[34] Ii S, Kitade H, Ishida S, Imai Y, Watanabe Y, Wada S. Multiscale modeling of human cerebrovasculature: A hybrid approach using image-based geometry and a mathematical algorithm. PLOS Computational Biology. 2020;16:e1007943. doi:10.1371/journal.pcbi.1007943.

[35] Guo L, Vardakis JC, Chou D, Ventikos Y. A multiple-network poroelastic model for biological systems and application to subject-specific modelling of cerebral fluid transport. International Journal of Engineering Science. 2020;147:103204. doi:10.1016/j.ijengsci.2019.103204.

[36] Józsa TI, Padmos RM, Samuels N, El-Bouri WK, Hoekstra AG, Payne SJ. A porous circulation model of the human brain for in silico clinical trials in ischaemic stroke. Interface Focus. 2021;11(1):20190127. doi:10.1098/rsfs.2019.0127.

[37] Padmos RM, Józsa TI, El-Bouri WK, Konduri PR, Payne SJ, Hoekstra AG. Coupling one-dimensional arterial blood flow to three-dimensional tissue perfusion models for in silico trials of acute ischaemic stroke. Interface Focus. 2021;11(1):20190125. doi:10.1098/rsfs.2019.0125.

[38] Li X, Zhou Z, Kleiven S. An anatomically detailed and personalizable head injury model: Significance of brain and white matter tract morphological variability on strain. Biomechanics and Modeling in Mechanobiology. 2021;20:403–431. doi:10.1007/s10237-020-01391-8.

[39] Payne S. Cerebral Autoregulation: Control of Blood Flow in the Brain. Cham: Springer International Publishing; 2016.

[40] Orlowski P, O'Neill D, Grau V, Ventikos Y, Payne S. Modelling of the physiological response of the brain to ischaemic stroke. Interface Focus. 2013;3. doi:10.1098/rsfs.2012.0079.

[41] Orlowski P, McConnell FK, Payne S. A mathematical model of cellular metabolism

during ischemic stroke and hypothermia. IEEE Transactions on Biomedical Engineering. 2014;61:484–490. doi:10.1109/TBME.2013.2282603.

[42] Mohamed Mokhtarudin MJ, Payne SJ. Mathematical model of the effect of ischemia-reperfusion on brain capillary collapse and tissue swelling. Mathematical Biosciences. 2015;263:111–120. doi:10.1016/j.mbs.2015.02.011.

[43] Mohamed Mokhtarudin MJ, Payne SJ. The study of the function of AQP4 in cerebral ischaemia-reperfusion injury using poroelastic theory. International Journal for Numerical Methods in Biomedical Engineering. 2017;33:e02784. doi:10.1002/cnm.2784.

[44] Konduri PR, Marquering HA, van Bavel EE, Hoekstra A, Majoie CBLM. In-Silico Trials for Treatment of Acute Ischemic Stroke. Frontiers in Neurology. 2020;11:1–8. doi:10.3389/fneur.2020.558125.

[45] Petkantchin R, Padmos R, Boudjeltia KZ, Raynaud F, Chopard B. Thrombolysis: Observations and numerical models. Journal of Biomechanics. 2022;132:110902. doi:10.1016/j.jbiomech.2021.110902.

[46] Luraghi G, Matas JFR, Dubini G, Berti F, Bridio S, Duffy S, et al. Applicability assessment of a stent-retriever thrombectomy finite-element model. Interface Focus. 2021;11:20190123. doi:10.1098/rsfs.2019.0123.

[47] Józsa TI, Padmos RM, El-Bouri WK, Hoekstra AG, Payne SJ. On the Sensitivity Analysis of Porous Finite Element Models for Cerebral Perfusion Estimation. Annals of Biomedical Engineering. 2021;49:3647–3665. doi:10.1007/s10439-021-02808-w.

[48] Padmos RM, Terreros NA, Józsa TI, Závodszky G, Marquering HA, Majoie CBLM, et al. Modelling the leptomeningeal collateral circulation during acute ischaemic stroke. Medical Engineering & Physics. 2021;91:1–11. doi:10.1016/j.medengphy.2021.03.003.

[49] Boodt N, Compagne KCJ, Dutra BG, Samuels N, Tolhuisen ML, Alves HCBR, et al. Stroke Etiology and Thrombus Computed Tomography

Characteristics in Patients With Acute Ischemic Stroke. Stroke. 2020;51:1727–1735. doi:10.1161/STROKEAHA.119.027749.

[50] Boodt N, van Schauburg PRWS, Hund HM, Fereidoonnezhad B, McGarry JP, Akyildiz AC, et al. Mechanical Characterization of Thrombi Retrieved With Endovascular Thrombectomy in Patients With Acute Ischemic Stroke. Stroke. 2021;52:2510–2517. doi:10.1161/STROKEAHA.120.033527.

[51] Arrarte Terreros N, van Willigen BG, Niekolaas WS, Tolhuisen ML, Brouwer J, Coutinho JM, et al. Occult blood flow patterns distal to an occluded artery in acute ischemic stroke. Journal of Cerebral Blood Flow & Metabolism. 2022;42:292–302. doi:10.1177/0271678X211044941.

[52] Arrarte Terreros N, Bruggeman AAE, van Voorst H, Konduri PR, Jansen IGH, Kappelhof M, et al. Bifurcation occlusions and endovascular treatment outcome in acute ischemic stroke. Journal of NeuroInterventional Surgery. 2022; p. neurintsurg–2021–018560. doi:10.1136/neurintsurg-2021-018560.

[53] van der Wijk AE, Lachkar N, de Vos J, Grootemaat AE, van der Wel NN, Hordijk PL, et al. Extravasation of Microspheres in a Rat Model of Silent Brain Infarcts. Stroke. 2019;50(6):1590–1594. doi:10.1161/STROKEAHA.119.024975.

[54] van der Wijk AE, Georgakopoulou T, Majolée J, van Bezu JSM, van der Stoel MM, van het Hof BJ, et al. Microembolus clearance through angiophagy is an auxiliary mechanism preserving tissue perfusion in the rat brain. Acta Neuropathologica Communications. 2020;8(1):1–14. doi:10.1186/s40478-020-01071-9.

[55] Georgakopoulou T, van der Wijk AE, Bakker ENTP, VanBavel E. Recovery of Hypoxic Regions in a Rat Model of Microembolism. Journal of Stroke and Cerebrovascular Diseases. 2021;30(6):105739. doi:10.1016/j.jstrokecerebrovasdis.2021.105739.

[56] Georgakopoulou T, van der Wijk AE, N T P Bakker E, VanBavel E, Majoie C, Marquering H, et al. Quantitative 3D Analysis of Tissue Damage in a Rat Model

of Microembolization. Journal of Biomechanics. 2021;128(September):110723. doi:10.1016/j.jbiomech.2021.110723.

[57] Migliavacca F, Luraghi G, Akyildiz AC, Gijsen FJH. Thrombus mechanics: How can we contribute to improve diagnostics and treatment? Journal of Biomechanics. 2022;132:110935. doi:10.1016/j.jbiomech.2021.110935.

[58] Dirnagl U, Iadecola C, Moskowitz MA. Pathobiology of ischaemic stroke: An integrated view. Trends in Neurosciences. 1999;22:391–397. doi:10.1016/S0166-2236(99)01401-0.

[59] Shipley RJ, Chapman SJ. Multiscale modelling of fluid and drug transport in vascular tumours. Bulletin of Mathematical Biology. 2010;72(6):1464–1491. doi:10.1007/s11538-010-9504-9.

[60] Chueh JY, Puri AS, Wakhloo AK, Gounis MJ. Risk of distal embolization with stent retriever thrombectomy and ADAPT. Journal of NeuroInterventional Surgery. 2016;8(2):197–202. doi:10.1136/neurintsurg-2014-011491.

[61] Ames A, Wright RL, Kowada M, Thurston JM, Majno G. Cerebral ischemia. II. The no-reflow phenomenon. American Journal of Pathology. 1968;52(2):437–453.

[62] Kloner RA, King KS, Harrington MG. No-reflow phenomenon in the heart and brain. American Journal of Physiology - Heart and Circulatory Physiology. 2018;315(3):H550–H562. doi:10.1152/ajpheart.00183.2018.

[63] Heiss Wosner G. Functional recovery of cortical neurons as related to degree and duration of ischemia. Annals of Neurology. 1983;14:294–301. doi:10.1002/ana.410140307.

[64] Jones TH, Morawetz RB, Crowell RM, Marcoux FW, FitzGibbon SJ, DeGirolami U, et al. Thresholds of focal cerebral ischemia in awake monkeys. Journal of Neurosurgery. 1981;54:773–782. doi:10.3171/jns.1981.54.6.0773.

[65] Garcia JH, Liu KF, Ho KL. Neuronal Necrosis After Middle Cerebral Artery Occlusion in Wistar Rats Progresses at Different Time Intervals

in the Caudoputamen and the Cortex. Stroke. 1995;26:636–643. doi:10.1161/01.STR.26.4.636.

[66] Astrup J, Siesjö BK, Symon L. Thresholds in cerebral ischemia - the ischemic penumbra. Stroke. 1981;12:723–725. doi:10.1161/01.STR.12.6.723.

[67] Alpers BJ, Berry RG, Paddison RM. Anatomical Studies of the Circle of Willis in Normal Brain. Archives of Neurology And Psychiatry. 1959;81(4):409–418. doi:10.1001/archneurpsyc.1959.02340160007002.

[68] Riggs HE, Rupp C. Variation in Form of Circle of Willis: The Relation of the Variations to Collateral Circulation: Anatomic Analysis. Archives of Neurology. 1963;8(1):8–14. doi:10.1001/archneur.1963.00460010024002.

[69] Papantchev V, Stoinova V, Aleksandrov A, Todorova-Papantcheva D, Hristov S, Petkov D, et al. The role of Willis circle variations during unilateral selective cerebral perfusion: a study of 500 circles. European Journal of Cardio-Thoracic Surgery. 2013;44:743–753. doi:10.1093/ejcts/ezt103.

[70] Boers AMM, Jansen IGH, Berkhemer OA, Yoo AJ, Lingsma HF, Slump CH, et al. Collateral status and tissue outcome after intra-arterial therapy for patients with acute ischemic stroke. Journal of Cerebral Blood Flow & Metabolism. 2017;37:3589–3598. doi:10.1177/0271678X16678874.

[71] Openstax. Anatomy and Physiology; 2020. `https://openstax.org/books/anatomy-and-physiology`.

[72] Bollmann S, Mattern H, Bernier M, Robinson SD, Park D, Speck O, et al. Imaging of the pial arterial vasculature of the human brain in vivo using high-resolution 7T time-of-flight angiography. eLife. 2022;11. doi:10.7554/eLife.71186.

[73] Hartmann DA, Coelho-Santos V, Shih AY. Pericyte Control of Blood Flow Across Microvascular Zones in the Central Nervous System. Annual Review of Physiology. 2022;84:1–24. doi:10.1146/annurev-physiol-061121-040127.

[74] Nishimura N, Schaffer CB, Friedman B, Lyden PD, Kleinfeld D. Penetrating

arterioles are a bottleneck in the perfusion of neocortex. Proceedings of the National Academy of Sciences. 2007;104(1):365–370. doi:10.1073/pnas.0609551104.

[75] Nishimura N, Rosidi NL, Iadecola C, Schaffer CB. Limitations of collateral flow after occlusion of a single cortical penetrating arteriole. Journal of Cerebral Blood Flow & Metabolism. 2010;30(12):1914–1927. doi:10.1038/jcbfm.2010.157.

[76] Shih AY, Blinder P, Tsai PS, Friedman B, Stanley G, Lyden PD, et al. The smallest stroke: Occlusion of one penetrating vessel leads to infarction and a cognitive deficit. Nature Neuroscience. 2013;16(1):55–63. doi:10.1038/nn.3278.

[77] Sakadžić S, Mandeville ET, Gagnon L, Musacchia JJ, Yaseen MA, Yucel MA, et al. Large arteriolar component of oxygen delivery implies a safe margin of oxygen supply to cerebral tissue. Nature Communications. 2014;5(1):5734. doi:10.1038/ncomms6734.

[78] Ji X, Ferreira T, Friedman B, Liu R, Liechty H, Bas E, et al. Brain microvasculature has a common topology with local differences in geometry that match metabolic load. Neuron. 2021; p. 1–20. doi:10.1016/j.neuron.2021.02.006.

[79] Cassot F, Lauwers F, Lorthois S, Puwanarajah P, Cances-Lauwers V, Duvernoy H. Branching patterns for arterioles and venules of the human cerebral cortex. Brain Research. 2010;1313:62–78. doi:10.1016/j.brainres.2009.12.007.

[80] Clark ME, Himwich WA, Martin JD. A Comparative Examination of Cerebral Circulation Models. Journal of Neurosurgery. 1968;29:484–494. doi:10.3171/jns.1968.29.5.0484.

[81] Cebral JR, Yim PJ, Löhner R, Soto O, Choyke PL. Blood Flow Modeling in Carotid Arteries with Computational Fluid Dynamics and MR Imaging. Academic Radiology. 2002;9:1286–1299. doi:10.1016/S1076-6332(03)80562-7.

[82] Chen L, Mossa-Basha M, Balu N, Canton G, Sun J, Pimentel K, et al. Development of a quantitative intracranial vascular features extraction tool on 3DMRA using semiautomated open-curve active contour vessel tracing. Magnetic Resonance in Medicine. 2018;79:3229–3238. doi:10.1002/mrm.26961.

[83] Walsh CL, Tafforeau P, Wagner WL, Jafree DJ, Bellier A, Werlein C, et al. Imaging intact human organs with local resolution of cellular structures using hierarchical phase-contrast tomography. Nature Methods. 2021;18:1532–1541. doi:10.1038/s41592-021-01317-x.

[84] Pudney C. Distance-Ordered Homotopic Thinning: A Skeletonization Algorithm for 3D Digital Images. Computer Vision and Image Understanding. 1998;72:404–413. doi:10.1006/cviu.1998.0680.

[85] Pries AR, Neuhaus D, Gaehtgens P. Blood viscosity in tube flow: dependence on diameter and hematocrit. American Journal of Physiology-Heart and Circulatory Physiology. 1992;263:H1770–H1778. doi:10.1152/ajpheart.1992.263.6.H1770.

[86] Kassab GS, Rider CA, Tang NJ, Fung YC. Morphometry of pig coronary arterial trees. American Journal of Physiology-Heart and Circulatory Physiology. 1993;265:H350–H365. doi:10.1152/ajpheart.1993.265.1.H350.

[87] El-Bouri WK, Payne SJ. A statistical model of the penetrating arterioles and venules in the human cerebral cortex. Microcirculation. 2016;23(7):580–590. doi:10.1111/micc.12318.

[88] Su SW. Modelling blood flow and oxygen transport in the human cerebral cortex. University of Oxford; 2012.

[89] Su SW, Catherall M, Payne S. The Influence of Network Structure on the Transport of Blood in the Human Cerebral Microvasculature. Microcirculation. 2012;19(2):175–187. doi:10.1111/j.1549-8719.2011.00148.x.

[90] Blinder P, Tsai PS, Kaufhold JP, Knutsen PM, Suhl H, Kleinfeld D. The cortical angiome: an interconnected vascular network with noncolumnar patterns of blood flow. Nature Neuroscience. 2013;16:889–897. doi:10.1038/nn.3426.

[91] Lorthois S, Cassot F, Lauwers F. Simulation study of brain blood flow regulation by intra-cortical arterioles in an anatomically accurate large human vascular network: Part I: Methodology and baseline flow. NeuroImage. 2011;54:1031–1042. doi:10.1016/j.neuroimage.2010.09.032.

[92] El-Bouri WK. Multi-Scale Modelling of the Microvasculature in the Human Cerebral Cortex. University of Oxford; 2017.

[93] Boas DA, Jones SR, Devor A, Huppert TJ, Dale AM. A vascular anatomical network model of the spatio-temporal response to brain activation. NeuroImage. 2008;40(3):1116–1129. doi:10.1016/j.neuroimage.2007.12.061.

[94] Payne SJ, Lucas C. Oxygen delivery from the cerebral microvasculature to tissue is governed by a single time constant of approximately 6 seconds. Microcirculation. 2018;25(2):e12428. doi:10.1111/micc.12428.

[95] Formaggia L, Quarteroni A, Veneziani A, editors. Cardiovascular Mathematics: Modeling and Simulation of the Circulatory System. 9. Milano: Springer Milan; 2009.

[96] Secomb TW. Blood Flow in the Microcirculation. Annual Review of Fluid Mechanics. 2017;49(1):443–461. doi:10.1146/annurev-fluid-010816-060302.

[97] Casson N. A flow equation for pigment-oil suspensions of printing ink type. In: Rheology of Disperse Systems. London, UK: Pergamon; 1959. p. 84–102.

[98] Fåhræus R, Lindqvist T. The viscosity of the blood in narrow capillary tubes. American Journal of Physiology-Legacy Content. 1931;96(3):562–568. doi:10.1152/ajplegacy.1931.96.3.562.

[99] Gerbstädt H, Vogtmann C, Rüth P, Schöntube E. The apparent viscosity of blood in glass capillaries of the smallest diameter. Die Naturwissenschaften. 1966;53(20):526–526.

[100] Gaehtgens P. Flow of blood through narrow capillaries: Rheological mechanisms determining capillary hematocrit and apparent viscosity1. Biorheology. 1980;17:183–189. doi:10.3233/BIR-1980-171-220.

[101] Pries AR, Secomb TW, Geßner T, Sperandio MB, Gross JF, Gaehtgens P. Resistance to blood flow in microvessels in vivo. Circulation Research. 1994;75:904–915. doi:10.1161/01.RES.75.5.904.

[102] Pries AR, Secomb TW. Microvascular blood viscosity in vivo and the endothelial surface layer. American Journal of Physiology - Heart and Circulatory Physiology. 2005;289:2657–2664. doi:10.1152/ajpheart.00297.2005.

[103] Krüger T, Kusumaatmaja H, Kuzmin A, Shardt O, Silva G, Viggen EM. The lattice Boltzmann method : principles and practice [electronic resource]. Switzerland: Springer; 2016.

[104] Pries AR, Secomb TW, Gaehtgens P, Gross JF. Blood flow in microvascular networks. Experiments and simulation. Circulation Research. 1990;67:826–834. doi:10.1161/01.RES.67.4.826.

[105] Secomb TW, Bullock KV, Boas DA, Sakadžić S. The mass transfer coefficient for oxygen transport from blood to tissue in cerebral cortex. Journal of Cerebral Blood Flow & Metabolism. 2020;40(8):1634–1646. doi:10.1177/0271678X19870068.

[106] Celaya-Alcala JT, Lee GV, Smith AF, Li B, Sakadžić S, Boas DA, et al. Simulation of oxygen transport and estimation of tissue perfusion in extensive microvascular networks: Application to cerebral cortex. Journal of Cerebral Blood Flow & Metabolism. 2021;41(3):656–669. doi:10.1177/0271678X20927100.

[107] Gould IG, Tsai P, Kleinfeld D, Linninger A. The capillary bed offers the largest hemodynamic resistance to the cortical blood supply. Journal of Cerebral Blood Flow & Metabolism. 2017;37(1):52–68. doi:10.1177/0271678X16671146.

[108] Hartung G, Badr S, Moeini M, Lesage F, Kleinfeld D, Alaraj A, et al. Voxelized simulation of cerebral oxygen perfusion elucidates hypoxia in aged mouse cortex. PLOS Computational Biology. 2021;17(1):e1008584. doi:10.1371/journal.pcbi.1008584.

[109] Schmid F, Tsai PS, Kleinfeld D, Jenny P, Weber B. Depth-dependent flow and pressure characteristics in cortical microvascular networks. PLOS Computational Biology. 2017;13(2):1–22. doi:10.1371/journal.pcbi.1005392.

[110] Schmid F, Barrett MJP, Obrist D, Weber B, Jenny P. Red blood cells stabilize flow

in brain microvascular networks. PLOS Computational Biology. 2019;15(8):1–29. doi:10.1371/journal.pcbi.1007231.

[111] Schmid F, Conti G, Jenny P, Weber B. The severity of microstrokes depends on local vascular topology and baseline perfusion. eLife. 2021;10. doi:10.7554/eLife.60208.

[112] Windberger U, Bartholovitsch A, Plasenzetti R, Korak KJ, Heinze G. Whole blood viscosity, plasma viscosity and erythrocyte aggregation in nine mammalian species: Reference values and comparison of data. Experimental Physiology. 2003;88:431–440. doi:10.1113/eph8802496.

[113] Pries AR, Secomb TW, Gaehtgens P. The endothelial surface layer. Pflügers Archiv - European Journal of Physiology. 2000;440(5):653–666. doi:10.1007/s004240000307.

[114] Krüger T, Varnik F, Raabe D. Efficient and accurate simulations of deformable particles immersed in a fluid using a combined immersed boundary lattice Boltzmann finite element method. Computers and Mathematics with Applications. 2011;61(12):3485–3505. doi:10.1016/j.camwa.2010.03.057.

[115] Freund JB. Numerical Simulation of Flowing Blood Cells. Annual Review of Fluid Mechanics. 2014;46(1):67–95. doi:10.1146/annurev-fluid-010313-141349.

[116] Závodszky G, van Rooij B, Azizi V, Hoekstra A. Cellular level in-silico modeling of blood rheology with an improved material model for red blood cells. Frontiers in Physiology. 2017;8(AUG):1–14. doi:10.3389/fphys.2017.00563.

[117] Závodszky G, Van Rooij B, Czaja B, Azizi V, De Kanter D, Hoekstra AG. Red blood cell and platelet diffusivity and margination in the presence of cross-stream gradients in blood flows. Physics of Fluids. 2019;31(3). doi:10.1063/1.5085881.

[118] Bernabeu MO, Köry J, Grogan JA, Markelc B, Beardo A, D'Avezac M, et al. Abnormal morphology biases hematocrit distribution in tumor vasculature and contributes to heterogeneity in tissue oxygenation. Proceedings of the National Academy of Sciences of the United States of America. 2020;117(45):27811–27819. doi:10.1073/pnas.2007770117.

[119] Enjalbert R, Hardman D, Krüger T, Bernabeu MO. Compressed vessels bias red blood cell partitioning at bifurcations in a hematocrit-dependent manner: Implications in tumor blood flow. Proceedings of the National Academy of Sciences of the United States of America. 2021;118(25). doi:10.1073/pnas.2025236118.

[120] Fåhræus R. The suspension stability of the blood. Physiological Reviews. 1929;9:241–274. doi:10.1152/physrev.1929.9.2.241.

[121] Pries AR, Ley K, Claassen M, Gaehtgens P. Red cell distribution at microvascular bifurcations. Microvascular Research. 1989;38:81–101. doi:10.1016/0026-2862(89)90018-6.

[122] Rasmussen PM, Secomb TW, Pries AR. Modeling the hematocrit distribution in microcirculatory networks: A quantitative evaluation of a phase separation model. Microcirculation. 2018;25:1–17. doi:10.1111/micc.12445.

[123] Gould IG, Linninger AA. Hematocrit Distribution and Tissue Oxygenation in Large Microcirculatory Networks. Microcirculation. 2015;22(1):1–18. doi:10.1111/micc.12156.

[124] Freear A, El-Bouri WK, Payne SJ. Quantifying the effects of haematocrit variability in cerebral microvascular networks. In: VPH2020. Paris (online); 2020.

[125] Lee JJ, Piersanti E, Mardal KA, Rognes ME. A Mixed Finite Element Method for Nearly Incompressible Multiple-Network Poroelasticity. SIAM Journal on Scientific Computing. 2019;41:A722–A747. doi:10.1137/18M1182395.

[126] Vardakis JC, Guo L, Peach TW, Lassila T, Mitolo M, Chou D, et al. Fluid–structure interaction for highly complex, statistically defined, biological media: Homogenisation and a 3D multi-compartmental poroelastic model for brain biomechanics. Journal of Fluids and Structures. 2019;91:102641. doi:10.1016/j.jfluidstructs.2019.04.008.

[127] Ainslie PN, Duffin J. Integration of cerebrovascular CO_2 reactivity and chemoreflex control of breathing: mechanisms of regulation, measurement, and

interpretation. American Journal of Physiology-Regulatory, Integrative and Comparative Physiology. 2009;296:R1473–R1495. doi:10.1152/ajpregu.91008.2008.

[128] Claassen JAHR, Thijssen DHJ, Panerai RB, Faraci FM. Regulation of cerebral blood flow in humans: physiology and clinical implications of autoregulation. Physiological Reviews. 2021;101:1487–1559. doi:10.1152/physrev.00022.2020.

[129] Lassen NA. Cerebral Blood Flow and Oxygen Consumption in Man. Physiological Reviews. 1959;39:183–238. doi:10.1152/physrev.1959.39.2.183.

[130] Ursino M, Lodi CA. Interaction among autoregulation, CO ¡sub¿2¡/sub¿ reactivity, and intracranial pressure: a mathematical model. American Journal of Physiology-Heart and Circulatory Physiology. 1998;274:H1715–H1728. doi:10.1152/ajpheart.1998.274.5.H1715.

[131] Payne SJ. A model of the interaction between autoregulation and neural activation in the brain. Mathematical Biosciences. 2006;204:260–281. doi:10.1016/j.mbs.2006.08.006.

[132] Spronck B, Martens EGHJ, Gommer ED, van de Vosse FN. A lumped parameter model of cerebral blood flow control combining cerebral autoregulation and neurovascular coupling. American Journal of Physiology-Heart and Circulatory Physiology. 2012;303:H1143–H1153. doi:10.1152/ajpheart.00303.2012.

[133] Tong Z, Catherall M, Payne SJ. A multiscale model of cerebral autoregulation. Medical Engineering & Physics. 2021;95:51–63. doi:10.1016/j.medengphy.2021.08.003.

[134] Attwell D, Buchan AM, Charpak S, Lauritzen M, MacVicar BA, Newman EA. Glial and neuronal control of brain blood flow. Nature. 2010;468:232–243. doi:10.1038/nature09613.

[135] Hall CN, Reynell C, Gesslein B, Hamilton NB, Mishra A, Sutherland BA, et al. Capillary pericytes regulate cerebral blood flow in health and disease. Nature. 2014;508(1):55–60. doi:10.1038/nature13165.

[136] Milanovic S, Shaw K, Hall C, Payne S. Investigating the role of pericytes in cerebral

autoregulation: a modeling study. Physiological Measurement. 2021;42:054003. doi:10.1088/1361-6579/abfb0a.

[137] Vovenko E. Distribution of oxygen tension on the surface of arterioles, capillaries and venules of brain cortex and in tissue in normoxia: An experimental study on rats. Pflugers Archiv European Journal of Physiology. 1999;437:617–623. doi:10.1007/s004240050825.

[138] Ances BM, Buerk DG, Greenberg JH, Detre JA. Temporal dynamics of the partial pressure of brain tissue oxygen during functional forepaw stimulation in rats. Neuroscience Letters. 2001;306:106–110. doi:10.1016/S0304-3940(01)01868-7.

[139] Vazquez AL, Masamoto K, Kim SG. Dynamics of oxygen delivery and consumption during evoked neural stimulation using a compartment model and CBF and tissue PO2 measurements. NeuroImage. 2008;42:49–59. doi:10.1016/j.neuroimage.2008.04.024.

[140] Hossmann KA. The two pathophysiologies of focal brain ischemia: Implications for translational stroke research. Journal of Cerebral Blood Flow & Metabolism. 2012;32(7):1310–1316. doi:10.1038/jcbfm.2011.186.

[141] Severinghaus JW. Simple, accurate equations for human blood O2 dissociation computations. Journal of Applied Physiology. 1979;46:599–602. doi:10.1152/jappl.1979.46.3.599.

[142] Hellums JD, Nair PK, Huang NS, Ohshima N. Simulation of intraluminal gas transport processes in the microcirculation. Annals of Biomedical Engineering. 1995;24(S1):1–24. doi:10.1007/BF02770991.

[143] Secomb TW, Hsu R, Beamer NB, Coull BM. Theoretical Simulation of Oxygen Transport to Brain by Networks of Microvessels: Effects of Oxygen Supply and Demand on Tissue Hypoxia. Microcirculation. 2000;7(4):237–247. doi:10.1111/j.1549-8719.2000.tb00124.x.

[144] Secomb TW, Hsu R, Park EYH, Dewhirst MW. Green's function methods for analysis of oxygen delivery to tissue by microvascular

networks. Annals of Biomedical Engineering. 2004;32(11):1519–1529. doi:10.1114/B:ABME.0000049036.08817.44.

[145] Elliott KAC. Metabolism of brain tissue slices and suspensions from various mammals. Journal of Neurophysiology. 1948;11:473–484. doi:10.1152/jn.1948.11.6.473.

[146] Nelson SR, Mantz ML, Maxwell JA. Use of specific gravity in the measurement of cerebral edema. Journal of Applied Physiology. 1971;30(2):268–271. doi:10.1152/jappl.1971.30.2.268.

[147] Kety SS, Schmidt CF. The nitrous oxide method for the quantitative determination of cerebral blood flow in man: theory, procedure and normal values. The Journal of clinical investigation. 1948;27:476–83. doi:10.1172/JCI101994.

[148] Gleichmann U, Ingvar DH, Lassen NA, Lübbers DW, Siesjö BK, Thews G. Regional Cerebral Cortical Metabolic Rate of Oxygen and Carbon Dioxide, Related to the EEG in the Anesthetized Dog. Acta Physiologica Scandinavica. 1962;55(1):82–94. doi:10.1111/j.1748-1716.1962.tb02421.x.

[149] Ganfield RA, Nair P, Whalen WJ. Mass transfer, storage, and utilization of O2 in cat cerebral cortex. The American journal of physiology. 1970;219(3):814–821. doi:10.1152/ajplegacy.1970.219.3.814.

[150] Nilsson B, Siesjö BK. A Method for Determining Blood Flow and Oxygen Consumption in the Rat Brain. Acta Physiologica Scandinavica. 1976;96(1):72–82. doi:10.1111/j.1748-1716.1976.tb10172.x.

[151] Mintun MA, Raichle ME, Martin WRW, Herscovitch P. Brain oxygen utilization measured with O-15 radiotracers and positron emission tomography. Journal of Nuclear Medicine. 1984;25:177–87.

[152] Madsen PL, Holm S, Herning M, Lassen NA. Average blood flow and oxygen uptake in the human brain during resting wakefulness: A critical appraisal of the Kety-Schmidt technique. Journal of Cerebral Blood Flow & Metabolism. 1993;13:646–655. doi:10.1038/jcbfm.1993.83.

[153] Poulsen PH, Smith DF, Østergaard L, Danielsen EH, Gee A, Hansen SB, et al. In vivo estimation of cerebral blood flow, oxygen consumption and glucose metabolism in the pig by [15O]water injection, [15O]oxygen inhalation and dual injections of [18F]fluorodeoxyglucose. Journal of Neuroscience Methods. 1997;77:199–209. doi:10.1016/S0165-0270(97)00127-1.

[154] Cui W, Zhu XH, Vollmers ML, Colonna ET, Adriany G, Tramm B, et al. Non-invasive measurement of cerebral oxygen metabolism in the mouse brain by ultra-high field 17O MR spectroscopy. Journal of Cerebral Blood Flow & Metabolism. 2013;33:1846–1849. doi:10.1038/jcbfm.2013.172.

[155] Zhu XH, Chen JM, Tu TW, Chen W, Song SK. Simultaneous and noninvasive imaging of cerebral oxygen metabolic rate, blood flow and oxygen extraction fraction in stroke mice. NeuroImage. 2013;64:437–447. doi:10.1016/j.neuroimage.2012.09.028.

[156] Henriksen OM, Vestergaard MB, Lindberg U, Aachmann-Andersen NJ, Lisbjerg K, Christensen SJ, et al. Interindividual and regional relationship between cerebral blood flow and glucose metabolism in the resting brain. Journal of Applied Physiology. 2018;125:1080–1089. doi:10.1152/japplphysiol.00276.2018.

[157] Goldman D. Theoretical models of microvascular oxygen transport to tissue. Microcirculation. 2008;15(8):795–811. doi:10.1080/10739680801938289.

[158] Krogh A. The number and distribution of capillaries in muscles with calculations of the oxygen pressure head necessary for supplying the tissue. The Journal of Physiology. 1919;52:409–415. doi:10.1113/jphysiol.1919.sp001839.

[159] Sakadžic S, Yaseen MA, Jaswal R, Roussakis E, Dale AM, Buxton RB, et al. Two-photon microscopy measurement of cerebral metabolic rate of oxygen using periarteriolar oxygen concentration gradients. Neurophotonics. 2016;3:045005. doi:10.1117/1.nph.3.4.045005.

[160] Mintun MA, Lundstrom BN, Snyder AZ, Vlassenko AG, Shulman GL, Raichle ME. Blood flow and oxygen delivery to human brain during functional activity:

Theoretical modeling and experimental data. Proceedings of the National Academy of Sciences. 2001;98(12):6859–6864. doi:10.1073/pnas.111164398.

[161] Wieringa PA, Stassen HG, Kan JJV, Spaan JA. Oxygen diffusion in a network model of the myocardial microcirculation. International journal of microcirculation, clinical and experimental. 1993;13:137–69.

[162] Goldman D, Popel AS. A computational study of the effect of capillary network anastomoses and tortuosity on oxygen transport. Journal of Theoretical Biology. 2000;206:181–194. doi:10.1006/jtbi.2000.2113.

[163] Fang Q, Sakadžić S, Ruvinskaya L, Devor A, Dale AM, Boas DA. Oxygen advection and diffusion in a three-dimensional vascular anatomical network. Optics Express. 2008;16:17530. doi:10.1364/OE.16.017530.

[164] D'angelo C, Quarteroni A. On the coupling of 1d and 3d diffusion-reaction equations: application to tissue perfusion problems. Mathematical Models and Methods in Applied Sciences. 2008;18(08):1481–1504.

[165] Gagnon L, Sakadžić S, Lesage F, Musacchia JJ, Lefebvre X, Fang Q, et al. Quantifying the microvascular origin of bold-fMRI from first principles with two-photon microscopy and an oxygen-sensitive nanoprobe. Journal of Neuroscience. 2015;35:3663–3675. doi:10.1523/JNEUROSCI.3555-14.2015.

[166] Hsu R, Secomb TW. A Green's function method for analysis of oxygen delivery to tissue by microvascular networks. Mathematical Biosciences. 1989;96(1):61–78. doi:10.1016/0025-5564(89)90083-7.

[167] Secomb TW, Alberding JP, Hsu R, Dewhirst MW, Pries AR. Angiogenesis: An Adaptive Dynamic Biological Patterning Problem. PLOS Computational Biology. 2013;9(3):1–12. doi:10.1371/journal.pcbi.1002983.

[168] Sweeney PW, Walker-Samuel S, Shipley RJ. Insights into cerebral haemodynamics and oxygenation utilising in vivo mural cell imaging and mathematical modelling. Scientific Reports. 2018;8:1–15. doi:10.1038/s41598-017-19086-z.

[169] Heijtel DFR, Mutsaerts HJMM, Bakker E, Schober P, Stevens MF, Petersen

ET, et al. Accuracy and precision of pseudo-continuous arterial spin labeling perfusion during baseline and hypercapnia: A head-to-head comparison with 15O H2O positron emission tomography. NeuroImage. 2014;92:182–192. doi:10.1016/j.neuroimage.2014.02.011.

[170] Chi OZ, Wei HM, Tse J, Klein SL, Weiss HR. Cerebral Microregional Oxygen Balance During Chronic Versus Acute Hypertension in Middle Cerebral Artery Occluded Rats. Anesthesia & Analgesia. 1996;82(3):587–592. doi:10.1097/00000539-199603000-00028.

[171] Golub AS, Pittman RN. Oxygen dependence of respiration in rat spinotrapezius muscle in situ. American Journal of Physiology - Heart and Circulatory Physiology. 2012;303(1):H47–H56. doi:10.1152/ajpheart.00131.2012.

[172] Wang J, Payne SJ. Mathematical modelling of haemorrhagic transformation after ischaemic stroke. Journal of Theoretical Biology. 2021;531:110920. doi:10.1016/j.jtbi.2021.110920.

[173] Wang J, van Kranendonk KR, El-Bouri W, Majoie CBLM, Payne SJ. Mathematical modelling of haemorrhagic transformation within a multi-scale microvasculature network. Physiological Measurement. 2022;doi:10.1088/1361-6579/ac6cc5.

[174] Broderick JP, Adeoye O, Elm J. Evolution of the Modified Rankin Scale and Its Use in Future Stroke Trials. Stroke. 2017;48:2007–2012. doi:10.1161/STROKEAHA.117.017866.

[175] Saver JL, Goyal M, van der Lugt A, Menon BK, Majoie CBLM, Dippel DW, et al. Time to Treatment With Endovascular Thrombectomy and Outcomes From Ischemic Stroke: A Meta-analysis. JAMA. 2016;316:1279–1288. doi:10.1001/jama.2016.13647.

[176] Jovin TG, Chamorro A, Cobo E, de Miquel MA, Molina CA, Rovira A, et al. Thrombectomy within 8 Hours after Symptom Onset in Ischemic Stroke. New England Journal of Medicine. 2015;372(24):2296–2306. doi:10.1056/nejmoa1503780.

[177] Goyal M, Menon BK, Van Zwam WH, Dippel DWJ, Mitchell PJ, Demchuk

AM, et al. Endovascular thrombectomy after large-vessel ischaemic stroke: A meta-analysis of individual patient data from five randomised trials. The Lancet. 2016;387(10029):1723–1731. doi:10.1016/S0140-6736(16)00163-X.

[178] Suzuki K, Matsumaru Y, Takeuchi M, Morimoto M, Kanazawa R, Takayama Y, et al. Effect of Mechanical Thrombectomy without vs with Intravenous Thrombolysis on Functional Outcome among Patients with Acute Ischemic Stroke: The SKIP Randomized Clinical Trial. JAMA. 2021;325:244–253. doi:10.1001/jama.2020.23522.

[179] Wintermark M, Sesay M, Barbier E, Borbély K, Dillon WP, Eastwood JD, et al. Comparative Overview of Brain Perfusion Imaging Techniques. Stroke. 2005;36. doi:10.1161/01.str.0000177884.72657.8b.

[180] Muir KW, Macrae IM. Neuroimaging as a Selection Tool and Endpoint in Clinical and Pre-clinical Trials. Translational Stroke Research. 2016;7:368–377. doi:10.1007/s12975-016-0487-1.

[181] Kidwell CS, Saver JL, Mattiello J, Starkman S, Vinuela F, Duckwiler G, et al. Thrombolytic reversal of acute human cerebral ischemic injury shown by diffusion/perfusion magnetic resonance imaging. Annals of neurology. 2000;47:462–469.

[182] Molina CA. Reperfusion Therapies for Acute Ischemic Stroke: Current Pharmacological and Mechanical Approaches. Stroke. 2011;42(1, Supplement 1):S16–S19. doi:10.1161/STROKEAHA.110.598763.

[183] Chueh JY, Kühn AL, Puri AS, Wilson SD, Wakhloo AK, Gounis MJ. Reduction in distal emboli with proximal flow control during mechanical thrombectomy: A quantitative in vitro study. Stroke. 2013;44(5):1396–1401. doi:10.1161/STROKEAHA.111.670463.

[184] Yemisci M, Gursoy-Ozdemir Y, Vural A, Can A, Topalkara K, Dalkara T. Pericyte contraction induced by oxidative-nitrative stress impairs capillary reflow

despite successful opening of an occluded cerebral artery. Nature Medicine. 2009;15(9):1031–1037. doi:10.1038/nm.2022.

[185] El Amki M, Glück C, Binder N, Middleham W, Wyss MT, Weiss T, et al. Neutrophils Obstructing Brain Capillaries Are a Major Cause of No-Reflow in Ischemic Stroke. Cell Reports. 2020;33(2):108260. doi:10.1016/j.celrep.2020.108260.

[186] Erdener Şefik E, Tang J, Kılıç K, Postnov D, Giblin JT, Kura S, et al. Dynamic capillary stalls in reperfused ischemic penumbra contribute to injury: A hyperacute role for neutrophils in persistent traffic jams. Journal of Cerebral Blood Flow & Metabolism. 2021;41:236–252. doi:10.1177/0271678X20914179.

[187] Yang GY, Lorris Betz A. Reperfusion-induced injury to the blood-brain barrier after middle cerebral artery occlusion in rats. Stroke. 1994;25(8):1658–1664. doi:10.1161/01.STR.25.8.1658.

[188] Lam CK, Yoo T, Hiner B, Liu Z, Grutzendler J. Embolus extravasation is an alternative mechanism for cerebral microvascular recanalization. Nature. 2010;465(7297):478–482. doi:10.1038/nature09001.

[189] Grutzendler J, Murikinati S, Hiner B, Ji L, Lam CK, Yoo T, et al. Angiophagy Prevents Early Embolus Washout But Recanalizes Microvessels Through Embolus Extravasation. Science Translational Medicine. 2014;6(226):226ra31. doi:10.1126/scitranslmed.3006585.

[190] Reeson P, Choi K, Brown CE. VEGF signaling regulates the fate of obstructed capillaries in mouse cortex. eLife. 2018;7:1–26. doi:10.7554/eLife.33670.

[191] Herson PS, Traystman RJ. Animal models of stroke: translational potential at present and in 2050. Future Neurology. 2014;9:541–551. doi:10.2217/fnl.14.44.

[192] Pound P, Ritskes-Hoitinga M. Is it possible to overcome issues of external validity in preclinical animal research? Why most animal models are bound to fail. Journal of Translational Medicine. 2018;16:304. doi:10.1186/s12967-018-1678-1.

[193] Cruz Hernández JC, Bracko O, Kersbergen CJ, Muse V, Haft-Javaherian M, Berg M, et al. Neutrophil adhesion in brain capillaries reduces cortical blood

flow and impairs memory function in Alzheimer's disease mouse models. Nature Neuroscience. 2019;22(3):413–420. doi:10.1038/s41593-018-0329-4.

[194] Daneman R, Prat A. The Blood–Brain Barrier. Cold Spring Harbor Perspectives in Biology. 2015;7:a020412. doi:10.1101/cshperspect.a020412.

[195] Abbott NJ, Patabendige AAK, Dolman DEM, Yusof SR, Begley DJ. Structure and function of the blood–brain barrier. Neurobiology of Disease. 2010;37(1):13–25. doi:10.1016/j.nbd.2009.07.030.

[196] Attwell D, Laughlin SB. An energy budget for signaling in the grey matter of the brain. Journal of Cerebral Blood Flow & Metabolism. 2001;21:1133–1145. doi:10.1097/00004647-200110000-00001.

[197] Howarth C, Gleeson P, Attwell D. Updated energy budgets for neural computation in the neocortex and cerebellum. Journal of Cerebral Blood Flow & Metabolism. 2012;32:1222–1232. doi:10.1038/jcbfm.2012.35.

[198] Levitan IB, Kaczmarek LK. The Neuron: Cell and Molecular Biology. 4th ed. Oxford University Press; 2015. Available from: `http://www.oxfordmedicine.com/view/10.1093/med/9780199773893.001.0001/med-9780199773893`.

[199] Aubert A, Costalat R. Interaction between astrocytes and neurons studied using a mathematical model of compartmentalized energy metabolism. Journal of Cerebral Blood Flow & Metabolism. 2005;25:1476–1490. doi:10.1038/sj.jcbfm.9600144.

[200] Bélanger M, Allaman I, Magistretti PJ. Brain energy metabolism: Focus on Astrocyte-neuron metabolic cooperation. Cell Metabolism. 2011;14(6):724–738. doi:10.1016/j.cmet.2011.08.016.

[201] Haydon PG, Nedergaard M. How do astrocytes participate in neural plasticity? Cold Spring Harbor Perspectives in Biology. 2015;7(3):1–16. doi:10.1101/cshperspect.a020438.

[202] Goyal M, Ospel JM, Menon B, Almekhlafi M, Jayaraman M, Fiehler J, et al. Challenging the Ischemic Core Concept in Acute Ischemic Stroke Imaging. Stroke. 2020; p. 3147–3155. doi:10.1161/STROKEAHA.120.030620.

[203] Marchal G, Rioux P, Petit-Tabou MC, Derlon JM, Baron JC, Serrati C, et al. PET imaging of cerebral perfusion and oxygen consumption in acute ischaemic stroke: relation to outcome. The Lancet. 1993;341:925–927. doi:10.1016/0140-6736(93)91214-7.

[204] Donnan GA, Davis SM. Neuroimaging, the ischaemic penumbra, and selection of patients for acute stroke therapy. The Lancet Neurology. 2002;1:417–425. doi:10.1016/S1474-4422(02)00189-8.

[205] Harston GWJ, Tee YK, Blockley N, Okell TW, Thandeswaran S, Shaya G, et al. Identifying the ischaemic penumbra using pH-weighted magnetic resonance imaging. Brain. 2015;138:36–42. doi:10.1093/brain/awu374.

[206] Koopman MS, Berkhemer OA, Geuskens RREG, Emmer BJ, van Walderveen MAA, Jenniskens SFM, et al. Comparison of three commonly used CT perfusion software packages in patients with acute ischemic stroke. Journal of NeuroInterventional Surgery. 2019;11:1249–1256. doi:10.1136/neurintsurg-2019-014822.

[207] Peerlings D, van Ommen F, Bennink E, Dankbaar JW, Velthuis BK, Emmer BJ, et al. Probability maps classify ischemic stroke regions more accurately than CT perfusion summary maps. European Radiology. 2022;32:6367–6375. doi:10.1007/s00330-022-08700-y.

[208] Bristow MS, Simon JE, Brown RA, Eliasziw M, Hill MD, Coutts SB, et al. MR perfusion and diffusion in acute ischemic stroke: Human gray and white matter have different thresholds for infarction. Journal of Cerebral Blood Flow & Metabolism. 2005;25:1280–1287. doi:10.1038/sj.jcbfm.9600135.

[209] Markus HS. Cerebral perfusion and stroke. Journal of Neurology, Neurosurgery & Psychiatry. 2004;75:353–361. doi:10.1136/jnnp.2003.025825.

[210] O'Neill DP, Peng T, Stiegler P, Mayrhauser U, Koestenbauer S, Tscheliessnigg K, et al. A three-state mathematical model of hyperthermic cell death. Annals of Biomedical Engineering. 2011;39:570–579. doi:10.1007/s10439-010-0177-1.

[211] Dijkhuizen RM, Sprenkel JWBVD, Tulleken KAF, Nicolay K. Regional assessment

of tissue oxygenation and the temporal evolution of hemodynamic parameters and water diffusion during acute focal ischemia in rat brain. Brain Research. 1997;750:161–170. doi:10.1016/S0006-8993(96)01343-1.

[212] Revett K, Ruppin E, Goodall S, Reggia JA. Spreading depression in focal ischemia: A computational study. Journal of Cerebral Blood Flow & Metabolism. 1998;18:998–1007. doi:10.1097/00004647-199809000-00009.

[213] Ruppin E, Ofer E, Reggia JA, Revett K, Goodall S. Pathogenic mechanisms in ischemic damage: a computational study. Computers in Biology and Medicine. 1999;29:39–59. doi:10.1016/S0010-4825(98)00044-4.

[214] Dronne MA, Boissel JP, Grenier E, Gilquin H, Cucherat M, Hommel M, et al. Mathematical modelling of an ischemic stroke: An integrative approach. Acta Biotheoretica. 2004;52:255–272. doi:10.1023/B:ACBI.0000046597.53669.ff.

[215] Chapuisat G, Dronne MA, Grenier E, Hommel M, Boissel JP. In Silico Study of the Influence of Intensity and Duration of Blood Flow Reduction on Cell Death Through Necrosis or Apoptosis During Acute Ischemic Stroke. Acta Biotheoretica. 2010;58:171–190. doi:10.1007/s10441-010-9100-2.

[216] DeGracia DJ, Huang ZF, Huang S. A nonlinear dynamical theory of cell injury. Journal of Cerebral Blood Flow & Metabolism. 2012;32:1000–1013. doi:10.1038/jcbfm.2012.10.

[217] Lang GE, Vella D, Waters SL, Goriely A. Propagation of damage in brain tissue: coupling the mechanics of oedema and oxygen delivery. Biomechanics and Modeling in Mechanobiology. 2015;14:1197–1216. doi:10.1007/s10237-015-0665-1.

[218] Lang GE, Vella D, Waters SL, Goriely A. Mathematical modelling of blood-brain barrier failure and oedema. Mathematical medicine and biology : a journal of the IMA. 2017;34:391–414. doi:10.1093/imammb/dqw009.

[219] Xue Y, El-Bouri WK, Józsa TI, Payne SJ. Modelling the effects of cerebral microthrombi on tissue oxygenation and cell death. Journal of Biomechanics. 2021;127:110705. doi:10.1016/j.jbiomech.2021.110705.

[220] Johnson CO, Nguyen M, Roth GA, Nichols E, Alam T, Abate D, et al. Global, regional, and national burden of stroke, 1990–2016: a systematic analysis for the Global Burden of Disease Study 2016. The Lancet Neurology. 2019;18(5):439–458. doi:10.1016/S1474-4422(19)30034-1.

[221] Gobin YP, Starkman S, Duckwiler GR, Grobelny T, Kidwell CS, Jahan R, et al. MERCI 1: A phase 1 study of mechanical embolus removal in cerebral ischemia. Stroke. 2004;35:2848–2853. doi:10.1161/01.STR.0000147718.12954.60.

[222] van Veluw SJ, Shih AY, Smith EE, Chen C, Schneider JA, Wardlaw JM, et al. Detection, risk factors, and functional consequences of cerebral microinfarcts. The Lancet Neurology. 2017;16(9):730–740. doi:10.1016/S1474-4422(17)30196-5.

[223] Virtanen P, Gommers R, Oliphant TE, Haberland M, Reddy T, Cournapeau D, et al. SciPy 1.0: fundamental algorithms for scientific computing in Python. Nature Methods. 2020;17:261–272. doi:10.1038/s41592-019-0686-2.

[224] Baek JH, Yoo J, Song D, Kim YD, Nam HS, Kim BM, et al. Predictive value of thrombus volume for recanalization in stent retriever thrombectomy. Scientific Reports. 2017;7(1):15938. doi:10.1038/s41598-017-16274-9.

[225] Xue Y, Georgakopoulou T, van der Wijk AE, Józsa TI, van Bavel E, Payne SJ. Quantification of hypoxic regions distant from occlusions in cerebral penetrating arteriole trees. PLOS Computational Biology. 2022;18:e1010166. doi:10.1371/journal.pcbi.1010166.

[226] Tarumi T, Zhang R. Cerebral blood flow in normal aging adults: cardiovascular determinants, clinical implications, and aerobic fitness. Journal of Neurochemistry. 2018;144:595–608. doi:10.1111/jnc.14234.

[227] Boas DA, Strangman G, Culver JP, Hoge RD, Jasdzewski G, Poldrack RA, et al. Can the cerebral metabolic rate of oxygen be estimated with near-infrared spectroscopy? Physics in Medicine and Biology. 2003;48:2405–2418. doi:10.1088/0031-9155/48/15/311.

[228] Sutton R. Reflex syncope: Diagnosis and treatment. Journal of Arrhythmia. 2017;33:545–552. doi:10.1016/j.joa.2017.03.007.

[229] Andersen LW, Holmberg MJ, Berg KM, Donnino MW, Granfeldt A. In-Hospital Cardiac Arrest. JAMA. 2019;321:1200. doi:10.1001/jama.2019.1696.

[230] Hankey GJ. Stroke. The Lancet. 2017;389:641–654. doi:10.1016/S0140-6736(16)30962-X.

[231] Goldberg I, Auriel E, Russell D, Korczyn AD. Microembolism, silent brain infarcts and dementia. Journal of the Neurological Sciences. 2012;322:250–253. doi:10.1016/j.jns.2012.02.021.

[232] Vuković-Cvetković V. Microembolus Detection by Transcranial Doppler Sonography: Review of the Literature. Stroke Research and Treatment. 2012;2012:1–7. doi:10.1155/2012/382361.

[233] Sheriff F, Diz-Lopes M, Khawaja A, Sorond F, Tan CO, Azevedo E, et al. Microemboli After Successful Thrombectomy Do Not Affect Outcome but Predict New Embolic Events. Stroke. 2020;51:154–161. doi:10.1161/STROKEAHA.119.025856.

[234] Grutzendler J. Angiophagy: mechanism of microvascular recanalization independent of the fibrinolytic system. Stroke. 2013;44:S84–6. doi:10.1161/STROKEAHA.112.678730.

[235] Mayzel-Oreg O, Omae T, Kazemi M, Li F, Fisher M, Cohen Y, et al. Microsphere-induced embolic stroke: An MRI study. Magnetic Resonance in Medicine. 2004;51:1232–1238. doi:10.1002/mrm.20100.

[236] Miyake K, Takeo S, Kaijihara H. Sustained decrease in brain regional blood flow after microsphere embolism in rats. Stroke. 1993;24:415–420. doi:10.1161/01.str.24.3.415.

[237] Rapp JH, Pan XM, Yu B, Swanson RA, Higashida RT, Simpson P, et al. Cerebral Ischemia and Infarction From Atheroemboli¡100 μm in size. Stroke. 2003;34:1976–1980. doi:10.1161/01.STR.0000083400.80296.38.

[238] Tsai MJ, Tsai YH, Kuo YM. Characterization of the pattern of ischemic stroke induced by artificial particle embolization in the rat brain. Biomaterials. 2011;32:6381–6388. doi:10.1016/j.biomaterials.2011.05.051.

[239] Lyden PD, Zivin JA, Chabolla DR, Jacobs MA, Gage FH. Quantitative effects of cerebral infarction on spatial learning in rats. Experimental Neurology. 1992;116:122–132. doi:10.1016/0014-4886(92)90160-R.

[240] Zhang HA, Gao M, Chen B, Shi L, Wang Q, Yu X, et al. Evaluation of Hippocampal Injury and Cognitive Function Induced by Embolization in the Rat Brain. The Anatomical Record. 2013;296:1207–1214. doi:10.1002/ar.22715.

[241] Rapp JH, Pan XM, Neumann M, Hong M, Hollenbeck K, Liu J. Microemboli Composed of Cholesterol Crystals Disrupt the Blood-Brain Barrier and Reduce Cognition. Stroke. 2008;39:2354–2361. doi:10.1161/STROKEAHA.107.496737.

[242] Taylor ZJ, Hui ES, Watson AN, Nie X, Deardorff RL, Jensen JH, et al. Microvascular basis for growth of small infarcts following occlusion of single penetrating arterioles in mouse cortex. Journal of Cerebral Blood Flow & Metabolism. 2016;36:1357–1373. doi:10.1177/0271678X15608388.

[243] Beishon L, Clough RH, Kadicheeni M, Chithiramohan T, Panerai RB, Haunton VJ, et al. Vascular and haemodynamic issues of brain ageing. Pflügers Archiv - European Journal of Physiology. 2021;473:735–751. doi:10.1007/s00424-020-02508-9.

[244] Goirand F, Le Borgne T, Lorthois S. Network-driven anomalous transport is a fundamental component of brain microvascular dysfunction. Nature Communications. 2021;12(1):7295. doi:10.1038/s41467-021-27534-8.

[245] Risser L, Plouraboué F, Cloetens P, Fonta C. A 3D-investigation shows that angiogenesis in primate cerebral cortex mainly occurs at capillary level. International Journal of Developmental Neuroscience. 2009;27:185–196. doi:10.1016/j.ijdevneu.2008.10.006.

[246] Zhu L, Hoffmann A, Wintermark M, Pan X, Tu R, Rapp JH. Do Microemboli Reach

the Brain Penetrating Arteries? Journal of Surgical Research. 2012;176:679–683. doi:10.1016/j.jss.2011.09.059.

[247] Esipova TV, Barrett MJP, Erlebach E, Masunov AE, Weber B, Vinogradov SA. Oxyphor 2P: A High-Performance Probe for Deep-Tissue Longitudinal Oxygen Imaging. Cell Metabolism. 2019;29:736–744.e7. doi:10.1016/j.cmet.2018.12.022.

[248] Gómez-de Frutos MC, García-Suárez I, Laso-García F, Diekhorst L, Otero-Ortega L, Alonso-López E, et al. Identification of brain structures and blood vessels by conventional ultrasound in rats. Journal of Neuroscience Methods. 2020;346:108935. doi:10.1016/j.jneumeth.2020.108935.

[249] Lugo-Hernandez E, Squire A, Hagemann N, Brenzel A, Sardari M, Schlechter J, et al. 3D visualization and quantification of microvessels in the whole ischemic mouse brain using solvent-based clearing and light sheet microscopy. Journal of Cerebral Blood Flow & Metabolism. 2017;37:3355–3367. doi:10.1177/0271678X17698970.

[250] Zhang MQ, Sun DN, Xie YY, Peng GY, Xia J, Long HY, et al. Three-dimensional visualization of rat brain microvasculature following permanent focal ischaemia by synchrotron radiation. The British Journal of Radiology. 2014;87:20130670. doi:10.1259/bjr.20130670.

[251] Zhang LY, Lin P, Pan J, Ma Y, Wei Z, Jiang L, et al. CLARITY for High-resolution Imaging and Quantification of Vasculature in the Whole Mouse Brain. Aging and disease. 2018;9:262. doi:10.14336/AD.2017.0613.

[252] Smith AF, Doyeux V, Berg M, Peyrounette M, Haft-Javaherian M, Larue AE, et al. Brain capillary networks across species: A few simple organizational requirements are sufficient to reproduce both structure and function. Frontiers in Physiology. 2019;10(MAR):1–22. doi:10.3389/fphys.2019.00233.

[253] Miller C, Padmos RM, van der Kolk M, Józsa TI, Samuels N, Xue Y, et al. In silico trials for treatment of acute ischemic stroke: Design

and implementation. Computers in biology and medicine. 2021;137:104802. doi:10.1016/j.compbiomed.2021.104802.

[254] Xue Y, Józsa TI, Payne SJ. Modelling human cerebral tissue damage caused by acute ischaemic stroke. In: 9th World Congress of Biomechanics. Taipei (online); 2022.

[255] Inoue M, Mlynash M, Christensen S, Wheeler HM, Straka M, Tipirneni A, et al. Early Diffusion-Weighted Imaging Reversal After Endovascular Reperfusion Is Typically Transient in Patients Imaged 3 to 6 Hours After Onset. Stroke. 2014;45:1024–1028. doi:10.1161/STROKEAHA.113.002135.

[256] Bala F, Ospel J, Mulpur B, Kim BJ, Yoo J, Menon BK, et al. Infarct Growth despite Successful Endovascular Reperfusion in Acute Ischemic Stroke: A Meta-analysis. American Journal of Neuroradiology. 2021;42:1472–1478. doi:10.3174/ajnr.A7177.

[257] Padmos RM, Józsa TI, El-Bouri WK, Závodszky G, Payne SJ, Hoekstra AG. Two-Way Coupling Between 1D Blood Flow and 3D Tissue Perfusion Models. In: Paszynski M, Kranzlmüller D, Krzhizhanovskaya VV, Dongarra JJ, Sloot PMA, editors. Computational Science – ICCS 2021. Cham: Springer International Publishing; 2021. p. 670–683.

[258] Arakawa S, Wright PM, Koga M, Phan TG, Reutens DC, Lim I, et al. Ischemic Thresholds for Gray and White Matter. Stroke. 2006;37:1211–1216. doi:10.1161/01.STR.0000217258.63925.6b.

[259] Chen C, Bivard A, Lin L, Levi CR, Spratt NJ, Parsons MW. Thresholds for infarction vary between gray matter and white matter in acute ischemic stroke: A CT perfusion study. Journal of Cerebral Blood Flow & Metabolism. 2019;39:536–546. doi:10.1177/0271678X17744453.

[260] Strogatz SH. Nonlinear Dynamics and Chaos. CRC Press; 2018. Available from: https://www.taylorfrancis.com/books/9780429961113.

[261] Roberts TPL, Rowley HA. Diffusion weighted magnetic resonance

imaging in stroke. European Journal of Radiology. 2003;45:185–194. doi:10.1016/S0720-048X(02)00305-4.

[262] Chopard B, Droz M. Cellular automata model for the diffusion equation. Journal of Statistical Physics. 1991;64:859–892. doi:10.1007/BF01048321.

[263] w Secomb T. A Green's function method for simulation of time-dependent solute transport and reaction in realistic microvascular geometries. Mathematical Medicine and Biology. 2016;33:475–494. doi:10.1093/imammb/dqv031.

[264] Józsa TI, Petr J, Barkhof F, Payne SJ, Mutsaerts HJMM. MRI-based computational model generation for cerebral perfusion simulations in health and ischaemic stroke. bioRxiv. 2022;doi:10.1101/2022.09.07.506940.

[265] Attwell D, Mishra A, Hall CN, O'Farrell FM, Dalkara T. What is a pericyte? Journal of Cerebral Blood Flow & Metabolism. 2016;36:451–455. doi:10.1177/0271678X15610340.

[266] Di Z, Wu X, Xie W, Lin X. Effect of Pericytes on Cerebral Microvasculature at Different Time Points of Stroke. BioMed Research International. 2021;2021:1–10. doi:10.1155/2021/5281182.

[267] Mazzeo MD, Coveney PV. HemeLB: A high performance parallel lattice-Boltzmann code for large scale fluid flow in complex geometries. Computer Physics Communications. 2008;178:894–914. doi:10.1016/j.cpc.2008.02.013.

[268] Krüger T, Holmes D, Coveney PV. Deformability-based red blood cell separation in deterministic lateral displacement devices—A simulation study. Biomicrofluidics. 2014;8:054114. doi:10.1063/1.4897913.

[269] Zhou Q, Fidalgo J, Calvi L, Bernabeu MO, Hoskins PR, Oliveira MSN, et al. Spatiotemporal Dynamics of Dilute Red Blood Cell Suspensions in Low-Inertia Microchannel Flow. Biophysical Journal. 2020;118:2561–2573. doi:10.1016/j.bpj.2020.03.019.

[270] Johnson S, Chueh J, Gounis MJ, McCarthy R, McGarry JP, McHugh PE, et al. Mechanical behavior of in vitro blood clots and the implications for acute ischemic

stroke treatment. Journal of NeuroInterventional Surgery. 2020;12:853–857. doi:10.1136/neurintsurg-2019-015489.

[271] Dwivedi A, Glynn A, Johnson S, Duffy S, Fereidoonnezhad B, McGarry P, et al. Measuring the effect of thrombosis, thrombus maturation and thrombolysis on clot mechanical properties in an in-vitro model. Journal of Biomechanics. 2021;129:110731. doi:10.1016/j.jbiomech.2021.110731.

[272] Kühn AL, Vardar Z, Kraitem A, King RM, Anagnostakou V, Puri AS, et al. Biomechanics and hemodynamics of stent-retrievers. Journal of Cerebral Blood Flow & Metabolism. 2020;40:2350–2365. doi:10.1177/0271678X20916002.

[273] Bredno J, Olszewski ME, Wintermark M. Simulation model for contrast agent dynamics in brain perfusion scans. Magnetic Resonance in Medicine. 2010;64:280–290. doi:10.1002/mrm.22431.

[274] Vahidkhah K, Diamond S, Bagchi P. Platelet Dynamics in Three-Dimensional Simulation of Whole Blood. Biophysical Journal. 2014;106:2529–2540. doi:10.1016/j.bpj.2014.04.028.

[275] Pias SC. How does oxygen diffuse from capillaries to tissue mitochondria? Barriers and pathways. The Journal of Physiology. 2021;599:1769–1782. doi:10.1113/JP278815.

[276] Wiemerslage L, Lee D. Quantification of mitochondrial morphology in neurites of dopaminergic neurons using multiple parameters. Journal of Neuroscience Methods. 2016;262:56–65. doi:10.1016/j.jneumeth.2016.01.008.

[277] Santuy A, Turégano-López M, Rodríguez JR, Alonso-Nanclares L, DeFelipe J, Merchán-Pérez A. A Quantitative Study on the Distribution of Mitochondria in the Neuropil of the Juvenile Rat Somatosensory Cortex. Cerebral Cortex. 2018;28:3673–3684. doi:10.1093/cercor/bhy159.

[278] El-Bouri WK, Payne SJ. Multi-scale homogenization of the mass transport equation in periodic capillary networks. In: CMBE2015. France; 2015.

[279] Russell MJ, Jensen OE, Galla T. Stochastic transport in the presence of spatial

disorder: Fluctuation-induced corrections to homogenization. Physical Review E. 2016;94. doi:10.1103/PhysRevE.94.042121.

[280] Russell MJ, Jensen OE. Homogenization approximations for unidirectional transport past randomly distributed sinks. IMA Journal of Applied Mathematics (Institute of Mathematics and Its Applications). 2020;85:161–189. doi:10.1093/imamat/hxz004.

[281] Price GF, Chernyavsky IL, Jensen OE. Advection-dominated transport past isolated disordered sinks: stepping beyond homogenization. Proceedings of the Royal Society A: Mathematical, Physical and Engineering Sciences. 2022;478. doi:10.1098/rspa.2022.0032.

[282] Brown WR, Thore CR. Review: Cerebral microvascular pathology in ageing and neurodegeneration. Neuropathology and Applied Neurobiology. 2011;37:56–74. doi:10.1111/j.1365-2990.2010.01139.x.

[283] Smith LA, Melbourne A, Owen D, Cardoso MJ, Sudre CH, Tillin T, et al. Cortical cerebral blood flow in ageing: effects of haematocrit, sex, ethnicity and diabetes. European Radiology. 2019;29:5549–5558. doi:10.1007/s00330-019-06096-w.

[284] Graff BJ, Harrison SL, Payne SJ, El-Bouri WK. Regional Cerebral Blood Flow Changes in Healthy Ageing and Alzheimer's Disease: A Narrative Review. Cerebrovascular Diseases. 2022; p. 1–10. doi:10.1159/000524797.

[285] Graff BJ, Payne SJ, El-Bouri WK. The Ageing Brain: Investigating the Role of Age in Changes to the Human Cerebral Microvasculature With an in silico Model. Frontiers in Aging Neuroscience. 2021;13. doi:10.3389/fnagi.2021.632521.

[286] Fox PT, Raichle ME. Focal physiological uncoupling of cerebral blood flow and oxidative metabolism during somatosensory stimulation in human subjects. Proceedings of the National Academy of Sciences. 1986;83:1140–1144. doi:10.1073/pnas.83.4.1140.